

Oliver T. Hofmann

Structure-to-Property Relationships in Metal/Organic Interfaces

DOCTORAL THESIS

For obtaining the academic degree of

Doktor der technischen Wissenschaften

Doctoral Programme of Technical Sciences
Technical Physics



Graz University of Technology

Supervisor:

Ao. Prof. Dr. techn. Egbert Zojer

Institute of Solid State Physics

Graz, October 2010

Deutsche Fassung:
Beschluss der Curricula-Kommission für Bachelor-, Master- und Diplomstudien vom 10.11.2008
Genehmigung des Senates am 1.12.2008

EIDESSTÄTTLICHE ERKLÄRUNG

Ich erkläre an Eides statt, dass ich die vorliegende Arbeit selbstständig verfasst, andere als die angegebenen Quellen/Hilfsmittel nicht benutzt, und die den benutzten Quellen wörtlich und inhaltlich entnommene Stellen als solche kenntlich gemacht habe.

Graz, am

.....
(Unterschrift)

Englische Fassung:

STATUTORY DECLARATION

I declare that I have authored this thesis independently, that I have not used other than the declared sources / resources, and that I have explicitly marked all material which has been quoted either literally or by content from the used sources.

.....
date

.....
(signature)

To my beloved wife, Susanne

Acknowledgments

I want to thank my supervisor, Egbert Zojer, for giving a chemist the opportunity to write this thesis in a physics department, for reading through the countless pages of reports and paper manuscripts that I produced, and for the long - not always serious - arguments of the strengths and weaknesses of DFT. Now, if there remains one good thing to say about DFT, that is: At least its not semiempirics.

I'd also to express my gratitude to Gerold Rangger for introducing me into VASP and SIESTA. Also, let me thank Georg Heimel for all his valueable input to my research, the patience to repeatedly read through 50+ pages of my confused conceptions of the processes on the interfaces, and for creating all these van-der-Waals parameters with me. Thanks also to Ferdinand Risser for all these long discussions about "what's really happening" (sometimes I'm not sure I understand anything anymore), and to David Egger for bridging the gap between self-assembled and charge-transfer monlayers that only existed in my own mind anyway. I'd also want to mention Mario Lang from the ZID, who provided quick and compentent support with all kind of computer troubles, making working with the clusters of the TU Graz a pleasure.

The time in this group would have been only half as fun and enjoyable without all the social activities. Thanks to Gerold for taking me to indoor-climbing and badminton when we just had to get out of office and away from our computers. Many thanks also to Anna Track for holding the "Egbert"-group together, for the good meals and for all the breaks, keeping us from getting overworked. Special thanks also to Piet Reuter, who kept the spirits high (pun intended) in those long Guitar Hero nights. Fortunately the Wii drums don't produce too much noise, or else I'd not be married today. I'm also glad Ferdinand Rissner came into our group and introduced the "helicopter trend". He did a great job to the model industry.

Last not least, I want to express my thanks and love to my familiy, both to the one I'm born into as well as to my in-laws, for all the help, and for supporting my desicion to get a PhD. Special thanks to my beloved wife, Susanne, who always listened to me and gave me hold. Without her, all this would not have been possible.

Abstract of the
PhD Thesis

Structure-to-Property Relationships in Metal/Organic Interfaces

Oliver T. Hofmann

*Institute of Solid State Physics, University of Technology, Graz
8010 Graz, Austria*

In the growing field of organic electronics, the junction between metal electrode and subsequently deposited organic material is one of the crucial part determining the functionality and efficiency of devices. In this work, relationships between the structure and the electronic properties of metal/organic interfaces are investigated. To that aim, theoretical calculations at the density functional theory level are presented for several systems and compared to experimental results where available. The studied systems include strong electron donor molecules, relatively large electron acceptor molecules, and an organic system which contains a dipolar group which is easily movable. Complementary studies are performed on all-organic interfaces consisting of covalently bound weak electron donors and acceptors, as well on three component systems involving metal surfaces and donor/acceptor charge-transfer complexes. From the information gathered in these studies, general structure-to-property relationships are formulated and tested on idealized model systems. In particular, the influence of the adsorption distance between metal and organic layer as well as the impact of the spatial position of dipole moments in charge-transfer metal/organic junctions is discussed. Both effects are investigated jointly in a study of N,N'-dialkylated viologens. Finally, a semi-classical model is developed which allows the estimation of the work-function modification induced by the adsorption of planar, π -conjugated molecules on coinage metal surfaces without an explicit treatment of the actual interface. To that aim, the processes occurring upon interface formation are revisited. Where possible, classical equations are applied, while quantum-mechanical effects are accounted for by an appropriate parameterization. The interdependence of the effects are treated self-consistently. Excellent results are obtained when applying the algorithm on a test set of more than 30 metal/organic combinations, with more than 90% of the predicted work-function modifications being within twice the error of the experiment.

Kurzfassung der
Doktorarbeit

Structure-to-Property Relationships in Metal/Organic Interfaces

Oliver T. Hofmann
Institut für Festkörperphysik, Technische Universität Graz
8010 Graz, Austria

Die Grenzfläche zwischen Elektrode und darauf aufgebrachtem organischen Material ist ein wichtiger, die Effizienz und Funktionalität bestimmender Teil von organoelektronischen Bauteilen. In dieser Arbeit werden Zusammenhänge zwischen dem Aufbau und den elektronischen Eigenschaften dieser Grenzflächen untersucht. Um Einsicht in die Wechselwirkungen zwischen den Teilsystemen zu erhalten werden Rechnungen auf Basis der Dichtefunktionaltheorie präsentiert. Soweit als möglich werden die Ergebnisse mit experimentellen Resultaten verglichen. Zu den untersuchten organischen Molekülen gehören starke Elektronendonoren, vergleichsweise große Elektronenakzeptoren, und ein metallorganisches System mit einer im Raum leicht bewegbaren, dipolaren Gruppe. Ergänzend wurden auch Rechnungen an rein organischen Grenzflächen, bestehend aus kovalent zu einander gebundenen schwachen Elektronendonoren und -akzeptoren, sowie an Dreikomponentengrenzflächen bestehend aus Metall und einem Donor/Akzeptor-Salz, durchgeführt. Aus der in diesen Studien gesammelten Informationen werden generell gültige "structure-to-property relationships" formuliert und an idealisierten Modellsystemen getestet. Insbesondere wird der Einfluss der Adsorptionsdistanz zwischen Metall und organischer Schicht sowie der Einfluss der räumlichen Position von Dipolmomenten in Metall / Organik Grenzflächen mit Ladungstransfercharakter diskutiert. Beide Effekte werden gemeinsam in einer Studie über N,N'-dialkylierte Viologene betrachtet. Schlussendlich wird ein semiklassisches Modell entwickelt, welches die Abschätzung der durch die Adsorption von planaren, π -konjugierten Molekülen induzierten Austrittsleistungsänderung ohne explizite Behandlung der Grenzfläche erlaubt. Dazu werden die Prozesse, die bei der Adsorption auftreten, noch einmal im Detail betrachtet. Soweit als möglich werden klassische Gleichungen zu deren Beschreibung angewandt, während quantenmechanische Effekte durch Parameterisierung berücksichtigt werden. Die wechselseitige Abhängigkeit der Effekte wird selbstkonsistent berücksichtigt. Die Anwendung des erhaltenen Algorithmus auf ein Testset von mehr als 30 Metall/Organik-System zeigt ausgezeichnete Resultate, wobei sich mehr als 90% der vorhergesagten Austrittsleistungsänderungen innerhalb des doppelten experimentellen Fehlers befinden.

Contents

1	Introduction	1
2	Theory and Employed Methodology	3
2.1	Current Understanding of Level Alignment in Metal/Organic Interfaces	3
2.1.1	Preface	3
2.1.2	Processes at the interface	3
2.1.3	Alternative Models	6
2.2	General Methodology	10
2.2.1	Preface	10
2.2.2	VASP	10
2.2.3	SIESTA	13
2.2.4	Gaussian03	14
2.3	Theoretical Background and Critical Assessment of the Employed Methodology	15
2.3.1	Preface	15
2.3.2	Basis sets	15
2.3.3	Density Functional Theory	18
2.3.4	Møller-Plesset perturbation theory	22
2.3.5	Configuration Interaction and Complete Active Space	28
3	Specific Systems	34
3.1	HV0 and TTF: Reducing the Metal Work Function beyond Pauli Push-back: A Computational Investigation of Tetrathiafulvalene and HV0 on Coinage Metal Surfaces	35
3.1.1	Preface	35
3.1.2	Abstract	36
3.1.3	Introduction	36
3.1.4	Methodology	38
3.1.5	Results and Discussion	39
3.1.6	Conclusion	51
3.1.7	Supporting Information	51
3.2	MV0: Gold work-function reduction by 2.2eV with an air-stable molecular donor layer	54
3.2.1	Preface	54
3.2.2	Experimental Setup	54
3.2.3	Experimental Results	55
3.2.4	Computational results	55
3.3	NMA: A High Molecular Weight Donor for Electron Injection Interlayers on Metal Electrodes	58

3.3.1	Preface	58
3.3.2	Geometries and optical excitation in solution	58
3.3.3	Metal/NMA-interfaces	60
3.4	HATCN as advanced hole-injection layer	63
3.4.1	Preface	63
3.4.2	Introduction	63
3.4.3	Experimental and Computational Details	64
3.4.4	HATCN on Ag(111)	66
3.4.5	Computational Investigation	69
3.4.6	Potential Application: Soft metallic contacts	75
3.4.7	HATCN on Cu(111)	79
3.4.8	HATCN on Au(111)	83
3.4.9	Conclusion	86
3.5	COHON	87
3.5.1	Preface	87
3.5.2	Computational Results	87
3.6	GaClPc: Orientational ordering and geometrical deformations of a molecule with a flexible dipole adsorbed on Cu(111)	90
3.6.1	Preface	90
3.6.2	Experimental Methodology	90
3.6.3	Experimental results	90
3.6.4	Computational Results	91
3.7	Cyclophanes: Organic/Organic interfaces with charge-transfer character?	97
3.7.1	Preface	97
3.7.2	Computational Methodology	97
3.7.3	First Generation Cyclophanes	98
3.7.4	Second Generation Cyclophanes	106
3.7.5	Third Generation Cyclophanes: Cyclophane substitutes	109
3.8	Three component interfaces	111
3.8.1	Preface	111
3.8.2	HV0 and F4TCNQ on Au(111)	111
3.8.3	F4TCNQ-HV0 on Ag (111)	117
3.8.4	HV0 on a Self-Assembled Monolayer	118
3.8.5	Conclusion	120
4	Structure-to-Property Relationships	121
4.1	Impact of the adsorption distance	122
4.1.1	Preface	122
4.1.2	Results and Discussion	122
4.1.3	Conclusion	125
4.2	Impact of the molecular bend: When do Dipoles Really Count?	126
4.2.1	Preface	126
4.2.2	Results and Discussion	127
4.2.3	Conclusion	135
4.2.4	Supporting Information	135

4.3	Work-function modification tuning by N,N'-dialkylation of doubly reduced viologen monolayers	143
4.3.1	Preface	143
4.3.2	Abstract	143
4.3.3	Introduction	144
4.3.4	Computational details and methodology	145
4.3.5	Adsorption geometries and energies	147
4.3.6	Interaction energy	148
4.3.7	Work-function modifications	152
4.3.8	Conclusion	156
4.3.9	Supporting Information	157
4.4	A Semi-Classical Model for fast Estimation of the Work-Function Modification Induced by Charge Transfer Monolayers	159
4.4.1	Preface	159
4.4.2	Abstract	159
4.4.3	Introduction	161
4.4.4	Current models	162
4.4.5	Results and Discussion	162
4.4.6	Conclusion	174
4.4.7	Methodology	174
4.4.8	APPENDIX: Limitations of the model	175
4.4.9	Supporting Information	176
5	Summary and Conclusion	183
6	Appendix: How to build flat organic donors / acceptors	187
6.1	Preface	187
6.2	Introduction	187
6.3	Methodology	190
6.4	Results and Discussion	190
6.4.1	Comparison of π -backbones	190
6.4.2	Conclusion	202
	Bibliography	205

1 Introduction

In recent decades the field of organic electronics has gained significant attention in the scientific community; not only have a myriad of articles been published, but also whole journals are now dedicated to this particular subject. Possible applications of organic electronic devices include light emitting devices (LEDs),^[1-3] thin film transistors (FETs),^[4-7] and organic photovoltaic cells (OPVs)^[1, 8, 9]. In December 2007, the development has reached a climax with the introduction of the first OLED-TV to the commercial market by Sony. Nonetheless, there is some consensus in the community that organic electronics won't be replacing inorganic technology anytime soon, if at all. Rather, organics will find a place *beside* inorganic, where each technology has its own strengths: Whereas silicon based devices are in general faster, smaller, and more durable, organic electronics prove advantageous in cost and mechanical flexibility, and are hence more suitable for large-area implementations. Potential applications are, e.g., low-cost RFID chips, light-emitting coatings in road tunnels, large-scale photovoltaic cells, electronic paper, or "smart clothing".

The interface between metal electrode and active material has been recognized as an important part of the functionality and performance of devices^[10-12] and named as area with large potential of improvement. Especially the injection (respectively, extraction) of charges ought to be facilitated. To that aim, several strategies have been proposed. The most popular among them are doping of the electrode by (earth)alkali or halogens atoms^[13-18], or functionalizing the surface with either covalently bound, dipolar self-assembled monolayers (SAMs)^[19-22], or small molecules which undergo charge transfer reactions with the substrate^[11, 23-27]. It is the aim of the present thesis to improve the understanding of the latter kind of systems. In particular, the electronic structure and the level alignment at interfaces between coinage metal (i.e., Cu, Ag, and Au) surfaces and strong electron donor and acceptor molecules are considered. In the course of this work, several different interfaces are investigated, mainly by means of theoretical methods. From observations on specific systems, general structure-to-property relationships are deduced, linking the chemical structure as well as the adsorption geometry to the work-function of the combined system.

The build-up of the thesis will be as follows: First, in chapter 2 an introduction is given on the electronic structure of metal/organic interfaces as presently understood in the literature. This section will be used to define the basics for the following chapters. In section 2.2, the default methodology used in this thesis is explained. Thereafter, a brief synopsis of theoretical background of the employed methodology is given. Here, the focus is not on explaining said methods (since this is done in more detail by textbooks), but rather on the description of their strengths and weaknesses. In this context, their applicability to the systems in question is critically assessed.

The main part of the thesis will start with chapter 3, in which realistic systems were analyzed. A large part of this work has been performed in close collaboration with the Humboldt University of Berlin, where the systems were analyzed experimentally using ultraviolet photoelectron spectroscopy (UPS), X-ray photoelectron spectroscopy (XPS), and scanning tunneling microscopy (STM). The section itself is divided into several subsections: sections 3.1, 3.2, and 3.3 are concerned with electron donors, while sections 3.4 and 3.5 deal with electron acceptors. Section 3.6 describes the interface between Cu and GaClPc, a dipolar molecule which undergoes hardly charge transfer at all. Finally, organic-organic interfaces are also considered: in section 3.7 the studies are extended to cyclophanes (donor-acceptor complexes which are covalently bound to each other), and in section 3.8, the effects of sequentially depositing strong electron donors and acceptors on metal surfaces are described.

From observations on these systems, general structure-to-property relationships can be deduced, which are tested on more conceptual (and experimentally inaccessible) systems in 4. In particular, the influence of the adsorption distance, i.e. the distance between organic material and metal electrode, is systematically investigated (see 4.1). As a next step, the impact of geometrical distortions upon adsorption and the spatial position of permanent dipoles is studied (see 4.2). Finally, an attempt to exploit the new-found knowledge is presented in section 4.3. The next section of the thesis (4.4) demonstrates the proof-of-principle that a semi-empirical non-atomistic model can be devised in which some of the electronic properties of metal/organic interfaces can be calculated from gas-phase properties of the organic and parameterized properties of the metal. Such a method bears the advantage that the relevant parameters can be calculated on a much faster timescale than the whole interfaces (hours vs. months), and allows for fast and efficient screening of new potential candidates for interface modifications.

After a few concluding remarks, the appendix shows some data on how molecules can be systematically functionalized to tune their properties to given values. Several parts of this work have lead or hopefully will lead to scientific publications in peer-reviewed journals. In those cases where I am (or will be) the main author of these publications, I took the liberty to literally transfer the paper into this thesis; this is the case in sections 3.1, 4.1, 4.2, and 4.3. In the preface to these sections, the contributions of the co-authors are clearly listed and the corresponding paper is cited. In papers where I am not the main author, only excerpts of the paper have been adopted. In accordance with ethical rules, these are set in quotation marks. Also, a facsimile of the paper header is included. Of course, also here the contributions of the other authors are clearly specified in the preface. The relevant sections are 3.2, 3.4, 3.3, and 3.6. Finally, some parts of this thesis were compiled from reports to the EU-project ICONTRON, which were co-written with Prof. Zojer and Dr. Rangger, but where the main part of the content was provided by myself (sections 2.3.5, 3.7, and 3.8).

2 Theory and Employed Methodology

The aim of this chapter is to provide the context for the remaining parts of the thesis. The reader should be given the ability to comprehend the obtained conclusions. At the same time, information on the employed methodology will be provided. This allows to reproduce the data, and at the same time avoids multiple repetitions within the following chapters. The theoretical background of the employed methods will be discussed briefly. Thereby, the focus will be laid on a discussion on the strengths and limitations of possible computational approaches, allowing the reader to independently judge the quality of the obtained results.

2.1 Current Understanding of Level Alignment in Metal/Organic Interfaces

2.1.1 Preface

In this section, the processes governing the level alignment between coinage metal electrodes and small organic molecules will be discussed. The concepts presented here represent the current state-of-the-art in literature. Of course, several reviews^[10, 11, 28, 29] on this topic have been written in the recent years, and it would be impossible to give a comprehensive overview over all them them. Therefore, for the sake of brevity, only the key aspects are described.

There are three models prevalent in literature. Here, the focus will be laid on explaining the level alignment in terms of partial charge transfer between organic layer and substrate, and the dipole moment that arise at the interface. This way of thinking is also used throughout the thesis, since it is the most appropriate one for strongly interacting system. The other models prevalent in literature are the induced density of states (IDIS) model, and the integer charge transfer (ICT) model. Both of them were developed for weakly interacting metal/organic interfaces. For the sake of completeness, they are briefly discussed at the end of the section.

Also, please note that this section is an only somewhat extended version of section 4.4, where the same processes are discussed again as background for the semi-empirical treatment and parameterization.

2.1.2 Processes at the interface

Partial charge-transfer

For the reader's convenience, the processes occurring at the metal/organic interface are discussed sequentially here, i.e., as if one happened after the other. It must be kept in mind, however, that in reality all processes occur simultaneously and, thus, interfere

with each other.

Figure 2.1a shows a schematic energy level diagram of a metal surface and molecular layer not in contact with each other. In this picture, VL denotes the vacuum level, which is commonly taken as reference point for the energy. Note, however, that VL denotes the vacuum level close the metal, which is *not* equal to the VL at infinite distance^[10]. The difference between VL at infinite distance at VL close to the metal is due to the presence of a so-called surface dipole: the electrons of the metal reach farther into space than the nuclei, which gives rise to a region of negative charge above the top layer of metal atoms. As long as the distance to the top metal layer is much smaller than the spatial extent of the surface, the charge-distribution is experienced as periodic sheet of dipoles^[10], which influences the electron potential energy according to Helmholtz equation (*see below*). Only for large distances, the charge distribution can be regarded as point dipole, and the potential decreases with the square of the distance. ^[10] The metal work function Φ is given by the difference of the metal Fermi energy (E_F) and the vacuum level above it. The monolayer is characterized by its highest occupied molecular orbital (HOMO) and lowest unoccupied molecular orbital (LUMO). The energy required (gained) by removing an electron from (into) the HOMO (LUMO) corresponds to the ionisation potential (IP) (electron affinity (EA)). In the hypothetical case of complete absence of interaction between monolayer and metal, the Schottky-Mott limit applies, i.e., the respective vacuum levels of the partners align.

As soon as the orbitals of a molecule spatially overlap with the metal electron wave functions, the electrons of the latter are repelled by the former and "pushed back" into the bulk metal, and the surface dipole decreases. This effect, known as "pushback" or "pillow" effect, is a purely quantum-mechanic phenomenon: When the wave functions of metal and adsorbate overlap, the fermionic nature of electrons demands orthogonalization of the orbitals. This induces a shift in the electrostatic potential, $\Delta\Phi_{PB}$, between the partners, as shown in 2.1b, and, as a net-effect, the work function of the combined system decreases. The pushback effect has been reported to reach significant values^[30-33], sometimes as much as 1 eV.^[34] When charge is brought near a metal surface, the substrate electrodes rearrange to screen the charge^[35, 36]. As a consequence of this polarization effect, \mathbf{P} , the addition or removal of an electron to/from a molecule is energetically more favorable on the surface than in gas phase. This manifests itself in a reduced HOMO-LUMO gap, as shown in 2.1c. Moreover, the orbitals describing the molecular monolayer form a set of bonding, non bonding, or anti bonding linear combinations with the metal bands. This results in an apparent broadening of the molecular states, as illustrated in 2.1d. The corresponding peaks in the density of states (DOS) can be classified as highest occupied π state (HOPS) or lowest unoccupied π state (LUPS).

As soon as the system relaxes into thermodynamic equilibrium, all molecular states up to the metal Fermi energy are occupied. Therefore, the location of the HOPS or LUPS with respect to the E_F is crucial for the type of interaction happening. If the LUPS is located below the Fermi edge, charge will be transferred from metal to molecule. Equivalently, a HOPS above the Fermi level loses electron density. Either way, the reaction induces charge transfer and hence a bond dipole density per area, μ_{CT}/A , which according to the classical solution of the Helmholtz equation

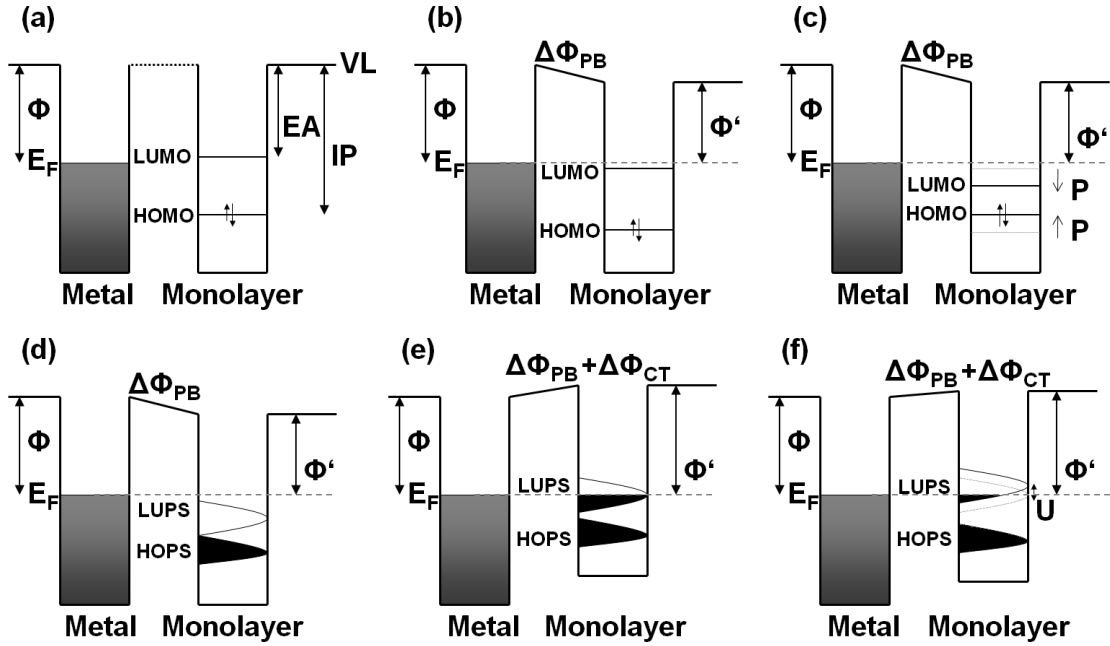


Figure 2.1: Schematic representation of interface energetic and level alignment in Metal / monolayer junctions. Φ denotes the work function of the pristine metal, E_F the metal Fermi energy, VL the vacuum level. HOMO is the highest occupied molecular orbital, LUMO the lowest unoccupied molecular orbital. HOPS and LUPS are the derived peak in the density of states. $\Delta\Phi_{PB}$ represents the work-function modification induced by Pauli pushback, while $\Delta\Phi_{CT}$ corresponds to the work-function modification induced by charge transfer. Φ' is the apparent, modified work-function of the combined system. **P** and **U** correspond to the shift of the orbital energies due to polarization of the metal and charging of the monolayer, respectively. (a): For the hypothetical case of non-interacting partners, the potential well of metal (left) and monolayer (right) align towards the same vacuum level, VL (straight line). The work function Φ of the metal is given by the difference of the metal Fermi level E_F and VL. Ionization potential (IP) and electron affinity (EA) are given by the difference of the energies of the discrete HOMO and LUMO level, respectively, to VL. (b): The pushback effect induces a shift in the vacuum potential, $\Delta\Phi_{PB}$, resulting in a different work function, Φ' , on one side of the surface. Also, the energy of the orbitals relative to the Fermi energy is altered. (c): Screening of excess charge near the metal surface by polarization of the metal electrons decreases the orbital HOMO-LUMO energy. (d): Due to the interaction, the formally discrete HOMO and LUMO broadens into a finite density of states, called HOPS and LUPS, respectively. (e): The low lying LUPS becomes partially filled (indicated by the partial black area in the graph), inducing a bond dipole which increases the vacuum level by $\Delta\Phi_{CT}$. (f): Charging the molecule changes the orbital energies relative to the Fermi-energy by **U** mitigating charge transfer.

$$\Delta\Phi_{CT} = \frac{\mu_{CT}}{\epsilon_0 A} \quad (2.1)$$

induces a shift in the electron potential energy, $\Delta\Phi_{CT}$, as shown in 2.1e. This shifts the potential landscape of the molecule relative to that of the metal. In equilibrium, the amount of charge transfer and the resulting realignment of the molecular states are such that the chemical potential in the partially charged molecule equals that of the metal. As a consequence of the broadening it is not unusual that the E_F cuts through a peak of the molecular DOS, so that the orbital derived states are only partially filled. In other words, non-integer net electron transfer is observed also experimentally in such strongly interacting systems.^[24, 37, 38] Upon charging the molecule, the electronic eigenstates are modified by the charging energy \mathbf{U} . This can be qualitatively rationalized by considering that a molecule with an excess (a missing) electron resists the addition (removal) of another one, which manifests itself as a change of the orbital energy relative to the vacuum level, as shown in 2.1f. Note that the sign for \mathbf{U} is the same for all orbitals in the molecule (even σ orbitals), but the magnitude of the effect can differ.^[39] Note that besides charging, also other effects such as adsorption induced geometrical distortions can contribute to the change of orbital energies. Summarizing, $\Delta\epsilon$, the change in the orbital energy levels between the Schottky-Mott limit and the actual equilibrium situation is given by the sum of all aforementioned contributions:

$$\Delta\epsilon = \Delta\Phi_{PB} + \Delta\Phi_{CT} + U + P \quad (2.2)$$

and the total work-function modification is given by

$$\Delta\Phi = \Delta\Phi_{PB} + \Delta\Phi_{CT} \quad (2.3)$$

2.1.3 Alternative Models

Apart from concept discussed above, two other models are prevalent in literature to explain the charge transfer behavior of metal-organic interfaces.

The Integer Charge-Transfer Model

This model^[40, 41] is commonly used to describe experiments on weakly interacting substrates or metals which are passivated by a thin insulating layer of hydrocarbons or an inert oxide layer. Thereby, it is assumed that the passivating layer reduces the effective work-function due to Pauli pushback, while at the same time preventing hybridization of the adsorbates π -states with the metal electrons. The charge-transfer occurs via a tunneling mechanism. The driving force is the energetic difference between the metal Fermi-level and the energy of so-called integer-charge-transfer (ICT) levels of the organic, at which pinning occurs^[42]. The integer charge-transfer levels correspond to (bi)polaronic states, and are denoted as E_{ICT-} for negatively charged and E_{ICT+} for positively charged monolayers. Charge transfer and pinning on these levels occurs only if E_{ICT+} is located above or E_{ICT-} is below the Fermi energy. In all other cases, vacuum level alignment is expected. Because these levels are localized on one component,

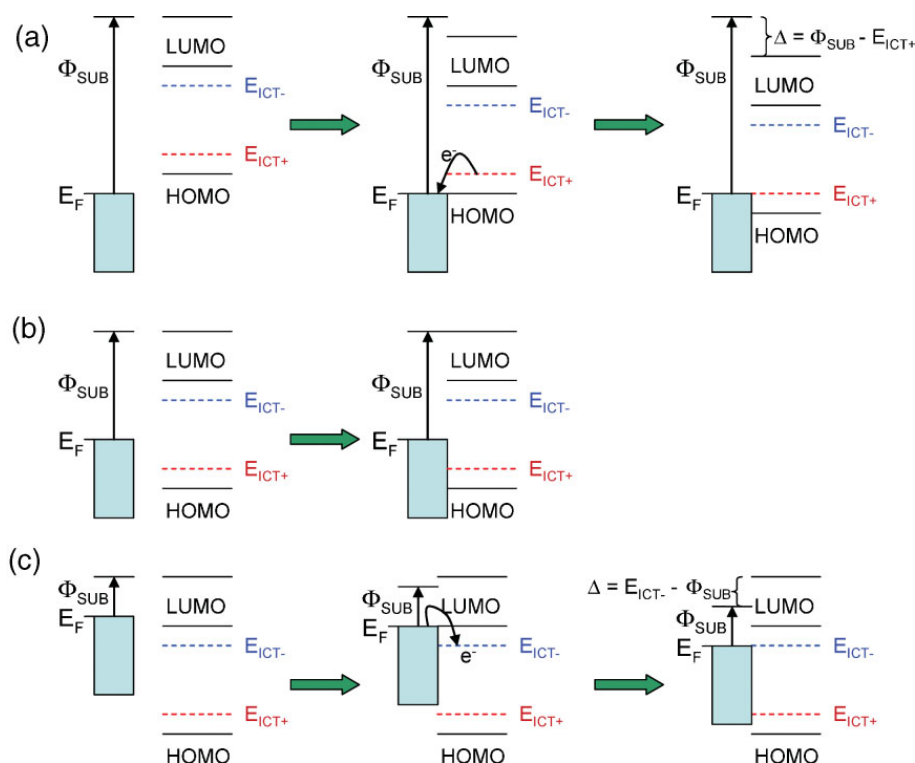


Figure 2.2: Schematic illustration of the level-alignment conception in the ICT model for organic molecules or polymers physisorbed on a substrate surface when a) $\Phi_{SUB} > E_{ICT+}$: Fermi-level pinning to a positive integer charge-transfer state, b) $E_{ICT-} < \Phi_{SUB} < E_{ICT+}$: vacuum level alignment, and c) $\Phi_{SUB} < E_{ICT-}$: Fermi-level pinning to a negative integer charge-transfer state. The charge-transfer-induced shift in vacuum level, Δ , is shown where applicable. Graphic reproduced from reference [29]

only partial transfer is not possible, i.e., only integer electrons are transferred. As a consequence, only a fraction of the molecules in the monolayer participate in the redox reaction. The charge-transfer induced dipole then shifts the vacuum level above the surface according to equation 2.1, thereby inducing a shift in the effective work-function. ICT states include full geometric and electronic relaxation of the adsorbate, and can therefore be identified with the adiabatic ionization potential, respectively, electron affinity. The changed electronic and geometric structure of the charged species affects the electronic levels compared to the neutral molecule, and as a consequence, new density of states corresponding to the ICT levels can be sometimes observed in ultraviolet photoelectron spectroscopy (UPS) experiments^[29]. Typically, these levels are shifted some tenth of eV into the formally forbidden HOMO-LUMO gap^[29]. A schematic representation of energy-level alignment as perceived in this model can be found in Figure 2.2.

Since the ICT levels are a material property, the effective work-function is independent of the Fermi-level of the substrate, provided that it is located sufficiently high or deep that charge-transfer is triggered. As consequence, each interface effective work

function will correspond to (i) E_{ICT+} if the Fermi-energy is larger than this value, (ii) E_{ICT-} if the Fermi energy is smaller than this value, or (iii) be equal to the metal work-function if the Fermi energy is between E_{ICT+} and E_{ICT-} . This gives rise to a “mark of Zorro” graph^[29]. Interestingly, a similar dependence is found computationally for the position of a biphenyl layer on top of gold which has been pre-covered with self-assembled monolayer to tune its work-function over a range of several eV^[43]. The notion of a constant work-function independent of the metal also complies well with the work of Rusu^[38], which finds the work function of PTCDA adsorbed on a variety of materials to be roughly constant. Nonetheless, it is also stated within the ICT model that the levels E_{ICT+} and E_{ICT-} cannot be calculated for a single molecule in gas phase, since they are subject to effects proprietary to metal/organic interfaces, such as screening of the excess charge on the monolayer. It is also found that these levels are only clearly separated from the orbitals they are derived from for large conjugated molecules or polymers. For smaller molecules, they coincide with HOMO and LUMO, respectively^[42], or are at least very close to them^[44]

The Induced Density of States Model

This model, which is an advancement of the Unified Defect Model of inorganic/metallic interfaces, aims at describing the *deviation* of real interfaces from the ideal Schottky-Mott limit, in which no interface dipole exists and the metal and the adsorbate share a common vacuum level. The origin of the deviation is attributed to Induced Density of Interface States (IDIS), which emerges in the former gap of the organic molecule upon interaction with the substrate and acts as a “buffer” for the transferred charge. Consequently, only partial charges are transferred per unit cell. The IDIS are sufficiently large that a Charge Neutrality Level (CNL) can be defined^[45]. This value, which is closely related to the chemical potential, is obtained by integrating the density of states up to the point where it contains as many electrons as the nuclei contain charge, i.e.

$$\int_{-\infty}^{CNL} DOS(E)dE = \sum_i Z_i \quad (2.4)$$

In the case of intermediate interactions, the CNL is assumed to become pinned to the Fermi-energy, in contrast to the polaronic states in the ICT model, or the orbital themselves as interpreted in this thesis. Because the position of DFT orbitals are pathologically incorrect, they are improved by adding a correction term^[46]. The screening of the metal is accounted for by fitting HOMO and LUMO to the experimental gap^[45]. To model the weak interaction with the substrate the IDIS model corrects them by accounting for self-interaction via a Greens-function approach^[45], extending the methodology beyond DFT. Although the CNL is sensitive to the position of the orbitals, it is robust with respect to the metal/molecule interaction, at least for weak and intermediate interactions as, e.g., perylene-3,4,9,10-tetracarboxylic-3,4,9,10-dianhydride (PTCDA) on Au even at different adsorption distances^[45, 47].

The deviation of the interface energetics from the Schottky-Mott limit is quantified

by introducing a slope parameter, S , given as

$$S = \frac{dE_F}{d\Phi_M} \quad (2.5)$$

A slope parameter of 1 corresponds to perfect vacuum level alignment without the presence of interface dipoles. It resembles the situation in the ICT model where E_F is between $E_{ICT,+}$ and $E_{ICT,-}$. The other extreme, $S = 0$, corresponds to rigid pinning, and is reminiscent of the cases $\Phi_{SUB} > E_{ICT,+}$ or $\Phi_{SUB} < E_{ICT,-}$. Typically, the IDIS model predicts values of S between these limiting cases^[45, 47]. Once the IDIS is known, the S can be calculated using the formula^[45]

$$S = \frac{1}{1 + 4\pi e^2 D(E_F) d A} \quad (2.6)$$

In this equation, $D(E_F)$ denotes the density of states of the adsorbate at the Fermi-level, d the adsorption distance, and A the size of the unit cell. It should be noted that $D(E_F)$ is also sensitive, besides others, to the adsorption distance, i.e. no simple $1/d$ dependence of Φ is expected. Indeed, S depends sensitively on this parameter. For the Au/PTCDA interface, between an adsorption distance of 2.8Å and 3.2Å, the slope parameter changes from 0.12 to 0.16. A serious drawback, which IDIS has in common with all DFT-based methods, is that the adsorption geometry is hardly ever known experimentally, and without accounting for dispersion contributions, calculations are not able to predict it adequately. Nonetheless, the IDIS model has been successfully applied to organic materials^[45], often predicting $\Delta\Phi$ within 0.1eV of the experimental value^[47-49]. A recent advancement to this model allows also to calculate the Pushback effect from the wave-function overlap^[34]. Unfortunately, however, this treatment fails for the model case of benzene on Au(111), where an extraordinarily large work-function reduction of 2.1eV is predicted instead of the experimental value of $\approx 1.1\text{eV}$ ¹.

¹Note that a reduction of more than 2eV can only be achieved by the strongest electron donors in this thesis (cf section 3.2, although benzene should be chemically inert^[50])

2.2 General Methodology

2.2.1 Preface

In this section, the way routine calculations were performed will be described, with the aim to avoid multiple repetition in the individual chapters of the thesis.

2.2.2 VASP

Calculations of metals, monolayers and metal/monolayer junctions were mainly performed using the VASP^[51–53] software package. VASP is a DFT band-structure code and employed periodic boundary conditions in all three spatial directions. Surfaces and interfaces are, however, only periodic in two dimensions (x and y). To break the periodicity in z-direction, the so-called slab approach was used, as illustrated in Figure 2.3. Thereby, the metal is modeled by a finite number of layers. Generally, 5 layers are found to sufficiently reproduce the metallic character of the substrate. For interface calculations, the organic layer is bonded to one side of the slab only. The metal respectively metal/organic system is then separated from its periodic replica by a large vacuum region. The vacuum must be sufficiently large to prevent overlap of the wave functions between the unit cells. To be on the safe side, interfaces with flat-lying organic monolayers were calculated in cell with a height of $\approx 36\text{\AA}$. Since the metal slab is less than 10\AA large and the adsorption distance of the molecules, even including eventual bending, never exceeds 5\AA , this corresponds to at least 20\AA of empty space. For systems with edge-on adsorbing molecules, which can be several 10\AA long, the height of the unit cell was increased to 50\AA by default. Many systems calculate exhibit a dipole moment in z-direction. In contrast to electron wave functions, which fall off fairly quickly in space, electrostatic interactions are of long-range nature. To prevent polarization in z-direction, an artificial dipole layer was introduced in the vacuum region, with the same magnitude but opposite sign of the dipole moment of the system.

Unless noted otherwise, all calculations employed the GGA-type exchange-correlation functional PW91^[54]. This functional tends to exhibit a bit of overbinding, i.e. it displays a shallow minimum even between systems which not covalently or ionic bonded. Since this behavior partly makes up for the lack of van der Waals (vdW) interactions, it is found to perform well for systems where these kind of interactions may become important. VASP employs a plane-wave basis set. The cutoff value was set to 273.894eV (20Ryd). Interaction between core and valence electrons were modeled by the projector-augmented wave (PAW) method^[55, 56]. In order to work with a constant basis set, the number of k-points in x- and y- direction was adjusted to the size of the unit cell, so that number of k-point times length of unit cell (in \AA) was roughly equal to 45\AA . The experimental packing of the monolayers is hardly ever known. Therefore, most calculations assumed a loose packing geometry in a rectangular $5 \times 3\sqrt{3}$ unit cell (roughly 15×15 , hence 3×3 k-points), to prevent artifacts from incorrect packing. An example of the unit cell is shown in Figure 2.3. In z-direction, only a single k-point was used. The k-point mesh was generated according to the Monkhorst-Pack method^[57]. The occupation followed the Methfessel-Paxton scheme^[58], with a broadening parameter of 0.2eV . All systems contained an even number of electrons and were

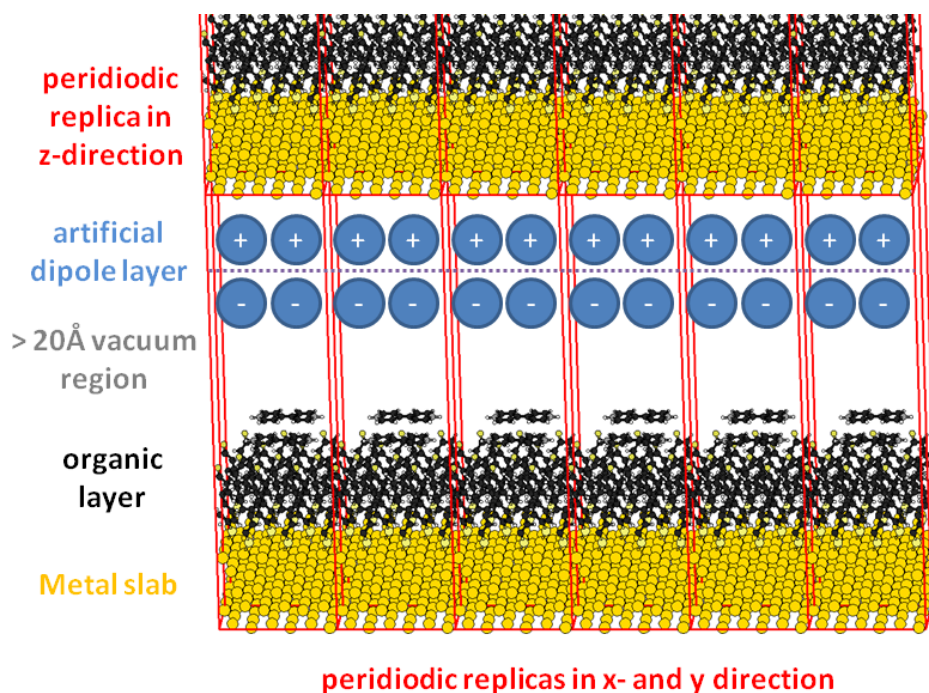


Figure 2.3: Schematic setup of a slab-approach calculations

calculated spin-restricted (spin-unpolarized). Calculations performed for a few test system confirmed the implicit assumption that the spin-unrestricted solution collapses to the spin-restricted one (cf. section 3.1). Geometry optimizations were performed using a damped molecular dynamics scheme. All atoms of the adsorbate and the top two layers of the metal were allowed to fully relax until the forces acting on them were smaller than $0.01\text{eV}/\text{\AA}$. During every SCF-cycle, the total energy of the system was converged to 10^{-4}eV . The optimizations were performed in Cartesian space. Additionally, it was ensured that the dipole moment was converged to $10^{-5}\text{e}\text{\AA}$. This was mostly done by setting the minimum steps of the SCF cycle sufficiently high. Only at the end of this work I modified the VASP code to directly control the dipole convergence via the keyword DDIFF, as described below. To determine the relative alignment of the levels, the density of states (DOS) has been projected onto spherical harmonics around the atoms of the organic layer. These projections are termed PDOS. If the PDOS contains all atoms of the organic substrate, the levels correspond to the sum of all molecular orbitals (in the LCAO sense). This special case is called MDOS. Integrating the MDOS over a given energy range yields the spatial electron density distribution. Such a plot is called local density of states (LDOS). The LDOS can also be exploited for the simulation of scanning tunneling microscopy (STM) experiments. Here, the approach of Tersoff and Hamman was used^[59]. In this model, the states probed by the STM tip are given by the integration of the DOS between the tip bias and the Fermi level. The tunneling current is then assumed to be proportional to the overlap between the probed states and an s-type orbital located at the hypothetical STM tip. To obtain a more realistic description of STM images, the tip was modeled as an extended object of 69 s-type orbitals arranged in a cone-like manner. The diameter of this structure is 2.1\AA with an

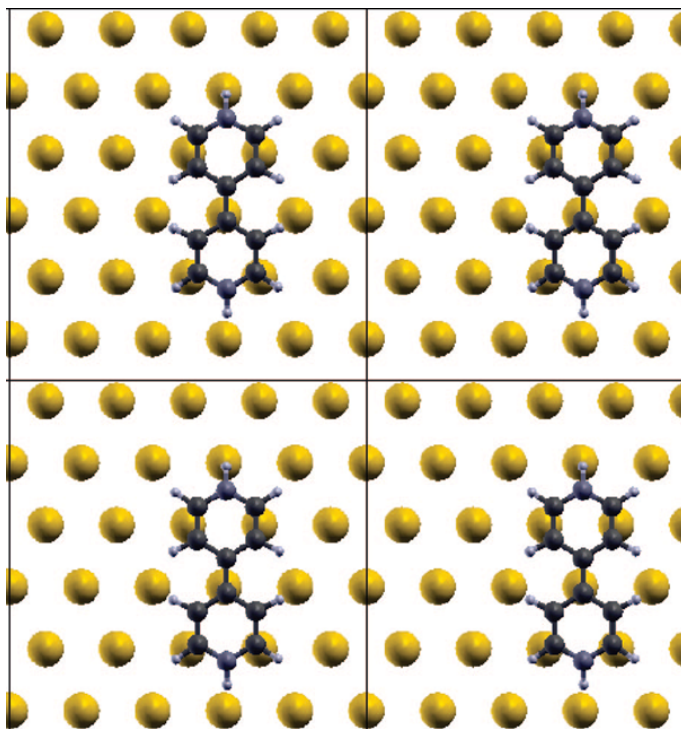


Figure 2.4: Section of the studied HV0 monolayer on the Au(111) surface. The gray lines indicate the $5 \times 3\sqrt{3}$ unit cell. Only the top metal layer is shown for the sake of clarity.

height of 0.8\AA . More details on the tip construction are given in reference [60].

Modification to VASP 5.2 for automatic dipole convergence

Like all other SCF algorithms, VASP minimizes the energy until a certain convergence threshold is reached. Unfortunately the dipole moment - which is often the more important quantity for our work - converges slower than the energy, and is thus often not yet converged when the calculation stops. Therefore, VASP 5.2 was modified to include an INCAR-tag which ensures dipole convergence as well.

The dipole convergence can be independently activated in all 3 spatial directions, as well as for the total value. To activate the convergence, simply include the tag(s)

$DDIFFX = \text{threshold}$ $DDIFFY = \text{threshold}$ $DDIFFZ = \text{threshold}$ $DDIFF = \text{threshold}$

in the INCAR file, where threshold is the convergence criterion desired. $DDIFF$ refers to the difference of the dipole moment total length (root of sum of squared of the individual components) between the current and the last SCF step. $DDIFFX$, $DDIFFY$ and $DDIFFZ$ refer to the difference of the dipole moment in x-, y-, and z-direction, respectively. If no such entry exists in the INCAR file, a default value of $100e\text{\AA}$ is assumed. This value is chosen deliberately large enough so that it is always fulfilled, i.e. the dipole convergence is de facto inactivated. The sequence in which the tags are included into the INCAR file matters not.

One should be aware that the dipole is still a very unsteady quantity - its difference

might fall below the threshold for a step or two, but increase again later. It is therefore suggested to choose the threshold about one order of magnitude lower than the actual accuracy desired. Also, keep in mind that the threshold is in units of eÅ, not in eV, and therefore must also be adapted to the size of the system.

For example, assume the work-function modification is desired with an accuracy of 0.01eV in a $5 \times 3\sqrt{3}$ unit cell. Here, the conversion factor between dipole and work function is ca. 0.8. Thus, the desired threshold is $0.01 / 0.8 = 0.0125$.

The modifications can be found in the following files, where they are marked by the comment "Added by OTH" Base.inc Main.F Reader.F Electron.F Electron_OEP.F Electron_all.F Electron_lhf.F

2.2.3 SIESTA

SIESTA^[61], much like VASP is also a band-structure DFT program employing periodic boundary conditions in all three spatial directions. Unlike VASP, however, SIESTA employs a linear combination of atomic orbitals (LCAO) basis set, which is beneficial for analysis when information about specific orbitals is desired. The prime example of this analysis is the molecular orbital density of states (MODOS), which contains the contributions of each molecular orbital to the total DOS. By integrating these up to the Fermi energy, the occupation of each orbital is obtained. The result yields the occupation of this orbital in electrons. The original version of Nelin et al.^[62] was modified by Lorenz Romaner^[63] so that the total charge of the system, obtained by the sum of all electron occupations minus the core charges, corresponds to a Mulliken type analysis^[64]. Therefore, the MODOS is subject to the same flaws as the Mulliken analysis:

- Occupations may be larger than 100% or smaller than 0, which is unphysical.
- Electrons associated with basis functions on different centers are divided equally between the partners.
- Since the basis set is incomplete, basis functions on one component 1 can contribute to describe the electron density on system 2. In this case, the electron is attributed to 1, even though it effectively belongs to 2.

A more general drawback common to most population analysis is that the dipole moment is typically not conserved. In the bachelor thesis of Bernhard Kretz, several charge partition schemes (Mulliken, ESP^[65], APT^[66], and NBO^[67]) were investigated for typical organic compounds. The dipole moment was only conserved for ESP charges (which are designed to fit the electrostatic potential around the molecule). For all other cases, large quantitative deviations were observed. In some situations, even the direction of the dipole moment was wrong! Of course, there is no correct way to partition the charge in a quantum-mechanical system, since charges of subsystems are not physical observables. In fact, there is no physical law governing where one subsystems ends and the other starts, and therefore, any partition between them must to some extent be arbitrary. It should therefore be kept in mind that molecular or atomic charges are auxiliary quantities and should not be interpreted too strictly.

It should also be pointed out that in SIESTA, a slightly different methodology than in VASP was used. Since the PW91 functional is not implemented, the PBE^[54, 68] functional was used. The pre-supplied double-zeta quality basis set DZP was employed. The core electrons were modeled by pseudo potentials, which were generated according to the Troullier-Martins scheme by Gerold Rangger^[69] and Matthias Gruber^[70]. No artificial dipole is available in the versions used throughout this thesis to prevent polarization of neighboring unit cells. Nonetheless, it was shown that when using the geometry obtained from the VASP calculations, the differences in the density of states is negligible between the two software packages^[63].

2.2.4 Gaussian03

Single molecule calculations were performed using Gaussian03^[71] (G03). Unlike the two aforementioned codes, Gaussian employs open boundary conditions, i.e. is able to treat the molecule as a isolated moiety. Although G03 is in principle able to employ periodic boundary conditions as well, this feature has not been tested or used in this work. For standard calculations the hybrid functional B3LYP was employed together with the basis set 6-31+G*. The diffuse functions in these basis sets are necessary to account for loosely bonded electrons when calculating the electron affinity via the Δ SCF approach (see below). For this method, average unsigned errors below 6 kcal/mol (0.26 eV) and below 4 kcal/mol (0.17 eV), respectively, were found^[72]. It has been reported that electron affinities (EAs) are in many cases computed too positive^[73], while ionisation potentials (IPs) are often too small^[74].

Whenever possible IPs and EAs were calculated explicitly, i.e., by subtracting the total energy of the neutral species from the energy of the charged radical ion:

$$\begin{aligned} IP &= E(\text{cation}) - E(\text{neutral}) \\ EA &= E(\text{anion}) - E(\text{neutral}) \end{aligned} \tag{2.7}$$

Since a full SCF calculation is performed for both the charged and the neutral species, this is called the Δ SCF approach. Please note that the definition employed for EA here - charged minus uncharged - yields the opposite sign of the definition of EA suggested by the IUPAC^[75]. Unless noted otherwise, all IPs and EAs are calculated as *vertical* values, which means that for the charged systems the optimized geometry of the neutral moiety is used. In a few cases, the *adiabatic* values will be discussed, which are obtained by full optimizing the molecule in both its neutral and its charged state.

Typically, no symmetry constraints were employed in order to prevent bias of the geometry optimization. Frequency calculations were performed for all obtained structures to ensure that a minimum on the potential energy surface was found, i.e., no decrease of energy with respect to any vibrational degree of freedom is possible. Calculations of neutral molecules were performed spin-restricted, while the radicals were computed spin-unrestricted.

2.3 Theoretical Background and Critical Assessment of the Employed Methodology

2.3.1 Preface

In this section, a synopsis of the methods employed throughout this thesis will be given. It is, however, not the intention to provide the reader with a sound theoretical basis on quantum-chemical methods. There are numerous textbooks more suited for this purpose. Rather, the focus will be laid on strengths and weaknesses, and in the following it will be assumed that the reader is familiar with the concepts of quantum mechanics and at least the ideas of the Hartree-Fock method.

The introductory parts of this section have been created with the use of Refs. [76–78].

2.3.2 Basis sets

A common feature of all methods in quantum chemistry is that the wave-functions of the electrons are expanded in some kind of finite basis set ^{II}. Several different schemes for this expansion have been proposed, each with their own merits and drawbacks. In this thesis, plane wave (PW) basis sets and linear combination of atomic orbitals (LCAO) basis sets are employed. On the matter of basis sets, a paper by Georg Kresse^[79] reads:

„local basis sets are often viewed with suspicion in the community applying plane waves basis-set superpositions ([because of] basis-set superposition errors), and likewise, the pseudopotential approximation and related methods are viewed as an unnecessary approximation for light elements by quantum chemists“.

The fact that both methods are employed in this work highlights its strong interdisciplinary character. In the next two subsections, the merits and drawbacks of PW and LCAO will be discussed with regard to the problems dealt with in this thesis.

Plane Waves

One method popular in solid-state physics is to expand the wave function in a set of plane waves (PWs). These kind of functions inherently fulfill the Bloch condition^[80]. Moreover, they bear the advantage of being easily integrated in reciprocal space (k -space), which significantly speeds up calculations. Of course, in practical applications only a finite amount of plane waves can be used. Their number is given by the so-called cutoff energy, i.e. all plane waves with an energy smaller than this energy are included. As the cutoff energy is the only quantity determining the quality of the basis set, plane-wave calculations can be systematically improved, and it is guaranteed that the result converges to the complete basis set limit. Since these functions are always orthogonal to each other, linear dependencies which complicate the optimization problem can never occur. The number of plane waves is also independent of the number of electrons in the system, which precludes basis set superposition errors (BSSEs)^[79] (see below).

^{II}Note that for a number of reason this includes also typical density functional theory calculations, which are usually depicted as a non-wave-function-based method.

The main drawback of PWs is that, to describe quickly varying electron density, the wavelength of the PWs must be sufficiently small, i.e. a larger number of plane waves is necessary. This problem is encountered mainly in the core region of the atoms, which, fortunately, doesn't participate in chemical reactions. The remedy is thus to separate core and valence electrons. While the latter are described by PWs, the former are taken to account by, e.g., a pseudopotential. Pseudopotentials can be defined as “[...] any potential which does not have bound core states but gives the same valence state energies than the 'real' potential”^[81]. In other words, a pseudopotential models the *influence* of the core electrons on the valence electrons, without explicitly calculating them in the actual calculation. As a result, the number of PWs necessary to obtain a well converged result is significantly reduced.

The most prominent advantage of PWs when dealing with solid state bodies, namely their periodicity, turns into a disadvantage as soon as non-3D-periodic systems are of interest, such as single molecules. In principle, it would be possible to treat a single molecule in gas phase when using a complete basis set. In practice, however, PWs usually cannot deal with non-periodic boundary conditions. To simulate such situations, periodic supercells are used, i.e., the molecule is treated in a unit cell just like any solid body. To avoid interaction between the (unwanted) periodic replicas, the molecule is surrounded by a sufficiently large amount of vacuum. Hereby, the vacuum must not only be vast enough to prevent overlap of the wave function between neighboring cells, but also to prevent mutual polarization due to electrostatic (multipole-multipole) interactions. Especially the latter decay slowly with the intermolecular distance. Including empty space in plane-wave calculations is problematic insofar as additional basis functions are needed to ensure that the electron density is zero there, which adversely affects the computational effort. The issue affects all bodies with a periodicity in less than three dimensions. For 2D-periodic systems, such as the metal/organic interface dealt with in this thesis, the problem of dipole-dipole interactions can be eliminated by inserting a virtual dipole layer with the same magnitude, but opposite sign into the vacuum region. It should be emphasized here that the problem of multipole-multipole interaction is not directly related to the employed basis set, but a general problem of 3D-periodic calculations. Other problems connected with periodic systems (and, hence, plane waves) include the inability to correctly calculate the energy of charged cells^[79, 82] (thus preventing the explicit calculation of ionization potentials and electron affinities via the energy differences of the charged and the neutral species) and the currently high computational demand for the evaluation of the exact exchange integral in reciprocal space^[83].

Linear Combination of Atomic Orbitals

In computational chemistry, the linear combination of atomic orbitals (LCAO) basis set is more commonly employed. As the name indicates, the basis functions are based on so-called atomic orbitals, although they are not exact solutions to the Schrödinger equation of any specific atom. For the sake of efficient integration, atomic orbitals are often expressed as a linear combination of Gaussian type orbitals centered on the nuclei. Gaussian type orbitals are essentially Gaussian functions multiplied with a spherical function to account for the symmetry of the corresponding electron. Of course, only one function per electron is strictly necessary to describe the system. It turned out,

however, that the description is substantially improved if more than one function is provided. Such basis sets, also called *extended basis sets*, are typically denoted as N zeta basis sets, with N being double, triple, etc., depending on the number of basis functions per electron. Typically, this treatment is only extended to valence electrons. To allow for a suitable description of effects perturbing the symmetry of the electron distribution, polarization functions consisting of Gaussian Type Orbitals of higher angular momentum are often added. Another way to augment the basis is the introduction of diffuse functions, which are Gaussian Type Orbitals reaching particular far out into space. While necessary to account for, e.g., weakly bound electrons, self-consistent field cycle including basis sets with diffuse functions tend to converge very slowly.

The main advantage of LCAO basis sets - apart from needing much fewer functions than a plane wave (PW) basis set - is that molecular orbitals can be directly obtained, which are a concept deeply rooted in chemistry and facilitate analysis of the generated data. For light elements there is also no need to employ any kind of approximation for the core electrons, and all-electron calculations are feasible. The emphasis there lies on light elements (which usually include all atoms at least up to Ar). Heavier elements, including the coinage metals, possess too many inert core electrons to justify their explicit calculations in view of the added computational effort. Also, for elements heavier than Ag, relativistic effects become important^[84] for the inner electrons. Since inclusion of relativity in actual calculations adds a significant computational overhead, the solution is to employ effective core potentials (ECPs), similar to the pseudopotentials used in PW calculations. LCAO calculations are not restricted to periodic boundary conditions, and are therefore better suited than PW basis sets to calculate charged components or employ methods including exact exchange.

Unlike for PWs, there exists no systematic way to improve a given basis set. Of course, by virtue of the variational principle adding any function to a given basis set will result in a lower, and hence "better" total energy. However, it is possible to generate imbalanced basis sets: When using too many functions with a high angular momentum, the optimizer might make use of them to account for deficiencies of the basis with lower momenta, thereby introducing artifacts in the electron distribution.^[77] Also, unless the new function is made orthogonal to all other functions already included in the basis set, it cannot be guaranteed that the basis will eventually converge to the basis set limit. The largest drawback of LCAO basis sets is, however, the basis set superposition error (BSSE). The BSSE arises from the fact that the number of basis functions is dependent on the number of electrons *and* that the basis functions are centered on the nuclei, making the quality of the basis geometry dependent. It describes the problematic that the basis functions centered on one part of the system can be used to improve the description of the electron distribution in other regions. As a consequence, interaction energies between two closed shell species (e.g., of metal/organic interfaces) are overestimated, and the bond length between them is computed too small. To obvious remedy for this problem is to improve the basis set size, as for a complete basis set, the BSSE vanishes. However, this approach is often impracticable due to the large computational cost associated with large basis sets. Alternative, approximate ways to correct for the BSSE have been devised^[85]. The perhaps most widespread of

them is the Counterpoise correction^[86], which is explained and used in section 2.3.4.

2.3.3 Density Functional Theory

Introduction to DFT

The original idea of density functional theory (DFT) was to optimize the electron density of the whole system at once, rather than to calculate the total wave-function. Independent of the size, the electron density can always be described with a set of 4 coordinates (three spatial plus the spin), whereas the traditional wave-function based approach requires the same number of coordinates for each electron. Hohenberg and Kohn demonstrated that for non-degenerate ground states, each electron distribution yields a different, unique ground-state energy^[87]. As a direct consequence, the electron density with the lowest ground-state energy must be the solution to the quantum-mechanical problem at hand. The functional connecting energy and electron density is called *density functional*. In analogy to the Hartree-Fock formalism, density functionals can be separated into four parts: the kinetic functional, the Coulomb functional, the exchange functional, and the correlation functional. Unfortunately, for the true many-body electron density, none of these four are known exactly. Early functionals for the kinetic energy were obtained from the expression of the kinetic energy in a non-interaction, uniform electron gas^[88]. Unfortunately, it turned out that this approximation yields very poor results. Ironically, the solution to this problem was to re-introduce one-particle wave functions, the Kohn-Sham (KS) orbitals^[89]. These orbitals represent hypothetical, non-interacting one-particle wave functions, which are constructed under the constraint that the sum of all one-particle densities (obtained by the square of the wave function) gives the correct many-body electron density. For these auxiliary functions, the exact kinetic energy functional can be formulated. It must be emphasized, however, that unlike the orbitals in Hartree-Fock theory, where the orbital energy is directly related to electron affinity or removal energies via Koopmans theorem^[90] KS orbitals bear no physical meaning, apart from the highest occupied molecular orbital (HOMO)^[91]. Nonetheless it is customary in literature to interpret the KS eigenvalues as one-particle energies^[92]. Indeed, strong correlations between the eigenvalues and ionisation potential (IP), respectively, electron affinity (EA) are often observed (see, e.g., refs. ^[93, 94]).

The Coulomb functional can be given by the classical expression for the electrostatic interaction between charged particles. In a quantum-mechanical system, however, it is impossible to differentiate between the electrons. Therefore, this term usually included the interaction of each electron with itself, which is unphysical. In Hartree-Fock theory, this is no problem, as this additional term is canceled by a corresponding term in the exchange part. In DFT, however, there is no guarantee for cancellation. This leads to the so-called self-interaction error (SIE). The problems arising from this error are discussed in more detail in section 2.3.3.

Exchange and correlation functionals are often treated together (and are called exchange-correlation functionals, E_{xc}). Nonetheless, they are commonly implemented separately, and some software packages (e.g., Gaussian03^[71]) allow almost arbitrary combinations of them. In principle, since orbitals are already introduced for the kinetic energy, it

would be possible to also calculate the exchange part exactly (which means using the formula from Hartree-Fock theory). Interestingly, though, this gives poor results, the reason being that the KS orbitals are not entirely the same as their HF counterparts^[95]. Unfortunately, the functional shape of the correct E_{xc} is not known, but if it was, the results produced by DFT would be correct^{III}. The employment of various levels of approximations is the origin of the existence of many flavors of DFT. Indeed, the implementations of the kinetic and the Coulomb functional are common for all functionals, and only E_{xc} differs. Exchange-correlation functionals are developed by accounting for physical and mathematical conditions (although it is also not uncommon that some of these are violated). Additionally, many of functionals are also high-level experimental or theoretical data. In the following, a brief summery on the ideas of the most important functionals will be given.

The **local density approximation (LDA)** calculates the exchange and correlation energies according to the limit of an uniform electron gas. This assumption is valid in systems with only slightly varying electron density, e.g. in some metals. The xc-functional depends only on the local electron density. The correlation functional has been fitted to high-quality Monte Carlo data, and according to its “inventors” (Vosko, Wilk, and Nusair) is called the VWN functional. Indeed, the VWN functional has become so popular among the LDA methods that these name are used interchangeably. LDA overestimates the bond strength (“overbinds”), which is sometimes exploited to “mimic” van-der-Waals interactions^[96, 97].

To account for strongly oscillating electron density that molecules and interfaces resemble, **generalized gradient approximation (GGA)** functionals were developed. In addition to the local electron density, these methods also include its gradient, making them semi-local. In this field, no particular function distinguishes itself. Within this thesis, two GGA-functionals were employed, PW91^[54] and PBE^[54, 68]. In general, GGA functional are known to underbind. Most interface calculations in this work feature PW91, since it has been shown that it performs slightly better for these calculations than other GGA functionals^[60, 98]. PBE is of similar nature than PW91. Unlike the latter, however, it does not predict an artificial bond between non-covalently bound systems^[99], and is therefore a natural starting point for improved functionals (see, e.g., the discussion of van-der-Waals interactions in the next section).

For small molecules, substantial improvements are made when using **hybrid functionals**, which mix a fraction of the Hartree-Fock exchange into E_{xc} . Although several different hybrid functionals are in use, the one that is arguably most popular due to the good results it produces is B3LYP^[100–102]. B3LYP is a clearly empirical functional, where the 3 parameters determining the amount of exact exchange, GGA-type exchange, and LDA-type exchange were determined by fitting to experimental data. Despite its great success, this functional does violate a physical boundary condition, since it does not satisfy the uniform density limit^[103]. As a consequence, it performs poorly for bulk

^{III} Actually, the reason for this is that correlation is defined as the difference between the Hartree-Fock results and the correct solution. Consequently, any solution with includes full correlation by definition yields the exact result.

metals^[83]. For interfaces, the situation is less clear. Although the adsorption process itself is well described, the properties of the surface are not, and it is generally recommended to use, e.g., HSE06 rather than B3LYP^[104]. It should be remembered, however, that including exact exchange is tedious in plane-wave calculations^[78], and it needs to be questioned whether the result cost justifies the increased computational.

Advantages and Limits of DFT

The large popularity of density functional theory (DFT) can be attributed mainly to the low computational expense of this method. As of today, systems involving up to 1000 atoms can be treated within adequate time. At a cost no higher than Hartree-Fock calculations, DFT includes at least partly electron correlation and is therefore in principle more accurate. Indeed, for many situations it performs as well or better than the post-Hartree-Fock methods MP2^[105] or coupled cluster^[106]. Additionally, even the empirical DFT functionals are sufficiently general to be applied to almost any system, in contrast to true semi-empirical methods which are restricted to the classes of systems they were parameterized for^{IV}.

Of course, there are also some serious disadvantages. The perhaps most obvious shortcoming is that DFT is a ground-state method, and as such incapable of dealing with excited states. For optical transitions, this problem can be overcome by performing time-dependent density functional theory calculations. There, the molecule is perturbed by an external electromagnetic field and the response of the electron density is monitored. The wavelength at which the electron density oscillates in resonance with the field corresponds to an optical excitation. However, it is still impossible to find the electron density of excited states (in particular of states with the same symmetry as the ground state), and therefore some properties remain elusive.

Apart from this fundamental issue, there are also some other failures of DFT (or, more exactly, the currently employed approximations in DFT), which are of fundamental relevance to the work presented in this thesis. The one limit that has drawn a lot of attention recently is the poor performance for **van-der-Waals** type interactions. While typically not of particular importance for single molecule calculations, van-der-Waals is the main binding force for molecular crystals. It can be expected that it plays a significant role in metal/organic junctions, since, on one hand, the organic monolayers represent a 2D case of such a molecular crystal. On the other hand, the contact area between organic layer and metal can be pretty large, especially for the charge-transfer monolayers considered in this thesis. It has been estimated that the inclusion of van-der-Waals interactions significantly affects the tilt angle of covalently bound anthraceneselenolate layers^[97], which directly affects interface properties such as the effective work-function. Romaner et al. also demonstrated that perylene-3,4,9,10-tetracarboxylic-3,4,9,10-dianhydride (PTCDA), a well-known electron acceptor, does not exhibit any binding to the underlying substrate without accounting for van-der-

^{IV}For example, semi-empirical methods can not be used to predict surface properties, since not enough high-quality data are available for parameterization.

Waals interactions^[99]. The main reason here is that van-der-Waals interactions are of non-local nature, and as such not adequately captured by (semi)local functionals. In the meantime, truly non-local functionals have been developed (vdW-DF)^[107], which were also applied to metal/organic interfaces^[96, 99], albeit with limited success. Another approach is to correct the total energy by a summation of dispersion energy contributions between all atoms in the system^[108, 109]. An advantage of the latter approach is that it can be connected to several different functionals, and that it requires little computational overhead. Unfortunately, however, the screening of the van-der-Waals forces by the bulk metal is not accounted for, thereby introducing a severe error in the computation^[110]. An extensive review on the possibilities to include this kind of interaction in DFT calculations, as well as its relevance for metal/organic interfaces, can be found in ref. ^[110]. Unfortunately, none of the above mentioned methods were available in our group until recently. Therefore, most calculations had to be performed without accounting for van-der-Waals interactions. A notable exception is part of the work shown in section 4.4. For this work, it was also necessary to generate our own set of parameter for Au, as outlined in section 4.4.8

Another issue is the already previously mentioned **self-interaction error (SIE)**. Unlike in Hartree-Fock theory, the exchange part does not fully correct for the Coulomb interaction of an electron with itself. This results in too high energies for occupied orbitals. Another consequence is that the density of states calculated with DFT does not agree well with data obtained by photoelectron spectroscopy, unless stretched and shifted. To make matters worse, this effect is not equal for all orbitals. Rather, it depends on their localization, since for more delocalized orbitals, the average distance is much larger^[111]. Qualitatively wrong results may arise when localized and delocalized orbitals interact with each other^[111]. It was also observed (by David Egger and Ferdinand Rissner) that the ordering of the frontier orbitals can be affected. For charge-transfer systems, this can lead to significantly wrong electron distributions. As the SIE favors delocalized electrons, partial is favored over integer charge transfer. This is particularly problematic for asymmetric systems AB, which do not dissociate to neutral components A+B at infinite distance^[112-114]. A similar effect can be observed for charged homoatomic molecules^[115]. Generally, long-range charge transfer is overestimated^[116]. symmetric systems AB, which do not dissociate to neutral components A+B at infinite distance^[112-114]. A similar effect can be observed for charged homoatomic molecules^[115]. Generally, long-range charge transfer is overestimated^[116].

It can be shown that for isolated systems, the total energy with respect to the number of electrons should be a piecewise linear function, exhibiting a discontinuity in its derivative at integer orbital occupation numbers^[117]. However, the expressions for LDA or GGA type functionals lack this **derivative discontinuity**^[111]. Like the SIE, the lack of derivative discontinuity results in an artificial thus an overestimation of the charge transfer, which has been demonstrated, e.g., for molecular systems polarized by an external field^[118]. The same effect can be held responsible for the deviation of DFT implementations from Janaks theorem^[91], which - for the exact density functional - equals the negative highest occupied molecular orbital (HOMO) eigenvalue to the molecular ionisation potential (IP). Since current functionals average over the discontinuity^[119],

the HOMO differs from the IP by approximately 50% of the effect of the derivative discontinuity^[120], which can easily be of the order of several eV^[120, 121].

Another important aspect concerning metal/organic interfaces is the absence of long-range screening in DFT calculations^[35, 36], called the Newns-Anderson effect^[99, 122]. This effect describes the fact that charge above a metal surface, i.e. in the form of a molecule cation or anion, is screened via electron rearrangements in the metal, which result in a screening potential equivalent to the hypothetical formation of image charges in the bulk. As a consequence, the energy required to charge a molecule near a metal is smaller than in gas phase. In other words, both the ionization potential and the electron affinity are reduced near the surface, which results in a larger reactivity of the interface. The lack of long-range screening in the calculation are a source of underestimation of charge-transfer in metal/organic systems. Hence, it partly counteracts overestimation caused by the self-interaction error and the lack of derivative discontinuity. A significant part of the success of DFT calculations for metal/organic interfaces can be ascribed to this cancellation. It should be stressed, however, that unlike the SIE and the lack of derivative discontinuity, the Newns-Anderson effect is dependent on the distance between the reaction partners, which somewhat biases calculations where the same interface is considered with different adsorption distances between metal and organic layer.

With all these restrictions, limits and drawbacks in mind, one might arrive at the conclusion that DFT is not well suited to describe molecules on metal surfaces. However, at present date DFT is the only method which can perform geometry optimizations for periodic systems with the size of metal/organic interfaces in reasonable time; all other methods include exact exchange and are thus too costly. It should also be stressed that DFT results compare surprisingly well with experiments, especially as far as the work-function modification is concerned^[24, 97, 123, 124]. Also the experimental error is typically quite large, and even for the well-investigated system of perylene-3,4,9,10-tetracarboxylic-3,4,9,10-dianhydride (PTCDA) on Ag(111), work-function modifications differing by more than 0.2eV have been reported^[99]. Finally, in the long run it is the aim of all the calculations presented here to extract general relationships and trends governing the interface energetics. Due to the similarity of the systems, it can often be expected that the errors introduced by employing the approximations made within DFT largely cancel, as explained in the appropriate section.

2.3.4 Møller-Plesset perturbation theory

Introduction to perturbation theory

Another concept to treat electron correlation is to include it perturbatively. The prerequisite for this idea is that (i) the unperturbed system can be solved and that (ii) the perturbation is relatively small. Then, the Schrödinger equation

$$\hat{H}\Psi = E\Psi \tag{2.8}$$

can be expanded in a Taylor like series with

$$\Psi = \lambda^0 \Psi_0 + \lambda^1 \Psi_1 + \lambda^2 \Psi_2 + \lambda^3 \Psi_3 + \dots \quad (2.9)$$

$$E = \lambda^0 E_0 + \lambda^1 E_1 + \lambda^2 E_2 + \lambda^3 E_3 + \dots \quad (2.10)$$

Here, λ is the perturbation parameter, and the subscripts to Ψ and E denote the order of the perturbation. Truncating the expansion after the zeroth order corresponds to the Schrödinger equation for the unperturbed system. Choosing the sum over the Fock operators as the unperturbed Hamilton leads to the Møller-Plesset perturbation theory (MP)^[125]. Although this choice frequently violates the assumption that the perturbation must be small, it bears the advantage of leading to a size-consistent method^V. Size-consistency means that the joint calculation of two non-interacting subsystems gives the sum of the energies of the individual systems, which is a natural prerequisite for the calculations of, e.g., adsorption energies. Due to the choice of the Hamiltonian, the unperturbed wave-function corresponds to the ground-state solution of the Hartree-Fock equations. The perturbation functions are connected to Slater determinants describing excited states. Thereby, each wave function includes excitations up to its order, i.e., the second-order wave function contains double excitations, the third order contains double and triple excitations, and so on. Unfortunately, the computational cost increases fairly rapidly as M^{n+3} , with M being the number of electrons and n the order at which the theory is truncated. MP4, i.e. fourth order MP, thus scales as M^7 and is only applicable to the smallest systems. Routine calculations for more realistic systems, which typically include on the order of 30-50 atoms, can only be performed at the MP2 level. Nonetheless, even at this truncation already 80%-90% of electron correlation are included (although its effects are typically overestimated), and MP2 is the most economical ab initio method for the inclusion of dispersion interactions^[77].

Regarding the systems of interest, the main drawback of MP2 is that it can only be applied to non-periodic systems. In reciprocal space, the evaluation of several integrals is tedious and time-consuming, and it is unlikely that periodic system containing more than a few (speak one to three) atoms per cell can be calculated at the MP2 level anytime soon^[126]. As a workaround, the system can be modeled non-periodically by a single molecule on a metal cluster. However, this approach bears several disadvantages. For one, a metal cluster will always display a finite gap between its occupied and unoccupied states^[127], thus not being really metallic. As such, the substrate does not exhibit a density of states in the direct vicinity of its Fermi level, which will affect the energetic of the charge transfer processes. Also, due to the lack of electrons, the Fermi level in a finite cluster is more easily varied due to “doping” by charge-transfer processes. Moreover, it can be expected that the binding energy between metal cluster and organic adsorbate will be severely overestimated^[128] due to the overestimation of correlation, the small energy differences in the orbital energies for pinned systems^[11, 129] which appear in the denominator in MP2, and due to unsaturated bonds on the borders of the cluster. Non-periodic calculations also fail to take into account that the metal/organic bond is part of an infinitely extended sheet of dipoles, thus neglecting the (de)polarization

^VNote that density functional theory (DFT) is size-consistent, too

induced by neighboring molecules, as well as the step in the vacuum potential that is induced by such a 2D-structure, but not by a single dipole^[129]. Finally, as MP2 calculations are often required to employ linear combination of atomic orbitals (LCAO) basis sets, it is subject to basis set superposition errors, as explained in section 2.3.2. Despite all these drawbacks, in order to get a feeling for how MP2 calculations perform for systems of interest in this work, a test system (F4TCNQ on Cu(111)) has been investigated.

A comparative study of MP2 and DFT: F4TCNQ on Cu(111).

In order to assess the quality of MP2 calculations, it was decided to model adsorbate/metal systems with finite clusters, employing both DFT and MP2. The results are then compared to DFT band structure calculations and to experiments. For preliminary investigations, the system 2,3,5,6-tetrafluoro-7,7,8,8 tetracyanoquinodimethane (F4TCNQ) (structure see Figure 2.5 on Cu(111)) was chosen, since both experimental and theoretical data were available^[24, 124]. This system is known to be strongly binding, so DFT can be expected to give reasonable results. Hence it is possible to evaluate the principal differences between these methods, before more complicated systems are considered. Since MP2 scales with the 5th power of the number of electrons, it is absolutely necessary to keep the metal cluster as small as possible. In turn, the binding sites between metal and molecule will be at the edge of the cluster, where also most spin density is collected. Although this system is comparably small, geometry optimization turned out to be impossible, as even the single point calculations took more than a week. It was therefore necessary to employ converged geometries obtained from band structure DFT calculations made earlier^[24], as well as to make use of symmetry where possible. Several authors before successfully described similar, smaller systems using either density functional theory or MP2. Noteworthy among them is, e.g., the work of Crispin et al.^[127], where systematically the influence of the cluster size has been investigated. It was found, that for acrylnitrile on Cu(100), a 9 atom metal cluster is large enough to give converged results for the work function^[130].

Methodology. All band structure calculations were done by Lorenz Romaner using the VASP software package, using a set of 3x3x1 k-points and convergence criteria of 10^{-2} eV for the energy and 10^{-4} eV for the gradient. The PW91 exchange correlation functional was employed. Details of these calculations, as well as the corresponding XPS / UPS experiments have been published elsewhere^[24, 124]. All finite cluster based calculations were performed using the Gaussian03^[71] software package. To create a suitable geometry, the converged geometry of F4TCNQ the band structure calculation was taken. The relaxed metal slab was substituted by an unrelaxed one in order to be able to make use of C_s symmetry (i.e. one mirror plane cutting the system in half along the long axis of F4TCNQ). In an attempt to reduce the system to a suitable size, all except the two uppermost layers were completely removed. From the remaining metal atoms, all atoms not positioned directly below the molecule or at positions possibly binding were removed. During the removal process, it was made sure that (i) the C_s symmetry is conserved and (ii) an even number of metal atoms survived, to prevent the need to employ spin-unrestricted methods. The resulting metal cluster consists of 32

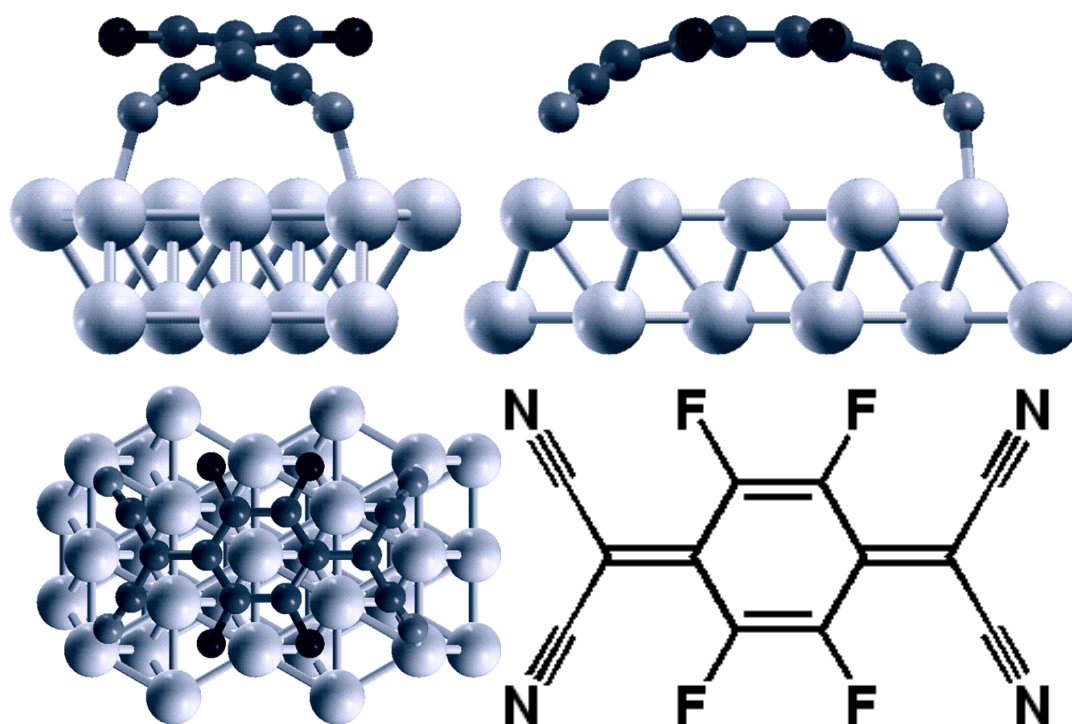


Figure 2.5: Geometry of F4TCNQ on a Cu(111) cluster. (a) front view, (b) side view, (c) top view. In (d), the structure of F4TCNQ is shown.

Cu atoms and is shown in Fig. 2.5.

For both DFT and MP2 calculations, the LANL2DZ basis set was employed. This double zeta basis is qualitatively comparable to 6-31G*, but replaces the inner electrons of the metal atoms by effective core potentials. To perform the correction for the basis set superposition error, calculations with the joint basis were performed. For calculations of the metal slab or the molecule alone, the respective other system was replaced by Ghost atoms (using the Element-Bq syntax). This way, only the nuclear charge and the corresponding number of electrons are removed from the system, while their basis functions are kept. Also the element information, which is part of the grid construction, is retained^[131]. To be consistent with band structure calculations, the exchange-correlation functional chosen for the DFT-calculations was pw91pw91, as implemented in Gaussian03.

Results and Discussion

The Metal Cluster. A finite ensemble of 32 atoms was used to emulate the infinite bulk. In order to estimate the quality of this approximation, the work function of the cluster is determined for both DFT and MP2 and compared to the experimental value. In the infinite metal, the work function is defined as the energy needed to remove or add an electron into the bulk and hence equal to the chemical potential μ . This roughly corresponds to the average of the ionization potential IP and the electron affinity EA

of finite molecules, which in the limit of a semi-infinite system ideally should be equal. For a finite size cluster however, it is unlikely that both properties already converged to the same value. Nonetheless, the chemical potential should already be close to the bulk work function. To estimate the work function of a cluster, it is therefore necessary to calculate the chemical potential μ as the average of ionization potential and electron affinity.

$$\mu = \frac{IP + EA}{2} \quad (2.11)$$

In principle, IP and EA can be estimated from the orbital eigenvalues of HOMO and LUMO via Koopmans theorem^[90]. To obtain more reliable data, IP and EA were also calculated explicitly by adding and removing one extra electron, respectively. This pathway requires two additional open shell calculations, which are quite computer time intensive. To keep it at a reasonable scale, such calculations were only done using restricted open shell algorithms(indicated by the prefix RO). Inserting the definitions of IP and EA into the formula for the chemical potential yields:

$$\mu = \frac{E(cation) - E(anion)}{2} \quad (2.12)$$

The results obtained for the chemical potential of a 32 atoms Cu cluster with different methods are given in Table 2.1.

In all finite cluster calculations, MP2 as well as DFT, severely underestimate the work function. In general, MP2 performs only modestly. Despite its significantly higher demand of computer time, it is off the experimental value by about 1 eV when calculating IP and EA directly. Estimating the work function via Koopmans theorem is even worse and gives unsatisfactory results, as does the calculation via Hartree-Fock energies. DFT cluster calculations, in contrast, approach the experiment within roughly half an eV. It can be expected that the failure to quantitatively describe the work function in the calculation is to some extent due to the neglecting of the surface dipole, which increases the work function in experiments. Note that the periodic slab calculation, which includes the surface dipole correction, is in very good agreement with the experimental value.

Table 2.1: Chemical potential for a 32 atom Cu cluster calculated with different methods and experimental work function for bulk Cu(111)

	Method	μ (eV)
HF (explicit)		2.39
MP2 (Koopman)		2.73
ROMP2 (explicit)		3.74
RODFT (explicit)		4.17
DFT periodic slab (VASP, PW91)		4.86
experimental work function		≈ 4.8

The combined system One important property of these systems is the binding energy between molecule and surface. It is well known that DFT fails here in some cases, even qualitatively^{e.g.} [132]. Here, the binding energy ΔE_{Bind} is defined as

$$\Delta E_{Bind} = E(combined) - E(metal) - E(molecule) \quad (2.13)$$

$E(Bind)$ is the energy of the system with the adsorbed molecule, $E(molecule)$ and $E(metal)$ are the energies of the molecule and metal, respectively, both fully optimized. Unfortunately, the basis set of molecule and metal are far from complete, and, therefore, the basis set of one part can help to compensate for the incompleteness of the other. Hence, it is necessary to account for this basis set superposition error. The simplest method to do so - and the most popular - is the so called Counterpoise correction^[86]. This requires some additional calculations: the energies of the molecule and the metal in the basis set at the geometry of the combined system using ghost atoms, and the calculation of their energy at the combined system geometry with only their own basis. The Counterpoise basis set superposition error (BSSE) is then given by

$$E_{CP} = E^*(metal) - E(metal) + E^*(molecule) - E(molecule) \quad (2.14)$$

The asterisk denotes that ghost orbitals are included in the basis set, and the geometry of molecule and metal are kept equal to that of the combined system. The total interaction energy, corrected for the BSSE is given by the binding energy minus the Counterpoise energy:

$$\Delta E_{Bind,CP} = \Delta E_{Bind} - \Delta E_{CP} \quad (2.15)$$

It should be kept in mind that the BSSE calculated this way is only an estimate, and neither an exact number nor an upper or lower bound. The corrected obtained binding energy must, therefore, also be regarded as estimate. The results of the calculations are given in Table 2.2.

Changing from periodic slab calculations using a plane-wave basis set to a finite cluster with a pseudopotential-augmented atomic centered basis set reduces the binding energy by ≈ 0.35 eV. (Note that it was estimated that the cluster would be overbinding, not underbinding). In a first guess, this could be attributed to the decreased contact surface between organic molecule and cluster, compared to the fully periodic slab. Alternatively, the reduction could be blamed on the incomplete basis set, or a severe overestimation of the BSSE by the Counterpoise scheme. Against the prior assumption, the introduction of electron correlation energy via MP2 does not increase binding energies over DFT, but in contrast, reduces it by more than 1 eV! One should, however, keep in mind that

Table 2.2: Calculated binding energies and Counterpoise BSSE correction for F4TCNQ on Cu(111) using DFT and MP2

Method	ΔE_{Bind} (eV)	E_{CP} (eV)	$\Delta E_{Bind,CP}$ (eV)
DFT (cluster)	-3.54	-1.29	-2.25
MP2	-5.05	-4.13	-0.92
DFT (periodic slab)	-2.6		

no geometry optimization at the MP2 level has been performed, while all calculations were done at the minimum of the DFT periodic slab calculation, rather than at its own minimum geometry. Although this does favor the DFT calculation, it is unlikely that it alone can account for the large energy difference. Another important observation is that the BSSE correction for MP2 is 4 times larger than the effective binding energy. It must be kept in mind that the Counterpoise corrections gives only an estimate of the BSSE, and in other words is not exact. This is particular problematic here: if the true BSSE is 20% larger than estimated by the Counterpoise scheme, than there would be no binding at all. Conversely if the BSSE is underestimated by 20%, the binding energy would double. Summerizing, the large value for the BSSE makes it impossible to confidently draw physical insight from the MP2 calculations.

2.3.5 Configuration Interaction and Complete Active Space

Introduction Configuration Interaction Methods

An alternative method to include correlation energy, i.e. to obtain a total energy that is closer to the correct energy than the Hartree-Fock result, is to expand the wave function in more than one Slater determinant. Because every determinant correspond to a specific electron configuration, this method is called *configuration interaction (CI)*. A convenient way to obtain (and, later, truncate) the configurations is to perform a Hartree-Fock calculation and treat the resulting wave-function as first approximation to the ground-state determinant. By taking none, one, two, etc. electrons and distributing them into the virtual orbitals, singly, doubly, etc. excited determinants are generated. There are two approaches that need to be distinguished. In typical configuration interaction calculations, all determinants are obtained by a single Hartree-Fock (or similar) calculation, and only the expansion coefficients are optimized. In multi configuration self consistent field (MCSCF) calculations, the expansion coefficients and the orbitals are simultaneously calculated.

For systems with more than just a few electrons, the number of excited determinants becomes quickly very large. For N electrons and $2K$ spin orbitals, there are

$$\binom{N}{n} \binom{2K - N}{n} \quad (2.16)$$

n -tuply excited determinants. The equation also shows that the effort does not only increase factorially with the number electrons, but also with the size of the basis set (which determines the number of available spin orbitals). Hence, the expansion into a set of determinants must be truncated in some way. There are two approaches to achieve this goal, which are often employed together.

The most intuitive way to limit the number of determinants is to include them only up to a certain level of truncation. Indeed, it can be theoretically deduced that for ground state properties the majority of the correlation effects are captured as soon as doubly excited determinants are included. Singly excited determinants are typically also included, mainly because there are only few of them, which leads to the CISD method.

Calculations including higher level excitations are computationally very expensive, and typically only performed on very small system to serve as benchmark for other, more approximate methods.

Another often invoked approximation is no neglect the impact of the core electrons and focus on the valence states instead, which are more important for the chemistry of the problem at hand. In this approach, only excitations including pre-specified occupied and virtual states are allowed. This is called the restricted active space method. Typically, the active space encompassed only a few frontier orbitals, i.e. the highest occupied and lowest unoccupied orbitals. Unfortunately, it is often difficult to judge beforehand which orbitals are important for the process to be described by the calculation, and if relevant orbitals are left out of the active space, qualitative wrong results can be obtained. Another problem concerning MCSCF calculations is that during the optimization of the orbitals, their relative ordering can change, rotating them in and out of the active space.

The main advantage of CI methods is that it gives the wave function sufficient flexibility to allow bonds to change their nature. A classical example here is the dissociation of H_2 . By construction, the ground state determinant used for the Hartree-Fock calculation enforces that both electrons are in the bonding orbital. Therefore, even at infinite distance, the wave function described H_2 as being 50% ionic (H^+H^-) and 50% the neutral atoms ($H\cdot H\cdot$). In a CI expansion, the antibonding orbital is also available, and the result are two 100% neutral atoms. The inclusion of additional determinants also significantly improves the description of systems where the ground state is a superposition of inequivalent resonance structures, e.g., with biradical and zwitterionic character. For these reasons CI methods are the benchmark method when it comes to the description of charge transfer processes. Unfortunately, except for full CI (i.e., CI without any truncation), they are not size consistent, effectively preventing the calculation of interaction energies.

In this thesis, the CAS method has been used. CAS is a MCSCF type calculation which performs a full CI calculation in a restricted active space.

A comparative study of CAS and DFT: F4TCNQ/HV0 charge transfer salt

To evaluate whether density functional theory (DFT) yields sufficiently reliable results for typical systems studied in this work, a charge-transfer complex was studied using different levels of theory. An all-organic interface was chosen over metal/organic junctions, since it contains less electrons and exhibits larger orbital energy differences, thus facilitating the CAS benchmark calculation. Also, these kind of systems are expected to be the most problematic ones for DFT. As a prototypical example, the charge transfer salt between the strong electron donor 1H,1'H-[4,4']bipyridinylidene (HV0) and the potent electron acceptor 2,3,5,6-tetrafluoro-7,7,8,8 tetracyanoquinodimethane (F4TCNQ) (chemical structure see bottom part of Figure 2.6) was selected. Since the weaker acceptor TCNQ already undergoes significant charge transfer with the weaker donor tetrathiafulvalene (TTF)^[133], it is likely that this complex also shows large charge transfer character. Please note that the results presented hereafter were presented in a more

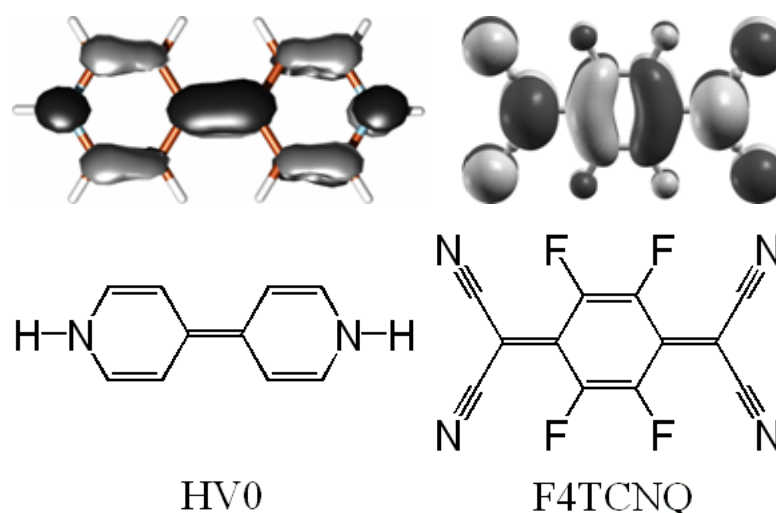


Figure 2.6: Top: Chemical structure of HV0 (left) and F4TCNQ (right). Bottom: HOMO of HV0 (left) and LUMO of F4TCNQ (right)

condensed form to the consortium of the EC project ICONCONTROL (EC-STREP-033197) in Deliverable 24.

Any complex between two organic molecules, even if the charge transfer is large, will be to a large extent governed by van-der-Waals forces, which are unfortunately inadequately described in most current DFT functionals. It is therefore pointless to perform geometry optimizations for this system. Rather, a good geometry must be “guessed”. To allow for a transfer of electrons between the two components, the responsible orbitals must overlap. Therefore, the best geometry - in the sense of the strongest interaction - is one where the overlap is maximized. The top part of figure 2.6 shows the HOMO of HV0 and the LUMO of F4TCNQ.

When accounting correctly for the signs of the lobes, one can derive two sensible geometries, which are shown in Figure 2.7. In one, both molecules are aligned with the long molecular axis parallel to each other, and the central ring of F4TCNQ is located exactly below one of the HV0 rings. This results in constructive interference (and hence maximal hybridization) between the lobe on the central HV0 bond and the lobe of the single F4TCNQ carbon atom connecting the ring with the outer cyano groups. Also, the overlap between the CN-groups and the HV0 ring is positive. On the backside, the overlap between the F4TCNQ ring and the other HV0 ring is practically zero. Another possibility is to rotate HV0 by 90 degrees, i.e. align the long molecular axis perpendicular to each other. Like in the former geometry, the central bond of HV0 is located above the connecting carbon atom in F4TCNQ. Here, constructive overlap occurs also between one side of the HV0 rings and the central F4TCNQ ring (of which lobe only the part with the correct sign is covered), and between the other side of the HV0 rings and the cyano groups. However, a small destructive contribution arising from the fluorine rings is also to be expected. In both conformations, it is assumed that the molecules remain planar. For the calculation of the total energy and the dipole moment, the distance between the components, which is a very crucial quantity for

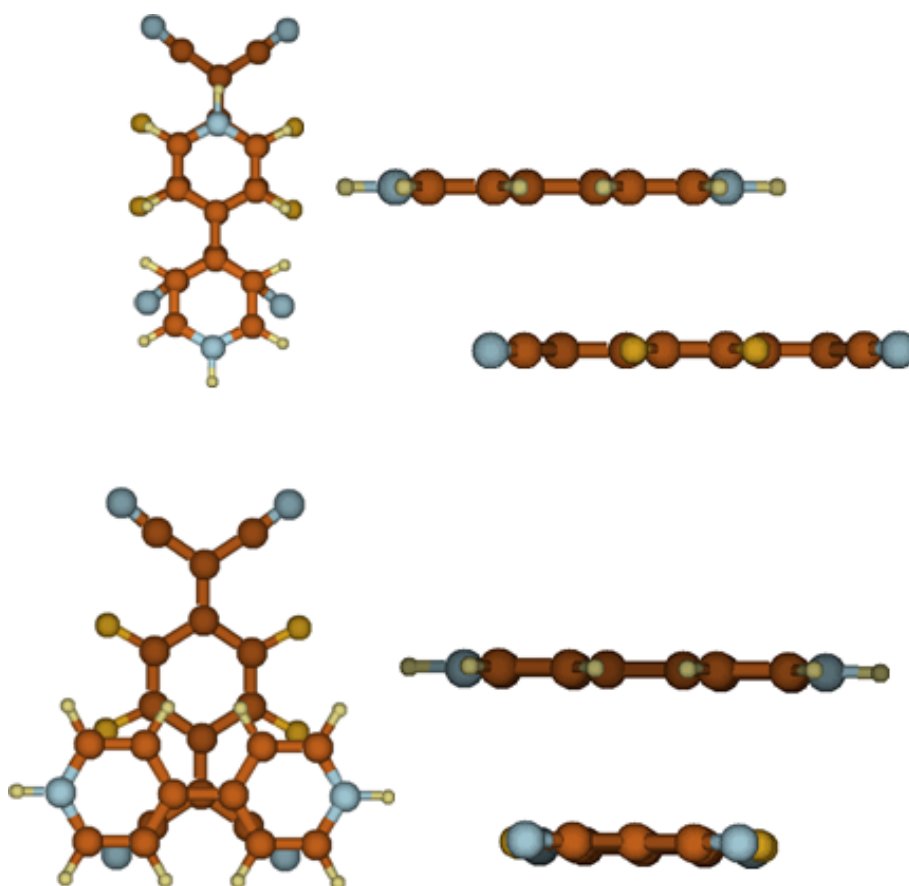


Figure 2.7: Proposed geometries for the F4TCNQ / HV0 complex, aligned parallel (top) and perpendicular (bottom). Color code: brown = carbon, white = hydrogen, blue = nitrogen, dark yellow = fluorine.)

our considerations, is systematically varied between 2.0 and 4.5 Å. Energetically, DFT calculations (functional: B3LYP / basis set: 6-31G(d,p)) predicts that conformations are fairly similar. At a donor-acceptor separation distance of 2.0 Å, the perpendicular conformation is lower in energy by 0.1 Hartree (2.7 eV). However, with increasing distance, the energy difference vanishes rapidly. At a more sensible distance of 3.0 Å, the difference is only 0.004 Hartree (0.01 eV). It should however be kept in mind that the total energy is not a good quantity here, since it suffers not only from the lack of van der-Waals interaction (which is certainly larger in the parallel than in the perpendicular conformation), but also from basis set superposition error, which was not accounted for.

In Figure 2.8 the evolution of the dipole moment with respect to the intermolecular distance is depicted. Obviously, the overlap is slightly more efficient in the parallel conformation than in the perpendicular alignment, since the dipole moment is larger by more than 0.5 Debye. Interestingly, in both conformations the evolution of the dipole moment is not monotonically. Rather, it shows a shallow minimum at ca. 3.5 Å. If the distance however falls below 2.5 Å, the dipole moment decreases rapidly. This effect can

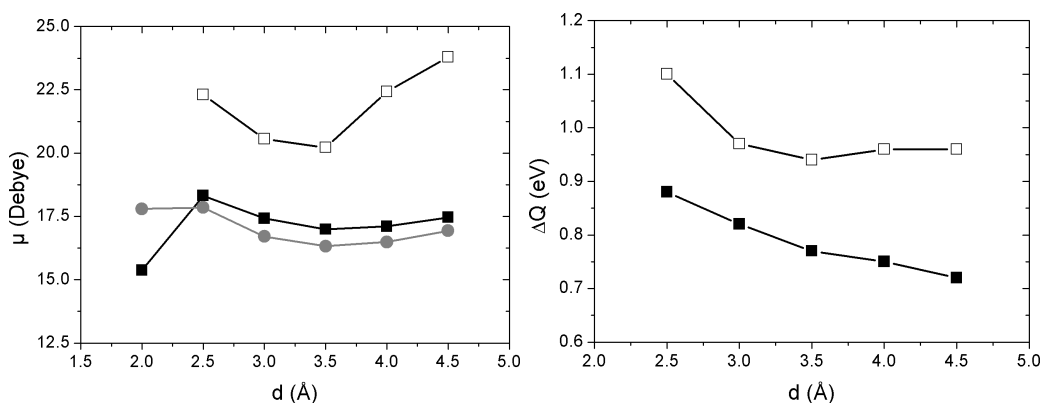


Figure 2.8: Left: Evolution of the dipole moment with increasing separation of the molecules. Right: Evolution of the transferred charge Q (as obtained from ESP charges) with increasing separation of the molecules. Lines intended as guide to the eye. Closed symbols are obtained from DFT (B3LYP / 6-31G**) calculations, open symbols from CAS(2,2) calculations with the 6-31G basis set). Boxes correspond to the parallel alignment, circles to the perpendicular conformation.

be tentatively attributed to Pauli-Pushback, which significantly distorts the electron clouds. This assumption is corroborated by the fact that the effect is more pronounced in the parallel conformation, which experiences more overlap than the perpendicular one.

In order to verify unexpected parabolic nature of the dipole evolution, the stability of the trend with respect to the chosen method is tested. As a first test, the perpendicular conformation at 3.5 Å distance is recalculated using a spin-unrestricted calculation. If triplet-contamination adulterates the solution, the largest effect should be found in this geometry, where the distance is large and the overlap small. However, no difference in dipole moment or total energy to the unrestricted calculation is found, i.e. the spin-unrestricted solution collapses into the restricted wave-function. The single-determinant nature of DFT imposes some bias on the result, since it does not allow easily for integer charge solutions, which require the inclusion of excited state determinant in the ground state wave function. In order to test whether this correction is important for the trends observed here, the dipole moment for the parallel geometry has been recomputed using the complete active space (CAS) method and the 6-31G basis set (i.e., without polarization functions to keep the basis set as small as possible). The calculations were limited to include 2 electrons and 2 orbitals (i.e., HOMO and LUMO, designated as CAS(2,2)). As shown by the open symbols in Figure 2.8a, the minimum around ca. 3.5 Å distance is correctly reproduced. For a single case (perpendicular, 3 Å distance), it was also tested that an extension of the active space up to 4 electrons and 4 orbitals does not affect the result significantly (the difference in the dipole moment is less than 5%). Between DFT and CAS, the total dipole moment obtained changes by several debye, which is most likely an artifact stemming from the different approach and the incomplete basis

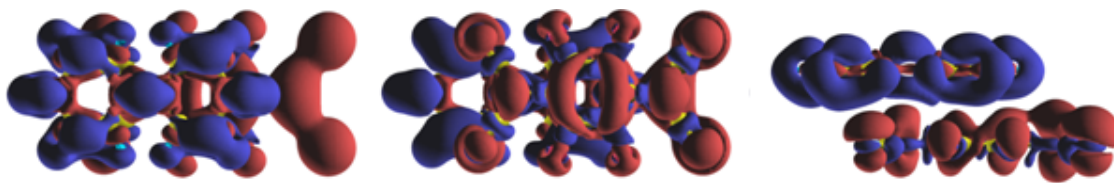


Figure 2.9: Charge density rearrangements of the F4TCNQ-HV0 complex. Red areas correspond to an increased electron density, while blue areas are reminiscent of electron density reductions.

set.

In order to quantify the charge transfer, ESP charges have been calculated and plotted in Figure 2.8. Using DFT, a charge transfer of about 0.9 electrons is predicted at an intermolecular separation of 2.5\AA , which slowly decays with increasing distance to about 0.7 electrons of 4.5\AA . This situation is qualitatively similar for CAS. Here, a transfer of 1.1 electrons is obtained at small distances. Upon increasing distance, the charge transfer is quickly reduced to ≈ 0.9 electrons.

To visualize what is happening in the complex, 3D charge rearrangements $\Delta\rho$ were obtained by subtracting the charge densities (ρ) of the isolated components from the charge density of the combined complex.

$$\Delta\rho = \rho_{CT-Complex} - (\rho_{HV0} + \rho_{F4TCNQ}) \quad (2.17)$$

The result is plotted from various angles in Figure 2.9. The shape of the charge rearrangements looks very similar to the HOMO of HV0 and LUMO and F4TCNQ, cf. Figure 2.6. This observation, together with the fact that the dipole moment is independent of the CAS-space used, allows for the conclusion that almost exclusively the frontier orbitals are involved in the electron-transfer process.

From the clear single-reference character of the charge rearrangements and from the same shape of the dipole-moment evolution as function of the intermolecular distance in DFT in CAS it can be concluded that DFT is able to yield reliable results for at least for this interface, which is typical for systems considered in this work.

3 Specific Systems

In this chapter, specific metal/organic and organic/organic interfaces will be investigated. Many of these case studies are joint theoretical and experimental work. The generally observed good agreement between “virtual” and “real” world demonstrates the reliability of the employed methods. Despite the diversity of the systems in this chapter, many common features are found, which are exploited in the next chapter to derive more general structure to property relationships.

The build-up of this chapter is as follows: First, interfaces between electron donors and metal surfaces are monitored. This starts by a computational analysis of the molecules 1H,1'H-[4,4']bipyridinylidene (HV0) and tetrathiafulvalene (TTF) on all three coinage metals. Both molecules are of similar size, but exhibit a significantly different ionization potential. In section 3.2, a joint experimental and theoretical study of N,N'-dimethyl-[4,4']Bipyridinylidene (MV0), a methylated derivative of HV0, is presented. To round up the picture of electron donors, the sterically demanding molecule 9,9'-ethane-1,2-diylidene-bis(N-methyl-9,10-dihydroacridine (NMA) is studied on Au experimentally and with density functional theory (DFT). The next section aims at interfaces of opposite polarity, i.e. between metals and electron acceptors. There, first a computational investigation of 1,4,5,8,9,12-Hexaaza-triphenylene-2,3,6,7,10,11-hexacarbonitrile (HATCN), adsorbed face-on on all three coinage metals is presented. Unique electronic properties of the HATCN/Ag interface are then demonstrated. A joint experimental and theoretical study shows that the metal/organic interfaces can be quite complicated, and a phase transition in the HATCN monolayer is demonstrated. To compliment the understanding of metal/acceptor interfaces, coronene-1,2,5,6,9,10-hexaone (COHON), which is of similar size as HATCN, but exhibits different docking chemistry, is investigated. As third type of metal/organic interface, the organometallic compound chlorogallium phthalocyanine (GaClPc) is studied on Cu(111). Although this molecule does not undergo significant charge-transfer with the metal, valuable insights are obtained from the strong geometric distortions upon adsorption and the thus induced charge rearrangements. To broaden the understanding of charge-transfer systems, the range of the investigations is extended to organic/organic compounds. In section 3.7, cyclophanes will be studied. This class of substances consists of an electron donor and an electron acceptor part where the overlap between the wave functions of the subsystems is enforced by binding them together covalently. The final section of this chapter will be concerned with three-component metal/organic/organic interface. Thereby, the top organic layer is a strong electron donor or acceptor, directly relating to the first to sections of this chapter. The nature of the sandwiched organic layer will be varied, consisting of either electronically active donor or acceptor compound or a self-assembled monolayer.

3.1 HV0 and TTF: Reducing the Metal Work Function beyond Pauli Pushback: A Computational Investigation of Tetrathiafulvalene and HV0 on Coinage Metal Surfaces

3.1.1 Preface

In metal/organic interfaces, electron donors present a particularly challenging field. Basic chemistry teaches that coinage metals, when in a chemical compound, usually come with positive oxidation numbers, i.e. are weak electron donors themselves. The most important question, therefore, is whether it is possible at all to find organic molecules which are sufficiently electron rich that they reduce the underlying substrate. Moreover, proving that such a reduction occurs is not easy, either. Charges of subsystems are not physical observables and thus not accessible by experiments, and although atomic or molecular charges are readily calculated, such calculations impose an arbitrary, not physically justified partitioning of the combined system and are, therefore, inherently flawed. Indirect proof of charge transfer can be mustered by observing the modification of the substrate work-function change induced by adsorption of a monolayer of the electron donor; transferring charge from the organic layer to metal must result in a work-function decrease. Unfortunately, however, charge-transfer is not the only possible reason for a work-function reduction. Indeed, adsorption of any body on a clean surface induces an effect called pushback [50], which yields a notable work-function decrease even for inert adsorbates [30]. It is, therefore, of paramount importance to demonstrate the metal work functions can be reduced beyond Pauli Pushback.

The following part is a reproduction¹ of the publication [37], see the facsimile in Figure 3.1. All VASP and Gaussian calculations were performed by myself. The SIESTA calculations were done with the help of Gerold M. Rangger. The results were interpreted in multiple discussions between all three authors of the paper.

¹Except for the sake of consistency in this thesis, the name “viologen” originally used for 1H,1'H-[4,4']bipyridinylidene in the paper was substituted by the name “HV0”.

Reducing the Metal Work Function beyond Pauli Pushback: A Computational Investigation of Tetrathiafulvalene and Viologen on Coinage Metal Surfaces**Oliver T. Hofmann, Gerold M. Ranggger, and Egbert Zojer****Institute of Solid State Physics, Graz University of Technology, Petersgasse 16, 8010 Graz, Austria**Received: July 31, 2008; Revised Manuscript Received: October 14, 2008*

Figure 3.1: Faksimile of the head of the publication showing all contributing authors as well as the date when the paper was recieved by the journal.

3.1.2 Abstract

Application of (sub)monolayers of organic molecules on metal electrodes in order to tune the effective work function has become a field of significant interest. Due to its low ionization potential and quinoidal structure, HV0 (1H,1'H-[4,4']bipyridinylidene) is proposed as a particularly potent work function reducing molecule. In the present contribution, its interaction with Au(111), Ag(111), and Cu(111) is compared to that of the prototypical electron donor tetrathiafulvalene (TTF) using density functional theory based band-structure calculations. The work function modification in both systems is found to be determined by a subtle interplay between effects due to adsorption induced geometric distortions and the donation of electrons from the respective molecular HOMO to the metal. The interfacial charge transfer is investigated in real space as well as in terms of changes in the occupation of the molecular orbitals. Overall, HV0 is found to be an excellent choice for decreasing the substrate work function. On gold, a reduction by up to -1.6 eV is predicted, resulting in the HV0 covered Au surface having a work function equivalent to that of pristine magnesium.

3.1.3 Introduction

Application of (sub)monolayers of conjugated organic molecules is a powerful way to control the interface energetic in modern (opto)electronic devices [11, 129]. One possibility is the use of self-assembled monolayers (SAMs), whose intrinsic dipole can be exploited to modify the effective work function [134–143]. Another approach is to employ (sub)monolayers of particularly electron rich or electron deficient molecules [11]. They induce charge transfer to/from the metal and hence a dipole (which in the following will be referred to as the bond dipole), which results in a work function change. Specifically, electron acceptors have been studied in great detail [24, 129, 132, 144–146]. It has been demonstrated that by variation of the acceptor strength or the coverage [11, 145] the work function of the substrate can be tuned continuously. The current state-of-the-art acceptor F4TCNQ (tetrafluoro-tetracyanoquinodimethane) has been shown to increase the metal work function by as much as 0.35 eV [144] on Au(111) and 0.60 eV on both Ag(111) [147] and Cu(111) [24]. Density functional theory (DFT) based calculations

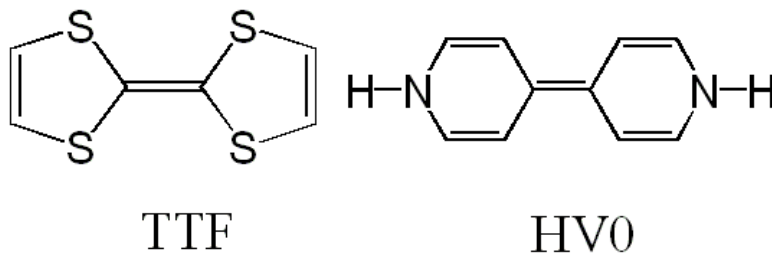


Figure 3.2: Molecular structures of TTF and HV0.

revealed that a complex mechanism of σ -donation and π -backdonation is responsible for the binding to the surface [24]. The resulting net-charge transfer then results in the above-described work function increase. Electron donors have been used to dope organic layers [129, 148, 149] but their application to tune interface properties is only rarely discussed in literature. Fernandez-Torrente et al. [25] have demonstrated that TTF (tetrathiafulvalene, see Figure 3.2) forms well ordered monolayers on a Au(111) surface, accompanied by a charge transfer of about half an electron. Larger, i.e.1, integer charge transfer, has been suggested [150] for tetrakis-dimethylaminoethylene, accompanying a work function reduction on polycrystalline gold by -1.3 eV. Experimentally, the effect of strong donors is difficult to assess. On the one hand, particularly electron rich molecules are often not stable in air, making them difficult to handle. On the other hand, the work function modification by charge transfer is difficult to separate from the ever-existent Pauli repulsion (i.e., the repulsion of the metal electron cloud due to electrons of the adsorbate). On coinage metals, this effect amounts to a work function reduction between around -0.4 eV for noble gases [32] and up to -0.7 eV for (inert) alkane chains [30]. Therefore, computational modeling provides an invaluable tool to actually understand the detailed mechanism behind the observed work function decrease and to suggest new materials suitable for work function reduction.

In this work, we propose HV0 (1H,1'H-[4,4']bipyridinylidene, see Figure 3.2) as a specifically potent molecule to reduce the substrate work function and thus to promote electron injection. HV0 and its derivatives are known as strong donors [151–154], which are particularly electron rich due the incorporation of the lone pairs of the pyridine nitrogen atoms into the π -system. Its extremely low ionization potential (vertical IP calculated to be 4.85 eV in gas phase at the B3LYP/6-31+G* level using Gaussian 03 [71]) is smaller than the work function of clean Au(111), which from our DFT band structure calculations is estimated to be 5.22 eV (consistent with experimental values for clean Au(111) surfaces) [11]. This is an ideal prerequisite for charge transfer. Moreover, upon oxidation, a quinoid to benzoid transition occurs. The resulting aromatic stabilization provides an additional driving force for charge transfer [155]. To better understand the properties of HV0 as a potent donor on a metal surface, we compare it to the prototypical donor TTF as a “benchmark” (see Figure 3.2). TTF is an electron rich molecule with a gas phase ionization potential of 6.34 eV (again at the B3LYP/6-31+G* level), i.e., 1.49 eV larger than that of HV0. Still, it is commonly used in charge transfer salts [156, 157] or as dopant [158, 159] and is known to transfer electrons to Au (vide supra). For the following discussion, the focus will be laid on the Au(111) surface, since

(i) Au is more commonly used as electrode material in electronic devices (e.g., organic thin film transistors) than other noble metals and (ii) the observed effects are most pronounced there. First, the adsorption geometry will be briefly discussed. Then, we will focus on the electronic structure, describe in detail the encountered charge transfer, and discuss the modification of the net work function. The latter turns out to result from a subtle interplay between contributions from the bond dipole and a molecular dipole due to adsorption induced geometric distortions. Finally, differences in the adsorption on Ag(111) and Cu(111) will be addressed.

3.1.4 Methodology

All calculations were performed using density functional theory (DFT). To study HV0 and TTF adsorbed on noble metal surfaces, band structure calculations were done employing a periodic slab approach, where the surface is described by a finite number of metal layers (five in the present calculations) together with the adsorbate. This results in an infinitely extended periodic metal surface (covered with the adsorbate) in the x - and y - directions; in the z -direction the repeated slabs are separated by at least 20 Å of empty space to avoid interaction between the individual slabs. Geometry optimizations and charge densities were computed using the VASP (Vienna Ab-initio Simulation Package) code [51–53], employing the PW91 [54] exchange-correlation functional. Electron interaction between valence and core was modeled by the projector augmented-wave method (PAW) [55, 56]. A plane-wave basis set with a cutoff energy of 20Ryd has been used (independent of the contents of the unit cell). The band structure was calculated on a $(3 \times 3 \times 1)$ Monkhorst-Pack grid [57] of k -points. The electronic states were occupied using the Methfessel-Paxton scheme [58] with a broadening of 0.2 eV. All calculations were done in a non spin-polarized manner; spin unrestricted test calculations performed for HV0 on Au(111) show negligible deviations from the restricted case, as demonstrated in the Supporting Information. We chose to study a single molecule in a $5 \times 3\sqrt{3}$ unit cell. This corresponds to the case of a loosely packed monolayer (no experimental unit cell for densely packed HV0 monolayers is known up to date; thus, to avoid artifacts due to an improper packing, we chose to study the limiting case of weakly interacting adsorbates). Moreover, this unit cell also allows a direct comparison with earlier calculations performed for the prototypical acceptor F4TNCQ [24]. For an estimate of the maximal work-function modification, a tightly packed monolayer was computed in a $3 \times 3\sqrt{3}$ unit cell. The positions of all atoms of the molecule as well as the top two metal layers were fully relaxed using a damped molecular dynamics scheme until the remaining forces were smaller than 0.01 eV/Å. In order to avoid artificial polarization of the slab due to the 3D periodicity of the system, an additional dipole of the same magnitude but opposite sign was automatically inserted into the vacuum region ^{II}. For the determination of the orbital occupation from the molecular orbital density of states (MODOS) [62, 63] SIESTA (Spanish Initiative for Electronic Simulations with Thousands of Atoms) [61] calculations were performed as described in ref [160]. It

^{II}One problem encountered in this context is if the self consistent field (SCF) cycle converges faster than the dipole of the system. In this case, the calculation stops before the final, correct value for the dipole is obtained. Thus, if necessary, additional SCF cycles were performed at the optimized geometries to achieve a convergence also of the unit cell dipole moment to less than 0.01 eÅ.

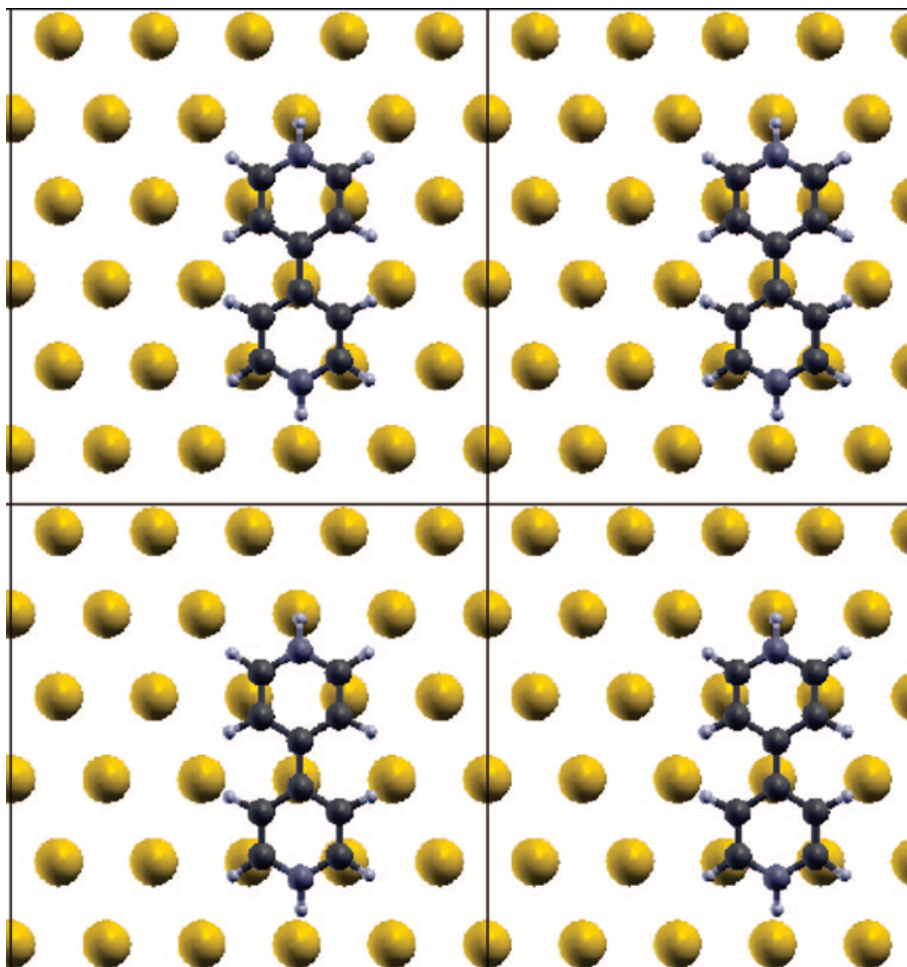


Figure 3.3: Section of the studied HV0 on Au surface. The gray lines indicate the $5 \times 3\sqrt{3}$ unit cell. Only the top metal layer is shown for the sake of clarity.

has been rigorously tested [63] that despite the methodological differences between the VASP and SIESTA (e.g., the latter uses atomic orbital basis sets instead of plane waves together with the PBE functional) deviations between the projected densities of states are negligible. This applies especially to the respective projections onto the molecular regions (MDOS). Graphics of the molecular geometries and 3D plots of the charge rearrangements were produced using the XCrysDen program [161].

3.1.5 Results and Discussion

Adsorption Geometry and Energy on Au(111).

It is well documented that both TTF and HV0 adsorb face on [25, 151]. In the $5 \times 3\sqrt{3}$ super cell on the Au(111) surface, alignment along the $[2\bar{1}\bar{1}]$ -direction was assumed, to be consistent with previous calculations on related systems [24]. Note that for TTF, Fernandez-Torrente et al. [25] suggested orientation along the $[01\bar{1}]$ -direction. We studied also that orientation (the corresponding results are contained in the Supporting

Information); deviations between the two orientations are, however, only minor. As shown in Figure 3.4, both molecules experience geometrical distortions upon adsorption. TTF adsorbs with the short molecular axis being slightly tilted with respect to the surface. As Figure 3.4 indicates, also the long molecular axis is not perfectly parallel to the top metal plane. Note that this is somewhat different from the geometry described in ref [25], where only rotation around the long molecular axis was found (for further details see Supporting Information). Here, none of the molecular axes is parallel to the substrate and all sulfur atoms are located at different distances from the metal surface. The vertical distance between the topmost metal layer and the lowest lying atom of TTF is computed to be 2.91 Å. Due to the above described adsorption geometry, the vertical distance between the lowest and the topmost atom of the molecule is relatively large (about 1.2 Å, compare Table 3.1, which also contains data for the adsorption on Ag(111) and Cu(111) to be discussed later). In this context it is interesting to mention that also when studying the adsorption of thiophene on Cu(110) using nonlocal functionals (thus aiming at properly including van der Waals interactions) a non coplanar adsorption geometry was found, i.e., the S atom was closer to the metal surface than the other atoms in the thiophene [96].

Despite its larger binding energy, HV0 is found at a larger distance from the surface than TTF. In the Au case, the smallest vertical metal-molecule distance is computed to be 3.49 Å (cf. Table 3.1). Unlike TTF, no significant tilt of either molecular axis with respect to the surface is observed. Moreover, no stable conformation with the amino hydrogen atoms pointing away from the surface could be found, as one might infer from the possible interaction of the nitrogen lone pairs with the metal electrons. Even if a starting geometry was biased in this way, the molecule relaxed into the conformer shown in Figure 3.4 with both hydrogen atoms pointing downward. As aromatic stabilization upon charge transfer can be a significant driving force for the transfer [155], it is useful to also analyze adsorption induced bond length changes. These are plotted for TTF and HV0 in Figure 3.5. Indeed, in particular HV0 undergoes a partial transition from a quinoidal to benzoidic geometry (i.e., all double bonds become longer and all single bonds in the backbone are shortened). This distortion induced stabilization is also consistent with the relatively large adsorption energies compared to TTF in spite of the larger metal to molecule distance (see Table 3.1). It also is a first indication for

Table 3.1: Structural Data for the converged Geometries of TTF and HV0 on Cu(111), Ag(111), and Au(111). Δz_{Dist} denotes the vertical distance between the topmost metal layer and the lowest atom of the molecule. Δz_{Mol} describes the vertical distance between the lowest and the topmost atom of the molecule. ΔE is the binding energy defined as the energy of the combined system E_{system} minus the total energy of slab E_{slab} plus monolayer $E_{monolayer}$.

	TTF			HV0		
	Au	Ag	Cu	Au	Ag	Cu
Δz_{Dist} (Å)	2.91	3.01	2.64	3.49	3.69	2.97
Δz_{Mol} (Å)	1.18	1.14	1.59	0.67	0.33	0.44
ΔE (eV)	-0.65	-0.41	-0.76	-0.51	-0.66	-1.10

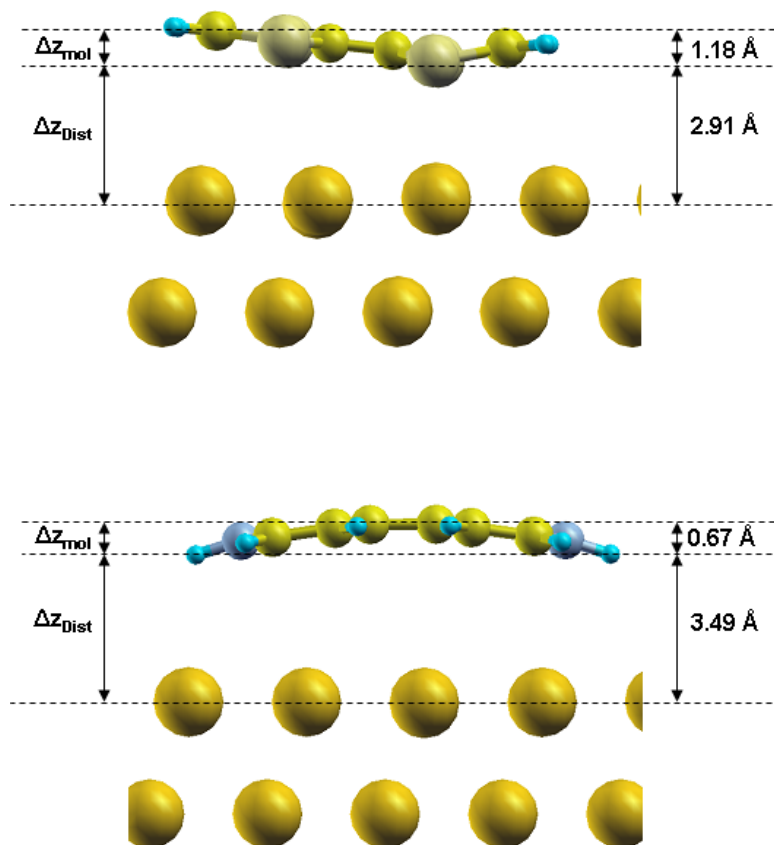


Figure 3.4: Relaxed geometry of TTF (top) and HV0 (bottom) on Au(111); for the sake of clarity only part of the unit cell and only the top two metal layers are shown. A top view of the complete unit cell is contained in the Supporting Information.

a particularly strong molecule to metal electron transfer in HV0. However, prior to discussing the implications of TTF and HV0 adsorption for the electronic properties of the metal surface, a methodological aspect needs to be addressed briefly.

A crucial parameter to assess the reliability of conclusions drawn from density functional theory calculations is the abovementioned binding energy between substrate and adsorbate. This is because especially in weakly interacting systems, van der Waals forces can become the dominant contribution. In the present case, the adsorption energies on Au (for other metals see Table 3.1) are found to be -0.65 eV for TTF and -1.25 eV for HV0. These energies are already quite sizable, but still only a fraction of those are associated with a “true” covalent chemical bond. They are also of a similar order of magnitude as van der Waals forces for comparable systems [96]. Unfortunately, common generalized gradient approximation (GGA) type functionals (like PW91 used here) do not correctly account for these interactions [98, 162, 163]. Hence, such calculations can give too large binding distances and too low binding energies, or even no binding at all [164]. To the best of our knowledge, the only case in which nonlocal functionals have been successfully applied to the interface between a conjugated organic molecule

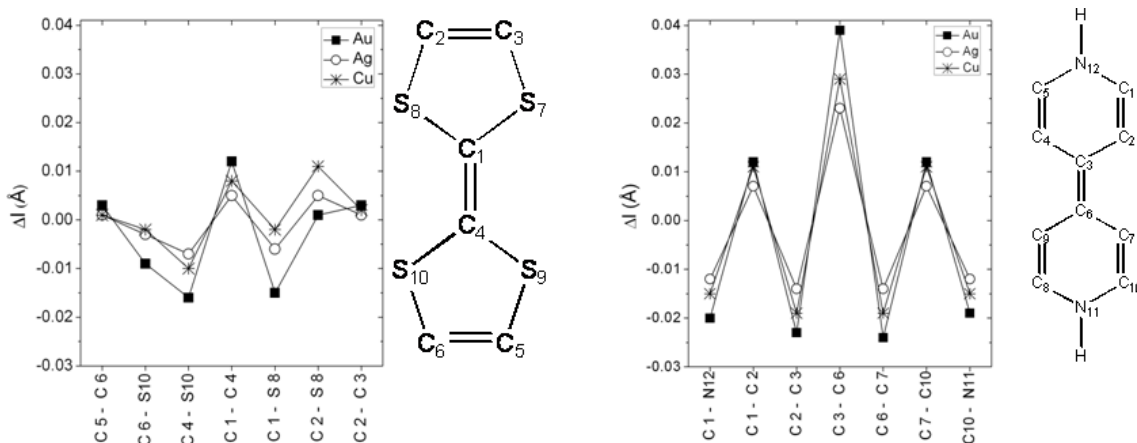


Figure 3.5: Bond length changes upon adsorption for TTF and HV0 on Au(111) (squares), Ag(111) (open circles), and Cu(111) (stars).

and coinage metals is thiophene on Cu in ref [96] discussed above. Complementary to GGA, local density approximation (LDA) functionals generally overbind [77], yielding too small molecule-metal distances. Based on that, it is reasonable to assume that in most instances the actual equilibrium distance between an organic adsorbate and the metal surface lies in between the two extreme cases provided by GGA and LDA calculations. Therefore, in order to back up our conclusions especially on the interface energetic discussed below, we also performed LDA test calculations (i.e., we mapped the total energy and the work function modification as a function of the metal-molecule distance using both GGA and LDA functionals). In the LDA calculations we found the minimum energy distance for TTF to be about 0.5 \AA closer to the surface, while the adsorption height of HV0 was reduced by about 0.75 \AA . Of particular interest for the present study are the resulting differences in the work-function modification, $\Delta\Phi$, for the GGA and the LDA derived equilibrium distances. Only minor differences are found when the equilibrium distance is varied between the limits given above; for TTF the work function decrease remains virtually the same, and for HV0 it increases by $<20\%$, when going from the LDA to the GGA equilibrium distances^{III}. These deviations do not affect any of the conclusions drawn below, which implies that the results are sufficiently stable to allow for a reliable analysis of TTF and HV0 adsorption.

Electronic Structure and Charge Transfer.

The key for understanding the consequences of TTF and HV0 adsorption is an in-depth analysis of the electronic structure of the modified surface. Figures 3.6 and 3.7 show the charge rearrangements upon adsorption, $\Delta\rho$, for HV0 and TTF, respectively. $\Delta\rho$ is calculated as the difference between the electron density of the combined system (metal plus adsorbate), $\rho_{combined}$, and the sum of the charge densities of the isolated metal slab,

^{III}Since it is not sensible to calculate the bend of the molecules at non-equilibrium distances, all calculations were done forcing the molecule into their planar, gas phase geometry. The electronic structure in all cases has been calculated at the GGA level

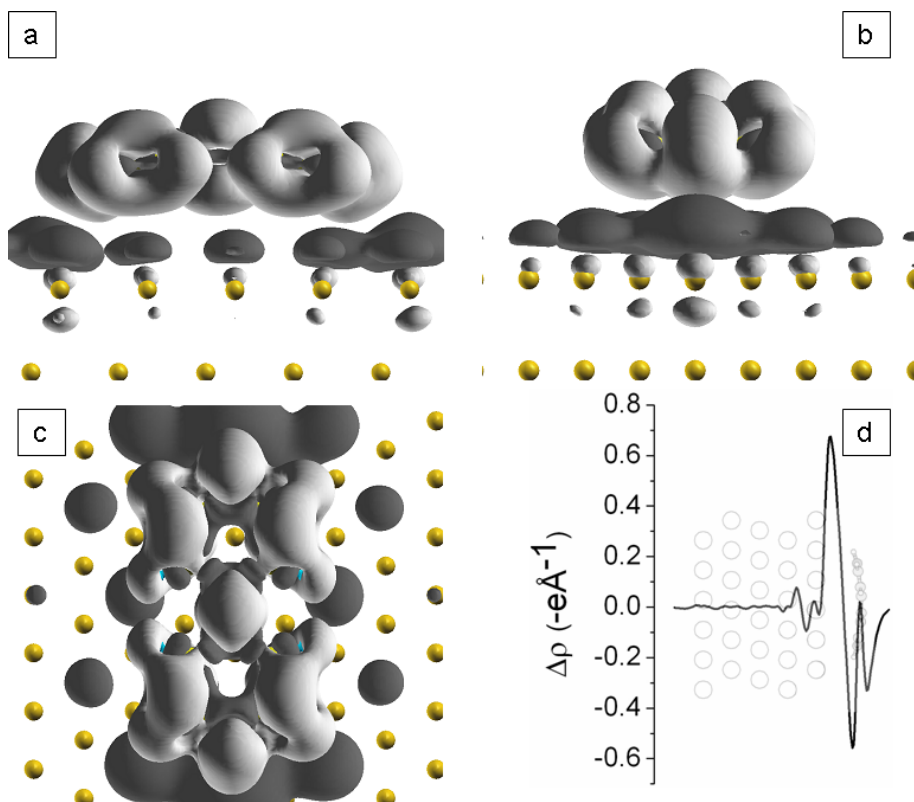


Figure 3.6: a-c: Isodensity representation of the charge rearrangements upon adsorption of HV0 on Au(111). Electrons flow from the light gray to the dark areas. Only a part of the $5 \times 3\sqrt{3}$ unit cell is shown for the sake of clarity. The isodensity values are set to $0.005 e^{-3}$. Part (b) has been obtained from (a) and (c) from (b) by counterclockwise rotation of 90° around the z - and the x -axis, respectively, i.e., the left nitrogen atom in (a) corresponds to the front nitrogen atom in (b) and the bottom nitrogen in (c). d: Electron density difference integrated over the x - y -plane within the unit cell; the system is shown in the background as a guide to the eye.

ρ_{slab} , and monolayer, $\rho_{monolayer}$, (both in their final, i.e., “adsorbed” geometries).

$$\Delta\rho(x, y, z) = \rho(x, y, z)_{combined} - (\rho(x, y, z)_{monolayer} + \rho(x, y, z)_{slab}) \quad (3.1)$$

For both HV0 and TTF, a strong depletion of electron density at the π -lobes, i.e., slightly above and below the molecule (light gray areas in Figure 3.6 as well as Figure 3.7), is observed, corresponding to a π -donation of electrons from the molecule into the metal. It is evident that much larger charge transfer occurs from HV0 than from TTF. From the 3D-plots, also (minor) changes in the charge density within the σ -skeleton are found (light and dark shaded areas close to the plane of the molecule; at the perimeter of the molecule, areas of reduced electron density in the π - and σ -systems overlap resulting in the peculiar shape of the displayed isodensity surfaces). From the plots showing the charge redistribution integrated over the x - y plane within the unit cell (i.e., parallel

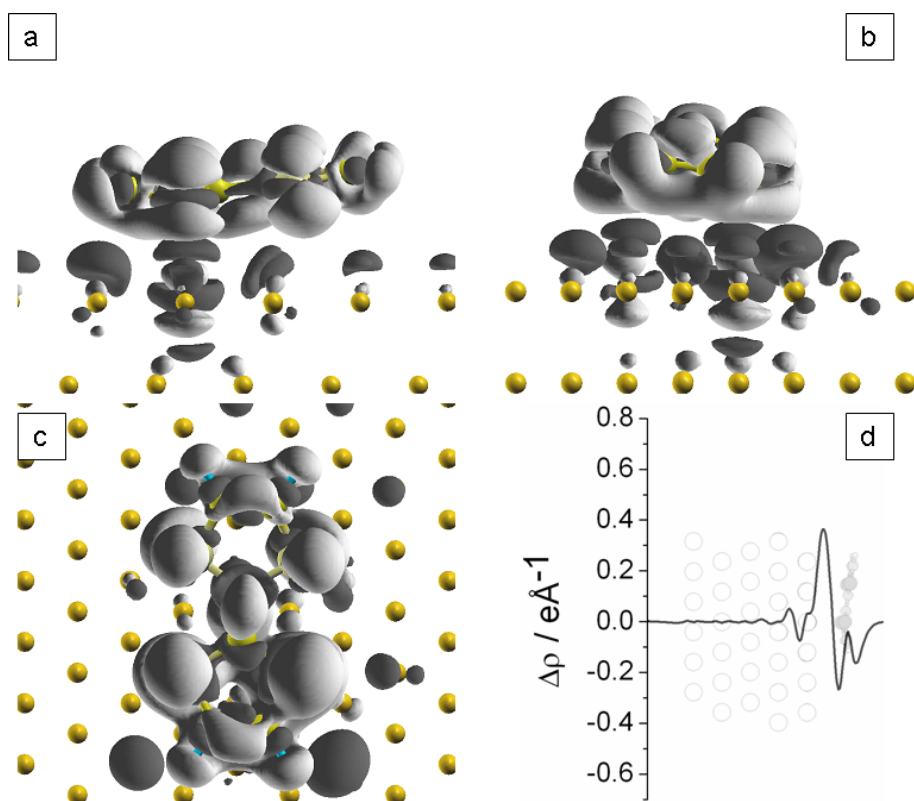


Figure 3.7: a-c: Isodensity representation of the charge rearrangements upon adsorption of HV0 on Au(111). Electrons flow from the light gray to the dark areas. Only a part of the $5 \times 3\sqrt{3}$ unit cell is shown for the sake of clarity. The isodensity values are set to $0.005 e^{-3}$. Part (b) has been obtained from (a) and (c) from (b) by counterclockwise rotation of 90° around the z - and the x -axis, respectively, i.e., the left nitrogen atom in (a) corresponds to the front nitrogen atom in (b) and the bottom nitrogen in (c). d: Electron density difference integrated over the x - y -plane within the unit cell; the system is shown in the background as a guide to the eye.

to the metal surface; Figures 3.6d and 3.7d) it, however, becomes clear that $\Delta\rho(z)$ is close to zero in the region that can be considered as the plane of the molecule. This indicates that in spite of the rearrangements within the σ -system, there is no net charge transfer to or from the metal; i.e., the σ -electrons do not actively participate in the bonding. Figure 3.6 also shows that the majority of the electrons are transferred from HV0 to the region just above the plane of the nuclei of the top metal atoms (geometric distortions of the metal surface due to the adsorption are negligible). The strongest accumulation of electron density in the metal occurs in the vicinity of the N-H parts of HV0 (in particular above the two Au atoms, which are the nearest neighbors to the amino hydrogen atoms) indicating that these are the regions of “strongest interaction”. Yet only a fraction of the transferred charge is confined to these places, and one finds an increased electron density in a metal region larger than the footprint of the molecule. Figure 3.7 shows that the situation for TTF is qualitatively similar to HV0, inasmuch

as most electron density is depleted from the π -system. Also, no net transfer to/from the σ -system is observed. There are, however, a few differences. Most notably, the rearrangements of the electron density are not as extensive as for HV0. In terms of bonding, significant electron density is accumulated below the sulfur atoms. It is also evident that not all sulfur atoms participate equally. Rather, the electron accumulation is more strongly pronounced where the respective sulfur atom is located closer to the surface. It should be noted that there is additional electron density buildup smeared out over the whole metal surface as can be seen for plots at reduced isodensity values. These are shown in the Supporting Information. Hence it can be concluded that a significant amount of electrons is transferred to the bulk metal, or more specifically, to the region just above the nuclei of the topmost gold layer.

To analyze the role played by the individual molecular orbitals of the adsorbate, the molecular orbital density of states, MODOS, was calculated by projecting the total density of states onto the bands derived from the molecular orbitals calculated in the absence of the metal [24, 165]. Upon hybridization of the initial molecular states with the metal band, the states shift and become broadened, some of them extending to (partially) above the Fermi edge. Since the states are only occupied up to the Fermi energy, the occupation (or the loss thereof) can be obtained by integrating the MODOS associated with each molecular orbital up the Fermi level. The corresponding values are shown in Figure 3.8.

The most significant change is a decrease in the HOMO occupation. Due to the electron donation from the molecule to the metal, the HOMO of HV0 (TTF) is only 60% (80%) filled. None of the other orbitals are strongly involved in the charge transfer, i.e., all other deviations from complete, respectively, zero filling are small (typically below 2%). This is in sharp contrast to other chemisorbed molecules, such as F4TCNQ [24] or CO [166], where the change in the occupation of the π -system (in those cases filling of the LUMO) is partly compensated by a comparably strong transfer of localized σ -electrons from the molecule to the metal. Table 3.2 summarizes the HOMO occupations on all metals, as well as the total transferred charge, ΔQ_{MODOS} . It is defined as minus the elementary charge times the summation over the occupation of all molecular orbitals after adsorption (i.e., the values plotted in Figure 3.8), n , minus the number of electrons in the isolated molecule, $N_{molecule}$.

$$\Delta Q_{MODOS} = -e \left(2 \sum_i n_i - N_{Molecule} \right) \quad (3.2)$$

The factor of 2 needs to be included as there can be up to two electrons in each orbital (i.e., all calculations are performed in the spin unpolarized manner). From this Mulliken-like analysis [63], a charge transfer of 0.44 electrons is found from TTF to Au(111)^{IV}. The value for HV0 is by about 50% larger (0.65 electrons)! This magnitude of charge transfer is on par with its state-of-the-art acceptor counterpart, F4TCNQ. An alternative way to look at the charge transfer is via integration of the plane integrated

^{IV}Note that there is no exact one-to-one correspondence of the transferred charge to the HOMO occupation, due to the spurious participation of other orbitals.

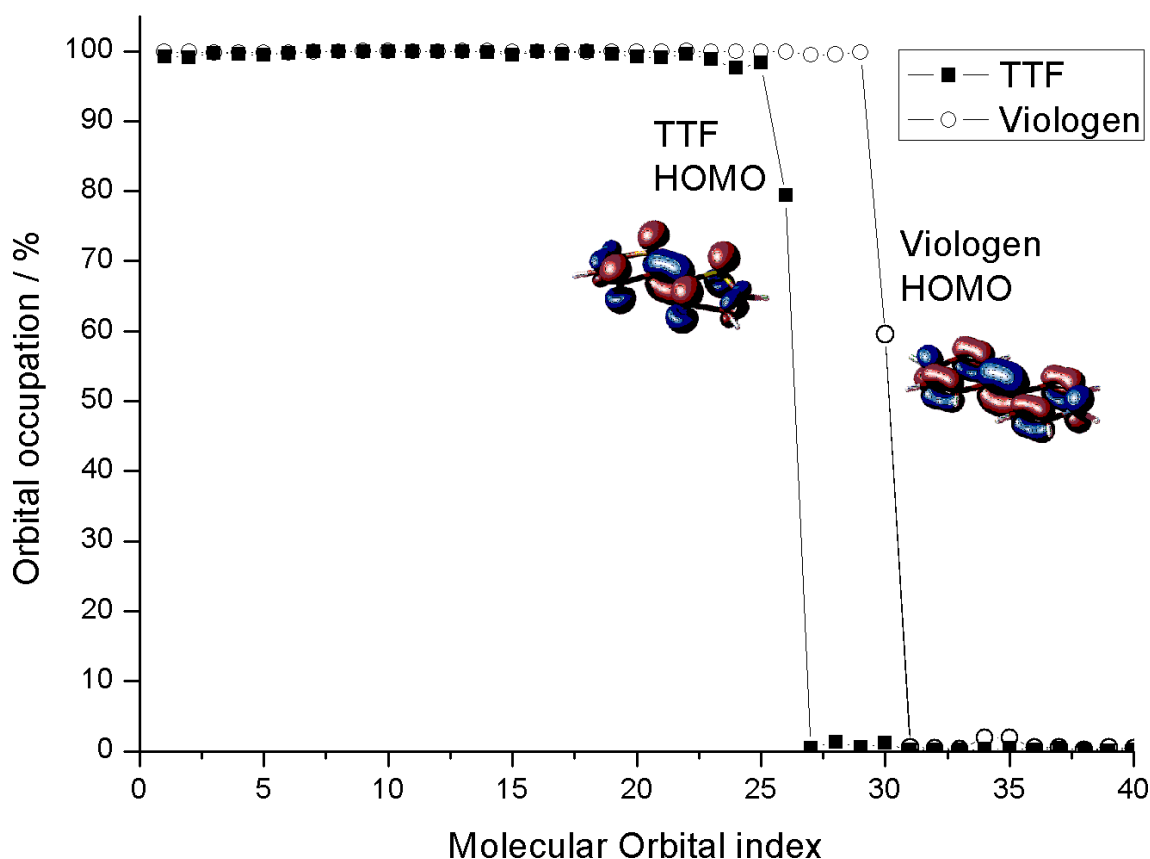


Figure 3.8: Occupation of the molecular orbitals of TTF and HV0 adsorbed on a Au(111) surface as derived from the MODOS (details see text). The inset shows the HOMOŠs of TTF and HV0 in their gas phase geometries.

charge density difference, $\Delta\rho(z')$, as shown in Figures 3.6d and 3.7d up to a specific height z .

$$\Delta Q_{Bond}(z) = \int_0^z \Delta\rho(z')dz' \quad (3.3)$$

Following this definition, ΔQ_{Bond} describes what amount of charge has been transferred from the region below to the region above the plane located at z (see Figure 3.9). High above the molecule and below the slab ΔQ_{Bond} must be zero, since the adsorption process is charge conserving. For values of z in the region of the interface between molecule and metal, the charge transfer between the molecule and the metal can be calculated. There is, however, no physically compelling choice of z , as there is no way of telling where the metal ends and where the molecule begins. Here, we define the metal as the electron accepting and the molecule as the electron donating part of the system. Hence, ΔQ_{Bond} , the net charge transfer between molecule and metal, is defined as the global maximum of $\Delta Q_{Bond}(z)$. The values of ΔQ_{Bond} are summarized in Table 3.2.

Qualitatively, ΔQ_{Bond} and ΔQ_{MODOS} agree very well. The differences between TTF

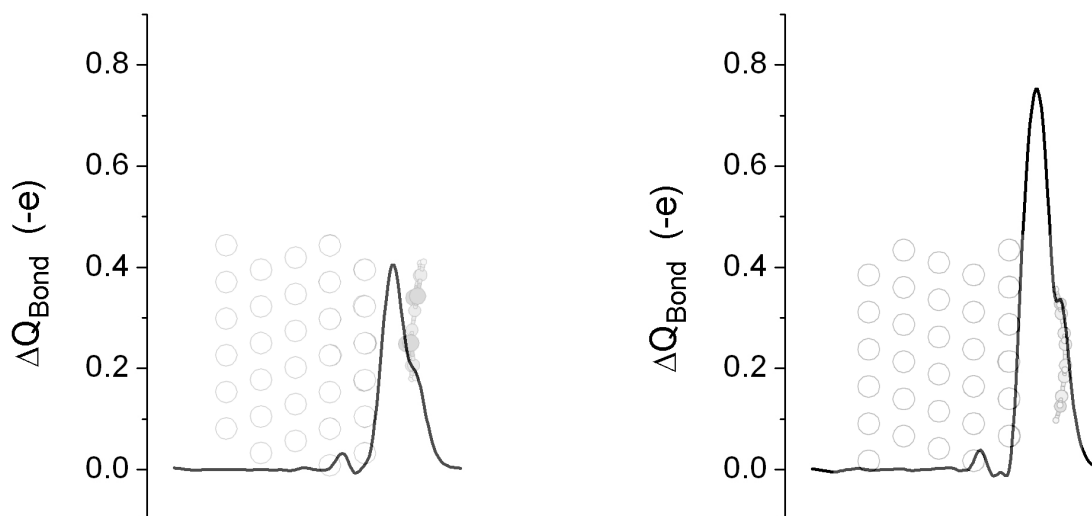


Figure 3.9: Total charge transferred, ΔQ_{Bond} , up to a position z for TTF (left) and HV0 (right) on Au(111) calculated according to eq 3.3. A plateau of ΔQ_{Bond} is resolved in the plane of the molecule; it is a manifestation of the fact that the σ -system of the adsorbate does not participate in the charge transfer process. For details regarding the definition of ΔQ_{Bond} see text.

and HV0 are, however, more pronounced in the case of ΔQ_{Bond} ; i.e., within this partitioning scheme, the electron donation from the adsorbate to the metal is almost twice as high for HV0 as for the reference donor TTF.

The Work Function.

The main goal of the surface modifications presented here is to modify the effective work function of the substrate in order to facilitate electron injection in organic devices. The change in the work function induced by a dipolar layer, $\Delta\Phi$, is given by the solution of

Table 3.2: HOMO occupation and charge transferred due to adsorption. The HOMO occupation is obtained by projecting the density of states of the combined system onto the HOMO of the isolated molecule [63]. ΔQ_{MODOS} is calculated by summation over the occupation of all orbitals and equals the Mulliken charge. ΔQ_{Bond} is given by the maximum of the integration of $\Delta\rho$ (details see text).

	TTF			HV0		
	Au	Ag	Cu	Au	Ag	Cu
HOMO occupation	79%	90%	84%	60%	77%	61%
ΔQ_{MODOS} (e)	-0.44	-0.28	-0.41	-0.65	-0.60	-0.54
ΔQ_{Bond} (e)	-0.40	-0.24	-0.30	-0.75	-0.47	-0.56

the Helmholtz equation for a dipole layer:

$$\Delta\Phi = \frac{q_e}{\epsilon_0 A} \mu_z \quad (3.4)$$

Here, A denotes the size of the unit cell, ϵ_0 the vacuum dielectric constant, q_e the charge of an electron (equalling $-e$), and μ_z the z -component of the dipole moment of the unit cell. The sign of μ_z determines whether the work function is increased or decreased. A dipole pointing away from the molecule toward the surface results in an increase of the apparent work function, while a dipole pointing in the opposite direction decreases it. The total dipole moment arising from the adsorption of TTF and HV0 can be partitioned into two contributions: the molecular dipole, μ_{mol} , and the bond dipole, μ_{bond} . The corresponding changes in the metal work function are referred to as $\Delta\Phi_{mol}$ and $\Delta\Phi_{bond}$. The former is a consequence of the geometry and the corresponding ground-state charge distribution of the molecule, disregarding any charge redistributions between metal adsorbate (here, the molecule is assumed to be already in the geometry it will adopt upon adsorption). It is particularly high in dipolar molecules that are properly aligned relative to the metal surface (for example, in thiol bonded SAMs on Au [143]). In the present case, the HV0 molecule would be centrosymmetric in the gas phase and the only reason why μ_{mol} does not vanish is because of the adsorption induced molecular distortions discussed above. In other words, for HV0 μ_{mol} is a consequence of the change of the molecular geometry upon adsorption. The net effect is, in fact, quite sizable and one obtains a value of μ_{mol} 1.3 Debye corresponding to $\Delta\Phi_{mol} = +0.22$ eV for one molecule in the $5 \times 3\sqrt{3}$ unit cell. This corresponds to an increase of the work function, which is the reverse of the effect one is aiming for when depositing electron rich molecules on metal surfaces. TTF, on the other hand, is calculated to be not perfectly planar even in the gas phase and thus already possesses a small dipole moment of 0.4 Debye. Due to the small geometrical distortions upon adsorption, the dipole moment of TTF is slightly reduced to $\mu_{mol} = 0.3$ Debye. This results in $\Delta\Phi_{mol} -0.05$ eV (i.e., a small work function decrease). The effect due to the charge rearrangements upon adsorption is accounted for by μ_{bond} , the dipole moment per unit cell, and by the resulting work-function modification, $\Delta\Phi_{Bond}$. The underlying processes include the charge transfer between substrate and adsorbate (including possible Pauli push back) as well as adsorption induced charge rearrangements within each moiety. μ_{bond} can be obtained from the plane integrated charge density redistribution (see equation 3.1 and Figures 3.6d and 3.7d) via

$$\mu_{bond,z} = \int_{uc} \int_0^z dz' \rho(z') \quad (3.5)$$

“UC” refers to the integration over the z -extent of the unit cell ^V. For TTF on Au(111), a μ_{bond} of 4.5 Debye is induced, resulting in $\Delta\Phi_{Bond}$ of -0.75 eV. The bonding of HV0 has a much larger effect. Besides transferring much more charge to the metal (vide supra), also the distance over which the charge is transferred is larger (due to the

^VThis equation can be derived by combining the Poisson equation with the Helmholtz equation (eq 3.4). It can be shown that, due to the integration over the whole unit cell and the resulting boundary conditions for the charge rearrangements, this definition of μ_{bond} is equivalent to the more “conventional” definition as $\mu_{bond,z} = \int_{uc} \rho(z) dz$

larger bonding distance), resulting in a significantly higher μ_{bond} of 7.25 Debye. Thus, as far as the consequences of the charge transfer are concerned, HV0 outperforms TTF on Au(111) by nearly a factor of 2, yielding $\Delta\Phi_{Bond} = -1.44$ eV. To the best of our knowledge, such a large potential shift through bond formation is unprecedented in literature^{VI}. The total effect on the work function, $\Delta\Phi$, is then given by the sum of both the molecular dipole and the bond dipole induced contributions.

$$\Delta\Phi = \Delta\Phi_{Bond} + \Delta\Phi_{Mol} \quad (3.6)$$

For both molecules, $\Delta\Phi_{Bond}$ (Table 3.3) is the main contribution. For TTF, it is slightly augmented by $\Delta\Phi_{Mol}$ resulting in a total work function modification of -0.80 eV. In the case of HV0, the adsorption induced bending leads to a reduction of the net effect. In total, we find $\Delta\Phi$ on Au(111) to be -1.20 eV. The magnitude is not only much larger than the pushback experienced due to physisorbed molecules on Au(111) surface but also outperforms most, if not all, electron donors reported in literature up to date. However, it should be stressed here that these numbers correspond to a loosely packed monolayer, for reasons explained in the Methodology Section. At sufficient coverage, it can be assumed that HV0 forms more tightly packed layers. Therefore, additional calculations were performed for a hypothetical tightly packed layer. Although without knowing the actual packing geometry this approach can be regarded only as a rough estimate of the actual effect. It is preferable over simply reducing A (the surface area per molecule) in eq 3.4, as it accounts for depolarization effects that occur when tightly packing parallel dipoles. In fact, it has been shown that such effects result in a sublinear increase of μ_{mol} and μ_{bond} as a function of coverage [167]. For the most simple tight packing conformation, we assumed that the individual molecules must be separated by at least twice the van der Waals radius of the terminal hydrogen atoms. Under these constraints, the smallest possible orthogonal unit cells is $3 \times 3\sqrt{3}$, i.e., the packing density is increased by 60%. In that conformation (without performing additional geometry optimization at the hypothetical tightly packed structure), $\Delta\Phi$ is computed to be as much as -1.59 eV, effectively reducing the work function of gold to that of pristine magnesium. In this context it should, however, be mentioned that the effective electron injection barrier could be lower on Mg as strong push back effects can be expected when covering the metal with the active material. That push back is likely to be larger than when depositing the active material onto a HV0 covered Au-electrode.

Influence of the Substrate Metal: Au(111) vs Cu(111) and Ag(111).

So far, the discussion focused on the adsorption on Au(111). In this paragraph, similarities and differences to the adsorption on the other coinage metals, namely, Ag(111) and Cu(111), will be elaborated. Since these materials are cheaper than Au and have a lower workfunction to start with, they are more likely to be employed as a starting material to be modified to achieve low work function electrodes in an organic (opto)electronic device. The adsorption energies are found to be -0.65 eV (Au), -0.76 eV (Cu), and -0.41

^{VI}Comment added for thesis: While this was true at the time the paper was published, this is not the case anymore. Measurements on a derivate of HV0 revealed work-function modification on Au(111) by 2.2eV, see next section

eV (Ag) for TTF and -1.25 eV (Au), -1.10 eV (Cu), and -0.66 eV (Ag) for HV0, see Table 3.1. It is noteworthy that in HV0, the interaction strength is largest on Au, i.e., the most noble metal of this series. Also in the case of TTF, the interaction with Au is favored over the usually more reactive Ag. Here, however, the adsorption energy on Cu is found to be strongest. The distance between molecule and substrate for both TTF and HV0 (also given in Table 3.1) is determined not only by the adsorption strength (i.e., adsorption energy) but to a large portion also by the “vertical extent” of the top metal layer. Consequently, a crucial parameter for the metal to molecule distance is the van der Waals radius r_{vdW} of the respective metal, especially if the types of interaction are qualitatively similar (compare also the discussion in ref 15). This results in the molecule being closest to Cu (r_{vdW} : 1.40 Å) and farthest from Ag (r_{vdW} : 1.72 Å). The distance to Au, which has an r_{vdW} of 1.66 Å, lies in between these values. It is, however, interesting to notice that despite the larger binding energy of HV0 and the smaller van der Waals radius of nitrogen (r_{vdW} : 1.55 Å) compared to sulfur (r_{vdW} : 1.80 Å), the vertical distance between substrate and molecule is always smaller for TTF than for HV0 (both in the GGA as well as LDA calculations). No qualitative differences are observed in the bonding mechanism on the different metals. In all cases, the HOMO becomes significantly depleted, while other orbitals only play a minor role. The amount of depletion and transferred charge differs from substrate to substrate, as is summarized in Table 3.2. The order is the same as for the binding energies, i.e., $\Delta Q_{Au} > \Delta Q_{Cu} > \Delta Q_{Ag}$; note that the differences between Au and Cu are relatively small, while on Ag significantly less charge is transferred. Since, as discussed above, $\Delta\Phi_{Bond}$ dominates over $\Delta\Phi_{Mol}$, the same sequence is also found for the work function modifications, $\Delta\Phi$ (see Table 3.3). As a consequence of that, despite the significant differences observed for the pristine metal surfaces, the work functions of the HV0 covered metals become very similar even at loose HV0 packing (4.01 eV for Au(111), 3.82 eV for Cu(111), and 3.64 eV for Ag(111)). For dense packing, even more similar work functions can be expected.

Table 3.3: Calculated Work Function of the Pristine (111) Metal Surface Φ , Work-Function Modification $\Delta\Phi$, Dipole Induced by the Bond Formation, μ_{Bond} , Associated Change in the Work Function $\Delta\Phi_{Bond}$, Dipole Moment of the Molecule, μ_{p} , and Associated Change in the Work Function $\Delta\Phi_{Mol}$

	TTF			HV0		
	Au	Ag	Cu	Au	Ag	Cu
Φ (eV)	5.22	4.46	4.87	5.22	4.46	4.87
$\Delta\Phi$ (eV)	-0.80	-0.53	-0.83	-1.21	-0.82	-1.05
μ_{Bond} (Debye)	-4.50	-2.70	-2.37	-8.66	-5.63	-5.83
$\Delta\Phi_{Bond}$ (eV)	-0.75	-0.45	-0.74	-1.44	-0.94	-1.32
μ_{Mol} (Debye)	-0.29	-0.45	-0.46	+1.30	+0.74	+1.07
$\Delta\Phi_{Mol}$ (eV)	-0.06	-0.08	-0.10	+0.22	+0.12	+0.24

3.1.6 Conclusion

In order to propose suitable organic adorbates for reducing the work functions of coinage metals, we have employed state-of-the-art density functional theory calculations to investigate the interaction between TTF as well as HV0 and the (111) surfaces of Au, Cu, and Ag. Focus was laid on the description of the Au interface, since the strongest effects were observed there. In all cases, a significant amount of charge is transferred from the molecular monolayers to the metal going clearly beyond what could be expected for mere Pauli push-back. Electron donation to the metal occurs via π -donation from the HOMO of the respective molecule. In this respect, TTF is found to be a good donor, transferring up to about 0.4 electrons into the metal. HV0, however, owing to its lower ionization potential and quinoidal structure, is an even stronger donor, donating up to 0.75 electrons. The resulting work function decrease is further enhanced by the large distance between HV0 and the metal. In HV0 this effect is to a small extent counteracted by the strong adsorption induced distortion of the molecule on the surface. In TTF the deviation from a planar molecular conformation even results in a slightly increased net effect. In total, the work function modification in loosely packed monolayers on Au(111) amounts to -0.82 eV for TTF and -1.20 eV for HV0. For a more tightly packed layer, a work function decrease by -1.59 eV is estimated for HV0, which holds particularly high promise for using HV0 coated metals as electron injecting electrodes in organic electronic devices.

3.1.7 Supporting Information

Assessment of the stability of the employed methodology

To ensure the stability of the employed spin un-polarized wavefunctions, spin-polarized test calculations have been performed for the system with the largest observed charge transfer (HV0 on Au(111)). The geometry of the spin-restricted system was used and a single point spin polarized calculation was performed with an independent guess for the initial charge density.

Additionally, a single point calculation with a reduced value for the Fermi smearing (0.05 eV instead of the original 0.2 eV) was performed. As table 3.4 shows, the obtained results for the total energy, the dipole moment of the system and the transferred charge between molecule and metal are virtually identical, i.e., independent of the applied method. The tiny differences between the restricted and unrestricted case are related to the convergence (since the start guess is not equal).

Analysis of the $[\bar{1}11]$ -oriented conformation of TTF.

In this section of the Supporting Information, we present some results for the suggested [25] geometry with TTF molecules oriented in the $[\bar{1}10]$ -direction. The reader will note that most numbers presented here differ only slightly from the conformation oriented in the direction, which was used in the main text of the paper. Due to the lack of physical impact, only calculations on Au were performed. The largest differences can

Table 3.4: Total energy, dipole moment μ , and transferred charge ΔQ_{Bond} for the different approaches described above. A rigorous definition of ΔQ_{Bond} can be found in the main text.

Spin Smearing (eV)	restricted 0.2	unrestricted 0.2	unrestricted 0.05
Total energy (eV)	-603.352	-603.357	-603.373
μ (eÅ)	1.53	1.54	1.52
ΔQ_{Bond} (e)	-0.75	-0.75	-0.75

be seen in the structural data, presented in Table 3.5. Similar to the result described in reference [25], we find a tilting by 7° (instead of 8°) at a vertical distance of 2.90Å (instead of 2.76Å). However, our obtained binding energy is slightly smaller, -0.69 eV instead of -0.86 eV . We attribute these differences to deviations in the details of the used methodology, i.e., the packing density and the exchange-correlation functional employed. Comparing the differently oriented conformers with each other, it is obvious that there are some differences concerning the tilt. Also, the vertical distance Δz is smaller by about 10% for the orientation, while the adsorption energy is 10% larger.

 Table 3.5: Structural data for the converged geometries of TTF in different orientations on the (111) face of Au. Δz denotes the vertical distance between the topmost metal layer and the lowest atom of the molecule. β refers to the tilt of the short and γ to the tilt of the long molecular axis with respect to the surface. ΔE is the binding energy to the surface.

	$[\bar{1}10]$	$[\bar{1}10]$ from [25]	$[\bar{1}\bar{1}2]$
Δz (Å)	2.90	2.76	2.91
β (ř)	≈ 7	≈ 8	≈ 2
γ (ř)	≈ 0	n/a	≈ 5
ΔE (eV)	-0.69	-0.86	-0.65

Table 3.6 shows the impact on the work function modification and its related quantities. It is found that $\Delta\Phi$ remains approximately the same, $\approx 0.8\text{ eV}$. The same is true for the charge transferred, which differs by less than 0.01 electrons. A somewhat larger, but still tiny impact is observed for the bond dipole, which, due to the smaller distance to the slab, decreases by 0.03 eV . However, this is made up for by the larger bend of the molecule, which increases the molecular dipole from -0.05 eV to -0.08 eV .

 Table 3.6: Total energy, dipole moment μ , and transferred charge ΔQ_{Bond} for the different approaches described above.

	$[\bar{1}10]$	$[\bar{1}\bar{1}2]$
$\Delta\Phi$ (eV)	-0.79	-0.80
$\Delta\Phi_{Bond}$ (eV)	-0.72	-0.75
$\Delta\Phi_{Mol}$ (eV)	-0.08	-0.06
ΔQ_{Bond} (eV)	0.41	0.40

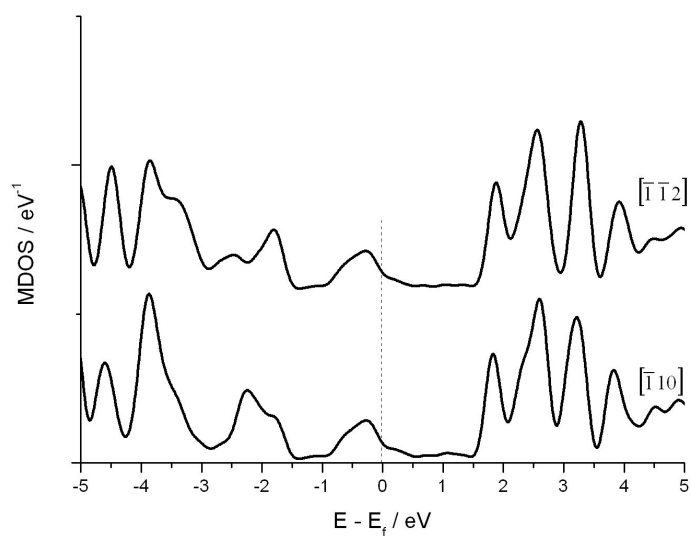


Figure 3.10: Comparison of the molecular density of states (MDOS) of TTF on Au, oriented in the $[\bar{1}\bar{1}0]$ and $[\bar{1}\bar{1}2]$ directions. The curves are offset for better visibility.

Figure 3.10 depicts the molecular density of states of both conformations. In both cases, the Fermi-energy intersects the peak associated with the molecular HOMO. Also, most other features of the plot remain qualitatively unchanged. An exception is the region between 3 and 2 eV below the Fermi energy, where a shift of the relative intensity of the double peak can be observed. Note that also, the shoulder at -3.5 eV almost disappears.

3.2 MV0: Gold work-function reduction by 2.2eV with an air-stable molecular donor layer

3.2.1 Preface

In the last section, it was shown theoretically that 1H,1'H-[4,4']bipyridinylidene (HV0) can significantly reduce the work function of Au(111). Unfortunately, HV0 is unstable vs. air, and therefore difficult to handle experimentally. Its dimethylated derivate, N,N'-dimethyl-[4,4']Bipyridinylidene (MV0), however, can resist oxidation under ambient conditions long enough to be transferred into an ultra high vacuum (UHV) chamber, where it is evaporated onto the Au sample and investigated. Therefore, in this section, it will be shown also experimentally that MV0 (chemical structure shown as inset in Figure 3.11) reduces the work-function of Au below that of pristine Mg. Also, the theoretical examination is extended to this molecule, which is then compared to its predecessor HV0.

The experimental results have been published in Ref. [123]. Synthesis of MV0 was performed by Ralph Rieger in the group of Klaus Müllen. ultraviolet photoelectron spectroscopy (UPS) measurements were performed in the group of and Norbert Koch by Benjamin Bröker, Ralph-Peter Blum, J. Frisch, and Antje Vollmer. Calculations were performed by myself.

In addition to the few theoretical details published in the above mentioned reference, a more detailed computational investigation of HV0 and MV0 was presented to the consortium of the ICONTROL-project (EC-STREP-033197) in deliverable D22. This document served as template for the theoretical data presented in this section. Note that a more detailed investigation on the impact of N,N'-alkylation of HV0 is given in section 3.1.

3.2.2 Experimental Setup

“UPS experiments were performed at the endstation SurICat (beamline PM4) at the synchrotron light source BESSY II Berlin, Germany^[168]. Spectra were collected with a hemispherical electron energy analyzer (Scienta SES 100) using an excitation photon energy of 35 eV. Additional UPS experiments were conducted at Humboldt-Universität using He I radiation and a Specs Phoibos 100 hemispherical energy analyzer. The secondary electron cutoff (SECO) spectra were obtained with the samples biased at -10 V in order to clear the analyzer work function. The error of energy values reported below is estimated to be ± 0.05 eV. Both experimental setups consist of interconnected sample preparation (base pressure $< 5 \times 10^{-8}$ mbar) and analysis (base pressure 1×10^{-10} mbar) chambers, which enable sample transfer without breaking vacuum. Metal single crystals were cleaned by repeated cycles of annealing (up to 550 °C) and Ar-ion sputtering. Organic materials were sublimed from resistively heated Al_2O_3 crucibles. The mass thickness of the organic layers was monitored with a quartz crystal microbalance. All experiments were carried out at room temperature. Alq_3 and C_{60} were used as received (Aldrich). MV0 was synthesized and stored under Ar atmosphere prior to use, and was exposed to air for a few minutes during source mounting. No color change to blue (indicative of the formation of the cation MV+) or transparent (indicative of the

dication MV2+) was observed for the MV0 powder^[169].”
- experimental details taken from ref. [123]

3.2.3 Experimental Results

UPS is an ideal tool to experimentally determine the work function. In photoelectron spectroscopy, a sample is exposed to light with a defined wavelength. When the photon interacts with an electron, it is annihilated and its energy $h\nu$ is added to the energy of the electron in the form of kinetic and potential energy.

$$h\nu = E_{kin} + E_{pot} \quad (3.7)$$

If the total energy is sufficiently large, the electron is excited into a state where it is no longer bound. It will thus be able to leave the sample. By measuring the kinetic energy of the emitted electrons, their potential energy (i.e., binding energy) inside the sample can be determined. To obtain the work function, the width of the spectrum, corresponding to the maximum and minimum kinetic energies, must be determined. The maximum kinetic energy originates from the most loosely bound electrons at the Fermi edge, while the minimum kinetic energy is only determined by the difference of sample and analyzer work function. Adjusted for the analyzer work function, which is known, the low energy electrons are also named secondary cutoff (SECO) electrons. The work function, Φ , of the sample is calculated via:

$$\Phi = h\nu - E_{kin,max} - E_{kin,min} \quad (3.8)$$

In the left part of figure 3.11, the low energy cutoff of a pristine and a MV0 covered Au(111) surface is shown along with the work functions calculated according to eq 3.8. A decrease of 2.2 eV is found upon deposition of the organic layer, much larger than the ≈ 1 eV expected from Pauli pushback only. Since MV0 has no notable dipole moment, this must clearly be attributed to charge transfer, which will be confirmed using results from DFT calculations. Also upon deposition on Cu(111) and Ag(111), large work-function decreases are observed, amounting to -1.5eV and -1.2eV, respectively.

The next logical step is to find out whether this reduction in work function can be utilized to obtain reduced charge-injection barriers, or whether MV0 electronically decouples the substrate from subsequently deposited layers. In the right part of figure 3.11, valence band spectra for typical electron transport materials deposited directly on Au and on MV0-covered Au are shown. The onset of the highest occupied molecular orbital (HOMO) in these spectra can be taken as indicator for the electron-injection barriers^[10], if the transport gap is known (for Alq_3 , see ^[170], for C_{60} , see ^[171, 172]). For Alq_3 and C_{60} , reductions of the barrier by ca. 0.8eV and 0.7eV are found, demonstrating the applicability of such interfaces in organic electronics.

3.2.4 Computational results

The geometry optimization of MV0 on Au(111) reveals two important differences to HV0: First, the adsorbed molecule is almost planar, similar to its gas-phase structure.

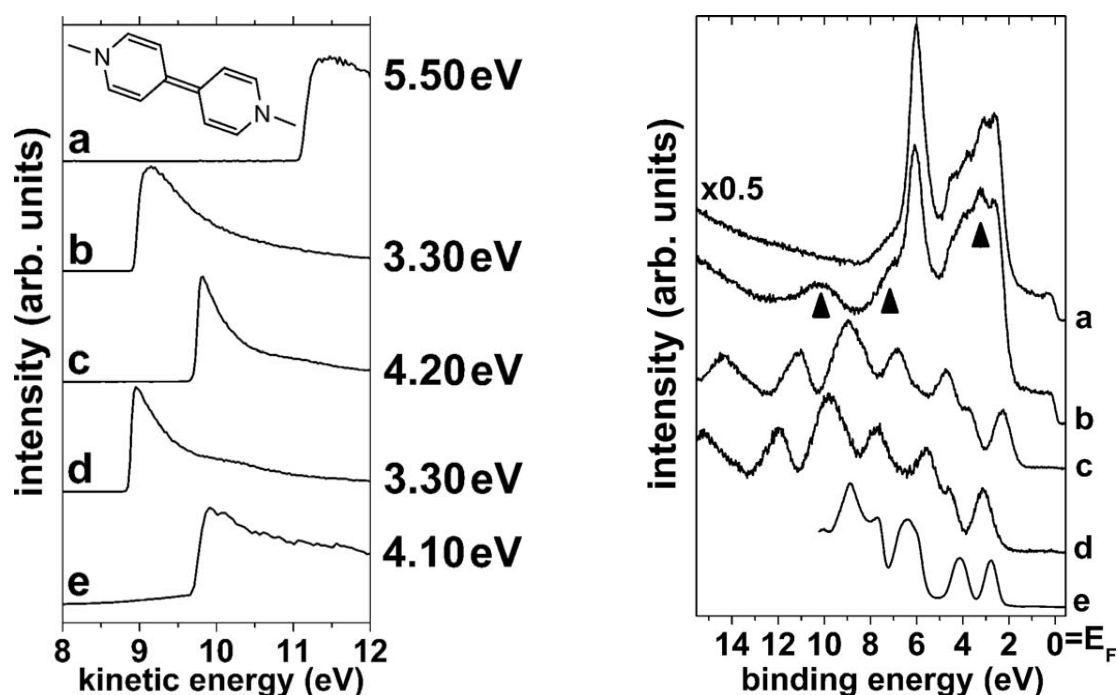


Figure 3.11: Secondary electron cutoff (left) and valence band (right) spectra for (a) pristine Au(111), (b) 0.5 Å MV0 on Au(111), (c) 30 Å Alq_3 on Au(111), (d) 30 Å Alq_3 on MV0 precovered Au(111), and (e) 45 Å C_60 on MV0 precovered Au(111). The sample was biased at -10 V during measurement. The inset shows the chemical structure of MV0. Figures taken from ref [123].

This is actually a quite unusual observation, as most molecules which undergo a strong charge transfer reaction experience significant distortions upon adsorption. Second, the molecule is overall a bit closer to the surface than its unmethylated relative. Nonetheless, the mechanism of charge transfer is basically the same, as electrons are transferred from the HOMO of the molecule to the metal. In Figure 3.12, the three-dimensional electron density rearrangements in HV0 and MV0 are shown. It is interesting to note that the peripheral substituent, i.e. the methyl group, is affected by the charge rearrangements, too. Electron depletion is observed near the outermost hydrogen atoms, in areas far from the π -orbitals. This can only be rationalized as manifestation of Pauli pushback. Note that the negative values here do NOT mean that there are fewer electrons than in the isolated monolayer; rather, there is less electron density than in monolayer and slab combined. Also, increased electron density is found between the backbone and the functional group, even extending beyond the σ -plane of the bond. Charge transfer cannot directly be made responsible here, since no π -orbital contributes to the bond between backbone and alkyl substituent. In a first, tentative analysis, this effect is assigned to a lack of repulsion. In the single molecule, electrons are excluded from these areas due to electrostatic (and Pauli) interaction with the π -orbitals. Upon adsorption, charge donation reduces the electron density in the π -orbitals and in turn more electrons can flow there. An alternative explanation for this unexpected behavior would be

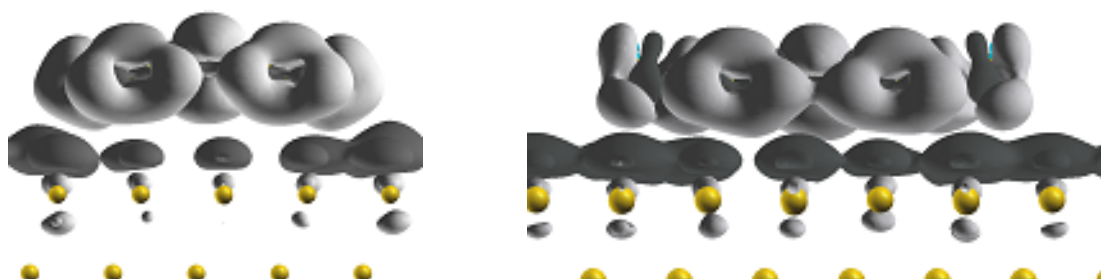


Figure 3.12: 3D Charge density difference of HV0 (left) and MV0 (right). Light areas denote regions of decreased, dark areas correspond to increased charge density.

hyperconjugation, i.e. the hybridization of σ -orbitals with the partially empty HOMO.

Since methyl groups are electron rich, the ionization potential of MV0 is smaller than that of HV0 (4.92eV vs. 5.10eV at the B3LYP / 6-31+G* level). Consequently, also slightly more electrons are transferred. Using the definition of ΔQ_{Bond} from section 3.1, 0.81 electrons are transferred. The resulting dipole reduces the work function by 1.40eV. As the molecule was found to be planar and, therefore, bear no dipole moment, this accounts for almost 100% of the total effect. Of course, the -1.40eV predicted by DFT are by no means in good agreement with the -2.2 eV measured experimentally. To find out whether this is an issue of the assumed packing density, MV0 has been recalculated in a more tightly packed layer, employing a $3 \times 3\sqrt{3}$ unit cell. Indeed, it is found that here, the work-function modification is increased to -1.9eV. It can still be argued that even this unit cell is too loosely packed, and it appears very likely that for a layer with the correct, experimental unit cell (which is unfortunately not known), the correct work-function modification would be obtained.

3.3 NMA: A High Molecular Weight Donor for Electron Injection Interlayers on Metal Electrodes

3.3.1 Preface

The third electron donor considered in this section is 9,9'-ethane-1,2-diylidene-bis(N-methyl-9,10-dihydroacridine) (NMA). This molecule, shown in 3.13, exhibits significant structural similarities to MV0, which was studied in the previous section. Both molecules exhibit a quinoidal structure in their neutral ground state and are sufficiently electron rich to undergo charge transfer with the high work function material Au. NMA, however, has a higher molecular mass, making it less prone to diffusion in real-world devices. Also, as will be shown below, in contrast to MV0 the charged form of NMA is not planar, but sterically strained.

The data presented hereafter have been published in reference [27]. Synthesis and solution-borne analysis of NMA was done in the group of Luca Beverina by Mauro Sassi, Riccardo Ruffo, and Giorgio A. Pagani. The characterization of the metal/organic interfaces was done by Benjamin Bröker, Ralf-Peter Blum, Antje Vollmer, and Johannes Frisch. Calculations of the orbital energies and optical excitation were performed by Georg Heimel, Egbert Zojer, and myself. In general, the buildup of this section will very roughly follow that of reference [27]. For the sake of brevity, the description of the synthesis also published in ref. [27] is omitted. This also applied to the X-ray photoelectron spectroscopy (XPS) results. Rather, the focus is put on the geometric and electronic changes induced by charge transfer, and on the work-function modifications induced by adsorption.

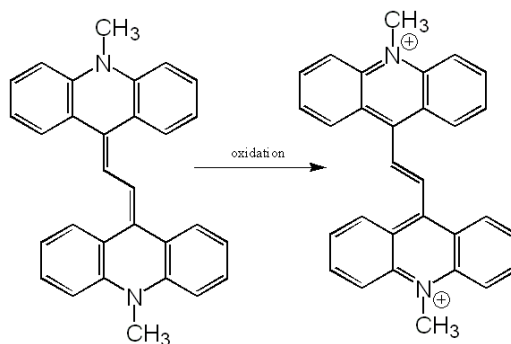


Figure 3.13: NMA in its neutral ground state (left) and its oxidized form (right)

3.3.2 Geometries and optical excitation in solution

The quinoidal bridge tries to enforce a close to planar backbone, which results in strong steric repulsions between the hydrogen atoms on the acridinic rings and the bridging ethenyl groups. As a result, the obtained geometries are not perfectly planar and appear distorted into a boat-like structure. Two (local) minimum configurations can be found, differing only by the relative alignment of the boats. In the energetically more favorable geometry, both point into the same direction (Conf. A in Figure 3.14), while the other

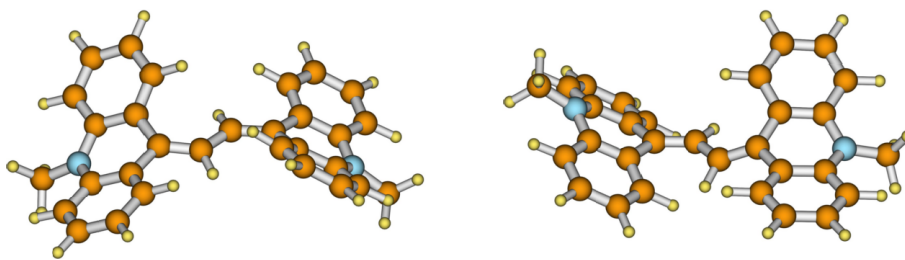


Figure 3.14: The two local minima found for NMA. Conformation A is shown on the left side, Conformation B on the right side.

geometry, being energetically higher by about 6.8 kJmol^{-1} , one of the boats is upside down (Conf. B in Figure 3.14).

The $S_0 \rightarrow S_1$ transition for the neutral state of both conformers is computed to be $\approx 2.59 \text{ eV}$ (478nm). This is in excellent agreement with the experimental absorption spectra of NMA in CH_2Cl_2 (shown in figure 3.15, which displays the first peak maximum at 2.61eV). Using the same geometries to calculate the first excitation energy for the dication, a gap of 1.3eV is predicted, i.e., the excitation energy is approximately halved with respect to the neutral species. This agrees well with observation for most conjugated organic molecules, especially organic semiconductors^[173–175]; however, it is in sharp contrast to the experimental results for NMA, where upon adsorption a blue-shift of the band gap to 452nm (2.75eV) is found (also shown in figure 3.15). The origin of this discrepancy can be traced back to geometry changes induced by the oxidation. In the neutral molecule, the bond between atoms b and c (see figure 3.13) is a double bond with a bond length of 1.37 \AA and thus prefers coplanarity between the ring system and the bridge. In contrast, in the dication, its character changes to single bond. Consequently, an increase of the bond length to 1.48 \AA can be observed, as well as increased flexibility with respect to torsion around the bond axis. While the dihedral angle between atoms a, b, c, and d is found to be 11° in the neutral molecule, it increases to as much as 50° in the oxidized molecule. This rotation reduces the wave-function overlap between the ring and bridge, thus significantly mitigating the conjugation in the molecule. As a consequence, the $S_0 \rightarrow S_1$ is found at larger excitation energies, and indeed, for the fully optimized dication values of 2.42eV and 2.57eV are computed for Conf A and Conf B, respectively. Additionally, it is found that the oscillator strength for the first excitation is smaller than in the neutral molecule, in agreement with the experimental observation. Also, the double peak feature of the oxidized form can be reproduced, as the second excitation is predicted to be in the visible spectrum at 3.80eV (320-340nm). It should be noted that the increase of the gap is not only due to the rotation of the rings, but can also be partly ascribed to the quinoid-benzoid transition. To test this, the dication geometry has been optimized under the constraint of keeping the torsional angles fixed. In this case, the $S_0 \rightarrow S_1$ is found at $\approx 2.20 \text{ eV}$.

To confirm the results obtained by glsDFT, the same calculations have been performed using the semi-empirical AM1 method. Although it is well known that AM1 gives poor results for the geometries of molecules involving nitrogen atoms, it usually does very well for optical spectra. Indeed, it is found that the results between the methods agree

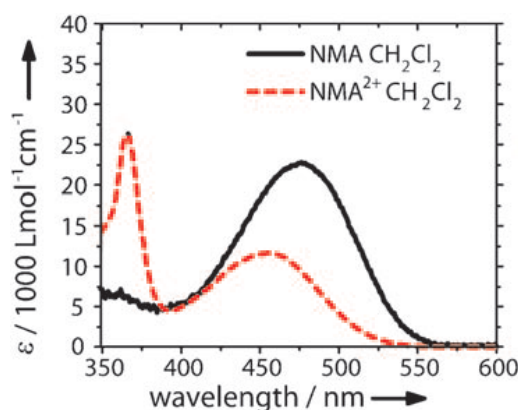


Figure 3.15: The two local minima found for NMA. Conformation A is shown on the left side, Conformation B on the right side.

very well, apart from a consistently blue-shifted excited state energy in AM1. The values for both methods are summarized in Table 3.7.

Table 3.7: DFT (INDO/CI) calculated energies (E), and associated oscillator strengths (OS), for the lowest excited states of NMA in its neutral and doubly oxidized form in the geometry of the neutral molecule and the geometry of the dication.

Geometry	Minimum of the neutral molecule						Minimum of the dication		
	Neutral Molecule			Dication			Dication		
Electronic configuration	E (eV)	E (nm)	OS	E (eV)	E (nm)	OS	E (eV)	E (nm)	OS
Conv. A	2.60 (3.06)	447 (406)	0.80	1.34 (1.46)	926 (849)	0.32	2.42 (2.98)	512 (416)	0.22
Conv. B	2.58 (2.97)	480 (417)	0.80	1.35 (1.58)	920 (785)	0.33	2.57 (3.09)	483 (3.01)	0.17

3.3.3 Metal/NMA-interfaces

The knowledge about the geometric and electronic changes upon adsorption provides the necessary basis to understand work-function modification induced by adsorption of NMA on coinage metal surface. These have been measured using UPS, employing the same method

Deposition of NMA on coinage metal yields in all cases a significant reduction of the work-function as measured by the secondary electron cutoff (SECO). Possible origins for this are Pauli pushback^[10, 50], the permanent dipole moment^[10], or charge transfer^[11]. On Au(111), the pushback effect can amount to anywhere between -0.53eV for noble gas adsorption^[32] to more than -0.7eV for inert alkane chains^[30]. Even larger values (up to -1.3eV) have been reported for (4,4'-bis [N-1-naphthyl-N-phenyl-amino]biphenyl (a-NPD))^[31, 144], however, alternative explanations should not be ruled out for this case. For Ag and Cu, the magnitude of the pushback is reported to be on the order of -0.7eV and -0.9eV, respectively^[176, 177]. In Figure 3.17, the work-function of the NMA/metal interfaces is shown as function of coverage. For Au(111), the work function saturates at 4.10eV, 1.40eV below the work function of the pristine crystal. On silver, the work-

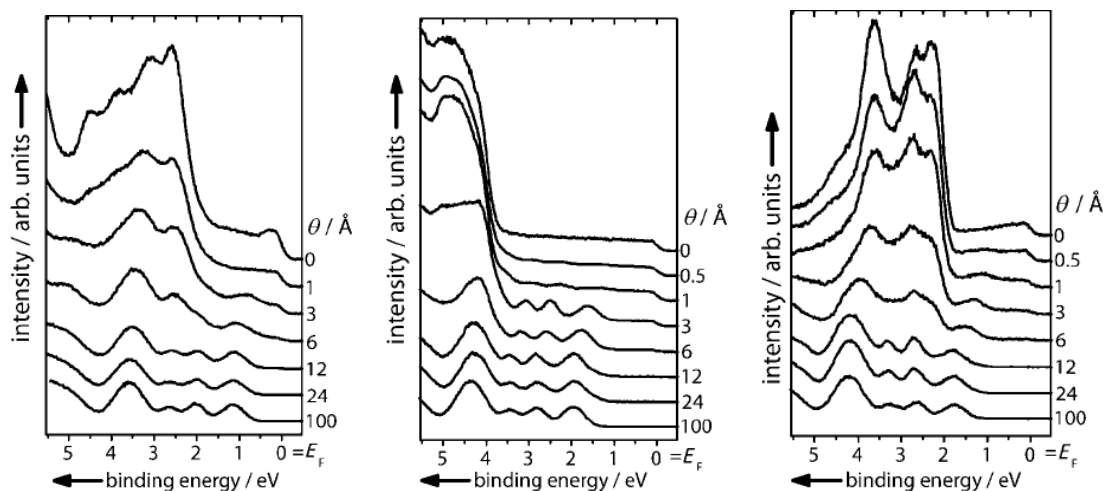


Figure 3.16: Valence band spectra for different nominal coverages of NMA on Au(111) (a), Ag(111) (b), and Cu(111) (c). All parts of the figure are taken from ref [27].

function reduction amounts to 1.0eV, and on Cu to 1.15eV, respectively. In all cases, the observed work-function reduction is slightly larger than the values reported for push-back. This effect is tentatively described to weak charge-transfer to the metal, although no direct evidence can be found in the valence band spectra. Also, it cannot be ruled out that a downward pointing permanent dipole moment is responsible for this effect. Normally, DFT modelling of the interface should be able to unravel this problem. Unfortunately, however, the large size of the molecule and the expected importance of van-der-Waals interactions for the molecular conformation on the surface^[178] and the adsorption distance^[109] makes this system hardly traceable on currently available computers.

Another interesting experimental discovery was made when Alq_3 was deposited on Au(111) pre-covered with 3, 6, or 12Å NMA to demonstrate the applicability for reduction of electron injection barriers. The adsorption induced changes of the electronic structure of the NMA/Au interface does not reach saturation before 12Å thickness, and hence in all three cases the Au/NMA interface displays a different effective work function, Φ' . It was found that the onset of the HOMO of Alq_3 , which is a measure for the electron injection barrier, displays a linear relationship to Φ' with a slope of -0.7, see Figure 3.17. Even more surprisingly, also the data point obtained for the Au/MV0 interface described in section 3.2 also fits this line perfectly well, despite a more than 1eV lower work-function. Since there is virtually no pushback anymore between Alq_3 and the organic layer, the deviation from the ideal slope of -1 indicates that there must be some electronic interaction between Alq_3 and the interface, most likely charge transfer. The identical slope of -0.7 for NMA and MV0 furthermore indicates that the interaction is related to the electronic properties of Alq_3 rather than the organic layer used to influence the work-function. Please note the strikingly similar behavior to the interfaces

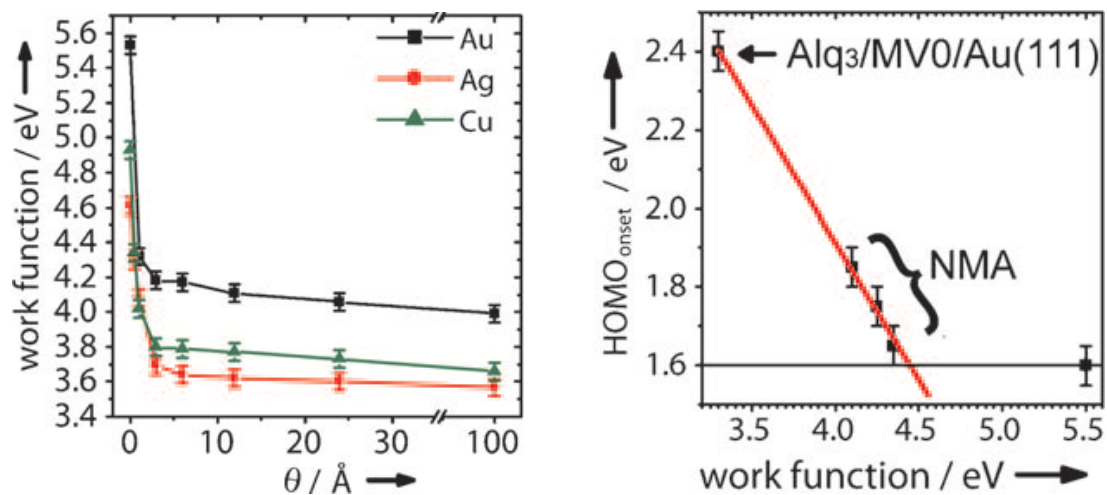


Figure 3.17: Left: absolute work function of metal single crystals upon NMA deposition as function of film thickness θ . Right: Alq_3 HOMO onset plotted versus the work function of the modified/pristine Au(111) substrate. Graphs taken from ref. [27].

shown in 3.8, where also possible reasons for this effect are discussed.

3.4 HATCN as advanced hole-injection layer

3.4.1 Preface

After the investigation of electron donor layers in the previous sections, the attention shall now be turned on electron acceptor layers. Generally, metal/acceptor interfaces are more commonly and intensely studied than their donor counterparts, since there, oxidation upon air exposure is not an issue their, and because the expected positive work-function modification induced upon adsorption makes charge-transfer clearly distinguishable from Pauli pushback. Highlights in this context are the strong acceptor 2,3,5,6-tetrafluoro-7,7,8,8 tetracyanoquinodimethane (F4TCNQ)^[24, 124, 144] and perylene-3,4,9,10-tetracarboxylic-3,4,9,10-dianhydride (PTCDA)^[45, 49, 99, 132, 164, 179–190], for which extensive experimental and computational results are published on all three coinage metals. In this (and the next two) sections, the investigations will be extended to the medium strength acceptor 1,4,5,8,9,12-Hexaaza-triphenylene-2,3,6,7,10,11-hexa-carbonitrile (HATCN).

The following part is an amalgam of two papers already published on this work^[191, 192], and additional computational (and partly also experimental) results on level alignment, the shape and magnitude of charge transfer, and the geometric features of the interfaces of HATCN with all three coinage metal surfaces. The above mentioned papers deal with the structural and electronic properties of HATCN on Ag(111). Their build-up has been largely adopted for the subsection on HATCN on Ag, but with modifications to combine the computation results presented therein, and to accommodate additional information. Ultraviolet photoelectron spectroscopy (UPS) experiments have been carried out by B. Bröker and R.-P. Blum in the groups of Norbert Koch under the beamline supervision of A. Vollmer. Scanning tunneling microscopy (STM) imaging was done by H. Glowatzki. HATCN was synthesized by R. Rieger at the MPI Mainz in the group of K. Müllen. VASP calculations have been done by myself, SIESTA calculations were carried out with the help of G.M. Rangger, in the group of E. Zojer. Interpretation of the experimental and computational results was done in multiple discussion between all the authors. Thereby, it needs to be highlighted that the idea of the phase transition, which finally led to a consistent picture of all experimental and computational results, was brought up by Egbert Zojer.

3.4.2 Introduction

Application of sub-(monolayers) of conjugated organic molecules on metal electrodes has significant potential for enhancing the performance of modern optoelectronic devices^[129, 193]. Molecules with either pronounced dipole perpendicular to the surface^[134–143], or with distinct electron accepting properties have been successfully employed^[16, 24, 194, 195] in order to modify the effective work function of electrodes. Of the latter class, the highly electronegative molecule F4TCNQ has risen considerable interest^[196–200] and at the moment is considered state-of-the art material. However, due to its relatively low mass, it is expected to be highly volatile at elevated temperatures, and issues concerning long-term stability and reproducibility of devices built with this molecule have been raised^[201]. Alternative solutions with higher mass and comparable electron affinity are

therefore demanded. Gao et al.^[202] realized a F4TCNQ-derivate by exchanging two fluorine with cyano groups, resulting in slightly higher mass and improved electron affinity, and hence better thermal stability.

In this work, we will present the molecule HATCN, chemical structure shown in the inset of figure 3.2 as possible substitute candidate. It is prepared by acid catalyzed condensation of cyclohexane-hexaone and diaminomaleic dinitrile as reported in the literature^[203, 204]. Having a molecular mass of 384 g/mol it is 1.4 times heavier than F4TCNQ (276 g/mol). Thus it is expected to exhibit considerably improved thermal stability. Unfortunately, on the other hand the electron affinity (EA) is slightly lower. Gas phase calculations of the vertical electron affinity show $EA = -3.53$ eV, as opposed to -4.12 eV at the B3LYP / 6-31+G* level. HATCN is well known in literature as electron deficient material^[205, 206], which exhibits up to four reversible one electron reductions in cyclovoltametry experiments^[207], depending on the solvent used. Charge transfer reactions with π -bases have also been reported^[207], as well as the formation of metal complexes with coinage and other transition metals^[208]. Recently, its intrinsic ability to form stable radical anions and dianions with a triplet ground state^[206] has been exploited to create molecular magnetic materials^[205]. As a consequence of its D_{3h} symmetric shape, HATCN is a prototype molecule for the formation of discotic mesophases^[209]. Such self-assembly can possibly be used to facilitate device fabrication. Indeed, light emitting devices based on HATCN derivates have already been reported^[210]. Donor-acceptor derivates of this molecule exhibit significant hyperpolarizability and hence good NLO (non-linear optic) properties^[211].

In this joint theoretical and experimental work, insights into HATCN adsorbed on the (111) surfaces of Cu, Ag, and Au is obtained. Synchrotron radiation UPS and XPS measurements are employed to monitor the valence band and the core levels and to determine the work function shift $\Delta\Phi$ as function of HATCN coverage. New density of states near the Fermi edge is explained with the help of 3D-Periodic DFT calculations. Bond formation between the metal and the molecule is discussed in terms of electron donation and -backdonation, in analogy to the Blyholder model^[166].

3.4.3 Experimental and Computational Details

Photoemission experiments were performed at the endstation SurICat (beamline PM4) at the synchrotron light source BESSY (Berlin, Germany)^[168]. Spectra were collected with a hemispherical electron energy analyzer (Scienta SES 100) with an energy resolution of 120 meV. A normal emission setup was used with the exception of valence band spectra, where the angle between sample and analyzer was 45° . Excitation energies for ultraviolet photoelectron spectroscopy (UPS) were 35 eV (10 eV pass energy). The secondary electron cutoff (SECO) was obtained with the sample biased at -10 V in order to clear the analyzer work function. For x-ray photoelectron spectroscopy (XPS) an excitation energy of 620 eV was used (50 eV pass energy). STM measurements were done using an Omicron VT-STM attached to a custom ultra high vacuum (UHV) system at Humboldt University Berlin. Both experimental setups consist of interconnected sample preparation (base pressure 1×10^{-8} mbar) and analysis (base pressure 1×10^{-10} mbar) chambers, which provided sample transfer without breaking UHV conditions. The metal single crystals were cleaned by repeated cycles of annealing (up

to 550°C) and Ar-ion sputtering. Photoelectron spectroscopy was used to verify the cleanliness. STM on Ag(111) revealed atomically flat terraces with typical width of 100 nm. HATCN was evaporated onto the surface by resistively heated pinhole sources. To obtain the mass thickness of the deposited film a quartz crystal microbalance was used. All experiments were carried out at room temperature. Fitting of the XPS spectra (mixed Gaussian and Lorentzian peaks and Shirley background) was done using the WINSPEC software (University of Namur).

“RAIRS experiments were conducted at the Zernike Institute of Advanced Materials using a Bruker IFS 66v/S spectrometer. The IR beam entered the UHV system through a KBr window and was directed onto the sample under an angle of 83° (to the surface normal). For detection the reflected beam left the chamber through another KBr window and hit a LN2 cooled HgCdTe detector. The spectrometer and the beam path from and to the UHV chamber were evacuated and the pressure kept in the mbar range. The spectra were recorded from 500 to 3000 cm^{-1} , the resolution of the spectrometer was set to 4 cm^{-1} and typically 500 scans were co-added which gives rise to a total acquisition time of about 3 minutes per spectrum. The spectrum of the clean substrate was taken as a background reference R_0 at the beginning of each experiment. Subsequent spectra were recorded in a time evolved mode during HATCN deposition and are displayed in reflectance as the ratio of the difference to the background spectrum $(R - R_0)/R_0$. The coverages listed in the figures are the nominal thicknesses read from the quartz crystal microbalance (QCM) before a new spectrum was acquired.

thermal desorption spectroscopy (TDS) was carried out using a quadrupole mass spectrometer (QMS). The QMS was tuned to the most relevant masses which were identified in advance by desorbing HATCN directly from the source into the QMS. The substrate could be heated up to 900 K by resistive heating. The same setup was also equipped with an UHV compatible Kelvin probe (KP) allowing for work function measurements. Advanced “off-null” detection as well as automatic control of the tip-to-sample spacing was used, which is an important requirement for accurate measurements.“

- *experimental details taken from ref. [192]*

Calculations were performed according to the default methodology described in section 2.2, with the following exceptions

- Owing to the large size of HATCN, a $7 \times 4\sqrt{3}$ unit cell was used, containing 56 metal atoms per metal layer and one HATCN molecule.
- Due to the vast computational demands, geometry optimizations were only performed using a three layer slab. Terminal single point calculations for the determination of the dipole moment of the system and the charge-rearrangement, as well as all related quantities, were carried out using a five layer metal slab as usual.
- The convergence criteria for the remaining forces of the molecule was set to 0.02 eV/Å.

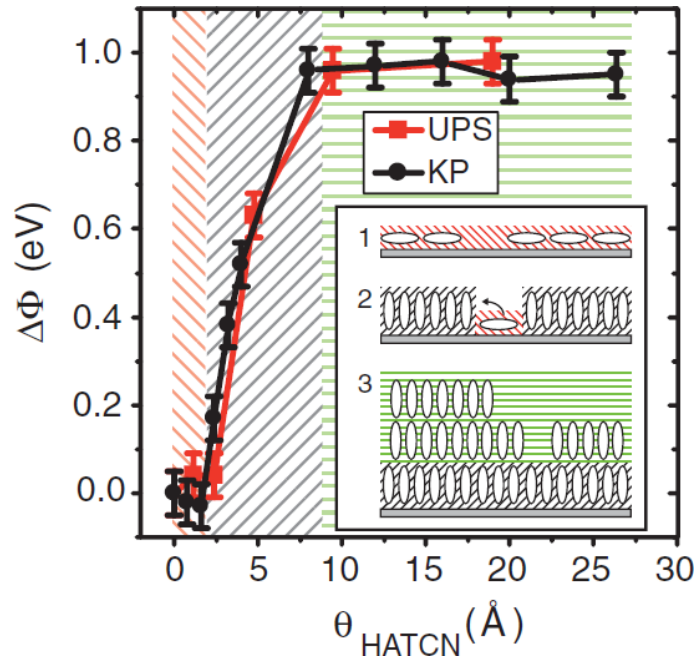


Figure 3.1: Work function change $\Delta\Phi$ relative to pristine Ag(111) as a function of nominal HATCN thickness Θ , obtained by UPS (red squares) and KP (black dots). The inset shows the proposed density-dependent orientation of HATCN on Ag(111). The color coding of the background shading represents the three different regimes referred to throughout the text: red = regime (i), black = regime (ii), and green = regime (iii). Figure and caption taken from ref ^[192].

Additionally, XPS core level shifts of carbon and nitrogen 1s electrons were calculated by modification of the corresponding pseudopotential. Methodological details are described elsewhere^[212–214]. Since the final state approximation was employed, core-hole screening is taken correctly into account. Note that only relative shifts can be obtained, not absolute values. Therefore, the reported shifts usually refer to the 1s electron of the respective atom species with the lowest binding energy; details are explained in the text.

3.4.4 HATCN on Ag(111)

In this work, the focus will be laid on the deposition of HATCN on Ag(111). Most effects are more pronounced here, compared to the deposition on Cu(111) and Au(111).

Structural Information and Experimental Work-Function Modification

The evolution of the work function upon deposition of HATCN on Ag(111) was measured as function of coverage using two separate methods, UPS and kelvin probe (KP) spectroscopy. The results are shown in Figure 3.1. For both methods, a very unusual shape of the obtained curve is observed. Whereas normally, the work function changes

rapidly with the coverage starting with the deposition of the very first molecules (see, e.g., 9,9'-ethane-1,2-diylidene-bis(N-methyl-9,10-dihydroacridine (NMA) in figure 3.17, HATCN displays a “delayed increase”. For coverage up to 2.5Å, the effective work function of the Ag/HATCN interface is found to change only by about 0.1eV. After exceeding 2.5Å nominal thickness, a rapid increase of the work-function modification is observed, saturating at ca. +1.0 eV at 8Å coverage. Beyond this point, additional deposition of HATCN shows no effect on the electronic levels of the system. Such a three-regime behavior is highly unusual. It cannot be rationalized by layer-by-layer or island-growth models, nor can depolarization of the dipoles account for it. Only two explanations seem to be plausible: Either layers beyond the first monolayer participate in the charge transfer, or the first HATCN layer undergoes a severe structural modification when exceeding a certain coverage threshold.

To shed light on this issue, TDS has been performed on HATCN/Ag interfaces. In this method, the HATCN/Ag interface is heated at approximately 1K/min, and the desorption of matter is measured using a mass spectrometer. This way, information about the interaction strength of adsorbate and substrate is obtained. The results are shown in Figure 3.2. For this system, two distinct masses have been found: 384g/mol, corresponding to the desorption of the whole HATCN molecule, and 52g/mol, indicating (CN)₂ fragments of the HATCN molecule. In analogy to the work-function evolution, three regimes can be distinguished. For very low coverage, no desorption of HATCN is observed at all up to a sample temperature of 900K. This is indicative of very high interaction strength between the first monolayer and the adsorbate. In regime (ii), only desorption of HATCN fragments (m = 52g/mol) occurs. Since no molecules were found to leave the surface intact, this is taken as indication that the interaction of the individual molecules with the Ag substrate is weakened, but still every molecule must be in direct contact. Only for regime (iii), joint desorption of whole HATCN molecules and HATCN fragments is observed, which leads to the conclusion that at this point layers are formed which show only weak physisorptive interaction with the surface.

To get additional insight into the orientation of HATCN on the surface, reflection absorption infrared spectroscopy (RAIRS) was performed for different coverages of HATCN on Ag(111). On the surface, the mirror dipole of the metal substrate imposes additional selection rules beyond the normal rules for IR spectroscopy. Concretely, only dipole moments perpendicular to the surface are IR active^[215]. The results are shown in Figure 3.3. Three characteristic peaks can be designated. Upon deposition of the first molecules, a broad band arises at 2185cm⁻¹. This band exhibits a Fano-type line-shape, which is a sign of charge-transfer^[216]. The band is also strongly shifter to lower wavenumbers compared to the reference spectrum of HATCN in KBr (green line in Figure 3.3), thus proving a negative charge on HATCN^[205]. At coverages corresponding to regime (ii), the intensity of this band diminished. Instead, two new bands are observed at 2229cm⁻¹ and 2243cm⁻¹. Whereas the intensity of the former, as function of the coverage, goes through a maximum, the intensity of the latter increases steadily. From these informations, the modes can be assigned to specific conformations of the HATCN molecules. The first mode is assigned to the CN-stretch vibration of HATCN being adsorbed face-on. This agrees with structural information obtained by STM imaging of the

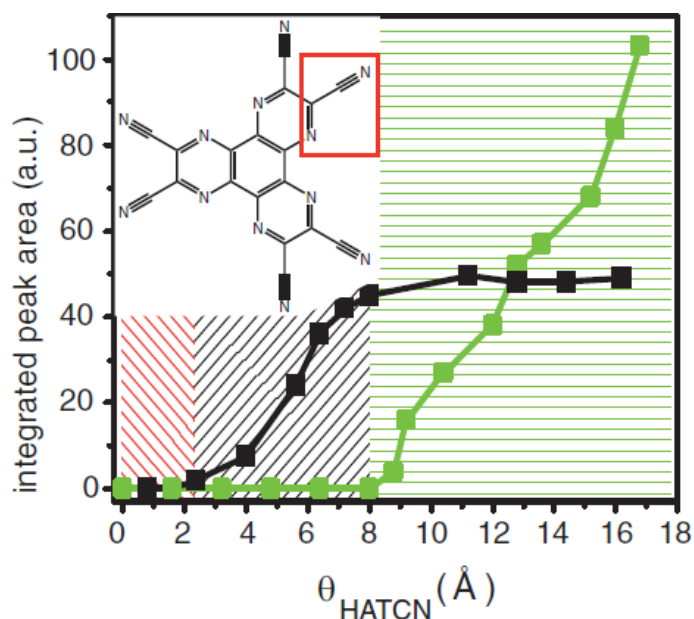


Figure 3.2: TD spectra of mass 384 g/mol (intactHATCN, green boxes) and mass 52 g/mol (HATCN fragment $(\text{CN})_2$, black boxes) for different θ on Ag(111). Data points were obtained by integrating the peak areas in the original TD spectra. The inset shows the chemical structure of HATCN. Figure taken from ref [192].

low-coverage phase, shown in the next section. The reason that this mode is IR-active at all can be found in the structural deformation of HATCN, also shown in the next section. Since this mode disappears completely from the spectrum at higher coverages, it is concluded that also the face-on conformation vanishes. Mode II at 2229cm^{-1} is attributed to the CN-stretch vibration upright standing HATCN molecules. In this case, only 2 out of 6 CN-groups interact directly with the surface, while the other 4 are practically free. Two reasons can be made responsible for the shift to higher wavenumbers compared to mode I. First, in the upright standing molecule less charge is transferred to HATCN, which is the main reason for the bathochromic effect. Second, the CN-group is now caught directly between two “walls”, the metal substrate and the molecule, which increases the steepness and thus curvature of the associated potential well. Mode III is in intensity, lineshape and energetic position very similar to the reference of HATCN in KBr, and therefore attributed to non-interacting HATCN, i.e., HATCN multilayer physisorbing on the HATCN/Ag interface.

The proposed conformations are summarized in Figure 3.1, and a direct link between the conformations and the evolution of the work-function modification can be established. In the low-coverage regime, HATCN is adsorbed face-on on Ag(111), inducing only a small work-function modification. Upon further deposition, the molecules reorient to an edge-on adsorbed faces. Thereby, the original face-on layer is cannibalized by the new conformation, and a complete face-transition takes place. In this high-coverage regime, the work function is increased significantly by up to ca. +1eV. Finally, after

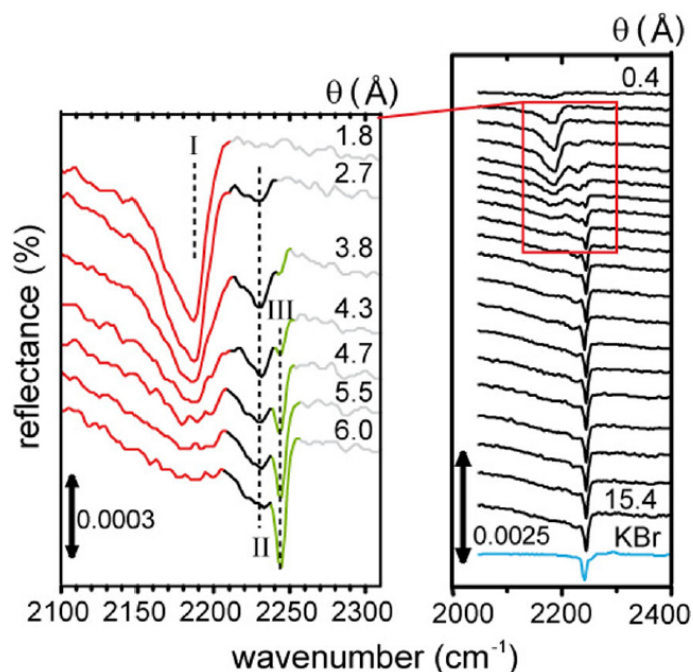


Figure 3.3: Right: RAIR spectra recorded during HATCN deposition on Ag(111) for the region of the CN stretch mode. Left: Zoom of right part (denoted by the red rectangle in the right panel) for Θ up to 6 Å. The color coding of the different spectral regions refers to the three regimes (i)–(iii) used in the text.

completion of the edge-on layer (or, more likely, starting during formation thereof), island growth occurs as HATCN molecules physisorb on the modified interface. These molecules do not interact with the substrate anymore, thus not contributing to the work-function of the sample anymore. To support this conclusion, extensive density functional theory (DFT) calculations have been carried out.

3.4.5 Computational Investigation

To obtain more insight in the chemical processes occurring at the interfaces, DFT calculations were employed. The low-coverage case will be discussed first. In interfaces between conjugated organic molecules and metals with strong adsorbate/substrate interaction, the substrate usually adopts a face-on geometry. The experimental unit cell, as obtained by STM measurements, is a honeycomb structure involving at least 2 molecules per cell. Unfortunately, this involves too many atoms to be readily traceable by DFT calculations, at least as far as a geometry optimization in a reasonable timescale is concerned. Therefore, it was decided to do the geometry optimization for a hypothetical loosely packed HATCN monolayer with a single HATCN molecule in an extended $7 \times 4\sqrt{3}$ unit cell to avoid artifacts due to incorrect packing while keeping the system at a reasonable size. Since no information about docking site and orienta-

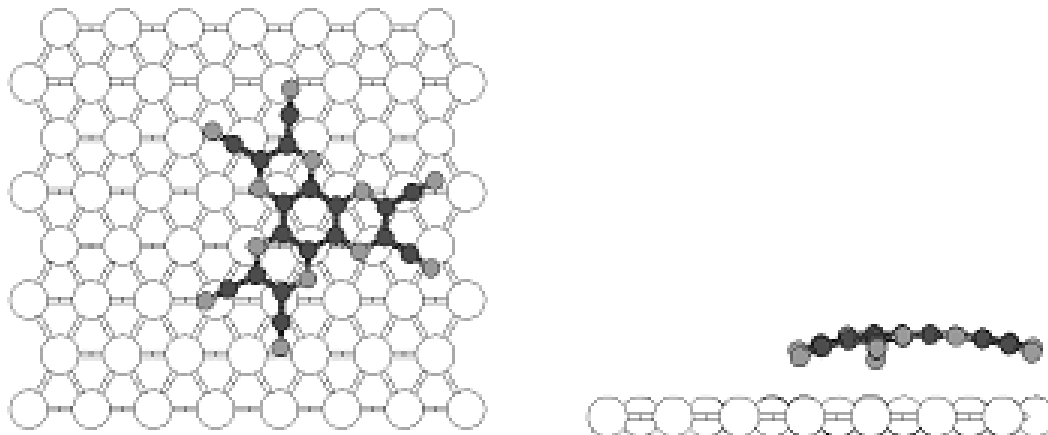


Figure 3.4: Fully relaxed geometry of HATCN on Ag(111). Black atoms correspond to carbon atoms, gray atoms to nitrogen, white atoms to Ag. Only the topmost metal layer is shown for the sake of clarity.

tion of HATCN on the surface is available, several different positions were tested. It turned out that within the convergence criteria employed as described in section 3.4.3, all conformations were energetically equal within 1 meV. It might, therefore, be inferred that no distinct docking site exists at all. Upon adsorption, the formally D_{3h} symmetric molecule loses its planarity and becomes strongly bent, in analogy to F4TCNQ^[24]. The vertical distance between topmost metal layer and molecule varies between 2.54 Å (lowest cyano nitrogen atom) and 3.65 Å (topmost inner ring carbon atom). Both values are similar to the experimentally determined adsorption distance of F4TCNQ on Cu(111), lending credibility to these calculation. Moreover, also the C_3 rotation symmetry is lost. The fully relaxed geometry is shown in Figure 3.4. The interaction strength between metal and adsorbate can be estimated by calculating the binding energy. To that aim, the energy of the combined system is subtracted from the energy of the individual components, where each part was fully relaxed. The binding energy between HATCN and Ag is found to be 0.71 eV. Note that DFT fails to account for van-der-Waals interactions. Thus, this value should be regarded as lower bound rather than the correct interaction energy.

Electron rearrangements upon adsorption are depicted in Figure 3.5. The modification of the plane averaged electron density, $\Delta\rho$ is shown as solid line. In analogy to the binding energy, the value is given by

$$\Delta\rho = \rho_{combined} - (\rho_{monolayer} + \rho_{slab}) \quad (3.1)$$

Hereby, the geometry of the individual systems is kept fixed at their final position, i.e. their coordinates in the combined system. A strong reduction and a pronounced minimum are observed near the topmost Ag layer. Electron density of the metal is

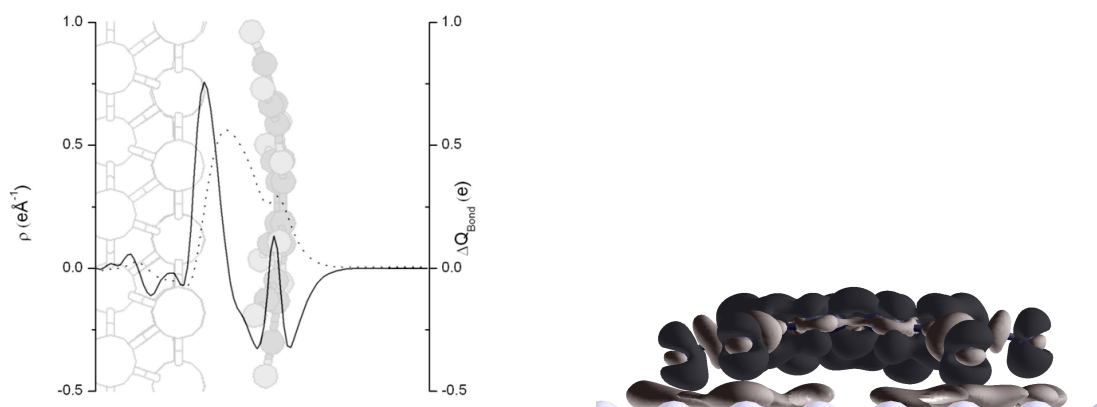


Figure 3.5: Left: Plane averaged electron density difference $\Delta\rho$ (solid line) and transferred charge ΔQ (dotted line). ΔQ is obtained by integration of $\Delta\rho$. An excerpt of the system is shown in the background as guide to the eye. Right: 3D Charge rearrangements upon adsorption of HATCN on Ag(111). Light regions correspond to negative sign, i.e. depleted electron density, while dark regions imply density buildup. An isovalue of 0.01 has been used. Only the top three layers of the metal are shown.

transferred to the maxima of the curve, which are located in two planes above and below the monolayer. The first, global maximum is located at the cyano groups, while the second, local maximum is found above the plane of the aromatic system, indicating the the filled orbital exhibits π -symmetry. The minimum between those peaks shows slightly negative values, pointing to a reduction of electron density in the σ -plane of the adsorbate. The right part of 3.5 illustrates the change in electron density in a 3D-fashion. Blue regions indicate electron depletion, while red areas show accumulation of density. Note the depletion of charge density where nitrogen lone pairs are located. Additional depletion in the σ -plane of HATCN is attributed to the N-C antibonding character of the formally unoccupied LUMO. An increase of electron density can be found in the π -plane of the molecule, as well as between the CN-nitrogen atom and the metal, which is indicative of the newly formed bond between metal and adsorbate.

The nature of orbitals participating in the charge transfer can be obtained by projecting the density of states onto the molecular orbitals of the isolated monolayer. The results in Figure 3.6 show a small reduction in the occupation of a group of low-lying orbitals, namely HOMO-23 to HOMO-18. All of these orbitals are connected to a combination of the electron lone pair of CN groups, and hence are of σ -symmetry. Hence, this group is made responsible for the forward-donation process. Occupation increase can be found on another group of orbitals: LUMO, LUMO+1 and LUMO+2, by 31%, 19%, and 16%, respectively. These orbitals strongly hybridize with the metal band, accepting in total about 1.3 electrons. The simultaneous filling of three orbitals at once is a consequence of the near-degeneracy of these orbitals, which is only lifted by the deviation of the adsorbed molecule from the C_3 (or D_3h) symmetry. This argument is illustrated by the molecular density of states MDOS, i.e. molecular contribution to the

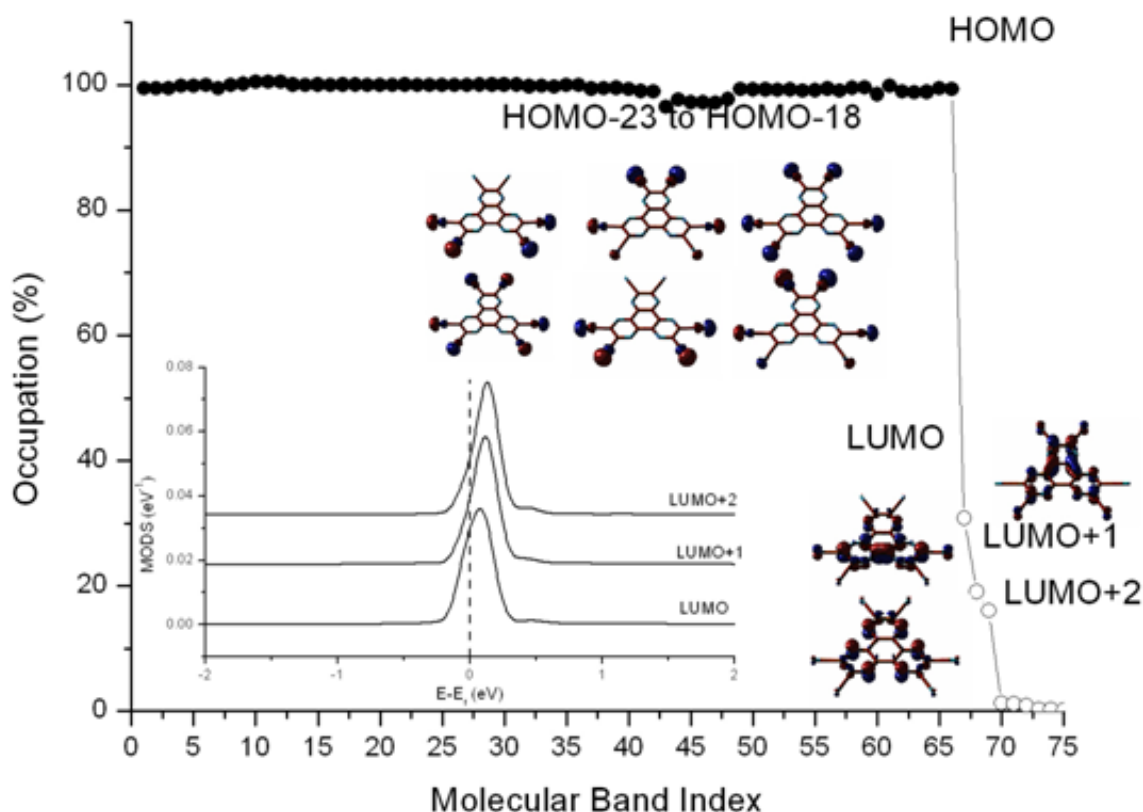


Figure 3.6: Molecular Occupation derived from projection of the electron density of the combined system onto molecular orbitals of the isolated molecule. Closed circles correspond to initially filled, open circles to initially unoccupied molecular orbitals. The corresponding orbitals are plotted as inset with a contour value of 0.05. The inset shows the molecular density of states associated with LUMO, LUMO+1, and LUMO+2

density of states of the system. The MDOS of the three accepting orbitals is shown in the inset of Figure 3.6.

Filling of the LUMO and near-degenerate partners does not cause a quinoid to benzoid transition, in contrast to the case of TCNQ and its derivatives. Lack of this powerful driving force for charge transfer explains the comparably low adsorption energies. Moreover, it is clear that filling of the LUMO alone cannot account for the total charge transfer, and more importantly, the bend of the molecule. Since it is of π -character, none of the carbon atoms experiences any stress to change their character from sp^2 to sp^3 . Indeed, the electronic rearrangements are more complex. In analogy to the Blyholder model^[166] for adsorption of carbon monoxide, the electron lone pairs of the cyano nitrogen atoms donate electrons into the metal bands. Formally, this renders the molecule positive. Since HATCN is the more electronegative partner in this reaction, it will in turn pull electrons back into the energetically next higher, appropriate orbital. This orbital is created by combining the CN- π -orbitals (or, rather, the former LUMO of the unper-

turbed molecule) with the metal bands. This interpretation is backed up by elongation of the C-N triple bonds upon adsorption, reminiscent of the the CO case. The driving force for bending the molecule is hence the need of the lone pair to be able to interact with the metal electrons. Maximum overlap would be achieved if the lone pairs pointed directly towards the surface, i.e. the CN group was located upright. Since there are six groups linked together, simultaneous upright positions of all of them are impossible to achieve. Hence the molecule finds the optimal compromise, leading to the observed (calculated) bend and the filling of the LUMO and its near-degenerate relatives.

The amount of charge transfer upon bond formation, ΔQ_{Bond} , can be inferred from integration of the plane averaged charge density difference from equation 3.1.

$$\Delta Q_{Bond} = \int_0^z \Delta \rho(z') dz' \quad (3.2)$$

The global maximum of this quantity gives the total number of electrons transferred from the metal, which is arbitrarily defined here as the region to left of the maximum, to the molecule, which is defined as the region to the right. An exact definition and discussion of this quantity is given in reference [167]. Here, a ΔQ_{Bond} value of 0.56 electrons is found, i.e. as a net effect approximately half an electron is transferred from the metal to HATCN. As a consequence of the charge transfer, a dipole (called bond dipole) arises, which is found to be as large as +6.0 Debye. At the same time, as a consequence of the bend of the molecule, a molecular dipole of -2.9 Debye perpendicular to the surface is induced. Via the Helmholtz equation, the dipole (i.e., the sum of the former contributions) can be directly related to a shift in the vacuum level above the system, modifying the work function by:

$$\Delta \Phi = \frac{\mu_z}{\epsilon_0 A} \quad (3.3)$$

Here, μ denotes the dipole, ϵ_0 the vacuum dielectric constant and A the size of the unit cell. In the case of a loosely packed monolayer as used in the calculations, the total shift amounts to +0.25eV, owing to the balance of a work-function increase of +0.54eV from the charge transfer and a work-function reduction of -0.26eV due to the bend. A possible explanation, which would be consistent with previous work^[167], would be that the work function is to first approximation linearly dependent on the coverage. Sublinear effects due to dipole depolarization were shown to be in the order of ≈ 0.05 eV even for molecules with significantly larger dipoles^[217, 218]. The coverage in this system, as modeled, is 0.24 *HATCN/nm*². From STM measurements (see next section), an experimental density of approximately 0.44 *HATCN/nm*² can be inferred. Extrapolating to the measured density of 0.44 *HATCN/nm*² would result in a predicted work function modification of +0.48 eV, which is about half an eV larger than the experimentally defined value. Interestingly, however, when calculating the HATCN/Ag interface in the experimentally determined unit cell, using the geometry obtained from the optimization of the loose monolayer, it is found that the total work-function remains almost constant at +0.2eV. This effect can be traced back to the fact that the work-function modification induced by both the bond dipole and the molecular dipole scale with the packing density (reaching values of +0.7 and -0.5eV, respectively), continuing to partly

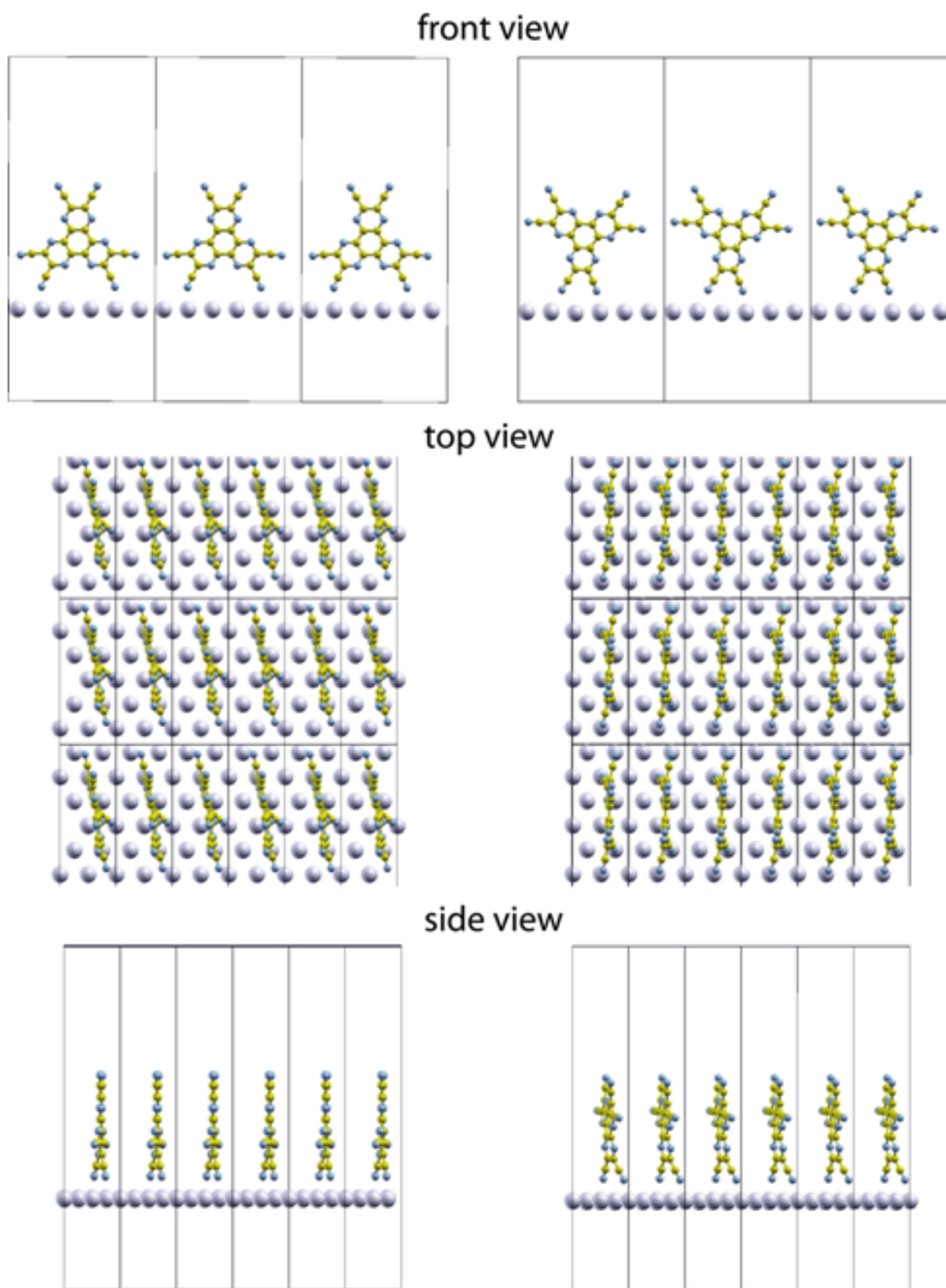


Figure 3.7: Front view (top) top view (middle) and side view (bottom) of upright standing HATCN adsorbing with its cusp (right) and 60° rotated (left). The unit cell is reproduced 6 times in the x and 3 times in the y direction. Figure taken from ref ^[192].

cancel each other out. The computational value of +0.2eV is in fair agreement with the experiment; the deviation can be attributed to geometry effects, especially the problem that the bend is likely overestimated, as is the adsorption distance. Better agreement could be reached when employing the actual, experimental coordinates of the HATCN molecule^[24, 109].

For the edge-on conformation of HATCN in the high-coverage regime, no experimental information of the ordering could be retrieved. It is thus likely that this phase either consists of a very complicated unit cell, or does not form a well-ordered layer at all. To rationalize the observed work-function modification and to get principle insight into the charge-transfer mechanism, a single perfectly upright-standing HATCN molecule in a $2 \times 3\sqrt{3}$ unit cell was assumed, as shown in Figure 3.7. The symmetry of the gas phase molecule is large retained in this conformation and hence, the molecular dipole moment is zero.

The mechanism of charge-transfer between metal and adsorbate is fundamentally altered. Whereas in the face-on conformation, the main contribution came from the π -system, in the edge-on conformation the charge rearrangements are more localized on the CN-group, as shown in Figure 3.8. This situation is reminiscent of covalently-bonded self-assembled monolayers^[22]. In agreement with the experiment, for the edge-on conformation a large positive work-function modification predicted. The calculated value of +2.4eV, however, is significantly too large. A quantitative agreement was not to be expected, though, since in the experimental situation apparently no ordered layer is obtained.

adsorbate is fundamentally altered. Whereas in the face-on conformation, the main contribution came from the π -system, in the edge-on conformation the charge rearrangements are more localized on the CN-group, as shown in Figure 3.8. This situation is reminiscent of covalently-bonded self-assembled monolayers^[22]. In agreement with the experiment, for the edge-on conformation a large positive work-function modification predicted. The calculated value of +2.4eV, however, is significantly too large. A quantitative agreement was not to be expected, though, since in the experimental situation apparently no ordered layer is obtained.

3.4.6 Potential Application: Soft metallic contacts

One of the prime challenges in molecular electronics is to make contact between the organic material and the electrode without altering the properties of the active compound. It was shown in this thesis that the metal substantially influence the geometry and molecular charge of an adsorbate, and it is plausible that also other properties, like the optical band gap, are affected. A remedy to this problem is to insert a buffer layer between metal and organic^[219–221]; however, such a buffer layer typically suppresses the metallic contact, introducing another charge-injection barrier to the device. In this section it will be reported that HATCN can be utilized as a buffer layer that proliferates the metallic contact to subsequently deposited C_{60} . At the same time, the honeycomb structure of the HATCN layer serves as a template for the fullerenes, allow-

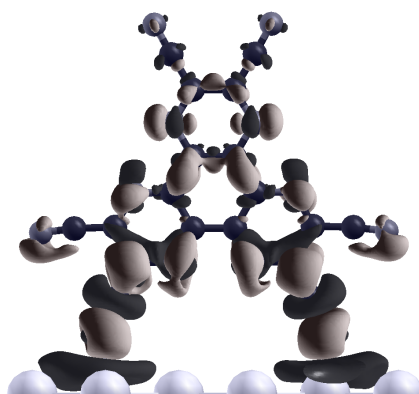


Figure 3.8: Light regions correspond to negative sign, i.e. depleted electron density, while dark regions imply density buildup. An isovalue of 0.01 has been used. Only the top three layers of the metal are shown.

ing STM imaging at room temperature, which is normally not possible. Also, despite the metallic contact, the bulk properties of C_{60} are retained in this heterointerface.

STM investigations at low coverages reveal a honeycomb structure with two HATCN molecules in a hexagonal unit cell with a lattice parameter of 2.0nm. Low energy electron diffraction experiments confirmed that this structure is valid for a larger region. To confirm that the observed STM image indeed corresponds to the face-on adsorbed HATCN conformation, DFT has been employed to simulate the picture using the Tersoff-Hamann approach as described in section 2.2. The structure is shown in Figure 3.9; excellent agreement between theory and experiment is obtained. In a honeycomb structure, six molecules form one closed ring, leaving a hole in its center. This hole can be used as template. Indeed, STM imaging reveals an inverted honeycomb for subsequently deposited C_{60} . Unfortunately, a reliable calculation of the STM picture by means of DFT is not possible, since the interaction between the fullerene and HATCN can be expected to be mainly determined by van-der-Waals interactions, which are not correctly accounted for in common GGA-type functionals. The adsorption energy of C_{60} on the HACTN layer is sufficiently large to allow for STM imaging of the overlayer at ambient temperature. It is also interesting to notice that a few single fullerenes without neighboring molecules are observed, which are, nonetheless, in registry with the position of the nanocavity matrix provided by HATCN/Ag(111), which can be inferred by theoretical extrapolation of the observed C_{60} - C_{60} distances. This indicates that the overlayer is not stabilized by intermolecular interactions of the C_{60} layer.

As next step, the question whether HATCN can provide metallic contact to the fullerenes must be tackled. UPS investigations of HATCN on Ag reveal additional intensity near the Fermi edge, marked in figure 3.10 with a “+”. From DFT calculations, this can be clearly attributed to a partially filled LUMO of the organic molecule hybridized with the metal bands. Metals, by definitions, are systems with partially occupied bands. Consequently, the HATCN/Ag has to be viewed as being metallic,

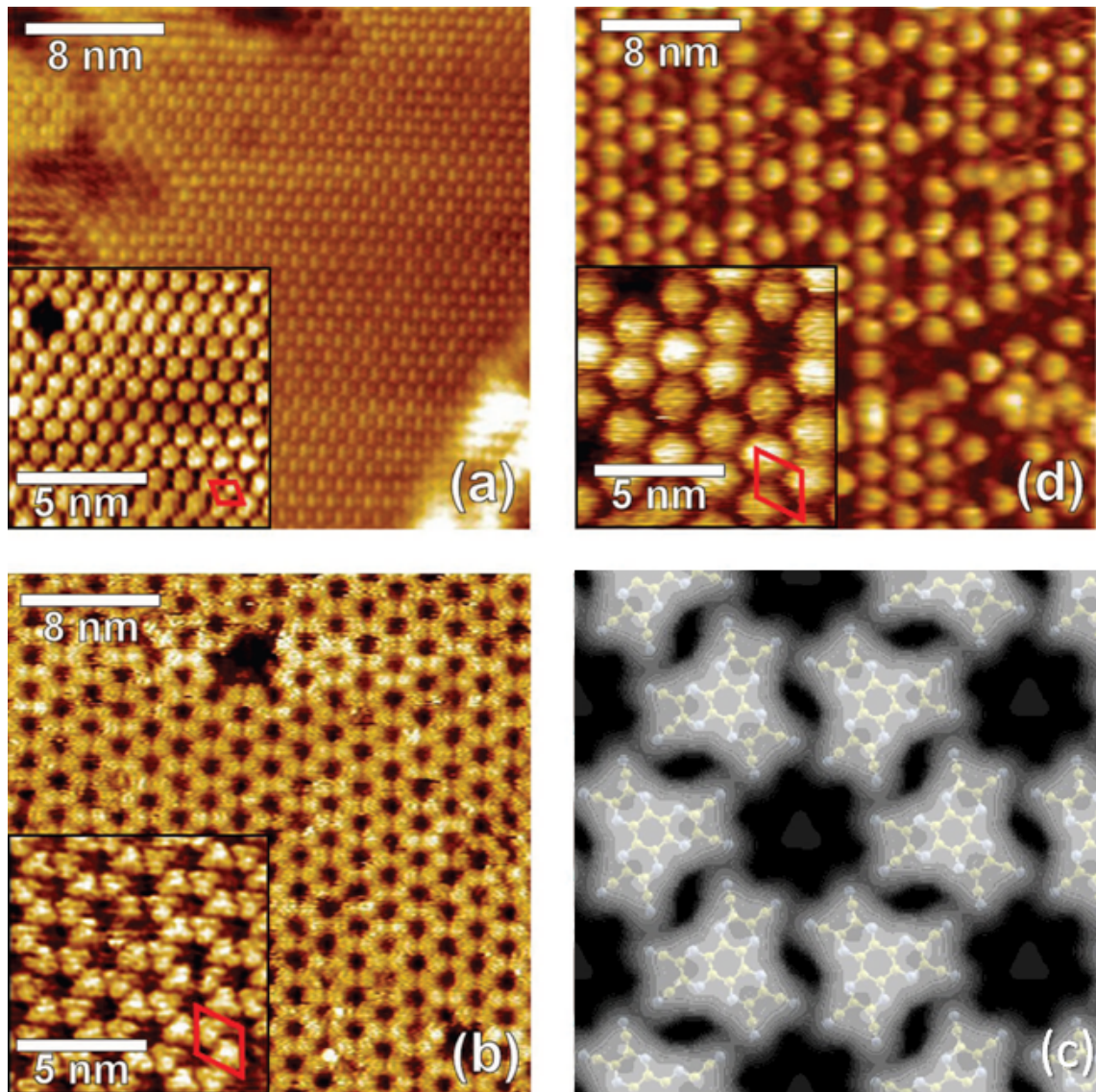


Figure 3.9: STM images of (a) monolayer C_{60} on Ag(111). (tunneling voltage $U_T = -0.1$ V, tunneling current $I_T = 0.8$ nA). (b) Monolayer HATCN on Ag(111). The inset resolves individual molecules; the red rhombus indicates the hexagonal unit cell with a) 0.96 nm ($U_T = -1.0$ V, $I_T = 0.3$ nA). (c) Simulated STM image of a HATCN monolayer on Ag(111) (details: see text). The structures of the individual HATCN molecules are overlaid as a guide to the eye to be able to correlate the STM picture with the molecular arrangement. (d) C_{60} submonolayer on HATCN/Ag(111) ($U_T = 1.0$ V, $I_T = 0.3$ nA). Inset: the red rhombus indicates the hexagonal unit cell with a = 2.0 nm ($U_T = 1.0$ V, $I_T = 0.1$ nA). Figure adapted from ref. ^[191]. (In the original publication, the wrong picture has been used for (c), which has been corrected here.)

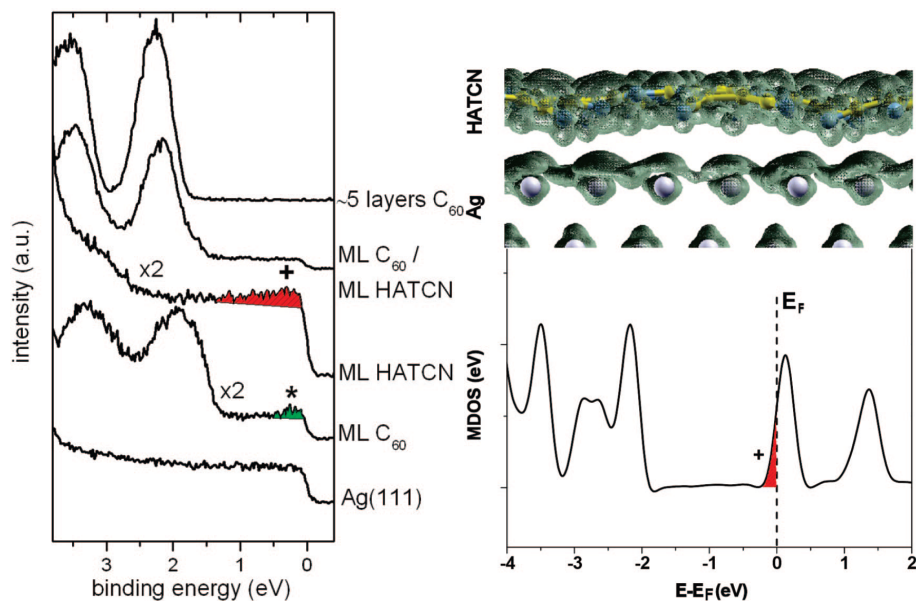


Figure 3.10: Left: UPS spectra of the valence region for the different samples as indicated (ML) monolayer). The LUMO-derived state at the Fermi level (0 eV binding energy) for $C_{60}/Ag(111)$ is marked by “*”. The LUMO-derived state for HATCN/ $Ag(111)$ is marked with “+”. Right top: Local density of states (LDOS) of HATCN on $Ag(111)$ in the arrangement shown in Figure 3.9, integrated in an energy window of 0.1 eV above and below the Fermi level E_F . The LDOS extends over both the molecule as well as the Ag substrate, indicating that the metallic character extends onto the HATCN molecules. Right bottom: Molecular contribution to the density of states (MDOS) of HATCN/ $Ag(111)$. The band associated with the HATCN LUMO is pinned right at E_F . The LUMO-derived state is marked with “+” and red shaded. Figures taken from ref. [191].

provided the spatial distribution of electrons at the Fermi-energy is delocalized between Ag and the organic layer. To find this out, the local density of states (LDOS) has been plotted in a window of $\pm 0.1\text{eV}$ around E_F . The result, shown in the right part of 3.10, clearly shows that the metallic character indeed extends to HATCN.

From UPS experiments it can also be inferred that the goal of retaining the bulk-properties of the fullerenes has been achieved. The spectrum of the $Ag/HATCN/C_{60}$ system is strongly reminiscent of the multilayer spectrum of C_{60} , both shown in the left part of Figure 3.10. The small differences can be attributed to the work-function modification induced by HATCN adsorption.

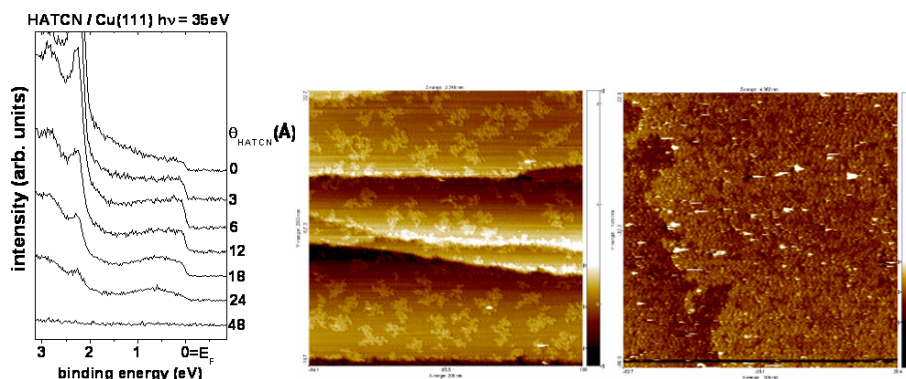


Figure 3.11: Left: UPS spectra of the valence region for HATCN deposited on Cu(111). Middle and right: STM images of HATCN has been deposited on Cu(111). Image (a) shows a nominal coverage of 2 \AA on an $200 \times 200\text{ nm}^2$ image ($U_T = -1.0\text{ V}$, $I_T = 1.0\text{ nA}$). (b) shows a higher nominal coverage on an area of $109 \times 109\text{ nm}^2$ ($U_T = -1.0\text{ V}$, $I_T = 0.3\text{ nA}$). Figures taken from ref. [191].

3.4.7 HATCN on Cu(111)

This section will deal with HATCN adsorbed on Cu as substrate. Qualitatively, most effects are similar to the situation on Ag(111). However, some differences can be observed, which will be elaborated here.

Experimental Results

The experimental UPS spectra recorded for the sequential deposition of HATCN on Cu(111) shown in the left part of Figure 3.11 are similar to the spectra on Ag(111) shown in Figure 3.10. An attenuation of Cu features is observed accompanied by an increase of strong molecular features centered at 4.58 and 7.60 eV binding energy (BE). The latter peak has a shoulder at the low BE side, similar to the multilayer spectra on Ag. The ionization energy of the multilayer film is found to be 9.28 eV. Additional intensity appears close to the Fermi edge, which can also be attributed to a partially occupied hybrid state of LUMO and metal bands. STM images on Cu(111) are shown in the right part of Figure 3.11. Small 2D islands with a dendritic shape form and grow in a confined area until a monolayer is almost closed. No ordered superstructure of HATCN on Cu(111) is, however, observed.

The change of the work function follows a similar trend as observed on Ag. But in contrast to the shallow increase until a coverage of 6 \AA in the Ag case, in the Cu case it slightly decreases from 4.94 (pristine Cu(111)) to 4.81 eV as shown in Fig. 3.12. With increasing coverage the trend is reversed and the work function increases to 5.54 eV at a film thickness of 48 \AA . The change in behavior both here and on Ag(111) is ascribed to a change in the adsorbate morphology.

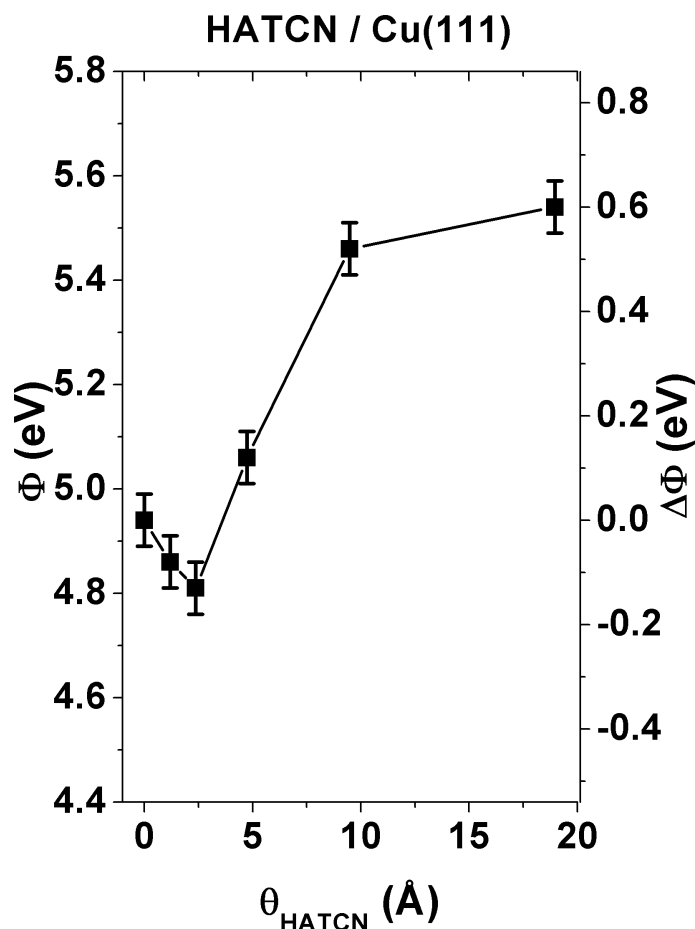


Figure 3.12: Absolute and relative work function change for the sequential deposition of HATCN on Cu(111) as determined from the secondary electron cutoff. Figure provided by Benjamin Bröker.

Computational results

For Cu, only the face-on geometry has been computationally investigated. From DFT optimization, the equilibrium distance between molecule and topmost layer is found to be 3.95 Å, which is unusually large. Nonetheless, strong bending of the molecule is observed, in analogy to the situation on Ag. The vertical distance between the lowest and highest HATCN atoms amounts to 0.78 Å. The calculations yield an adsorption energy of -0.54 eV. Electron rearrangements upon adsorption and the influence on the electrostatic potential are depicted in Figure 3.13. Qualitatively, the situation is very similar to the situation on Ag. Formation of one or several metal-molecule bonds is observed, indicated by the reduction of charge density in the vicinity of the metal and the concurrent increase near the molecule. The density buildup is confined to regions above and below the plane of the molecule. Quantitatively, the total charge transferred is computed to be 0.33 electrons, about 2/3 the value for Ag. Still, the work function shift due to the charge transfer dipole formation is as large as 0.55 eV, driven by the large molecule-metal distance. The shift in vacuum level due to the molecular dipole is

found to be -0.24 eV, resulting in a net work function modification of $+0.31$ eV. Embarrassingly, this is not even in qualitative agreement with the experimental results, which predict a small work-function reduction for the low-coverage phase.

The failure to correctly account for the experiment can be at least partly attributed to the arguably too large (calculated) distance between molecule and metal, which in turn gives a too large bond dipole. The overestimation of the vertical distance arises from the lack of non-local interactions, e.g. van-der-Waals forces, in the computations. This impact of the adsorption distance is investigated in more detail in section 4.1.

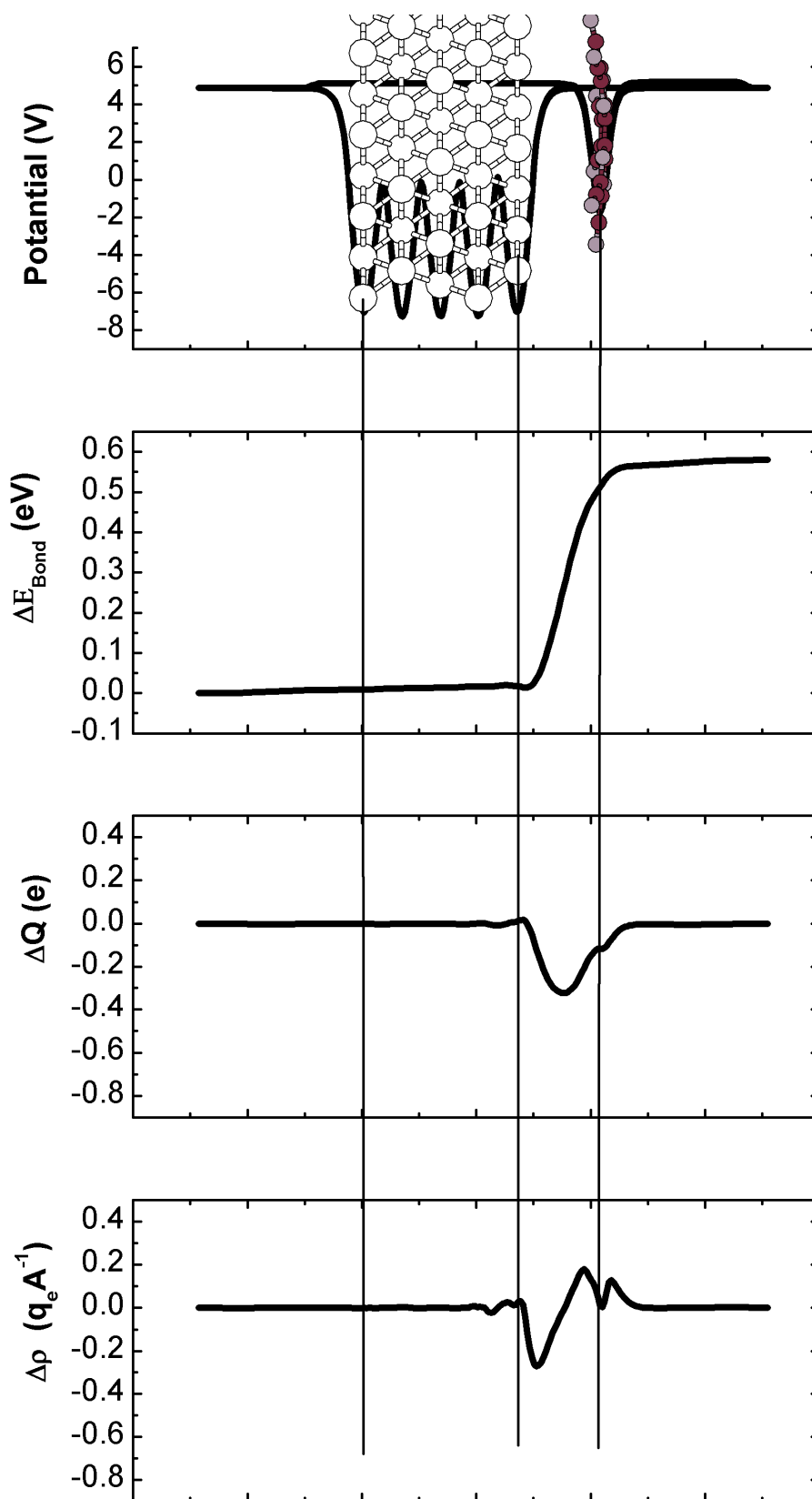


Figure 3.13: Plane averaged change of electron density ρ , charge Q , bond dipole ΔE_{BD} and electrostatic potential (bottom to top) of HATCN on Cu(111)

3.4.8 HATCN on Au(111)

Some final remarks will be made with regard to the deposition of HATCN on Au(111). Gold is the most noble and hence least reactive metal of this series. In contrast to the strong to modest interactions with Ag and Cu (“chemisorption”), only weak effects are expected here. Thus, DFT is pushed right to its limits.

Experimental results

UPS valence band spectra (graph not shown here) on gold show a weaker attenuation of the metal features, but two molecular peaks can be observed at 4.5 and 7.8 eV binding energy. In contrast to the deposition on Ag and Cu, the Fermi edge is clearly visible for the thickest film on gold. Thus the ionization energy for the multilayer film cannot be extracted from the onset of the highest occupied molecular orbital (HOMO) of HATCN. The work function, judging from the secondary electron cutoff, rapidly decreases upon deposition of HATCN, see Figure 3.14. At some point, around approximately 12 Å, the trend reverses. However, the increase of the work function proceeds very slowly. Even for 48 Å film thickness, $\Delta\Phi$ remains negative, in contrast to the situation of Ag and Cu. Moreover, masking of Au features is only observed for the first few Å of film deposition, after which they remain almost constant. STM pictures showed only disordered clusters on Au(111). This finding is backed up by the fact that metal features are not completely masked at even high film thickness. Hence, HATCN on Au is proposed to follow Vollmer-Weber growth, i.e., forms islands/cluster without closing a wetting layer.

Computational Results

Like for Cu, only the face-on monolayer has been investigated. Following the expected order $\text{Cu} > \text{Ag} > \text{Au}$, the binding energy of this system is lowest in this series, namely -0.34 eV. The computed minimum distance between molecule and surface is found to be 4.10 Å, which is not very realistic anymore. Also the bend of the molecule is smallest in the series. The vertical distance between lowest and highest atom amounts to 0.4 Å. The calculated rearrangements in electron density, total charge transferred, and the bond dipole as well as the corresponding plane averaged electron potential energy are depicted in Figure 3.15. In contrast to the experiment, the overall picture qualitatively resembles the situation for the other metals. Electron density from the metal is transferred to regions closely above and below the molecule. As expected, the amount of charge transferred is significantly lower, 0.16 electrons. Due to the large molecule-metal distance of more than 4 Å, the bond dipole is still considerable, and induces a vacuum level shift of +0.24 eV. As a consequence of the reduced bend, the shift in vacuum level due to the molecular dipole is quite small, only -0.07 eV. Thus, DFT predicts $\Delta\Phi$ to be +0.17 eV. It is to stress here that the calculated net work function change is positive, which is in striking contradiction to the experiment. Again, the obvious overestimation of the adsorption distance, as well as the general overestimation of the charge-transfer distance should be held responsible for this discrepancy. Additionally, it is not very surprising that the calculation for a hypothetical well ordered monolayer on Au does

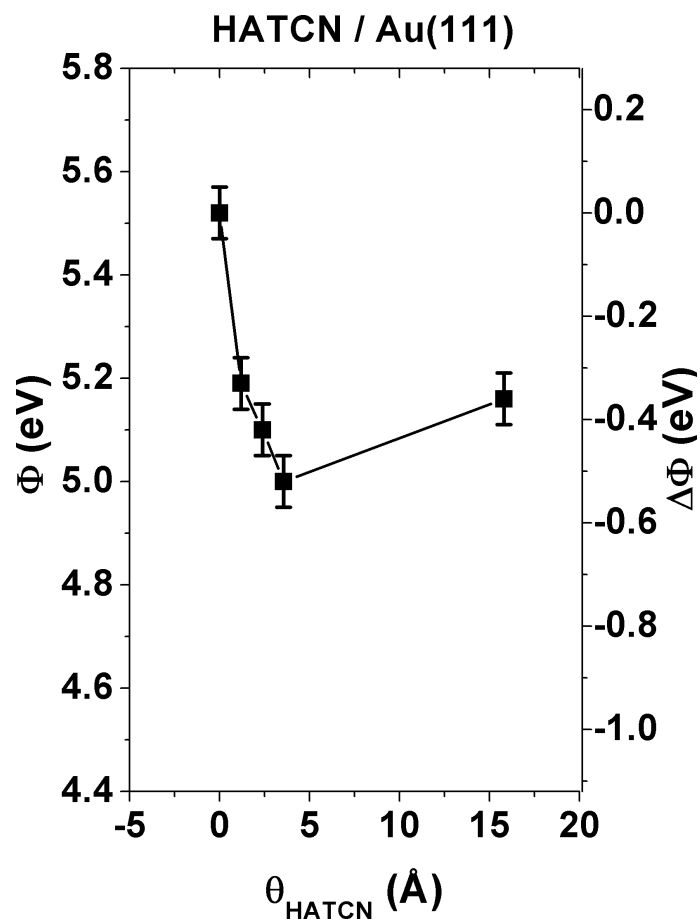


Figure 3.14: Absolute and relative work function change for the sequential deposition of HATCN on Au(111) as determined from the secondary electron cutoff. Picture and data provided by Benjamin Bröker

not concur with the experiments performed for a system which apparently does not exhibit a closed monolayer at all.

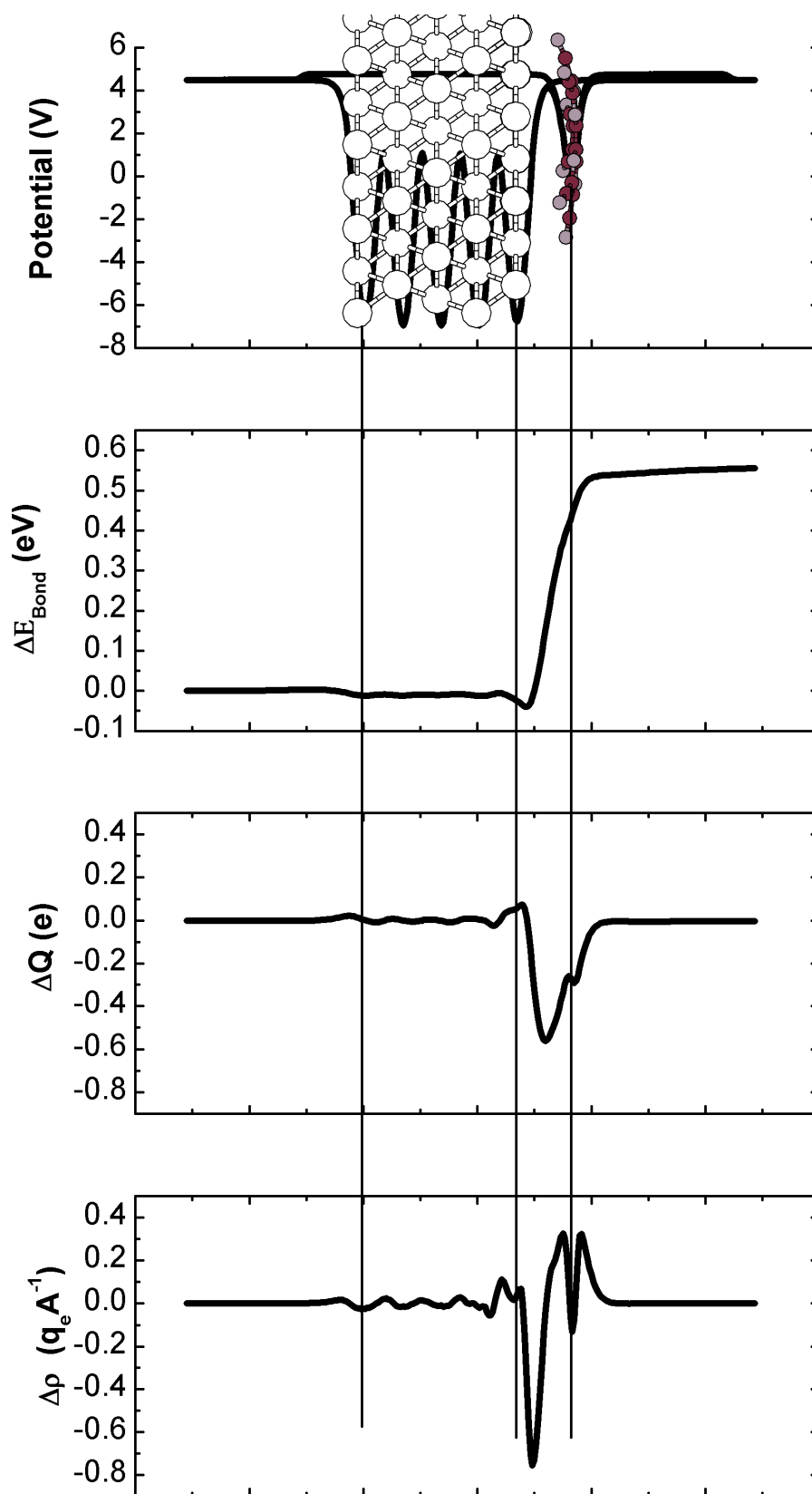


Figure 3.15: Plane averaged change of electron density ρ , charge Q , bond dipole ΔE_{Bond} and electrostatic potential (bottom to top) of HATCN on Au(111)

3.4.9 Conclusion

It has been shown that the interaction between coinage metals and the intermediate acceptor HATCN differs significantly between Ag, Cu, and Au. While for silver, nicely closed monolayers are formed which can serve as template and metallic contact to subsequently deposited organic material, only dendritic growth is observed on Cu, and even less order is found experimentally on Au. This fits well with the computed decrease of the interaction strength along this series. It was found that the first, chemisorbed layer of HATCN undergoes a phase transition upon increasing material deposition: for low coverages of the organic material, a face-on conformation is observed. At higher coverages, the face-on molecules reorient to more or less upright standing molecules and incorporate further material into this layer. Although explicitly only proven for the case of HATCN on Ag, the work-function evolution also hints at similar effects at least on Cu, and most likely also on Au. Concerning the face-on phase in the low-coverage regime, only for HATCN on Ag a satisfactory agreement between the work-function modification measured experimentally and computed by DFT is obtained. In the cases of weaker interaction, large quantitative and qualitative errors occur. This is, on one hand, attributed to the overestimation of the adsorption distance and the exaggeration of charge-transfer by DFT in general. On the other hand, also the non-concurrence between the assumed closed monolayer for the calculation and the real sample, which is likely a disordered, amorphous phase, likely plays a big role. The high-coverage phase was studied computationally only on Ag(111). Qualitatively, the increase of the work function could be rationalized, albeit with a strong overestimation resulting from the unknown structure of this layer. It was also found that the mechanism of charge-transfer shifts from a Blyholder-type donation-backdonation mechanism, which involves the whole molecules, to a mechanism more familiar from self-assembled monolayers centered mostly on the regions of the HATCN in intimate contact with the metal.

3.5 COHON

3.5.1 Preface

As second electron accepting molecule, coronene-1,2,5,6,9,10-hexaone (COHON) was investigated. Its chemical structure is shown in Figure 3.16. The COHON molecule was synthesized by the Mainz group as precursor molecule for larger graphene sheets. Within the IControl project, also its potential for work-function modification of coinage metal surfaces was investigated. From gas phase calculations at the B3LYP / 6-31+G* level, a vertical electron affinity of -3.42 eV is obtained, which is of the same order of magnitude as for HATCN (-3.53 eV). Both molecules are also structurally similar, since in gas phase they exhibit D_{3h} point group symmetry, and both molecular have the same number of atoms contributing to the π system. A notable difference, however, is that the general build-up of the COHON molecule is somewhat more compact, and the docking groups are significantly shorter.

For HATCN reliable computational results were only obtained on Ag. Therefore, COHON is investigated only on this metal. The results reported here were also reported in the same wording to the consortium of the ICONTROL project in Deliverable 22, part 3. At the moment, publication of the results is not intended. All calculations performed for this section were performed by myself. Conclusions were drawn in multiple discussions with Egbert Zojer and Gerold Rangger.

3.5.2 Computational Results

Unfortunately, to the best of our knowledge, no experimental unit cell is known up to date. Therefore, COHON was investigated theoretically in the default $5 \times 3\sqrt{3}$ unit cell, assuming a loose packing regime in order to avoid artifacts from improper interactions between the individual molecules. Upon adsorption, the formally planar COHON molecule becomes bent, with the outer keto groups working as docking groups and pointing towards the metal, as shown in Figure 3.16. This behavior is in close analogy to HATCN, as well as most other charge-transfer molecules investigated in this project so far. A notable exception is perylene-3,4,9,10-tetracarboxylic-3,4,9,10-dianhydride (PTCDA), which remains almost perfectly planar^[132], and for which the binding energy calculated by DFT (excluding dispersion interactions) is zero^[99]. In COHON, the oxygen atoms are found at about 2.3Å above the top Ag-layer, and ca. 1.1Å below the central phenyl ring, as shown in Figure 3.16. Furthermore, a slight distortion of the C_3 symmetry is observed, as every docking groups tries to get into an energetically optimal position. This results in a lifting of the degeneracy of orbitals, which will be discussed below.

The strong electronegative nature of the keto-groups strongly polarizes the molecule. As consequence of the bending, a molecular dipole in z-direction, i.e., perpendicular to the surface, is induced. This dipole points towards the surface, and according to the Helmholtz-equation leads to a significant decrease of the electrostatic potential above the sample by -0.79 eV. This is opposite to the desired effect of electron acceptors, which is a work-function increase. The bending, however, can also be interpreted as

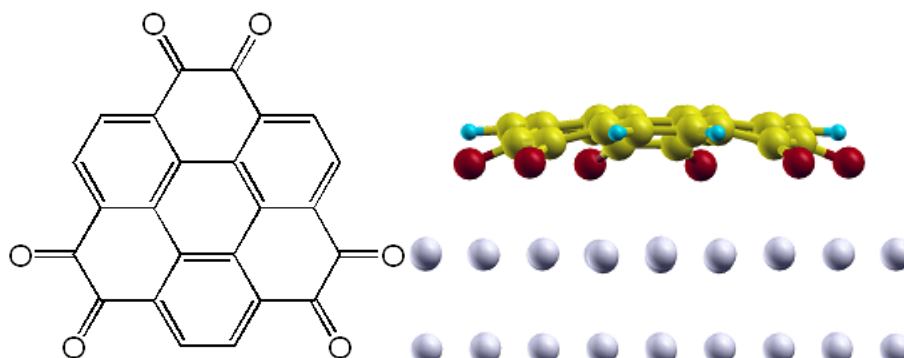


Figure 3.16: Left: chemical structure of COHON. Right: Front view of the optimized adsorption geometry of COHON on Ag(111).

an unambiguous sign of chemisorption. Charge transfer is an integral part of most chemical reactions, and due to the large electron affinity of COHON, electrons are transferred from the metal to the molecule. In Figure 3.17, the plane integrated charge rearrangements upon adsorption are shown.

Directly above the surface of the topmost metal layer, a significant decrease of electron density is observed, labeled as **I**. This peak indicates the back-donation of metal electrons to the COHON molecule; also, this region is where Pauli-pushback can be observed. At the same time, also an increase of electron density directly at the position of the central phenyl ring, designated as **II**, is observed, which can be ascribed to forward-donation. Three main areas are identified where the electron density is increased: First, the peak labeled **1**, which is located almost halfway between molecular plane and metal. The electrons in this region most likely belong to (a lone pair of) the oxygen atoms, rendering them even more negative. This can also be seen in the 3D rearrangements, where a region of negative charge is found in the prolongation of the C=O bond. This is in sharp contrast to the cyano substituted molecules investigated so far, like HATCN or F4TCNQ, where in the prolongation of the CN bond always a reduction of electrons was observed. Furthermore, two peaks are found directly above and below the molecular plane, labeled as **2a** and **2b**. These regions belong to the π -plane of the molecule, as demonstrated by the 3D charge rearrangement plot. From the integration of $\Delta\rho$, the transferred charge ΔQ is obtained. In accordance with the convention employed in the previous sections, the region below the maximum of ΔQ is defined as the metal, and the region above as molecule. Within this definition, the transferred charge is given by the maximum of ΔQ , which in the present case is 0.82 electrons. Since the molecule becomes negatively charged in the adsorption process, a bond dipole is created which points away from the surface. In the loose packing regime, the corresponding potential increase amounts to +1.20eV. Together with the molecular dipole discussed above, this adds up to a total work-function change of +0.41eV. Thus, more than half of the work-function increase due to the charge transfer is compensated by the consequences of the molecular distortion. Due to the similar size and shape to HATCN, it is quite reasonable to assume that a real monolayer of COHON will form a

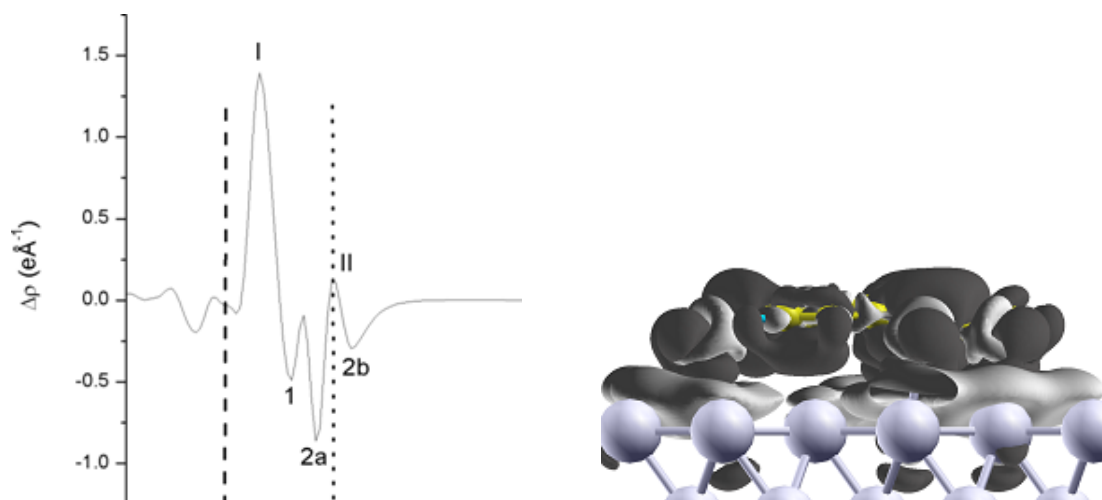


Figure 3.17: Left: Plane integrated charge rearrangements of COHON upon adsorption. The dashed line indicates the top metal layer, while the dotted line corresponds to the central phenyl ring of COHEN. Right: 3D charge difference density. Dark areas indicate increased, light areas reduced electron density.

similar unit cell. Table 3.1 reports the work function shifts for such a “tightly” packed layer of COHON, and compares it to the same results for HATCN, which were in part already discussed in section 3.4. Please note that the “loose” packing regime for HATCN required a larger unit cell, and is therefore not equal to that of COHON. It is interesting to notice that for both molecules, the total work function change $\Delta\Phi$ is reduced slightly (or rather, remains almost constant) in the tight packing compared to the loose regime. The reason for this counterintuitive effect is not perfectly clear yet, and can neither be explained by depolarization effect nor a change of the charging energy of the molecules.

Table 3.1: Transferred charge ΔQ , molecular dipole induced shift of the work function $\Delta\Phi_{mol}$, bond induced shift of the work function $\Delta\Phi_{bond}$ and induced work-function modification $\Delta\Phi$ for the loose packing and the packing of the experimental (“tight”) HATCN unit cell. Please note that loose packing for COHON and HATCN does not refer to the same size of the unit cell.

Molecule	Packing	ΔQ (e)	$\Delta\Phi_{mol} / \Delta\Phi_{bond}$	$\Delta\Phi$
COHON	loose	0.82	-0.79	1.20 0.41
COHON	tight	0.79	-0.93	1.31 0.38
HATCN	loose	0.56	-0.26	0.54 0.26
HATCN	tight	0.41	-0.55	0.79 0.24

It is also noteworthy that the predicted net work-function modification induced by adsorption of COHON is larger than that of HATCN, despite the slightly worse electron affinity. It is also worth pointing out that the charge transferred to COHON is almost twice as large as for HATCN, which would be completely unexpected if the electron affinity is the only driving force. Indeed, *a posteriori*, at least the latter effect can be understood from the studies presented in section 4.2.

3.6 GaClPc: Orientational ordering and geometrical deformations of a molecule with a flexible dipole adsorbed on Cu(111)

3.6.1 Preface

In this section, the focus is shifted away from strong electron donor and acceptor adsorbates to chlorogallium phthalocyanine (GaClPc), an organometallic compound (see Figure 3.18) with a permanent dipole moment, which is investigated theoretically as well as experimentally. The study of a non-redox-active compound provides complementary information on the processes occurring upon formation of metal/organic interfaces.

Experimental and part of the theoretical results shown in the following section will be published in a paper by Gerlach et al. which is currently under review in *Physical Review Letters*. Since this thesis is mainly concerned with the computational results, the experimental findings will only be briefly sketched here. In the computational part, extended information on the attempts to determine the adsorption geometry are reported. The final part concerned with the electron rearrangement upon adsorption is a reproduction of the corresponding part of the Supporting Information for the paper of Gerlach et al. X-ray standing wave (XSW), X-ray photoelectron spectroscopy (XPS) and ultraviolet photoelectron spectroscopy (UPS) measurements have been performed by A. Gerlach and S. Duhm in the group of F. Schreiber under the beamline supervision of J. Zegenhagen. Supplementary metastable atom electron spectroscopy (MEAS) was done in Japan by S. Kera. Density functional theory (DFT) calculations have been performed by myself. Interpretation of the computational results was done in multiple discussion between E. Zojer and myself.

3.6.2 Experimental Methodology

“The XSW experiments were carried out at beamline ID32 of the European Synchrotron Radiation Source (ESRF) in Grenoble. Using the (111)-reflection of the copper substrate we have taken data in back-reflection geometry^[186, 222], i.e. corresponding to the lattice plane spacing $d = 2.08\text{\AA}$ with photon energies around $E_{Bragg} = 2.97\text{ keV}$. The UPS experiments for different coverages were performed with a photoelectron spectrometer equipped with a standard He I light source (photon energy 21.2 eV) in our home laboratory. The Cu(111) crystal with a small mosaicity was prepared under ultra-high vacuum conditions by repeated cycles of argon sputtering and annealing (base pressure $4 \times 10^{-10}\text{ mbar}$). The GaClPc material was purchased from Sigma-Aldrich, purified by gradient sublimation, and thoroughly degassed in the vacuum chamber. With a calibrated quartz microbalance typical deposition rates of $0.2\text{\AA}/\text{min}$. were realized. For all experiments reported below the substrate temperature was held constant at 80° .”

- taken from Gerlach et al., *Phys. Rev. Lett.*, submitted

3.6.3 Experimental results

From XPS data, it becomes evident that multiple signals are of sufficiently high quality to be used for the determination of the atomic position using the XSW technique.

Effectively, the 1s core level signals of carbon and nitrogen have been used, along with the $2p_{1/2}$ signal of Ga and the KLL-Auger electrons from Cl. The modulo-d ambiguity of XSW^[223] states that the same signal is obtained for atoms with positions differing by exactly the lattice distance of the substrate (2.08Å in the case of Cu(111)). It is, therefore, not possible to obtain a unique geometry. Rather, two possibilities must be envisioned for each atom:

- C: 2.36Å or 4.44Å
- N: 2.62Å or 4.70Å
- Ga: 2.14Å or 4.23Å
- Ca: 1.88Å or 3.96Å

Larger distances can be excluded, since for metal/adsorbate separations above 6Å no significant interaction exists any more. The XSW-data allow for two distinct conformations: In the “Ga-down”-case, the Ga atom is closer to the surface than the Cl atom, giving rise to a bond length between them of 1.82Å. The second possibility is that the Cl atom is closer to the Cu substrate, with a Ga-Cl distance of 2.35Å. This conformation will be called “Cl-down”. Independent of the orientation of the Ga-Cl bond, the Pc ring can be found at low (≈ 2.5 Å) or at high (≈ 4.5 Å) position. UPS experiments revealed a work-function modification of ca. -0.35 eV upon adsorption, with is stable for a large coverage range. Only upon annealing, a further decrease to -0.6eV is observed. To aid the interpretation of the results, DFT calculations have been performed.

3.6.4 Computational Results

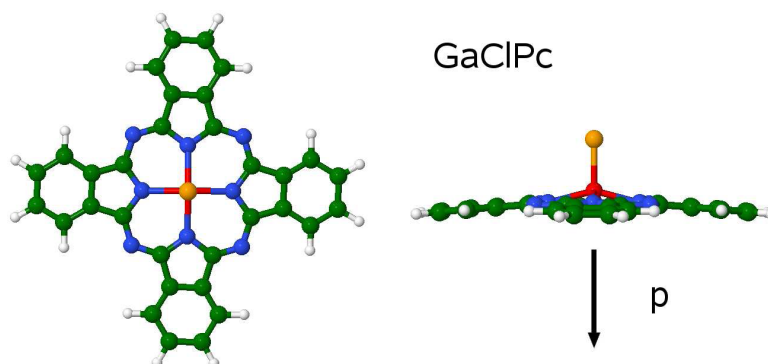


Figure 3.18: Geometry of GaClPc as obtained by geometry optimization in Gaussian03^[71]. Green atoms: carbon; white atoms: hydrogen; blue atoms: nitrogen; red atom: gallium; yellow atom: Cl. The arrow indicates the direction of the dipole moment. Figure taken from Gerlach et. al, submitted.

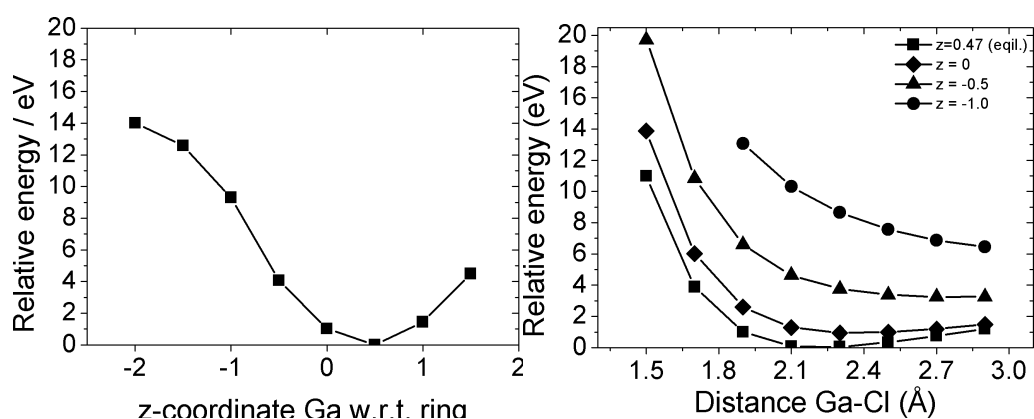


Figure 3.19: Energy profile w.r.t. the shift of the Ga-Cl bond perpendicular to the Pc-ring (top) and of the Ga-Cl-bond distance at different positions of the Ga atom relative to the Pc-ring (bottom).

Gas phase calculations

Optimization of the gas phase structure of GaClPc at the B3LYP / 6-31G(d,p) level of theory yields a Ga-Cl distance of 2.21 Å, with Ga being ca. 0.5 Å above the ring (more specifically, above the topmost nitrogen atoms of the Pc-ring). While the bond length is closer to the Cl down geometry, the distance between Ga and the Pc-ring fits the Ga down geometry significantly better. In order to estimate which degree of freedom - the bond length change of Ga-Cl or the shift of the Ga-Cl bond through the ring - is energetically more demanding, their respective energy evolution was mapped with respect to perturbation along these modes, while keeping the all other coordinates at their fully optimized value. As Figure 3.19 (top) shows, moving the Ga atom through the ring by 1.5 Å as required by the Cl down geometry costs a significant amount of energy, up to ca. 9 eV. (Note: technically, to comply with the statement that N is located above C, it would not suffice to pull the Ga-Cl as whole below the ring to obtain the Cl down geometry, but the Ga Cl bond would need to be inverted and pushed upwards). In contrast, compressing the Ga-Cl bond by 0.4 Å, as requested by the Ga down geometry, would need only ca. 1 eV. Mapping the energy profile of the Ga-Cl bond after pulling Ga through the ring reveals that longer bond distances become more favorable. However, at large Ga displacements (>0.5 Å), no minimum for the Ga-Cl bond at distances <3 Å is found. Using the experimental geometries as described above and calculating the corresponding total energy without any further optimization reveals that the combined effects of the displacements favor the relative coordinates of the Ga down geometry, which exhibits 3.0 eV lower than the energy of the Cl down geometry. The energetics indicate that if the ring is in the low position, Ga down is more plausible, since Cl down would require too large displacement of the Ga-Cl bond. In contrast, if the ring was located in the high position, the Ga down geometry can be excluded, as the energetic of the bond length clearly favor the Cl down geometry.

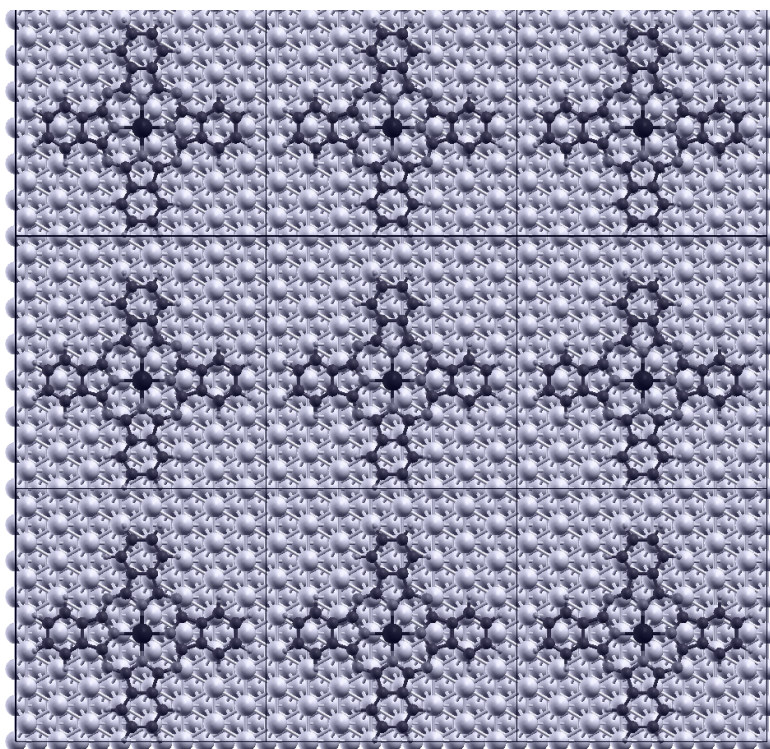


Figure 3.20: Unit cell employed for the calculation of GaClPc on Cu(111), repeated three times in x- and y-direction.

Calculations on the surface

Geometry optimization. In order to estimate whether the chemisorption with the Cl atom being closer to the surface is energetically more favorable than the Ga down geometry, both geometries were optimized on the surface of a 3 layer Cu(111) slab using the PW91 functional and a plane wave basis set with a cutoff of 20Ryd. All atoms of GaClPc were allowed to fully relax their z-coordinate, i.e. the distance to the metal, while their x- and y- position were kept fixed in order to speed up the calculation.

Energetically, both starting geometries relax to approximately the same total energy value, with the Ga down geometry being slightly more favorable (by 0.05 eV in a tightly packed monolayer, and 0.19 eV at half coverage). In terms of geometry, the Ga down start structure relaxed the Ga atom to 4.15Å and the Cl atom to 6.35Å, which are much larger distances to the metal than measured. The Cl down geometry performs better, with the Ga atom at 4.45Å and the Cl atom at 2.09Å, i.e. ca. 0.2Å above the measured positions. However, in both cases, the Pc ring is found at an adsorption height of ca. 3.5Å, i.e. between the position of the high and the low geometry. It is not clear whether this failure is to be attributed to the missing description of van-der-Waals forces in the DFT functional, which would draw the Pc-ring too close, or whether the ring does not reach larger adsorption distances because the forces acting on the individual atoms are too small. Therefore, it cannot be clearly stated whether the high or low position of

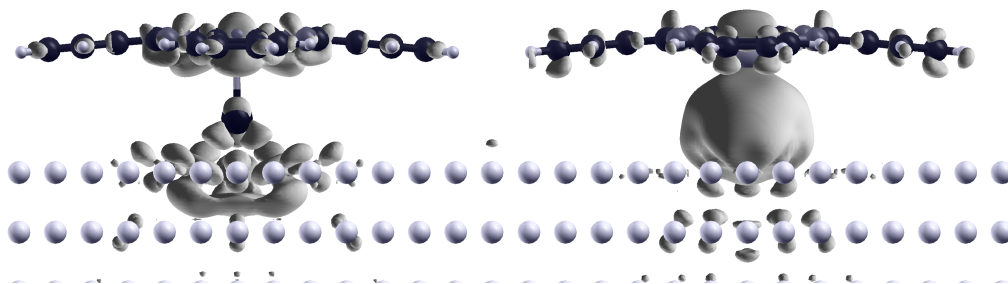


Figure 3.21: Charge rearrangements upon adsorption of GaClPc on Cu(111). Left: Electron density increase; right electron density decrease. Chosen isodensity value: $0.0025 e/\text{Bohr}^3$

the ring is more likely. With the failure to calculate the position of the ring at a realistic value, there is no reason to assume that the adsorption height of Ga or Cl are correctly reproduced. For such obviously wrong geometries also the adsorption energy differences are meaningless. These calculations must therefore be regarded as inconclusive. Because a distance of ca. 2.5\AA appears to be rather small for the physisorbed ring, it was decided (by A. Gerlach) that the “high” position is the more plausible one.

Interaction with the surface at experimental geometries. To reproduce the experimental structure as closely as possible, the following approach was chosen: As a first step, the geometry of the isolated GaClPc molecule was optimized using Gaussian03^[71] (B3LYP/6-31G(d,p)). The resulting geometry is slightly non-planar, with the average z-coordinate of the carbon atoms being 0.18\AA below the average nitrogen position. Next, the macrocycle was placed above the surface such that the average lateral position of the carbon respectively nitrogen atoms comply with the experiment within the experimental error (chosen average carbon distance: 4.49\AA ; chosen average nitrogen atom 4.67\AA). For the carbon atoms a larger deviation from the measured average distance was accepted, as the latter quantity is subject to a larger experimental uncertainty due to the smaller coherence. The Ga and Cl atoms were placed underneath the macrocycle at the experimentally determined positions. Note that this results in a concave (i.e. “umbrella”-like) adsorption geometry, while in gas phase GaClPc adopts a convex (“inverted umbrella”) shape \hat{U} a deviation that can be attributed to specific interaction with the surface. The lateral position of the molecule was chosen such that the Cl atom comes to lie above the hcp-hollow site of the Cu(111) surface. Since the exact unit cell of GaClPc on Cu(111) is unknown, a loose GaClPc monolayer (1 molecule per 310\AA^2 Cu) with a rectangular unit cell (see Fig. 3.20) was assumed to avoid artifacts resulting from spurious intermolecular interactions. From other metallophthalocyanines it is known that the full monolayer approximately covers $210^2/\text{molecule}$ ^[224]. Hence, our calculations roughly correspond a coverage of $2/3\text{ML}$.

Upon contact with the surface, not only the geometry of the adsorbate, but also the charge density of GaClPc and the underlying metal undergoes significant distortions,

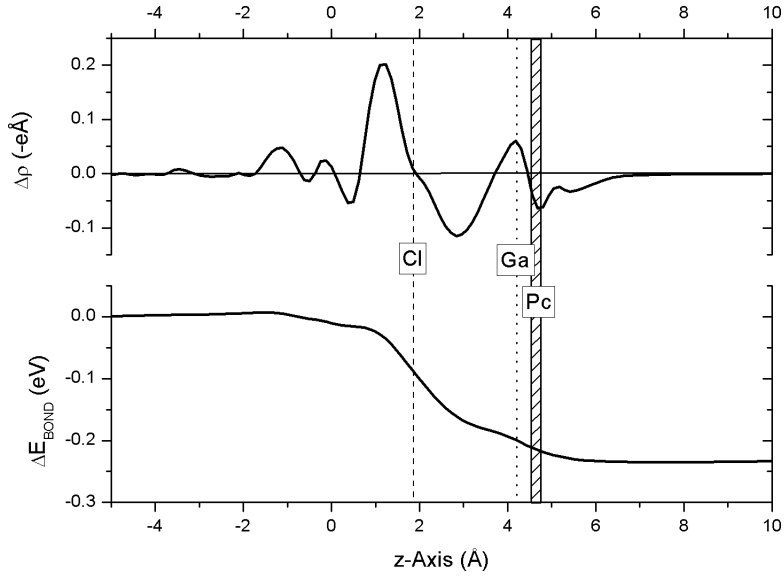


Figure 3.22: Plane-integrated charge rearrangements $\Delta\rho$ (top) and ΔE_{bond} (bottom) as function of the vertical position z . Zero denotes the plane of the topmost metal layer. The vertical lines denote the positions of the Ga and Cl atoms and the region of nuclear positions of the Pc macrocycle.

changing the effective work function by ΔE_{bond} . Figure 3.21 shows a three-dimensional isodensity plot of these charge rearrangements, calculated as

$$\Delta\rho(x, y, z) = \rho_{combined} - (\rho_{monolayer} + \rho_{slab}) \quad (3.4)$$

Since such an isodensity plot is difficult to interpret quantitatively as its shape depends on the actually chosen isodensity value, we also plotted the z -dependence of the charge rearrangements integrated over the xy -plane of the unit cell in the top part of Fig. 3.22. The main effects are an electron density increase in the region of the Ga atom and underneath the Cl as well as in parts of the metal layer (Fig. 3.21, left panel) as well as an electron density decrease engulfing the Cl atom (Fig. 3.21, right panel) being most pronounced in the region of the Ga-Cl bond (Fig. 3.22, top panel). At this point the question arises, whether the strong increase in the electron density approximately 1.3\AA above the top Cu layer is a consequence Pauli pushback of the electron tail of the metal by the Pc macrocycle^{VII} or linked to a more specific electronic interaction between GaClPc and the Cu(111) surface due to the proximity of the Cl atom and the top Cu layer. To test that, we performed a calculation in which we removed the Ga and Cl atoms and saturated the Pc by two hydrogens. The induced dipole is virtually zero in these calculations^{VIII}, indicating that Pauli pushback of the macrocycle does not play a role for the present adsorption geometry. Interestingly, in the plane of the chlorine atom the net $\Delta\rho$ vanishes, which can be explained by a cancellation of the

^{VII}Considering the large area over which such a pushback would occur it is not necessarily visible in Fig. 3.21 for the chosen isodensity value

^{VIII}To within the dipole convergence criteria of the SCF cycle.

electron density increase directly at the chlorine atom (Fig. 3.21, left panel) and the decrease in the larger sphere around it (Fig. 3.21, right part). The decrease of electron density between the halogen and the Ga atom results in a decrease of the strength of the Ga-Cl bond. This correlates well with the observed increase of the bond length to 2.35Å (XSW measurements) relative to its gas phase value of 2.21Å (DFT calculated). In the region of the Ga atom, again a net increase of electron density is observed, accompanied by a decrease of electron density within the Pc ring. From this data we conclude that the main effect upon adsorption is a redistribution of charge from the Ga-Cl σ -bond into a σ' orbital, weakening the Ga-Cl bond as well as increasing the electron density mainly in the region below the Cl-atom.

To link these charge rearrangements to the bonding induced energy changes, ΔE_{bond} , we show in the bottom panel of Fig. 3.22 the evolution of the electron, potential energy following from $\Delta\rho$ by solving Poisson's equation. The largest decrease is found in the region around the Cl atom consistent with the strong electron density rearrangement from the area of the Ga-Cl bond to the region between Cl and Cu. In addition to the work-function reduction of -0.35eV induced by the electron rearrangements discussed above, the Cl-down geometry also displays a molecules dipole moment inducing a further reduction of -0.20 eV. The observed total work-function modification of -0.55 eV for the Cl-down geometry is in astonishingly good agreement with the results obtained by UPS after annealing.

3.7 Cyclophanes: Organic/Organic interfaces with charge-transfer character?

3.7.1 Preface

In this section, organic/organic interfaces will be investigated. Understanding these interfaces is important for the future development of all-organic devices, as well as to improve the knowledge on the processes occurring between metal electrodes pre-covered with organic charge-injection layers, as described in the previous sections, and subsequently deposited active material. Here, the structural class of cyclophanes will be the focus. In this type of material, an electron donor and an acceptor are kept together by covalent bond, as illustrated in Figure 3.23. The idea of these interfaces is to enforce wave-function overlap between the organic molecules, with the hope to trigger charge-transfer even in systems which are normally chemically inactive with respect to each other.

The results shown in this section have also been reported in the same wording to the ICONTROL consortium in the deliverables D22 (generation I), D23 (generation II) and D24 (generation III). Only computational results are shown, since most of the molecules turned out not to be synthesizable, and those which were did not yield interesting and thus properly analyzed experimental results.

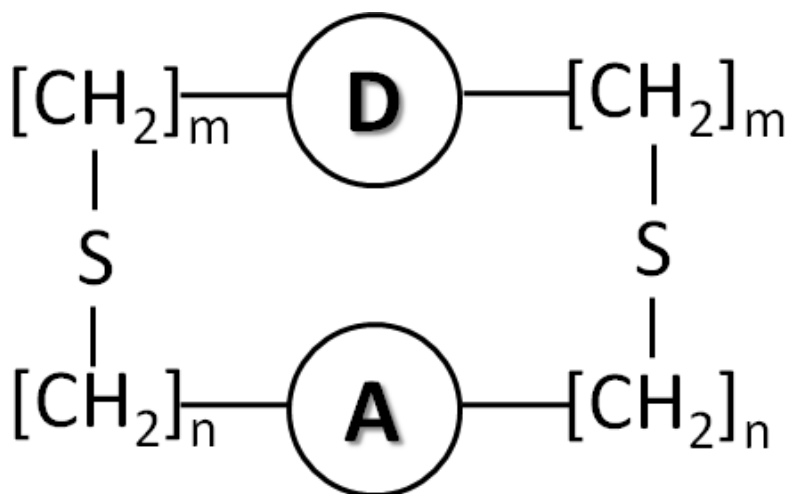


Figure 3.23: Schematic representation of cyclophanes.

3.7.2 Computational Methodology

Since cyclophanes are somewhat outside the standard type of interfaces investigated, the methodology has been slightly adjusted. All gas phase calculations were performed using the Gaussian03 package^[71]. Density functional theory (DFT) was chosen as adequate level of theory, since it is known to perform well for ionization potentials (IP) and electron affinities (EA), when using the finite energy differences of neutral and charges species as described in section 2.2. B3LYP was chosen as exchange-correlation func-

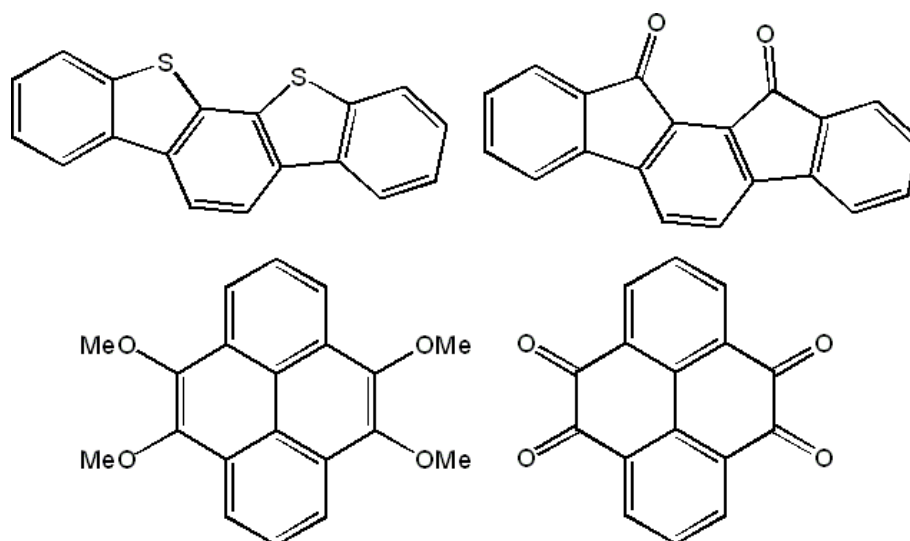


Figure 3.24: Candidates for electron donor and electron acceptor pairs for cyclophane synthesis

tional. The basis set employed was 6-31G(d,p). Vertical ionization potential denotes that the geometry of the radical cation (anion) was kept fixed at the geometry of the neutral molecule. No symmetry constraints were used to prevent any bias of results. The use of diffuse basis set functions was deemed unnecessary here, as the charge transfer is judged from VASP calculations, which uses a plane wave basis set. VASP calculations have been shown to accurately predict eventual charge transfer, as demonstrated in previous sections. Calculations of the monolayer were performed using the VASP program^[51–53], which allows for a 3D periodic repetition of a unit cell. In order to simulate different packing regimes, the size of the unit cell was altered between $10 \times 10 \text{ \AA}$ and $25 \times 25 \text{ \AA}$. 25 k-points were sampled for the smallest unit cell using a Monkhorst-Pack grid together with a Methfessel occupation scheme (broadened by 0.2 eV). Appropriately less k-points were used for the smaller systems. For the VASP calculations, the GGA functional PW91 was employed, along with a plane wave basis set with a cutoff energy of 20 Ryd. The test calculations shown in section 2.3.5 demonstrate that DFT has sufficient predictive power to tackle the problem at hand.

3.7.3 First Generation Cyclophanes

Cyclophanes of the type shown in Figure 3.23 represent an interesting class of molecules. Being composed of an electron rich and an electron poor molecule, they are supposed to exhibit both low ionization potential and (high) electron affinity. Both entities are, however, not conjugated throughout the linkage, and are therefore expected to work more like mixed organic layers. As a first step, the properties of isolated cyclophanes are characterized focusing on various physical observables (like optical spectra) that would facilitate their characterization after synthesis. The donor and acceptor pairs for the first generation are shown in Figure 3.24

To obtain better conceptual understanding, we started with the Donor/Acceptor

combination shown in Figure 3.24. Different linkage length ($n=m=1$; $n=1$ and $m=2$, denoted as 1a and 1b, respectively) were used to improve understanding of distance dependence and flexibility. Larger chains were not systematically investigated, as the number of possible conformers soon exceeds practical limits.

Isolated D1 and A1 entities

Before the characterization of the cyclophanes is presented, a short overview over the isolated donor / acceptor properties will be given. The donor molecule of combination 1, 11,12-Dithia-indeno[2,1-a]fluorene, is a planar molecule of C_{2v} point group symmetry with a vertical ionization potential of 7.16 eV. This is mediocre when compared to other molecules investigated before, but good enough for conceptual studies. (For comparison, with the same method, the vertical ionization potential of pentacene is 5.95 eV). It has also the advantage of being stable in air. The dipole moment is calculated to be 1.58 Debye, and, as is to be expected for a planar molecule, lies completely in y direction (i.e., the direction of the short molecular axis). Upon relaxation of the cation, the ionization potential drops by 0.06 eV to 7.10 eV. As can be expected by such a small difference, no significant structural changes take place.

The theoretical optical spectrum up to 5.0 eV (≈ 248 nm) contains three singlet bands of significant intensity (i.e, only excitations with oscillator strength $f > 0.1$ were selected). They can be attributed to the $S_0 \rightarrow S_2$ transition at 4.09 eV (303 nm) with an oscillator strength f of 0.52, $S_0 \rightarrow S_6$ at 4.82 eV (257 nm) with $f = 0.19$ and $S_0 \rightarrow S_9$ with an excitation energy of 5.01 eV (247 nm) and an oscillator strength of 0.65, respectively. The first visible excitation, which is of relative intense nature, is governed by $HOMO - 1 \rightarrow LUMO$ (CI-coefficient 0.62), $HOMO \rightarrow LUMO + 1$ (CI: 0.17), $HOMO - 2 \rightarrow LUMO$ (CI: 0.14) and $HOMO \rightarrow LUMO + 4$ (CI: -0.13) contributions. The optical gap ($S_0 \rightarrow S_1$) of the donor molecule is computed to be 3.80 eV wide. It is mainly associated with a $HOMO \rightarrow LUMO$ transition, which is optically forbidden due to symmetry reasons.

The corresponding acceptor, indeno[2,1-a]fluorene-11,12-dione, also belongs to the C_{2v} symmetry group Exhibiting a vertical electron affinity of -1.11 eV and an adiabatic electron affinity of -1.26 eV, it also has to be considered as average when compared to other examples (the vertical electron affinity of the “state-of-the-art” acceptor F4TCNQ is -3.67 eV within the same method.) It has, however, the advantage of using the same backbone as its donor counterpart. Its dipole moment is computed to be 5.71 Debye, thus being a very polar molecule. Similar to the donor counterpart, the dipole moment is located along the short molecular axis. In the energy range up to 5.0 eV (≈ 248 nm), four bands are found: The $S_0 \rightarrow S_4$ transition at 3.19 eV (389 nm), $S_0 \rightarrow S_8$ at 4.06 eV (305 nm), a more intense band at 4.58 eV (271 nm) corresponding to $S_0 \rightarrow S_{13}$ and another one at 4.81 eV (258 nm) corresponding to $S_0 \rightarrow S_{16}$. Their oscillator strength f is 0.13, 0.23, 0.42 and 0.70, respectively. The optical band gap is 2.64 eV wide, with a computed f of 0.0000, it is, like for Dibenzo[d,d']benzo[1,2-b;5,4-b']dithiophene, *de facto* forbidden. Interestingly, this transition does not correspond to the $HOMO \rightarrow LUMO$ transition,

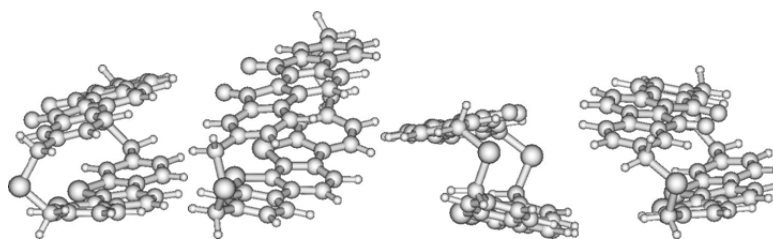


Figure 3.25: Optimized ground state geometry of the four conformers of 1a

but rather to a combination of $HOMO - 1 \rightarrow LUMO$ and $HOMO - 3 \rightarrow LUMO + 1$. The $HOMO \rightarrow LUMO$ excitation, which is $S_0 \rightarrow S_2$, possesses an energy of 2.73eV (455 nm), and is also optically forbidden. Again, the lack of transition dipole moment can be attributed to the identical symmetry of the involved orbitals. Hence, not only will it be undetectable in transient absorption experiments, but also no quantum yields for luminescence experiments can be expected. This behavior is reminiscent of the ketonic defect states in polyfluorenes (see publications by List et al. and Zojer et al.)

D1 and A1 as part of the cyclophane

Several conformations are possible for combining these molecules to a cyclophane. On one hand, when put on top of each other, their dipole moment can point in the same direction (*par*), or in the opposite (*anti*). Also, the C-S-C angle of the linkage can be orientated the same way (*cis*) or vice versa (*trans*). All four possible combinations were created as start geometry and allowed to relax fully. Their relative energies, IPs, EAs and dipole moments are listed in the 3.2 below and the resulting conformations are shown in Fig. 3.25.

In this context it has to be mentioned that the reported dipole moments largely correspond to the mere addition of the dipole moments of the individual components; i.e., no significant charge transfer is observed as is also evidenced by an analysis of the Mulliken charges: The maximum change of atomic charge of 0.02 times the elementary charge is observed for the S atoms of D1. Otherwise changes in atomic charges are typically nearly an order of magnitude smaller.

In order to provide data for an eventual experimental characterization, and to get a hint about the amount to which the two π -systems are coupled, the optical spectrum up to 4.00 eV (i.e., first 40 vertical transitions) was calculated and compared to the isolated donor/acceptor entities. The vertical excitation energies along with their os-

Table 3.2: relative energy ΔE (including zero-point energy correction), vertical and adiabatic ionization potential IP / electron affinity EA and Dipole moment μ of compound 1

Dipole orientation	C-S-C orientation	ΔE (kJ/mol)	vertical IP (eV)	adiabatic IP (eV)	vertical EA (eV)	vertical EA (eV)	$ \mu $ (Debye)
Par	Cis	3.73	6.69	6.61	-1.14	-1.30	8.99
Par	Trans	0.00	6.70	6.62	-1.15	-1.31	7.04
Anti	Cis	6.16	6.73	6.60	-1.20	-1.36	5.92
Anti	Trans	3.67	6.67	6.57	-1.13	-1.31	3.26

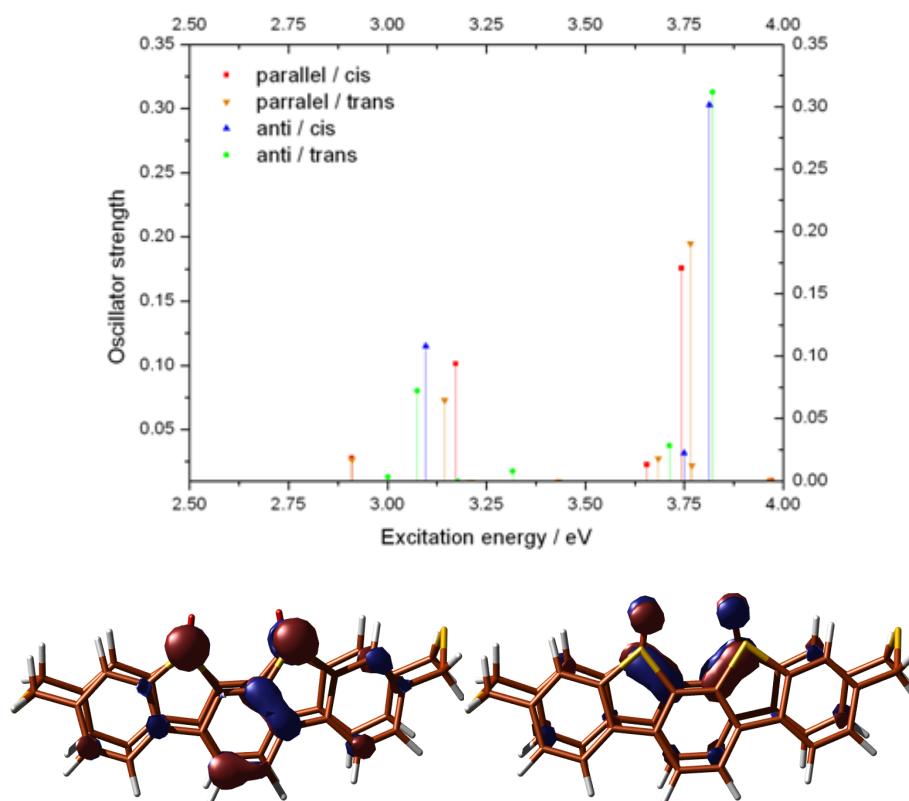


Figure 3.26: Top: Vertical excitations of all four 1a-conformers. Bottom: HOMO (left) and LUMO (right) of Cyclophane 1a

oscillator strength are provided in Fig. 3.26. It is no surprise that all four spectra are very similar. The band gap, equivalent to the $S_0 \rightarrow S_1$ transition lies around 2.6 eV and is (almost) forbidden, which points to the fact that hardly luminescence will be observable. The low transition dipole in this case arises from spatial separation of the frontier molecular orbitals; it does not come as surprise that the HOMO of the cyclophane is almost exclusively localized on the donor, while the LUMO can be found on the acceptor part of the cyclophane (cf. Fig. 3.26). However, a closer look at the orbitals from HOMO-10 up to LUMO+10 (see extended report) reveals that localization on donor or acceptor is not observed for every orbital. Hence, we can expect to find three types of excitations with significant oscillator strength: Those that arise from (and end in) orbitals localized on the donor, those that arise from orbitals localized on the acceptor, and finally, those that originate from a mixed orbital.

The only excitations (up to the 40th vertical transition, i.e. up to ≈ 4.0 eV) that supposedly will be seen in transient absorption experiments are the $S_0 \rightarrow S_9$ and the $S_0 \rightarrow S_{17}$ (parallel) / $S_0 \rightarrow S_{18}$ (anti) transitions. The former has similar intensity in all cases and lays around 3.12 eV. Since the energetic position is equal within 0.1 eV, it will be difficult, if not impossible, to tell those peaks apart in experimental room temperature spectra. The latter optical transition is located around 3.78 eV and also

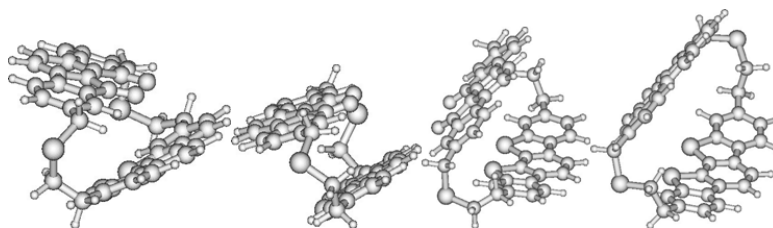


Figure 3.27: Optimized ground state geometry of the four conformers of 1b

differs by less than 0.1 eV. However, the oscillator strength is significantly lower for parallel alignment of the dipole. It should be noted that these excitations are neither in position nor in strength equivalent to those found for the isolated entities. Especially the stronger one utilizes some low lying orbitals, which actually contain contribution at both molecules simultaneously.

Upon increasing linkage length, the cyclophane experiences much more freedom to escape the repulsing π -system overlap. Consequently, in **1b**, the “scissor”-like structure mentioned for **1a** is extremely pronounced for molecules which are forced on top of each other, see Fig. 3.27. The molecules which, due to appropriate conformation of the linker, are allowed to separate each other in y-direction are also less bent. As the data collected in Table 3.3 show, the energy differences in this molecule are bigger than in **1a**. The most stable conformers (of those investigated) are those which have C-S-C bonds in trans-“trans”, thus allowing for the separation mentioned above. Again, the orientation of the molecular dipoles seems to have no significant input on the relative stability, as the respective “par” and “anti” combinations are degenerate within the accuracy of the method. It is interesting to notice that ionization potentials and electron affinities, both vertical and adiabatic, are more volatile than for the homologue with the shorter linker. The optical excitation, again, are very similar for all four conformers, exhibiting only minor differences.

Isolated D2 and A2 entities

As in the section above, before the cyclophane itself is discussed, a short overview of the corresponding donor and acceptor will be presented. The electron rich molecule, 4,5,9,10-tetramethoxyppyrene, exists in various conformations which differ only by the position of the methoxy groups. They are, however, practically degenerate in energy, and do not significantly differ in their electronic structure. Moreover, they can more or less freely convert into each other. Therefore, it was assumed that conformational

Table 3.3: relative energy ΔE (including zero-point energy correction), vertical and adiabatic ionization potential IP / electron affinity EA and Dipole moment μ of compound 1

Dipole orientation	C-S-C orientation	ΔE (kJ/mol)	vertical IP (eV)	adiabatic IP (eV)	vertical EA (eV)	vertical EA (eV)	$ \mu $ (Debye)
Par	Cis	19.13	6.71	6.63	-1.20	-1.40	9.29
Par	Trans	3.68	6.72	6.61	-1.30	-1.51	7.71
Anti	Cis	19.83	6.63	6.48	-1.13	-1.36	2.81
Anti	Trans	0.00	6.65	6.55	-1.14	-1.35	3.45

differences in this case do not really matter, and all calculations were performed with the geometry presented below, i.e., with two methyl groups pointing up and two methyl groups pointing down. Thus, the molecule is quasi symmetric with respect to inversion, belonging to the point group C_i . Due to the four methoxy groups, the vertical ionization potential of pyrene drops from 6.94 eV to 6.52 eV. Upon relaxation of the charged species, an adiabatic ionization potential of 6.35 eV is reached. As a result of the quasi-symmetric structure, the net dipole moment of the molecule is zero.

The UV-Vis spectrum of this compound shows two bands with significant oscillator strength (i.e., $f > 0.1$) below 5.0 eV. The lower energetic one is the $S_0 \rightarrow S_1$ transition at 3.57 eV (347 nm) with an oscillator strength of 0.24. The transition is dominated by $HOMO \rightarrow LUMO$ in combination with $HOMO - 1 \rightarrow LUMO + 1$. The respective (td-dft derived) CI-coefficients are 0.61 and -0.23. Due to this non-vanishing overlap between the frontier orbitals, which is attributed to the change of symmetry from the HOMO (symmetric with respect to inversion) to the LUMO (antisymmetric with respect to inversion), this substance is likely to exhibit noticeable quantum yields in fluorescence experiments. The other visible transition is associated with the transition into the S_5 state. Its energy is calculated to be 4.49 eV (275 nm), with an oscillator strength of 0.36. Dominant contributions are $HOMO - 1 \rightarrow LUMO$ (0.51), $HOMO \rightarrow LUMO + 1$ (-0.35), $HOMO - 2 \rightarrow LUMO + 3$ (0.14), and $HOMO - 5 \rightarrow LUMO + 2$ (0.10).

The corresponding acceptor, Pyrene-4,5,9,10-tetraone, is derived from the same backbone. Unlike its donor counterpart, it is not only really symmetric with respect to inversion, but also possesses 3 C_2 symmetry axes, thus being a member of the D_{2d} point group. Equipped with four keto groups aimed at depriving the backbone of its electrons, the vertical electron affinity changes from 0.09 eV for pyrene to -1.97 eV. Relaxation of the charged molecule yields an adiabatic EA of -2.11 eV. Due to its high symmetry, Pyrene-4,5,9,10-tetraone is a non-dipolar molecule.

The UV-VIS spectrum of this compound exhibits no strong bands up to 5.0 eV. Indeed, there are only four excitations with nonzero oscillator strength: $S_0 \rightarrow S_5$, $S_0 \rightarrow S_{10}$, $S_0 \rightarrow S_{11}$, and $S_0 \rightarrow S_{18}$. The first one possesses a transition energy of 3.06 eV (405 nm) at an oscillator strength of 0.06 eV. It corresponds to $HOMO - 2 \rightarrow LUMO$ with a (dft-derived) CI-coefficient of 0.06. The excitation to the S_{10} state happens at an energy of 3.89 eV (319 nm) and exhibits an f of 0.10, thus being the strongest transition in the investigated interval. The involved dominant contributions are $HOMO - 4 \rightarrow LUMO$ (CI = 0.62), $HOMO - 2 \rightarrow LUMO + 2$ (CI = 0.27) and $HOMO - 7 \rightarrow LUMO + 1$ (CI = 0.14). Relatively close in energy to the former excitation lies the transition to S_{11} , which exhibits an energy of 3.94 eV (314 nm). Also the oscillator strength is similar, f being 0.09. The orbitals participating are identified to be $HOMO - 3 \rightarrow LUMO + 1$ (CI = 0.65) and $HOMO - 2 \rightarrow LUMO + 2$ (CI = -0.12). Due to the similar excitation energy and transition dipole to $S_0 \rightarrow S_{10}$, it can be expected that in absorption experiments at ambient conditions, only one peak as superposition of these two will be found.

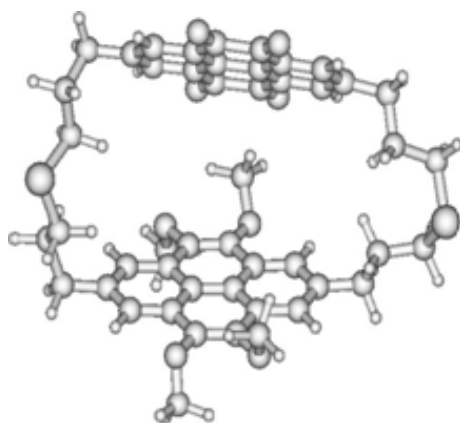


Figure 3.28: Optimized ground state geometry of Cyclophane 2 chosen for actual computations

D2 and A2 as part of the cyclophane

Due to the large size of the linkage between donor and acceptor molecule, a large number of possible conformers exist. (As first estimate, there are two possibilities (i.e., directions) for every atom in the linker not directly linked to one of the basis molecules, for every atom of each linker. That gives conformers, minus a few that are geometrically impossible, as they end are too far away to allow the closure of the ring. At best (last atom is determined by the choices before, second linker is completely determined by the choices of the first one, still 16 unique geometries survive). Obviously, that ends up with far too many choices to compute at DFT level. (Yet, simulated annealing was tried to get reasonable input geometries for all possible conformers, but did not yield results). Since the investigation for 1 revealed that the position of the linker does not significantly influence the electronic properties of the cyclophane (and since it is likely that anyway the chains are flexible enough at room temperature that all conformers can interchange into each other), just one conformer was more or less randomly chosen.

Upon vertical removal of one electron, the total energy of the system changes by 6.37 eV, which, surprisingly, is slightly better than for the isolated donor molecule (for which vertical IP was 6.52eV, *vide supra*). Relaxation of the radical cation leads to an adiabatic IP of 6.12 eV. The vertical electron affinity was computed to be -2.07 eV, the adiabatic -2.26 eV. These values are also slightly better than the ones of the isolated molecule.

The dipole moment of the optimized ground state geometry was computed to be 2.48 Debye. To get a conception to what extent the dipole is based on the donor/acceptor molecules, the linker was removed while the positions of the molecules were kept fixed in space. The result of 0.53 D indicates that most of the permanent dipole moment measured for any real substance will originate in the position of the linkage atoms, especially the sulfur atoms. This indicates that there is no significant net long-range charge transfer.

Due to the localization of the HOMO at the donor part and the LUMO at the accep-

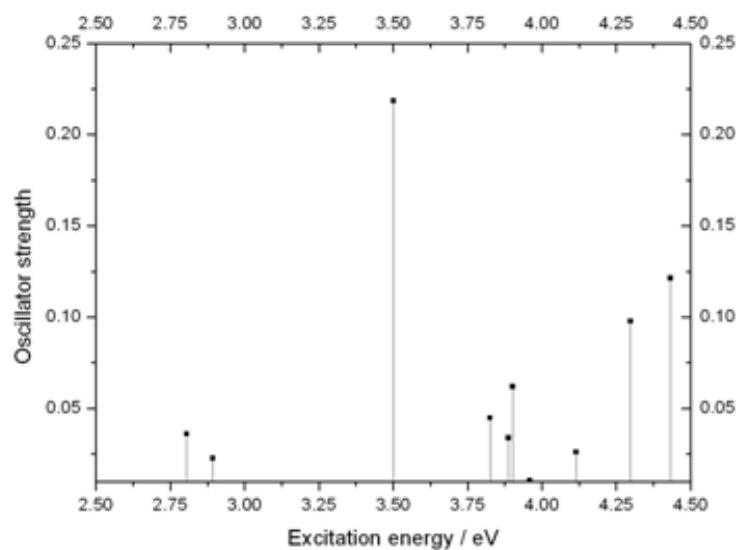


Figure 3.29: Optimized ground state geometry of Cyclophane 2 chosen for actual computations

tor part, the S_0/S_1 transition is optically forbidden. The calculated band gap is very low, exhibiting transition energy of only 1.13 eV. A calculated line spectrum of the cyclophane based on its vertical transitions up to 4.50 eV (i.e., the first 60 excitations) is shown in Fig. 3.29. Note that the scale chosen for the oscillator strength (y-axis) is so low that in fact, only two excitations fulfill the (arbitrary) requirement of $f > 0.1$. The first one, being more intense with an oscillator strength of 0.22 and an excitation energy of 3.50 eV (354 nm) is based on transitions $HOMO \rightarrow LUMO + 3$ (CI-coefficient 0.59), $HOMO \rightarrow LUMO + 4$ (0.14) and $HOMO - 1 \rightarrow LUMO + 5$ (CI: 0.17). The second one is located at 4.43 eV (279 nm), showing an oscillator strength of 0.12. The involved orbitals are $HOMO - 4 \rightarrow LUMO + 3$ (CI: 0.59) and $HOMO \rightarrow LUMO + 5$ (CI: 0.24).

Properties of a D2/A2 pair as a function of the inter-molecular distance

Considering the lack of pronounced charge transfer in all investigated types of cyclophanes, we have performed a more systematic calculation in which we placed the two molecules in a cofacial conformation and systematically increased the inter-molecular distance. In order to ensure that the above trends are not a consequence of the used basis set, we have included diffuse functions for the present study (6-31+G*), as here the computational demands are not as high. The resulting dipole moment of the dimer as well as the relative energy are shown in Fig. 3.30. The latter shows that there is NO pronounced energy minimum - i.e., there is no chemically bound charge transfer complex. Also for the dimer one can see that already at a distance of 3.5 Å the total dipole moment is by less than 1.5D higher than at 6 Å. At that distance, which roughly corresponds to the inter-molecular distance in compound **2**, a clear saturation of the evolution of the dipole moment is visible, which indicates that the total dipole moment

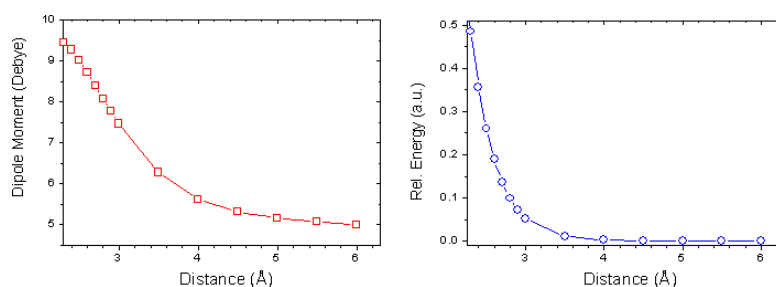


Figure 3.30: Optimized ground state geometry of Cyclophane 2 chosen for actual computations

corresponds to the sum of that of the individual chromophores (the main origin of that dipole moment at that distance are the methoxy groups in D2, which have been oriented in a parallel fashion to allow for small inter-molecular distances)

3.7.4 Second Generation Cyclophanes

The aim of this subsection is to computationally characterize the cyclophane shown in Figure 3.31 as an isolated entity as well as a monolayer film. The molecules have been suggested by the partners from MPI-Mainz in the course of the month 18 meeting of the ICONTROL-project).

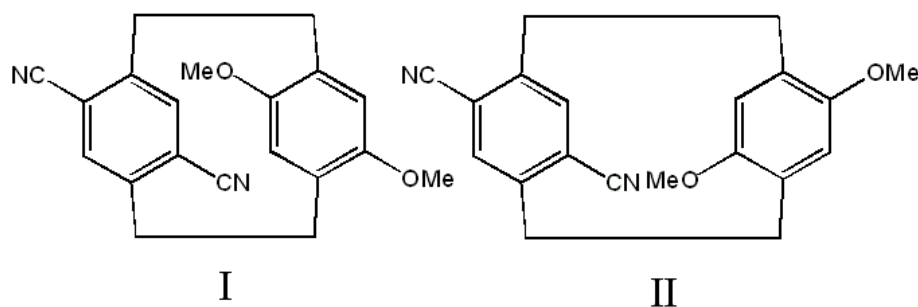
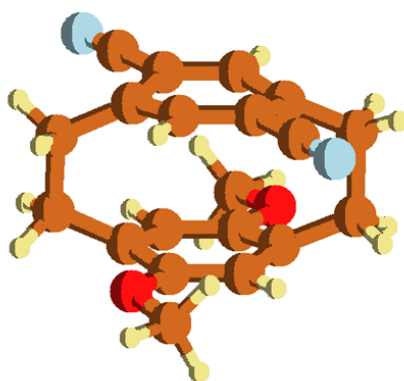


Figure 3.31: Chemical structure of the investigated cyclophane; two possible isomers are shown.

Gasphase calculations

For the Cyclophane depicted in Figure 3.31, two different conformers are conceivable. In one conformer (**I**) the side groups of the phenyl rings would be located on top of each other, while in the alternative conformer (**II**), the side groups can be found on the opposite sides of each other. Energetically, **I** is found to be energetically higher than **II** by ca. 0.09 eV (8.6 kJ/mol), i.e. less than 3.5kT. This energetic difference can be attributed to mutual steric hindrance of the donor/acceptor side groups. Hereafter, this report will only refer to the energetically lower lying conformer **II**, since this will

Figure 3.32: Equilibrium structure of cyclophane conformer **II**

be most likely the predominant conformer after synthesis.

In Figure 3.32, the equilibrium geometry of the cyclophane is shown. Both phenyl rings remain almost flat, with small deviations from planarity. Larger deviations from planarity are observed for the carbon atoms where the bridge is attached, indicating a perturbation of the aromaticity of both components.

The vertical ionization potential and electron affinity were computed to be 7.10 eV and -0.63 eV, respectively. Therefore, the cyclophane shows a similar low ionization potential as the individual donor part (6.94 eV) and a similar electron affinity to the acceptor part (-0.49 eV)^{IX}. Also, the highest occupied molecular orbital (HOMO) of the cyclophane is fully localized at the donor part, while the lowest unoccupied molecular orbital (LUMO) is localized at the acceptor part of the molecule. From the Mulliken charges, only a minor charge transfer can be inferred; in the cyclophane, the net charge of the donor part is 0.05e, while the charge of the acceptor part is -0.07 e. (The missing 0.02e are found at the bridging carbon atoms).

Monolayer calculations

In order to estimate the applicability of these cyclophane as charge injection layer, hypothetical monolayers at different densities were computed. It was assumed that in these layers, all molecules assemble with the dipole point in the same direction. (In the reverse case, the net dipole would be zero, resulting in no effect at all). The unit cells featured had all a quadratic base, ranging from 10x10Å to 25x25Å in steps of 5 Å, as shown in Figure 3.33. In the third dimension, the unit cell was chosen to be 40Å large, preventing any interactions between the individual layers. As consequence of the small amount of charge transferred, the intra molecular dipole is quite small. In the least densely packed layer, it is computed to be $0.30e^{-1}$ (1.44 Debye). This is significantly

^{IX}Note that ionization potential and electron affinity between cyclophane and individual components are only comparable if one assumes that the basis set superposition error affects the neutral molecule and the charged species equally and hence cancels.

less than dipoles obtained for substituted biphenyles, which are usually at least one order of magnitude larger. The dipole here, however, seems to be almost unaffected by depolarization effects. Only in the smallest unit cell, with the individual cyclophanes being spaced apart only by a few Å, a noticeable depolarization is observed. In Fig. 3.34, the evolution of the dipole and its accompanying shift in the work function are depicted. It is shown there that despite the depolarization induced reduction of the total dipole, the work function is modified stronger the more densely the layer is packed, due to the $1/A$ dependence in the Helmholtz equation.

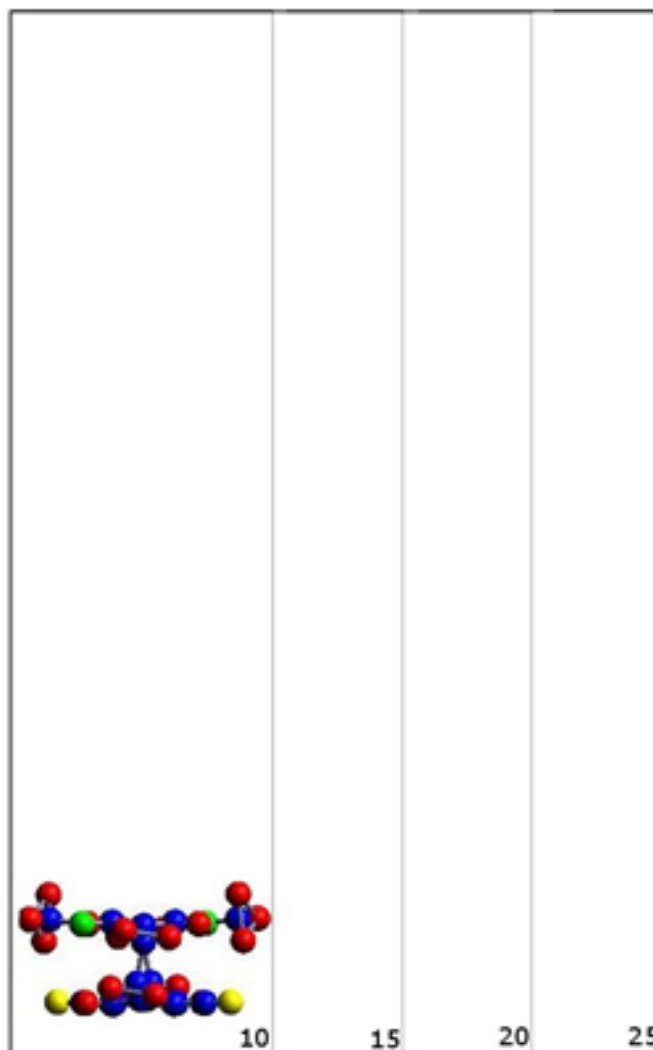


Figure 3.33: Unit cells used for the simulation of cyclophane monolayers. Numbers are given in Å. The blue ball correspond to carbon atoms, the red ones to hydrogen. The green atoms depict oxygen, while the yellow balls are nitrogen atoms.

Within the methodology used, no significant charge transfer between the donor and

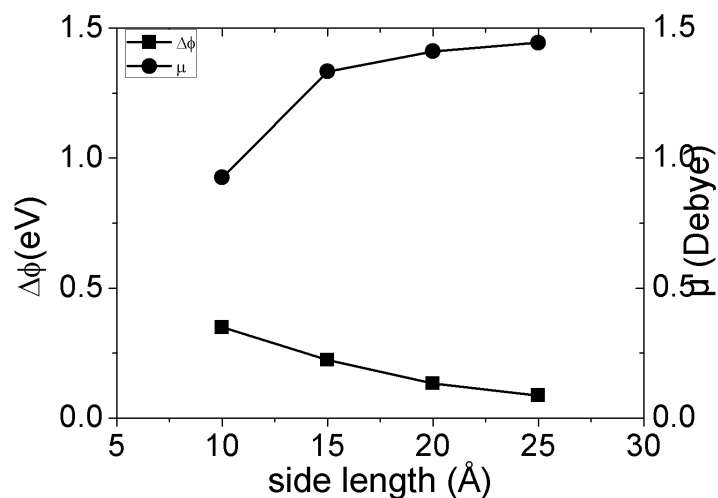


Figure 3.34: Evolution of dipole and work function modification as function of the unit cell size.

the acceptor part of the cyclophane was found. It should be critically remarked here that DFT is known to fail in some cases for charge transfer; however, charge transfer between metal and adsorbate was found to be well described within this project. Therefore, it is likely that the individual components are too weak donors respectively acceptors to effectively form a strong charge transfer complex. Consequently, its application as monolayer on metals or at organic/organic heterojunctions in order to modify charge injection barriers seems questionable. No significant depolarization was found upon the calculation of ever more densely packed monolayers.

3.7.5 Third Generation Cyclophanes: Cyclophane substitutes

Since the synthesis of actual cyclophanes as originally suggested in the IControl-proposal turned out to be more challenging expected, the molecule 4NB, shown in Figure 3.35 was chosen as similar substitute. This molecule consists of an electron poor cyanophenyl-group as acceptor part and an electron rich trimethoxyphenyl-group as donating moiety. Both functionalities are connected via ethynyl bonds (which act as spacer to allow for a more planar structure) to the naphthalene backbone.

To obtain the geometry of this molecule, a full optimization in gas phase at the B3LYP / 6-31G(d,p) level was performed. The result is shown in Figure 3.35. While the acceptor part is located approximately in the plane of the backbone, the donor group deviates significantly from it. This skewed geometry is obviously a result of the steric repulsion between the two phenyl-rings and the effort to maintain maximal π -overlap with the backbone. Since donor- and acceptor-group avoid each other in this geometry, there is hardly if any orbital overlap between them. Therefore, no direct charge transfer between these two is possible, unless mediated by the π -system of the backbone. Consequently, only a moderate dipole moment of 6.41 Debye is found. Naturally, this dipole is

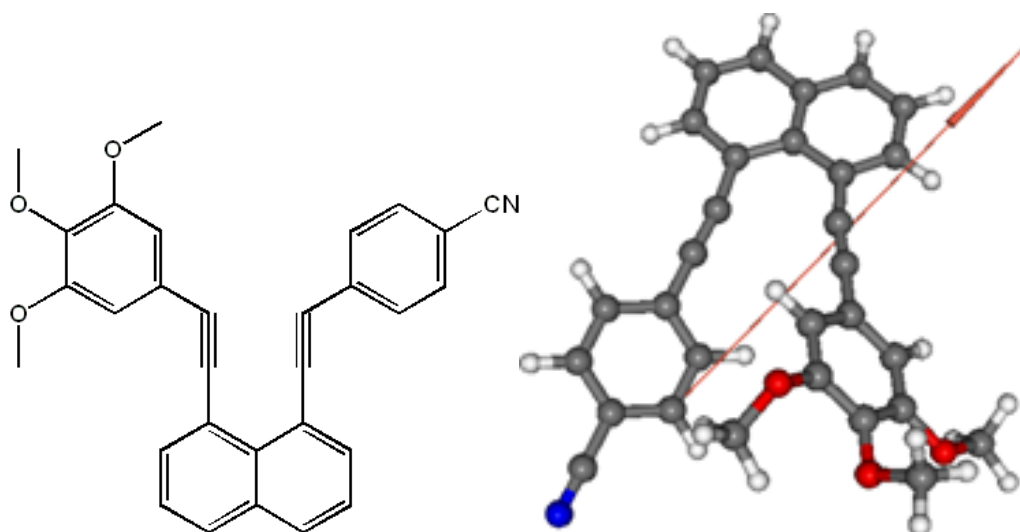


Figure 3.35: Left: Structure formula of 4NB. Right: Optimized geometry of 4NB

a superposition of an “intrinsic” part due to the non-planar structure and the “extrinsic” charge transfer. To approximately quantify the amount of charge transfer occurring between cyanophenyl and trimethoxyphenyl, their respective atomic charges have been summed up. This quantity is inherently arbitrary (as it is no observable). Therefore, we chose to use the RESP charge partition scheme, which creates the charges according to the dipole moment of the molecule (which itself is the important quantity for future work-function modifications and shown as red arrow in Figure 3.35). The donor part of the molecule is predicted to be almost neutral, while a negative charge of 0.25 electrons is found on the backbone and the corresponding negative charge on the acceptor. From gas phase, single-reference DFT calculations, it can thus be concluded that no intramolecular charge transfer takes place. To verify these results, charges and dipole moment has been recalculated using the complete active space approach, including 4 electrons and 4 orbitals. No significant deviations to the DFT results are found. At the DFT level, the cyclophane substitute exhibits a quite a low vertical ionization potential (6.69 eV), which is comparable to the IControl-candidate donor HMT (6.66 eV). Since for the latter molecule, no work-function modification beyond pushback was found experimentally (compare deliverable D22), it is unlikely that 4NB will donate electrons into the metal. Likewise, the electron affinity was found to be -0.90 eV, which is presumably too low to allow for a spontaneous charge transfer. Therefore, no additional surface dipole on the metal-molecule interface is to be expected beyond the ever-existing Pauli pushback. The work function modification induced by the cyclophane substitute is, like for all molecules with permanent dipole moment, very dependent on the morphology. In case the molecule lies face on with the backbone (or the donor/ acceptor-part for that matter) on the surface, the projection onto the surface normal would be very small and hence almost no active work-function modification will occur. Only if the molecule would adsorb edge on, it would work almost like a typical SAM, and create comparable work-function modifications.

3.8 Three component interfaces

3.8.1 Preface

In this section, the adsorption of strong electron donors and acceptors on surfaces which are pre-modified with an organic layer will be discussed. In this context it is studied how the net work function for these three-component systems differs from the direction adsorption of the individual components on the pristine surface. To elaborate the role of the sandwiched organic part, special focus is laid on the charge rearrangements and induced changes in the density of states.

The results shown here were also presented in a more contracted way, but a similar wording, to the consortium of the ICONTROL project in deliverable D24. The data also serve as foundation for proposal to the DFG (Deutsche Forschungsgemeinschaft) that is currently being written. Calculations have been performed by myself; interpretation of the results has been done in multiple discussions with Egbert Zojer and Ferdinand Rissner.

3.8.2 HV0 and F4TCNQ on Au(111)

The strongest donor and acceptor that have been studied in our group so far are HV0 and F4TCNQ, respectively. Their tendency to undergo charge transfer reactions with coinage metal surfaces has been discussed in section 3.1 for HV0 and in various papers^[24, 124] for F4TCNQ. Also, their potential to form charge-transfer complexes has been demonstrated in section 2.3.5, where also the ability for DFT to describe these complexes qualitatively correct has been confirmed. In this section, the effect of adsorbing HV0 on F4TCNQ pre-covered Au, and vice versa, of F4TCNQ on HV0 pre-covered gold, is studied.

Different possible conformations of the HV0/F4TCNQ compound were discussed in section 2.3.5. On the surface, only the conformation with parallel alignment and 3.0Å separation between the individual molecules on Au(111) was investigated. The adsorption height was set to 3Å above the top metal layer. The intermolecular distance is to the left of the dipole minimum found for both DFT and CAS (cf. section 2.3.5, and is therefore in the region where we believe that DFT - and the partial charge transfer it imposes - correctly captures the important physics. To allow for comparison with earlier calculations, the complex was put in the default $5 \times 3\sqrt{3}$ unit cell. This corresponds to a very loosely packed monolayer. No optimization of the structure has been performed, since the lack of the important van-der-Waals forces renders within the employed framework of semilocal DFT this task futile. The complex can be adsorbed on the surface in two possible ways, either with the donor side down or with the acceptor side down.

For the monolayer of the F4TCNQ-HV0 complex, the dipole moment in this unit cell - using the PW91 functional - is found to be 2.07 eÅ (9.92 Debye). Dividing this quantity by the intermolecular distance (3Å), a charge transfer of 0.69 electrons from the donor to the acceptor is inferred, which is slightly below the value found in gas phase (see also section 2.3.5. Because the monolayer is quite loosely packed, it is not

perfectly clear whether this reduction is due to the periodic nature of the monolayer, i.e. depolarization, or simply an artifact owing to the different methodology (especially the employed functional). When the donor side faces the metal surface, the permanent dipole moment of the complex points downwards (i.e., towards the metal), thus imposing a positive shift in the vacuum level by virtue of the Helmholtz equation. In this setup, the value amounts to +1.65 eV. Vice versa, for the acceptor side being closer to the surface, a work function reduction by the same amount is induced. Before the actual results on the surface are presented, it should first be discussed what one might expect. Actually, two different viewpoints could be adapted.

(i) In the first scenario, one could consider the deposition of both molecules (i.e., the charge-transfer complex) together. In the complex, both components have already reacted with each other, and their chemical potential has equalized. It therefore is neither a particularly good electron donor nor electron acceptor. In this scenario, the expected work function modification after deposition on the surface would be governed by the permanent dipole moment of the charge-transfer complex, minus some tenths of an eV owing to Pauli pushback.

(ii) Alternatively, the complex could be deposited sequentially on the surface (as is most likely would have to be done in a real experiment). In this case, the second layer effectively faces a surface with an already modified work-function. For example, when HV0 is put on an Au surface first, a vacuum level shift of about -1.22 eV is induced (cf. section 3.1). Subsequently deposited F4TCNQ would, therefore, experience an effective work function somewhat lower than that of Ag(111), and one would therefore expect it to induce a dipole which increases the electron potential again by ≈ 1 eV. In other words, the effects of both monolayers to some extent cancel each other, and only a small net work-function modification would be observed.

In the next paragraphs, both points of views will be considered. Starting with the “joint deposition” system, in the case when the HV0-side of the complex faces the Au(111) surface (which will be referred to as “HV0 down” from here on), the permanent dipole moment induces an increase of the vacuum level. Upon contact with the surface, however, DFT calculations predict that the work-function changes from 5.22eV to 5.61eV, i.e. the work-function modification is +0.39eV only. This corresponds to an unexpectedly large bond dipole of -1.26eV. Complementary, if F4TCNQ is located near the surface (“F4TCNQ down”), a work function decrease of -1.65eV is created by the permanent dipole moment, which is supposed to be augmented by Pauli pushback. On adsorption, the work function decreases from 5.22eV to 3.49eV, i.e. by -1.73eV. In this case, the bond dipole almost vanishes (amounting only to -0.07 eV). The situation is thus qualitatively different from the first situation.

Interestingly, the net work-function modification for both systems surpasses the effect of the single component on the surface, regardless whether it is calculated at a hypothetical distance of 3Å or fully optimized. Rather, the charge-transfer salt shows results reminiscent of only the top molecule at about 6Å distance to the surface. In both cases, it appears as if the work-function modification of the molecule which is not

in direct contact with the surface outweighs its counterpart. Indeed, if only the net effect is considered, one could believe that the electronic contribution of the middle part of the three-component system metal-donor-acceptor can almost be disregarded. Table 3.5 lists the values for the single components adsorbed at different distances, as well as for the combined charge transfer complex on the Au surface.

One could arrive at the conclusion that the sandwiched layer works mainly as a spacer molecule enforcing a larger metal-molecule distance, which apparently improves the total work-function modification as shown Table 3.5. In order to learn more about the mechanism governing the work-function change, the left part of Figure 3.36 shows a 3-dimensional representation of the charge rearrangements for the case of HV0 down. Note that the flow of electrons here has been calculated with respect to the combined complex (i.e., viewpoint ii), not with respect to sequential deposition. The strong acceptor F4TCNQ only participates negligibly in the electron rearrangements. Only the molecule in direct contact with the surface, HV0, donates significant charge to the metal surface, thus giving rise to a large bond dipole. By integration of the plane-averaged electron rearrangements, a total charge transfer from the surface to the complex of 0.52 electrons is obtained. It can therefore be concluded that the first impression, namely that the molecule at the interface only acts as spacer component, is definitely not correct.

In the F4TCNQ down situation, shown in the right part of Figure 3.36, almost no electron rearrangements are observed, which is consistent with the vanishing bond dipole (the work-function modification is identical to the dipole moment of the charge-transfer complex). This lack of interaction is actually quite surprising. Not only does F4TCNQ not accept any charge - in sharp contrast to the situation of isolated F4TCNQ on Au(111), where a charge transfer of 0.35 electrons is found^[124] - but also no sign of pushback is observed. Since the pushback decays rapidly with distance, it typically affects the region below and above the molecule differently. Filling the LUMO of F4TCNQ would be expected to be almost symmetric with respect to the molecular plane (with little asymmetry induced because of the bond dipole). Therefore, if both effects were superimposed, one would still expect to see some charge rearrangement near the molecular plane. Obviously, this naive conception is wrong - since Pauli pushback is existent in every system, it can only be concluded that the filling of the LUMO almost exactly cancels this effect.

To get a more quantitative conception about the processes occurring on the surface,

Table 3.4: Net work-function modification ($\Delta\Phi$) induced for F4TCNQ, HV0, and the combined HV0/F4TCNQ complex in the geometries HV0 down and F4TCNQ down at the optimized geometry (opt), and at 3Å and 6Å distance to the Au(111) surface

$\Delta\Phi$	Opt	3Å	6Å
F4TCNQ	0.33eV	0.25eV	0.52eV
HV0	-1.22eV	-1.06eV	-1.63eV
HV0 down		+0.39eV	
F4TCQ down		-1.73eV	

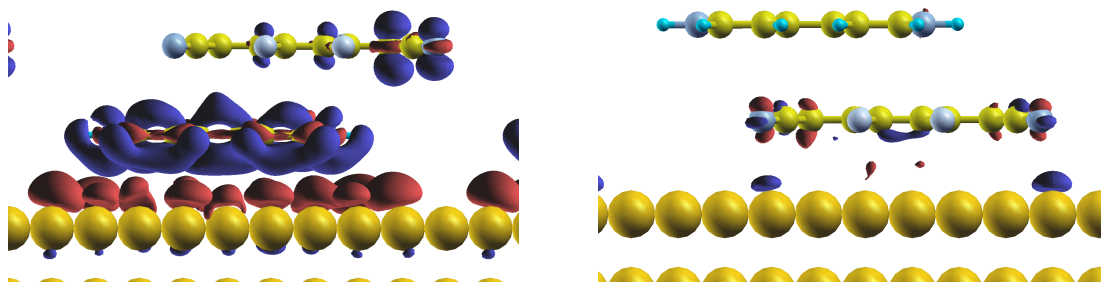


Figure 3.36: Charge density rearrangements of the F4TCNQ-HV0 complex on Au(111), with HV0 (left), and with F4TCNQ directly facing the surface. Red areas correspond to increased electron density, while blue areas are reminiscent of electron density reductions. The rearrangements are calculated with respect to sequential deposition.

Figure 3.37 shows the plane-averaged charge rearrangements for the case of HV0 down and F4TCNQ down. In the first case, even though the charge transfer to F4TCNQ includes much less electrons than to HV0, we find that the bond dipole monotonically decreases over the whole monolayer. This is not true in the F4TCNQ down case, where the evolution of the bond dipole shows negative values between the surface and F4TCNQ, which is to ca. 30% compensated in the region between F4TCNQ and HV0. (Note, however, that on the same scale as HV0 down, the bond dipole for F4TCNQ would rather look like a straight line). Also shown in Figure 3.37 are the charge rearrangements upon adsorption. In the HV0 down scenario, the prototypical case for charge rearrangements in donor/acceptor-type molecules investigated in this thesis is observed, as the flow of electrons typically takes place directly above and below the molecular plane, but not (or only to a very small extent) within it. For both molecules, a distinct asymmetry in the peaks with respect to the σ -plane can be observed. This commonly observed feature is often attributed to Pauli-pushback, because (a) the polarizability of conjugated molecules perpendicular to their molecular plane is typically very low and (b) such an asymmetries are also present for pushback only systems, e.g. benzene on Au(111). If this was the reason, no discernible asymmetry should have been observed for F4TCNQ here, since 6\AA above the surface, there is almost no electron density from the metal that can be “pushed back”. Yet such asymmetry exists even in more extreme cases. Even in the hypothetical case of HV0 located 10\AA above the surface, a significant difference between electron donation below and above the molecular plane can be found. It must therefore be concluded that this kind of feature is indeed rather a manifestation of the evolution of the electron potential energy (i.e., the bond dipole). Interestingly, no such asymmetric behavior is found in the F4TCNQ down conformation. Indeed, the charge rearrangements here are very untypical, as the sigma-plane of F4TCNQ is located at an electron donation peak, and another reduction of electron density is observed between metal and charge transfer complex. HV0, on the other side, is apparently completely unaffected by the adsorption in this geometry.

The whole charge-rearrangement picture looks different if sequential deposition is as-

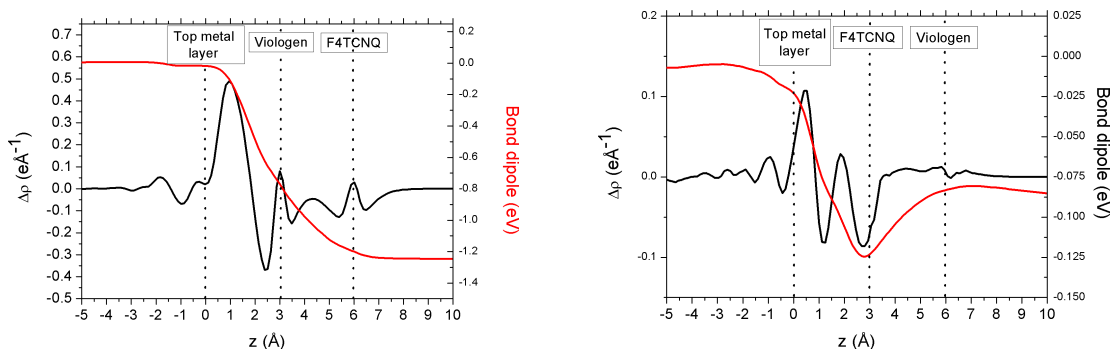


Figure 3.37: Plane-averaged charge rearrangements (black) and bond dipole (red) for HV0-F4TCNQ on Au(111), in HV0 down conformation (left) and F4TCNQ down geometry (right).

sumed. The 3-dimensional charge rearrangements as well as the plane-averaged results for both orientations are shown in Figure 3.38. Of course, the net work function remains the same, since it is only dependent on the dipole of the combined system. The 3D representation of the charge rearrangements show that upon deposition on HV0-precovered gold, F4TCNQ does not only accept electron density from the HV0 interlayer, but also from the metal surface, as evidenced by the lobes above each Au atom. This observation is corroborated by the plane integrated results (shown in the bottom of Fig 3.38), which show the typical distinct loss of electron density $\approx 1.6\text{\AA}$ above the metal surface. Vice versa, for HV0 on F4TCNQ-precovered Au, donation into both subsystems is observed. This is in interesting contrast to earlier findings by F. Rissner et al.^[43], who calculated a biphenyl layer on top of SAM covered Au surfaces. For these systems, it was found that the charge rearrangements are only short-ranged and only affect the SAM, leaving the gold almost unaffected. The implications are discussed in a later paragraph, where HV0 on was computed on top of a SAM.

In Figure 3.39, the density of states of the complex as free-standing monolayer without metal, as well as on the surface, is depicted. As consequence of the orbital overlap, the HOMO of HV0 and the LUMO of F4TCNQ have formed a bonding and an antibonding combination with equal contributions from both components. Both states are located right around the Fermi edge, the former being below and the latter above it, with almost no energy gap between them. Hence, only the bonding combination is occupied. Naturally, upon adsorption the extended nature of the bond dipole affects the molecular levels of F4TCNQ and HV0 differently. On the surface, the symmetric nature of the frontier orbitals is perturbed. In the HV0 down scenario, the bond dipole shifts both HV0 and F4TCNQ levels to lower energy, but F4TCNQ, being at the outer rim of the system, more so. Consequently, the levels are polarized in a way that the bonding combination is more strongly located on F4TCNQ. As no states are created or annihilated in this process, the energetically less favorable antibonding combination consequently is localized more on HV0. The alignment of the states with respect to the Fermi level of the system indicates that the charge-transfer salt as a whole loses charge.

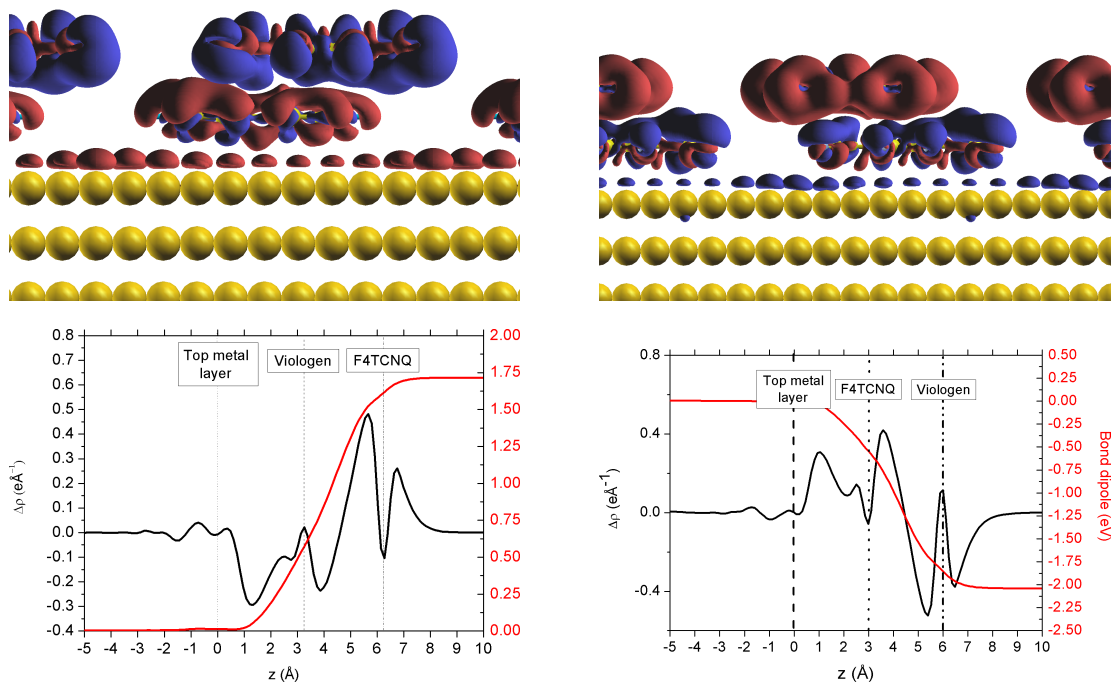


Figure 3.38: Top: 3-dimensional charge density rearrangements of the F4TCNQ-HV0 complex on Au(111), with HV0 directly facing the surface (left) and F4TCNQ facing the surface (right). Red areas correspond to increased electron density, while blue areas are reminiscent of electron density reductions. Bottom: Plane-integrated charge rearrangements and bond dipole

In the case of F4TCNQ down, virtually the same situation is observed for the frontier orbitals, despite the lack of a significant bond dipole. Rather, the change in electron potential energy here is induced directly by the permanent dipole of the charge-transfer salt. The only difference to the HV0 down situation is found for the relative alignment to the Fermi level of the system, which indicates here that the monolayer accepts charge (although very little), thus weakening the bond between the F4TCNQ and HV0.

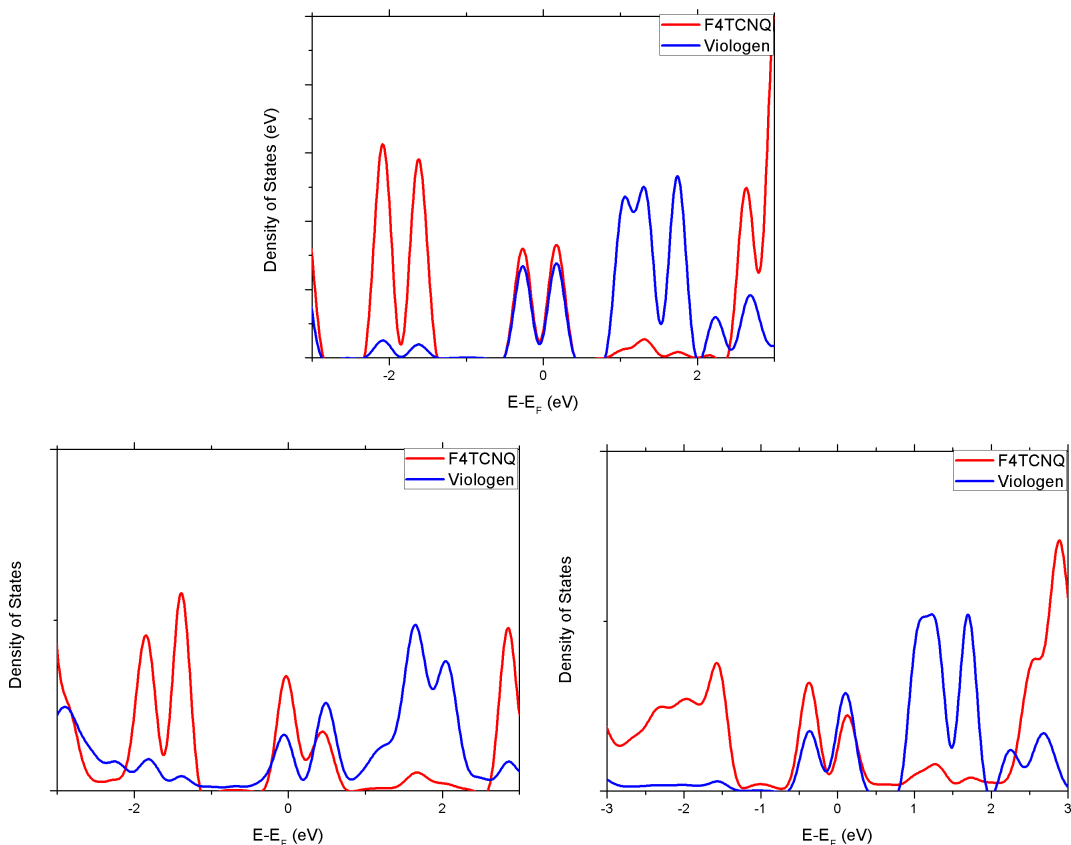


Figure 3.39: Density of States of the free-standing HV0-F4TCNQ complex (top) and of the molecule adsorbed on the surface in the HV0-down (left) and F4TCNQ down (right) geometry E_F refers to the Fermi energy of the respective system.

3.8.3 F4TCNQ-HV0 on Ag (111)

To find out which of the features described above are inherent of metal/donor/acceptor interfaces and which are artifacts stemming from the gold substrate, which is a more donor-friendly material due to its high work function, the same calculations have also been performed on Ag(111), which, by virtue of its lower work function, is more prone to undergo reactions with electron acceptor materials.

The unit cell used for the calculation is of the same size as for the Au case. Hence, also the same vacuum level change from the monolayer is obtained, i.e. ± 1.65 eV, depending on the orientation. On the surface, a net work-function modification of -1.16 eV is obtained for the case where F4TCNQ faces the surface (F4TCNQ down), corresponding to a positive bond dipole of 0.49 eV (compared of ≈ -0.1 eV on Au). In the HV0 down situation, the predicted work function modification is only 0.96 eV, owing to negative bond dipole of -0.69 eV (-1.7 eV on Au). In both cases, the bond dipole becomes more positive, since HV0 reacts less with the surface, but F4TCNQ more. Table 3.5 summarizes the work-function modification for the single components as well as the

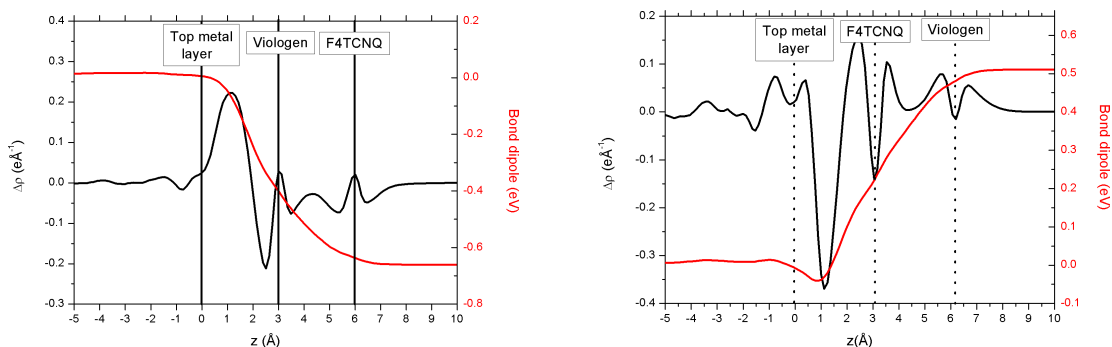


Figure 3.40: Plane integrated charge rearrangements (black) and bond dipole (red) for HV0-F4TCNQ on Ag(111), in HV0 down conformation (left) and F4TCNQ down geometry (right).

charge-transfer salt in both possible conformations.

Similar to the situation on Au(111), the obtained work-function modification is quite similar to the situation where the molecule in contact with the surface would not be present. Still, as shown in Figure 3.40 it is the molecule in direct contact which takes the workload of the charge transfer occurring on adsorption. Unlike the situation on Au(111), however, on Ag(111) clear and significant electron rearrangements occur in both conformations. The direction of the charge transfer is always determined by the molecule in direct contact. I.e., in the HV0 down conformation, both molecules donate charge to the metal, while in the F4TCNQ down conformations, increased electron density is observed on both molecules.

3.8.4 HV0 on a Self-Assembled Monolayer

In the two previous paragraphs it was shown that upon sequential deposition, the second monolayer undergoes charge transfer with both the intermediate layer and the metal substrate. This is in apparent contradiction to earlier results of organic/organic interfaces. F. Rissner calculated a biphenyl layer on top of several different self-assembled monolayers (SAM)^[43]. Regardless of the composition and the electronic structure of the

Table 3.5: Net work-function modification ($\Delta\Phi$) induced for F4TCNQ, HV0, and the combined HV0/F4TCNQ complex in the geometries HV0 down and F4TCNQ down at the optimized geometry (opt), and at 3Å and 6Å distance to the Ag(111) surface

$\Delta\Phi$	Opt	3Å	6Å
F4TCNQ	+0.51eV	+0.67eV	+1.08eV
HV0	-0.82eV	0.65eV	-1.08eV
HV0 down		+0.96eV	
F4TCQ down		-1.16eV	

SAM, it was found that only the organic interlayer participates in the charge transfer, while the electron density of the metal is left almost unchanged. To test whether there is a fundamental difference between the adsorption of the rather inert organic molecule biphenyl and strong donors / acceptors, HV0 was calculated on top of SAM consisting of 4'-fluorobiphenyl-4-thiol adsorbed on Au(111). This SAM was chosen because, by itself, it only influences the Au work-function marginally (by +28 meV). The metal Fermi energy lies between its HOMO and LUMO, and hence it cannot assume metallic behavior after adsorption (in contrast to strong charge-transfer monolayers, which always form partially occupied bands). Unfortunately, the $5 \times 3\sqrt{3}$ unit cell in which the calculations for F4TCNQ/HV0 have been performed is incommensurable with the SAM. Therefore, all calculations were performed in a $3 \times 3\sqrt{3}$ unit cell. HV0 was assumed to adsorb 3Å above the fluorine atom and kept at its gas phase structure. Due to the lack of van-der-Waals interaction in the methodology, no optimization was performed.

On adsorption of the donor, the work-function of SAM-pre-covered Au(111) is changed to 3.32 eV, i.e. almost halfway between the work-functions of Mg (3.66 eV) and Ca (2.87 eV). With respect to the pristine Au(111), the work-function decreases by -1.9 eV, exceeding the work-function modification of fully optimized HV0 (i.e., at $\approx 3.5\text{Å}$ adsorption distance) in the same unit cell by 0.3 eV ($\approx 20\%$).

In the top part of Figure 3.41, a 3-dimensional representation of the charge rearrangements upon adsorption of HV0 on the SAM-modified Au surface is given. Obviously, HV0 undergoes a strong charge transfer. In analogy to the results of biphenyl on the same SAM, the electrons are not donated to the metal, but to the SAM. This is particularly noteworthy insofar as the charge transfer, obtained by integration over the electron rearrangements, is relatively large, 0.36 electrons. A closer inspection of the SAM shows that the electron density increase appears to be similar for all molecules of the organic layer, and not localized to those in close proximity to the HV0 molecule. Therefore, every molecule of the otherwise not particular electron poor SAM accepts about 0.06 electrons. The bottom part of the Figure shows the plane-integrated charge rearrangements. Also here it can be seen that the metal virtually does not participate in charge transfer with HV0. Rather, most of the electron density transferred from HV0 is accepted roughly 0.5Å above the fluorine atom as well as ca. 1.3Å and 5.1Å below it. The latter positions belong to the 1 and the 4'-position of 4'-fluorobiphenyl-4-thiol, respectively. Thus, virtually the same situation as in the calculations of F. Rissner is observed. This still leaves the question why HV0 on a SAM behaves so differently than HV0 on top of an electron acceptor.

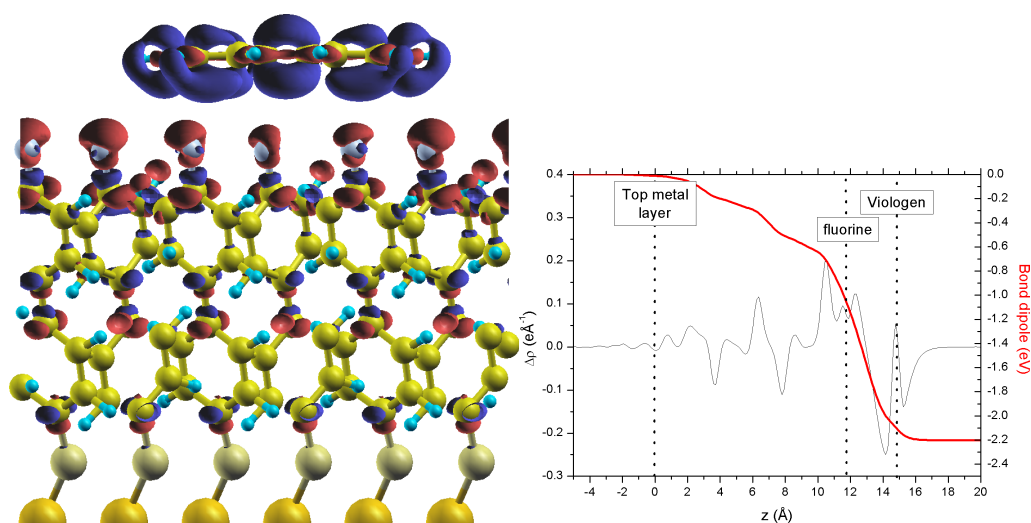


Figure 3.41: Charge density rearrangements of HV0 on a SAM-modified Au(111) surface. Red areas correspond to increased electron density, while blue areas are reminiscent of electron density reductions. An isocontour value of $0.005 \text{ e}\text{\AA}^{-3}$ was used.

3.8.5 Conclusion

The results of HV0 on a SAM and HV0 on top of F4TCNQ indicates that regardless of the mechanism of charge transfer (which is dependent on the viewpoint anyway), the evolution of the potential is always such that the frontier orbital of the outmost molecule is pinned at the Fermi energy. This can be achieved by either by significant charge transfer or a correct alignment of the permanent dipole (as, e.g., in the case of F4TCNQ down on Au). Consequently, it appears that the electronic structure of the intermediate organic layer is of no importance to the total work-function modification; whether “soft metallic” charge transfer monolayer, SAM, or isolator, it probably does not matter. The only property of importance is the relative distance between the outer charge transfer monolayer and the metal. In this context it should be reminded that the distance dependence as calculated by DFT is probably not a very trustworthy quantity, since the distance-dependent polarization is neglected (compare 2.3.3).

4 Structure-to-Property Relationships

In the previous chapter, specific realistic systems were considered. From the differences and the similarities of these, general conclusions about structure-to-property relationships can be drawn. In this chapter, these conclusions will be explicitly formulated and tested on idealized systems. Thereby, idealized systems refer to metal/organic interfaces in which deliberate control is exerted over the details of the adsorption geometry, in particular, the bending, the adsorption distance, and the packing density. Most of the systems are unrealistic in a sense that they cannot be realized experimentally. Therefore, the conclusions drawn are obviously not directly verifiable in the real world. However, the distinct control over these details allows to easily single out the impact of specific influence factors. In the long run, understanding these factors will allow to devise advanced molecules which take advantage of found effects.

The build-up of this chapter is as follows: First, the impact of the adsorption distance will be monitored. Section 3.8 already gave strong hints that this quantity plays a decisive role for the achievable work-function modification. Here, the impact will be tested on three molecules: N,N'-dimethyl-[4,4']Bipyridinylidene (MV0), 2,3,5,6-tetrafluoro-7,7,8,8 tetracyanoquinodimethane (F4TCNQ), and coronene-1,2,5,6,9,10-hexaone (COHON). In the next section, the role of bending will be discussed. All charge-transfer molecules investigated in these thesis showed a pronounced downward bending of the peripheral groups, which in all cases induced a dipole moment mitigating the desired work-function change. It will be studied whether this effect is really critical for the total work-function modification, or if it is compensated by other means. Also, the impact of the spatial position of the molecular dipole moment will be looked at. Finally, the knowledge won by these computer experiments will be applied to a set of molecules, which are systematically modified to exploit these structure-to-property relationships. The intention of this section is to highlight the complex interplay between the individual effects occurring in metal/organic interfaces, as well as to demonstrate potential applicability of the found rules.

4.1 Impact of the adsorption distance

4.1.1 Preface

In this section, charge-transfer monolayers adsorbed at different distances to the metal will be investigated. Although in real world experiments, directly lifting up a molecule is not possible, there exist indirect ways to achieve this goal. It has been shown, for example, that using NaCl spacer layers has a significant impact on the position of the frontier orbitals^[225, 226]. It is also perceivable that cargo-lifer SAMs^[227] inserted between metal and charge-transfer monolayer are able to create at least two stable conformations with different adsorption distances. Before presenting the results, it should be reminded that these investigations are prone to some errors of DFT. As discussed in section 2.3.3, DFT overestimates charge-transfer in general. To make matters more complicated, the dissociation limit to open shell is also not correctly described. However, since this section deals with dissociation into closed shell subsystems, it is not sure whether this is also a problematic issue here. Another important effect not described by DFT is the screening of charge by long-range correlation of electrons in the metals^[35, 36], which has a profound impact on the electron addition and removal energies as a function of the adsorption distance. It should also be clear that all computations here are equilibrium calculations, predicting charge transfer even if the tunneling probability for electrons would be too low to be observed on laboratory timescales. Despite all these shortcomings, DFT performs well at reasonable distances, which is illustrated by the generally good agreement of theoretical and experimental results shown within this thesis. It is not clear, however, which range these reasonable distances encompass, and the results for large distances shown below should be viewed with appropriate caution.

Due to the discussed shortcomings, the results presented hereafter are not directly intended for publication, at least not until supporting calculations (at the GW or CAS level) directly verify them. Rather, they are thought of as a foundation for discussion, and to understand the general behavior of metal/organic interfaces when treated with density functional theory (DFT). All calculations have been performed by myself, and interpretation was done in multiple discussions with Egbert Zojer, Georg Heimel, Ferdinand Rissner, David Egger, Gerold Rangger, and Anna Track.

4.1.2 Results and Discussion

In section 3.8, it was stated that upon increasing the metal/molecule distance, the work-function modification can be enhanced. To find out why this is the case, a series of calculations of 1H,1'H-[4,4']bipyridinylidene (HV0) adsorbed on Au(111) have been performed where the adsorbate layer is systematically placed farther away from the surface. In order to obtain easily interpretable results, the molecule was assumed to be planar and bear no permanent dipole moment. In Figure 4.1, the evolution of the work function with respect to the metal/molecule distance is shown. It is clearly demonstrated that for this system, the induced work-function modification is almost doubled if the system separation is increased from 3 Å to 10 Å. Considering that the work-function reducing is already quite large at small distances, this relationship deserves further attention.

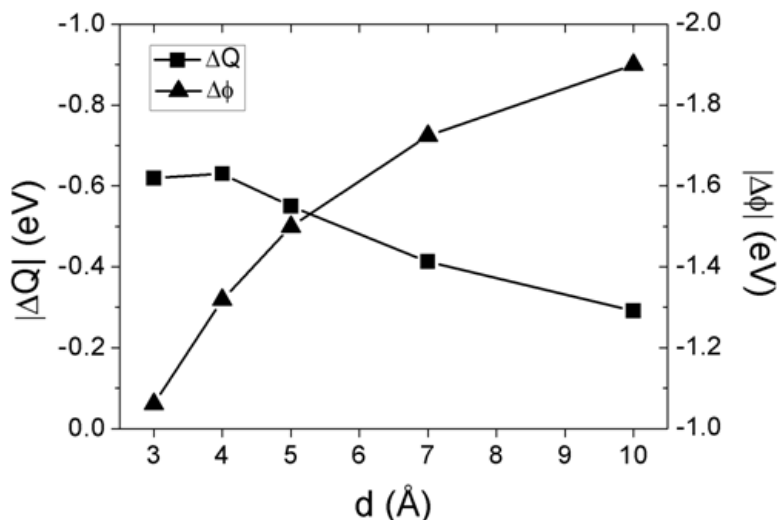


Figure 4.1: Transferred charge Q and work function modification $\Delta\Phi$ of HV0 on Au(111) at different metal-molecule distances, d .

To understand the reason for the strong dependence, it must be remembered that HV0 is in the Fermi-level pinning regime, i.e. in the combined system its highest occupied molecular orbital (HOMO) is located right at the Fermi-energy of the metal. Since the HOMO energy is related to the ionization potential (although, of course, strictly it must not be interpreted as such), the observation is equivalent to the statement that the ionisation potential (IP) is a function of the adsorption distance. In principle, a similar function is known: The ionization potential corresponds to the energy needed to remove one electron from the system, leaving a positive charge behind. In contrast to the free molecule in gas phase, near the metal the positive charge is screened by polarization of the metal electrons, thereby lowering the energy of this state and reducing the IP. The energy gain upon screening, P , depends on the distance^[36] as $1/d$. However, this means that the IP - and hence the work function - becomes smaller for molecules closer to the substrate, in contrast to the behavior shown in Figure 4.1. Also, as discussed above this mechanism is absent in normal DFT functionals^[35], which is fortunate insofar as it else would have masked the effect observed here.

An alternative, more plausible explanation would be a change in the so-called charging energy, U . This effect describes the tendency of any charged system to resist further charging, inter alia by virtue of coulomb repulsion. This effect has also been shown experimentally, e.g., for C_{60} on Ag^[39]. It manifests itself as lowering of the HOMO energy upon (partial) charging of an electron donor. Figure 4.1 also shows the evolution of the transferred charge, ΔQ , obtained by integration of the electron rearrangement as in the earlier sections. Obviously, ΔQ becomes smaller with the separation of metal and monolayer. This is not completely unexpected and can be rationalized by the following gedankenexperiment.

Assume that the pinned level, originally at energy ϵ is only infinitesimally broad and

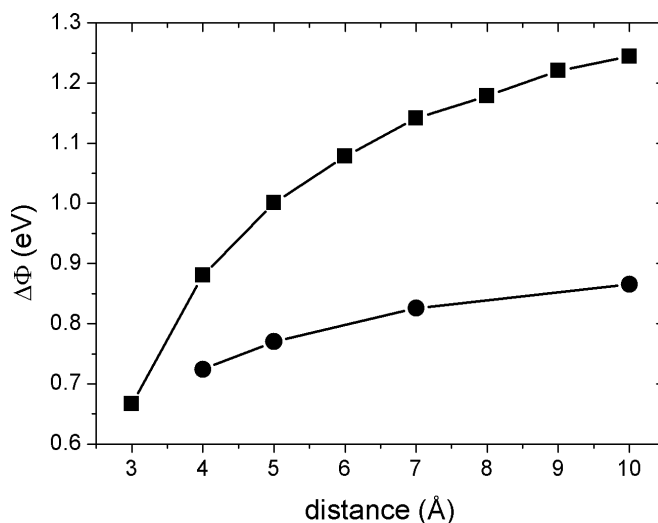


Figure 4.2: Work function modification $\Delta\Phi$ of F4TCNQ (boxes) and COHON (triangles) as function of the distance to the Ag(111) surface.

not subject to change in energy upon interaction with the substrate. Furthermore, the system should be in the Fermi-pinning regime. A necessary requirement in this case is that ϵ aligns with the Fermi energy of the metal, which is realized by a shift in the vacuum level between those levels according to the Helmholtz equation. In lieu of a permanent dipole, this shift must be realized by charge transfer. Under the constraints of this gedankenexperiment, the corresponding dipole must be *independent* of the adsorption distance. As a direct consequence, the transferred charge must decrease with increasing separation. Now, when the interaction with the substrate is “turned on”, the charging energy draws the HOMO energy to lower energies, closer to the Fermi energy. The dipole needed to bridge the energy between ϵ and the Fermi energy becomes smaller, and hence the charge transfer is mitigated. Since this directly depends on the amount of ΔQ , the mitigation is larger for smaller the adsorption distances. To put it differently, ΔQ decreases more slowly than the charge-transfer distance increases, resulting in an enhancement of the work-function modification at large separations.

To demonstrate that this effect applies to many Fermi-level pinned systems, Figure 4.2 shows the work-function modification to distance relationship for F4TCNQ and, on a less tight grid, COHON on Ag(111) in the same $5 \times 3\sqrt{3}$ unit cell; again, both molecules have been assumed to be planar. It is particularly interesting to notice that the amount of the work-function modification enhancement is different for both molecules, being much more pronounced on the smaller and more potent acceptor F4TCNQ. This can be explained by the charging energy being smaller on more extended systems, since the charge can be delocalized over a larger area.

The distance dependent evolution of the work function was also investigated by Romaner et al. for perylene-3,4,9,10-tetracarboxylic-3,4,9,10-dianhydride (PTCDA) on Ag(111), Cu(111), and Au(111)^[99]. Also there, a significant increase of the work-function modification was observed with increasing adsorption distance. However, it

appears that at least for Ag and Cu, the work-function modification reaches a saturation already at very small metal / monolayer separations of $\approx 3\text{\AA}$. Tentatively, this is attributed to the small electron affinity of PTCDA, which results in only very little transferred charge and consequently very small charging energies at all distances.

4.1.3 Conclusion

Since the screening induced (de)stabilization of HOMO and LUMO is absent in these calculations, it is not clear whether these results are directly applicable to charge-transfer layers being placed at more remote distances from the surface. In retrospect, the results presented here are more to be understood as impact of the charging energy rather than as impact of the adsorption distance. However, it is important to notice that in DFT, the charging energy is very sensitive to the separation of the subsystems. Therefore, this section underlines that the correct description of the adsorption distance is of crucial importance if the correct electronic structure is desired. The results also clearly show that the charging energy is an adverse effect to the work-function modification, and the design of improved molecules should aim to keep this as low as possible. This can be done, as shown above, by choosing larger molecules. Also control over the bend of the molecule might prove to be a suitable way to influence ΔQ , which will be elaborated in section 4.2. An indirect conclusion from these data here is also that more densely packed monolayers, in which the potential step between metal and molecule can be realized by a smaller dipole, will also be subject to less charging energy, and hence induce a larger work-function modification.

4.2 Impact of the molecular bend: When do Dipoles Really Count?

4.2.1 Preface

This section will be concerned with the effect of dipoles in charge-transfer monolayers adsorbed on coinage metal surfaces. Specifically, the impact of the spatial position of the dipoles will be investigated, directly relating to the downward bending found for most charge-transfer molecules investigated in the Specific Systems part of this thesis.

The results presented here are submitted to Nano Letters. The following section will be a reproduction of the manuscript. Geometry optimisation of the SAM shown in the last part of this section has been performed by David Egger. All other calculations were performed by myself. The results were interpreted and refined in multiple discussions with David Egger and Egbert Zojer.

Abstract

Deposition of monolayers of strong electron donors or acceptors on metal surfaces in many cases results in a metal-independent work function as a consequence of Fermi-level pinning. This raises the question, whether in such a situation molecular dipoles, which are also frequently used to tune the interface energetic, still can have any impact. We use density-functional theory to show that the spatial position of the dipoles is the determining factor and that only dipoles outside the immediate metal-molecule interface allow work-function changes beyond the pinning limit.

Introduction

In the field of organic electronics, controlling the work function, $\Delta\Phi$, of metal electrodes has been named as one of the most important tasks in order to improve device performance^[11]. This can, for example, be achieved by introducing of a dipolar layers at the interface^[10]. In this context, large work-function modifications have been demonstrated using covalently bonded self-assembled monolayers^[45, 134, 136–138, 140–142, 228–230]. An alternative and particular promising method to exert influence over Φ is the application of an organic monolayer consisting of molecules that are sufficiently strong electron donors or acceptors. In that case, significant interfacial charge transfer is observed and the Fermi-level gets pinned. While there is still a debate in the community about which level of the organic is actually responsible for the pinning (e.g., the charge neutrality level^[45], a (bi)polaron level^[231], or the HOMO / LUMO itself^[24]), it is commonly accepted that the alignment occurs due to the formation of an interface dipole layer, emerging from the (covalent or charge-transfer driven) bond between the metal and the monolayer. Experimentally it has been established that in the case of Fermi-level pinning the work function of the combined metal/monolayer system, Φ' , is independent of the Fermi level of the underlying metal (e.g., see Refs. ^[29, 44, 179, 193, 231–233]). At the same time, molecular geometries are known to become distorted in the adsorption process^[24, 37, 124, 132, 222, 234], thereby inducing additional molecular dipoles even in otherwise flat molecules. An instructive way for analyzing the total work-function

modification, $\Delta\Phi$, is then to decompose it according to the origin of the contributing dipoles^[22, 235]. I.e., $\Delta\Phi$ can be viewed as the superposition of (i) the part arising from molecular dipoles, ΔE_{mol} , and (ii) the part resulting from charge rearrangements induced by electronic interaction of molecule and metal, ΔE_{bond} :

$$\Delta\Phi = \Delta E_{mol} + \Delta E_{bond} \quad (4.1)$$

For self-assembled monolayers that are not in the Fermi-level pinning regime it could even be shown explicitly that ΔE_{mol} and ΔE_{bond} are independent of each other and can be varied separately^[143].

This gives rise to a seeming contradiction: How can the molecular dipole contribute to the work-function modification, if all that counts in the case of Fermi-level pinning^[38] was the energetic position of the molecular level at which pinning occurs? Solving this puzzle is also important from a practical point of view, as it relates to the question, whether one can use molecular dipoles to go beyond work-function modifications dictated by Fermi-level pinning. That the latter can indeed be a severe limitation for the achievable $\Delta\Phi$ has, for example, been shown recently for SAMs with dipole moments distributed along the molecular backbone^[236].

Therefore, we performed density functional theory (DFT) based band-structure calculations on carefully chosen test systems with strong charge transfer character, where molecular dipoles with different magnitude and at different spatial locations are introduced either via modification of the geometry or systematic chemical derivatization. Employing periodic boundary conditions in all three dimensions allows to employ the Helmholtz equation for the calculation of work-function modifications, as well as to take molecule-molecule interactions and depolarization effects into account. For these calculations the VASP^[51–53] code has been used and the results have been visualized using XCrysden^[161]. The employed methodology is well tested and has been successfully applied to reproduce experimental data^[24, 123, 124]. It is explained in more detail in the Supporting Information section, along with further details on the approach to calculate $\Delta\Phi$, ΔE_{mol} and ΔE_{bond} , as well as the employed unit cells and adsorbate structures.

4.2.2 Results and Discussion

A set of prototypical systems, where large contributions from ΔE_{mol} and ΔE_{bond} occur simultaneously are monolayers of the strong acceptor 2-(4-Dicyanomethylene-2,3,5,6-tetrafluoro-cyclohexa-2,5-dienylidene)-malononitrile F4TCNQ (see Figure 1a) on coinage metals^[24, 124]. F4TCNQ covered Cu(111), Ag(111), and Au(111) surfaces display virtually the same work functions determined by pinning^[124]. Ultraviolet photoelectron spectroscopy (UPS) and corroborating DFT calculations indicate a strong net charge transfer from the metal to the molecular monolayer giving rise to a substantial charge-transfer induced ΔE_{bond} ^[124]. Additionally, X-ray standing wave measurements on Cu(111) reveal that the cyano-groups at the periphery of the molecule are located 1.2Å closer to the surface than the central ring^[24]. DFT calculations show that the similar bending occurs on all coinage metals^[124]. These observations have been confirmed

for the related molecule TCNQ on Cu(100)^[237]. This bending down of the polar -CN groups causes a substantial value of ΔE_{mol} , which is of the same order of magnitude as ΔE_{bond} . Both have opposite sign and, consequently, partly cancel each other. Thus, in spite of the observed Fermi-level pinning, the actual work-function modification appears to arise from a subtle interplay between charge-transfer and bending-induced dipoles.

To analyze the actual influence of the molecular bend and hence ΔE_{mol} , DFT calculations for a densely packed monolayer (1 molecule per 115\AA^2) of F4TCNQ on Ag(111) in an experimentally motivated unit cell (see supporting information) were performed with the molecular backbone fixed to the optimized adsorption distance of 3.57\AA ^[124]. Then, the CN-groups were systematically flexed as shown in Figure 4.1b. This bending reflects a somewhat hypothetical situation, but, as will become clear below, serves as an excellent test-bed to explain the effects determining the interface energetic. The contributions of ΔE_{mol} and ΔE_{bond} to $\Delta\Phi$ were calculated and are shown in Figure 4.1c. For ΔE_{mol} , a linear dependence on the -CN out-of-plane bent is found with values ranging from -0.98 eV to +0.98 eV. The dotted line in Figure 4.1c represents the (hypothetical) situation of a constant ΔE_{mol} , i.e. the situation one would encounter if $\Delta\Phi$ was determined by ΔE_{mol} plus the value of ΔE_{bond} of the planar geometry. The calculated $\Delta\Phi$ (solid squares in Figure 4.1c), however, displays a markedly different evolution: When the cyano-groups are located between the backbone and the metal, i.e. the cyano groups are downward bent as in the actual adsorption geometry found in experiment, we observe only a very weak dependence of $\Delta\Phi$ on the position of the -CN groups. The evolution of ΔE_{bond} with the -CN bending largely compensates the change of ΔE_{mol} and the work-function of the F4TCNQ covered surface is determined by Fermi-level pinning (the fact that $\Delta\Phi$ does not remain absolutely constant will be explained below). In sharp contrast to the situation described above, upward bending of the -CN groups hardly affects ΔE_{bond} . Hence, the actual evolution of $\Delta\Phi$ closely matches the hypothetical situation described by the dotted line, and work-function modifications beyond the “pinning-limit” can be observed. This asymmetric dependence of $\Delta\Phi$ on the bending does not arise from interactions between the -CN groups and the Ag(111) surface, as it is also observed when F4TCNQ is located 10\AA above the metal surface and is also not limited to the F4TCNQ/Ag interface (see Supporting Information). At this point it should be emphasized that this is also not an artifact arising from molecule-molecule interaction or depolarization effect. One arrives at the same conclusions by performing the same calculations for a different packing motif (also shown in the Supporting Information).

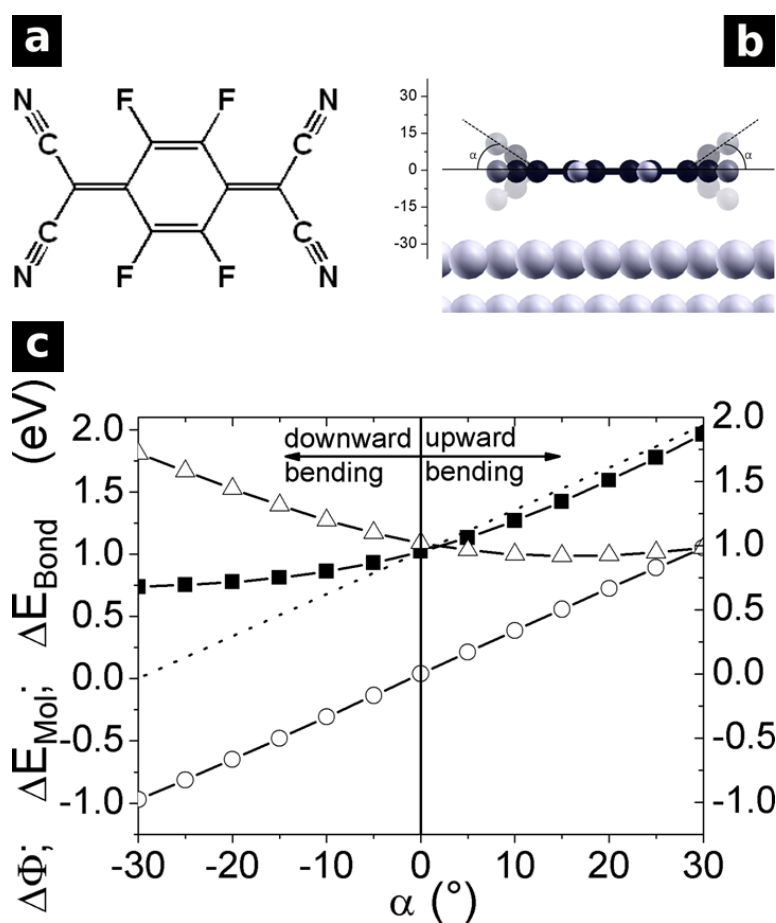


Figure 4.1: a) Chemical structure of 2-(4-Dicyanomethyl-2,3,5,6-tetrafluoro-cyclohexa-2,5-dienyl)-malononitrile (F4TCNQ) b) Structure of planar F4TCNQ on Ag(111) with the bending illustrated by the semi-transparent atoms, and the chemical structure of F4TCNQ. c) Evolution of $\Delta\Phi$ (closed boxes), ΔE_{Mol} (open circles), and ΔE_{Bond} (open triangles) as a function of the bending of the cyano-groups in F4TCNQ. The vertical solid line indicates the planar structure and the dotted line indicates the evolution of $\Delta\Phi$ in the hypothetical case of ΔE_{Bond} being unaffected by the bent (details see text)

The origin of this observation rather lies in the spatial location of the molecular dipoles (here the -CN groups) relative to the region in which the charge rearrangements between metal and molecule occur: Fermi-level pinning, by definition, requires the pinned molecular state at ϵ to align with the substrate's Fermi energy, E_F . This leads to a relative shift of the potential landscapes of the metal and the monolayer by an energy ΔE that equals the difference between ϵ and E_F (cf., Figure 4.2a). It can be achieved by charge rearrangements between the metal and the molecular layer giving rise to ΔE_{bond} . Introducing a dipole-layer between the metal and the adsorbate as schematically shown by the vacuum energy discontinuity in Figure 4.2b (highlighted by an arrow and, here, representing ΔE_{mol}) must not change the relative alignment between ϵ and E_F . I.e., ΔE needs to remain the same and the impact of the additional dipole layer has to be

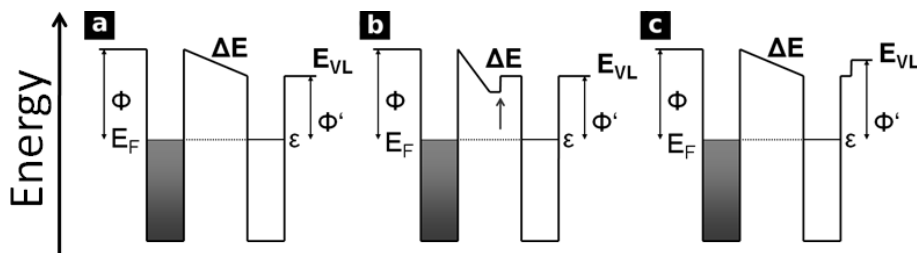


Figure 4.2: Schematic representation of the interface energetics in Fermi-level pinned metal monolayer interfaces. The left potential well represents the metal, the right well corresponds to the molecular monolayer. E_F denotes the Fermi energy, ϵ the energy of the pinned level, and E_{VL} the vacuum level. Φ and Φ' are the work-function of the pristine metal and the work-function of the joint system, respectively. ΔE is the potential drop required to align ϵ and E_F . In (a), the situation without any molecular dipole is shown; (b) depicts the interface energetic with a molecular dipole induced potential step (indicated by the arrow) between metal and molecule. In (c), the situation for the potential step being located above the metal/monolayer junction is shown.

compensated by a larger (or smaller) ΔE_{bond} . To a first approximation (vide infra), also sample work-function Φ' would not be affected by the additional dipole layer. If, however, the dipole layer was introduced above the region where the states responsible for pinning are localized (Figure 4.2c), this would not interfere with Fermi-level pinning and, thus, it would have no impact on the energetics in the region between the metal and the molecular layer. In this case, ΔE_{bond} would remain constant and the ΔE_{mol} would change the vacuum energy (E_{VL}) above the system. This results in a modified sample work function Φ' in spite of pinning. The situation outlined in Figures 4.2b (c) is strongly reminiscent of what is shown in Figure 4.1c for downward (upward) bending of the -CN groups. Indeed, when plotting the electron potential energy for a hypothetical free-standing F4TCNQ layer perpendicular to the long molecular axis (Figures 4.3a and b), or the plane averaged electron potential energy (Figure 4.3c), one sees that the vacuum energy changes only above that side of the layer towards which the -CN groups are bent.

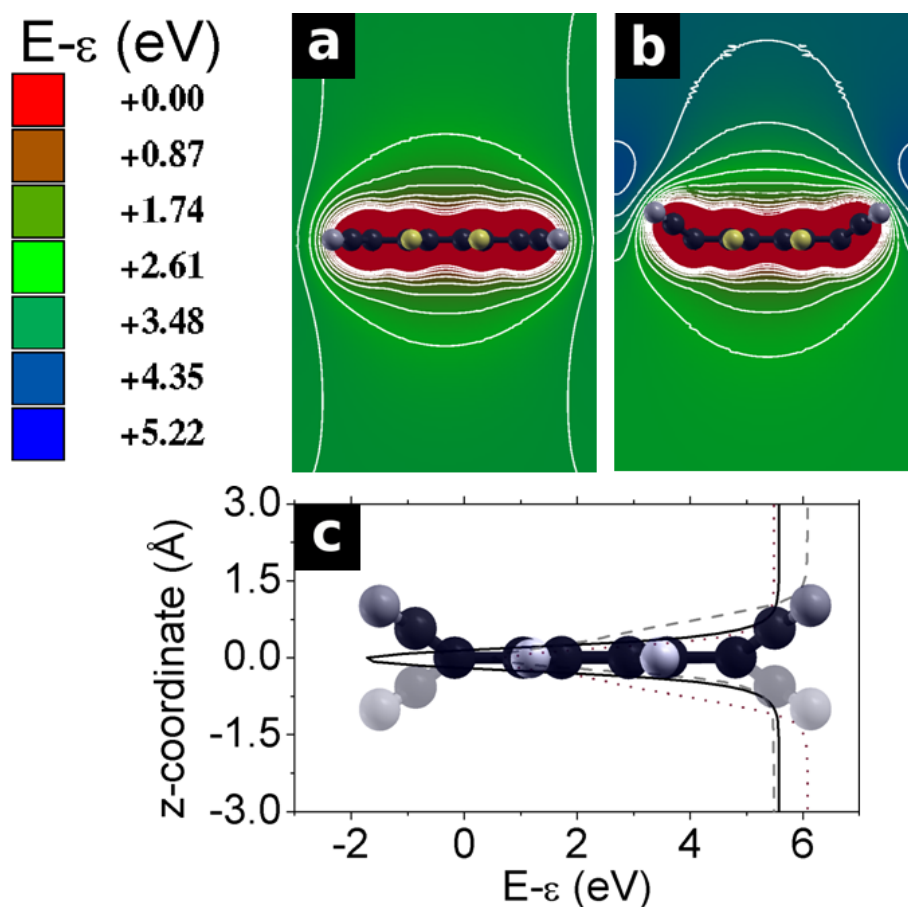


Figure 4.3: Electron potential energy (relative to $\epsilon = 0$) for a hypothetical free-standing F4TCNQ perpendicular to the long molecular axis for the planar (a) and the bent (b) geometry. White lines are isodensities representing a step of ca. 0.3 eV. (c) shows the electron potential energy averaged over the plane parallel to the surface for the planar (solid black line), downward bent (dashed light grey) and upward bent (dotted dark grey) geometry.

At this point the question arises to what extent other parameters like the adsorption distance play a role and whether effects like the distance dependent Pauli push-back^[50] are of any relevance. Following the above considerations, one might come to the conclusion that neither of them counts, as Pauli push-back is an intrinsic part of ΔE_{bond} and changing the charge-transfer distance will be compensated by a different amount of transferred charge in a straightforward manner. In this context, one, however, must not forget that charging the molecular layer per se affects the energetic position of molecular levels^[39] and hence also the position of the pinning level ϵ . This, naturally, changes ΔE in Figure 4.2(a)-(c) and consequently also the system work function Φ' . The dependence of the work-function change on the adsorption distance has indeed been documented in a computational study on 3,4,9,10-perylene tetracarboxylic dianhydride (PTCDA) adsorbed on coinage metals^[99]. Another effect is that geometric distortions also change the molecular eigenstates, thus affecting the position of the pinning level (cf. support-

ing information). A combination of the above described aspects is responsible for $\Delta\Phi$ being not exactly constant for the downwards bent -CN groups as shown in Figure 4.1c. Nevertheless, the pronounced asymmetry in the evolution of $\Delta\Phi$ with the out-of-plane bend, α is clearly a consequence of the different location of the molecular dipole relative to the charge-transfer region.

To illustrate that the above described mechanism does not depend on the specific system, we next discuss a conceptually different example: Doubly reduced methylviologen (MV0) is a potent electron donor, which has been shown experimentally to reduce the work function of a Au surface by 2.2 eV^[123]. For this compound, we found an almost perfectly planar adsorption geometry (cf. section 4.3. To endow the molecule with an intrinsic dipole moment, we have replaced one hydrogen atom in each of the methyl groups by fluorine (FMV0; see Figure 4.4a, top). In a monolayer of FMV0, the magnitude and spatial position of the intrinsic dipole can be tuned by a rotation of the peripheral $-CH_2F$ groups (see Figure 4.4b). Here we study FMV0 on a Au(111) in a $5 \times 3\sqrt{3}$ unit cell, corresponding to (sub)monolayer coverage (1 molecule per 226\AA^2) in analogy to the investigation of doubly reduced viologen in section 4.3. A study at full coverage is prevented by the fact that the structure of a densely packed monolayer consisting of MV0 or its derivatives is not known.

Due to symmetry reasons, an upward and a downward rotation of the terminal groups affect ΔE_{mol} in the same way (open circles in Figure 4.4c). Moreover, in perfect analogy to F4TCNQ on Ag(111) and in agreement with the above reasoning, it is found that when the C-F dipole is located between the metal and the plane of the molecule (negative angles in Figure 4.4c), ΔE_{bond} almost perfectly counteracts the evolution of ΔE_{mol} . This results in a hardly changing $\Delta\Phi$ determined solely by pinning. For positive angles, the C-F dipole is found outside of the immediate interface (i.e., outside the charge-transfer region). Therefore, ΔE_{bond} remains constant regardless of ΔE_{mol} , and $\Delta\Phi$ strongly depends on the rotation angle.

To demonstrate that Fermi-level pinning is a necessary requirement for the asymmetry, we studied also fluorethane (Figure 4.4a, bottom), a wide-gap insulator that does not undergo charge-transfer with an Au(111) surface and bears an intrinsic dipole moment, whose orientation can be easily tuned. For the sake of consistency, we assumed the same adsorption distance (3.53\AA between the top metal layer and the carbon atoms) as for FMV0. To account for the smaller size of the molecule, a $3 \times 3\sqrt{3}$ unit cell was chosen (1 molecule per 45\AA^2), again representing the case of a loosely packed monolayer. (This results in a higher dipole density than for FMV0 discussed above resulting also in a larger ΔE_{mol}). Figure 4.4d shows the evolution of $\Delta\Phi$, ΔE_{bond} , and ΔE_{mol} with respect of the rotation of fluorethane along its C-C bond. Since no significant charge transfer occurs at the interface, ΔE_{bond} is generally small (-0.2-0.3eV), and varies only as the individual atoms change their distance to the surface, thereby slightly modulating Pauli push-back (note that in the absence of Fermi-level pinning changes in the push-back will not be compensated by interfacial charge-transfer as described for the above cases). The variations in ΔE_{mol} are much larger (between -1.4eV and +1.4eV) and, therefore, determine the trend for $\Delta\Phi$ for positive and negative angles. I.e., they

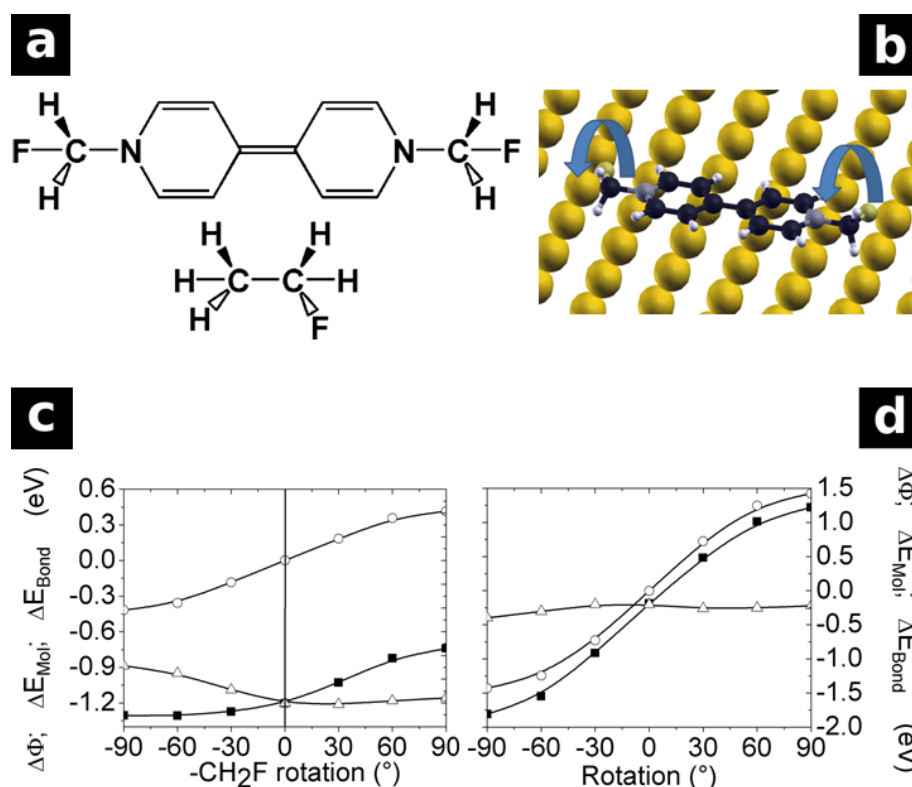


Figure 4.4: a) Chemical structure of 1,1'-Bis-fluoromethyl-1H,1'H-[4,4']bipyridinylidene (FMV0) and fluorethane. b) Structure of FMV0 adsorbed on Au(111). The arrow indicates the rotation of the CH_2F -groups. c) Evolution of $\Delta\Phi$ (closed squares), ΔE_{mol} (open circles), and ΔE_{bond} (open triangles) as function of the rotation of the CH_2F substituent of FMV0. Lines are b-spline interpolations to the calculated values and intended as guide to the eye. d) like c, for the rotation for fluorethane along its C-C bond.

are no longer compensated by ΔE_{bond} for molecular dipoles between the monolayer and the metal. The larger absolute magnitude for ΔE_{mol} compared to FMV0 is simply a consequence of the higher packing density.

At this point the question arises whether the above described effect is only valid for flat lying molecules which undergo changes in their geometry, or whether the same trends can also be reproduced on Fermi-level pinned self-assembled monolayers. These bear the advantage that they can be derivatised in a straightforward manner (vide infra). A suitable example is substituted [2,5';2',5'']terpyrimidine^[236] on Au(111)¹ shown in the left part of Figure 4.5.

¹While Fermi-level pinning has been observed experimentally for MV0 and also F4TCNQ, such molecules to the best of our knowledge have not yet been investigated experimentally. As a consequence, bearing in mind the well known band-gap problem of DFT, it cannot be guaranteed that Fermi level pinning actually occurs in this SAM. This does, however, in no way affect the fundamental conclusions drawn here

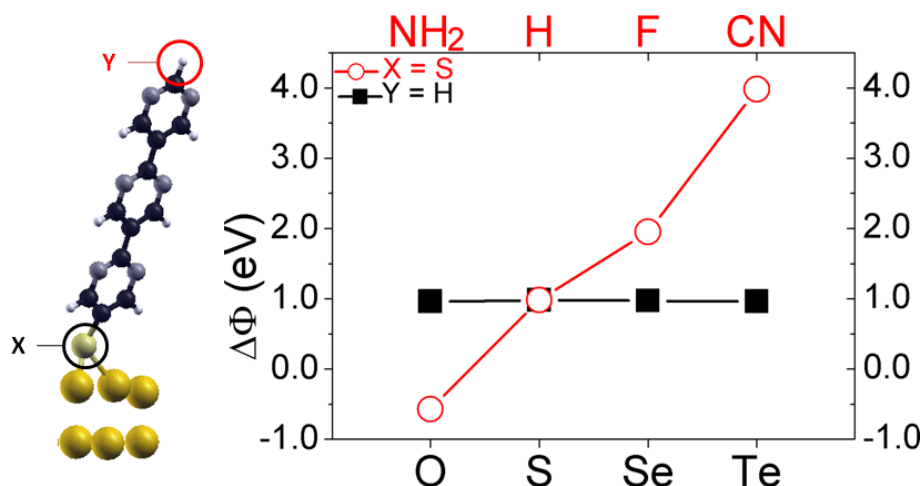


Figure 4.5: Left: Chemical Structure of the terpyrimidine SAM. Black balls represent carbon atoms, grey denote nitrogen, white balls are hydrogen atoms, golden atoms represent Au. The black circle indicates the location of the docking group, while the red circle show the location of the head group. Right: Modification of the work function of a Au(111) surface by a densely packed terpyrimidine SAM with different docking groups (closed black boxes, head group = H) and with different head groups (open red circles, docking group = S).

Here, X denotes the functional group which binds the monolayer covalently to the gold surface, and Y is the head-group to be functionalized by dipolar substituents. The pinned level is located in the polar backbone of the monolayer. The right part of Figure 4.5 shows the induced work-function modification for X = O, S, Se, and Te (Y = H). Despite the different bonding chemistries, $\Delta\Phi$ does not change at all for the whole series. This is in sharp contrast to what one observes for a non-pinned terphenyl-backbone, where varying X results in $\Delta\Phi$ values differing by up to 1.4 eV (details see Supporting Information). Note that for the sake of comparability, the geometries were kept fixed at the structure of the sulfur-substituted compound and a packing density of 2 molecules per 45\AA . Figure 4.5 also displays the effect of varying the head-group in the thiolate-bonded terpyrimidine (Y = H, NH₂, F, and CN). Since the dipole layer created by the -Y substituents is outside the “charge-transfer” region, i.e., “above” the pinning-level, a work-function modification beyond pinning can be observed as expected from the above considerations. For Y=CN this results in exceptionally large value for Φ' . A value of $\Delta\Phi=3.98\text{eV}$ and thus should yield a work-function of the SAM-covered Au(111) surface as high as 9.20 eV. To what extent such “super-dipole layers” will actually be observed in practice, only time can tell and will greatly depend on whether the necessary molecules can be made and form well-ordered and densely packed monolayers.

4.2.3 Conclusion

To summarize, we have shown that whether molecular dipole layers play a role for the work function of Fermi-level pinned metal/monolayer systems is crucially determined by the position of that layer. When the molecular dipoles are within the region affected by the pinning-induced charge rearrangements, they have virtually no effect on the final work function of the system. This is because in that case the molecular dipoles are compensated by variations in the charge-transfer dipoles arising from the metal-molecule interaction. The finding holds true independent of the type of the adsorbed system (flat-lying donor or acceptor layer, or SAM), the charge transfer distance, and the origin of the molecular dipole (bending and rotation of substituents or change in docking groups). When, however, the molecular dipoles are located above the metal-molecule charge-transfer complex, their effect will be additive to that resulting from the pinning itself. Keeping that in mind will allow the design of novel systems that give rise to work-function modifications of unprecedented magnitude.

4.2.4 Supporting Information

Methodology

Calculations were performed with the VASP code^[51–53] at the GGA-DFT level, using the PW91 functional. VASP employs periodic boundary conditions in all three spatial directions, accounting for the (semi)infinite extension of the systems. To model the surface, the so-called “repeated slab-approach” was chosen. In this approach, the metal is represented by a finite number of layers (here: five), where on one side the molecular layer is adsorbed. Successive slabs are separated in z-direction by a sufficient amount of vacuum ($>20\text{\AA}$). In order to prevent mutual polarization of the unit cells, a counteracting dipole layer was inserted in the vacuum region. A plane wave basis set with a cutoff of 20 Ryd was used. The interaction between valence electrons and the core was described using the projector augmented plane wave method (PAW)^[55, 56]. Occupation of the band structure followed the Methfessel-Paxton scheme^[58]. The number of k-points, which were constructed according to the Monkhorst-Pack method^[57], was adjusted to the size of the respective unit cells: For the flat-lying molecule F4TCNQ, the experimentally motivated $\begin{pmatrix} 4 & -1 \\ 4 & 0 \end{pmatrix}$ unit cell was used in analogy to earlier calculations^[124]. For FMV0, a single molecule per $5 \times 3\sqrt{3}$ was chosen to represent the case of a loosely packed monolayer in order to prevent artifacts from incorrect packing. Both kinds of systems were sampled with $3 \times 3 \times 1$ k-points. The smaller molecule fluorethane was modeled as a single molecule in a $3 \times 3\sqrt{3}$ cell.

Self-assembled monolayers consisting of substituted terpyrimidines or terphenyls were modeled with two molecules per $3 \times \sqrt{3}$ cell, arranged in a herringbone-pattern as found experimentally for biphenylthiole^[238]. The exact geometry of terpyrimidine was taken from Ref ^[236]. For the terphenylthiolate SAM, a full geometry optimization was performed in internal coordinates using the gadget-tool^[239] until the forces acting on the atoms were smaller than 0.01 eV/Å. The $3 \times \sqrt{3}$ cells were sampled by a grid of $8 \times 5 \times 1$ k-points. All top-view of all surfaces is shown in Figure 4.6

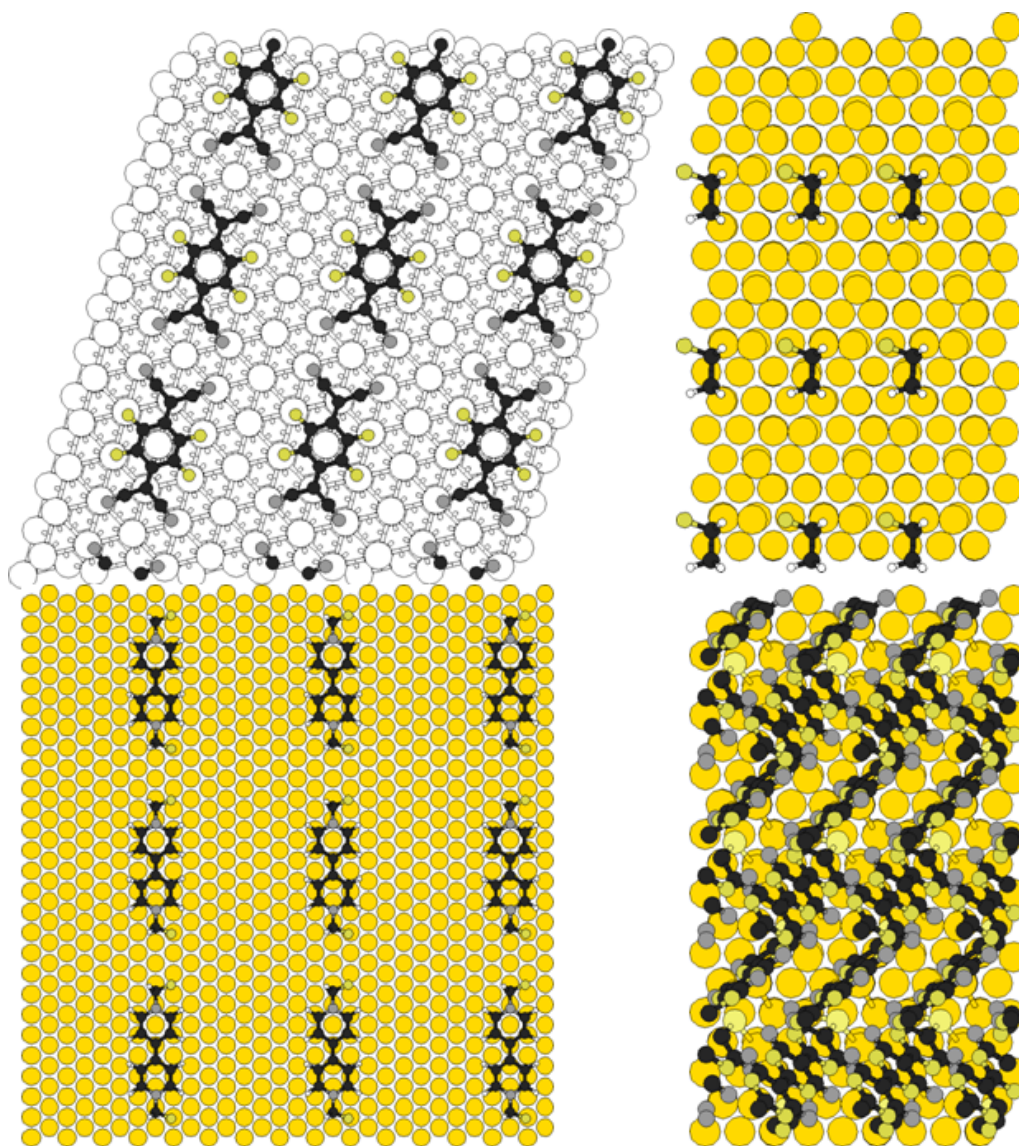


Figure 4.6: Employed unit cell, replicated three times in x- and y-direction, of F4TCNQ on Ag(111) (top left), and fluorethane (top right), FMV0 (bottom left), and terpyrimidinethiole (bottom right) on Au(111).

The work-function modification, $\Delta\Phi$, was calculated according to the Helmholtz equation

$$\Delta\Phi = \frac{\mu_{sys}}{\epsilon_0 A} \quad (4.2)$$

Here, μ_{sys} denotes the dipole moment of the combined metal/monolayer system given by the counter-dipole mentioned above, A is the unit cell size and ϵ_0 the vacuum permittivity. To calculate ΔE_{Mol} , the dipole moment μ_{Mol} of the monolayer was calculated in its adsorbed geometry, but without the metal. In analogy to eq. 4.2, ΔE_{Mol} is then given by

The work-function modification, $\Delta\Phi$, was calculated according to the Helmholtz equation

$$\Delta E_{Mol} = \frac{\mu_{mol}}{\epsilon_0 A} \quad (4.3)$$

Finally, equation was then used as definition to obtain ΔE_{Bond} :

$$\Delta E_{Bond} = \Delta\Phi - \Delta E_{Mol} \quad (4.4)$$

Note that by definition, ΔE_{Bond} includes all kind of electronic interactions between metal and monolayer, i.e. covalent bonds, charge transfer, Pauli pushback, etc.

To create the bent geometries of F4TCNQ, the molecule was fully optimized in gas phase. Using a z -matrix editor, the cyano groups were bent by setting the dihedral angle 1-2-3-4 (numbering according to Figure 4.7) to $180^\circ - \alpha$, with *alpha* being the ‘‘bending angle’’ shown in Figure 4.1. All other dihedrals were kept at 180° and 0° , respectively. The obtained geometries were then placed above the surface so that all atoms except the cyano groups (numbers 3 and 4) are located at the same z -coordinate. For the calculations in the main text, the adsorption distance, given as difference between the z -coordinate of the F4TCNQ central ring and the topmost metal layer, is set to 3.3\AA , according to XSW-measurements for this system. In the corroborating calculations shown in the supporting information, the adsorption distance was set to 10\AA .

For FMV0, also a full gas phase optimization was performed. Initially, both fluorine atoms were placed in the plane of the backbone, and symmetry constrains were employed to ensure that the molecule remains perfectly planar. Subsequently, both CH₂F groups (indicated by numbers 1-3 in Figure 4.7) were simultaneous rotated around the axis given by C-N bond (numbered as I and II). The rotation was performed such that the fluorine-atoms were always on the same side of the molecule, i.e. the mirror-plane perpendicular to the long axis was preserved. The situation with both fluorine atoms located in the plane was chosen to represent 0° rotation. The obtained geometries were then placed above the surface such that all atoms of the backbone are located at the same z -position. The difference between this z -coordinate and the topmost metal layer was defined as adsorption distance. For the calculations in the main text, an adsorption distance of 3.53\AA was chosen, according to the adsorption distance of fully optimized MV0. In the corroborating calculations presented in the supporting information, the adsorption distance was set to 5.00\AA .

Fluorethane was optimized in gas phase prior to generation of the monolayer geometries. The molecule was constrained to the eclipsed conformation. In the absence of experimental data on the correct packing on Au(111), a $3 \times \sqrt{3}$ unit cell was chosen,

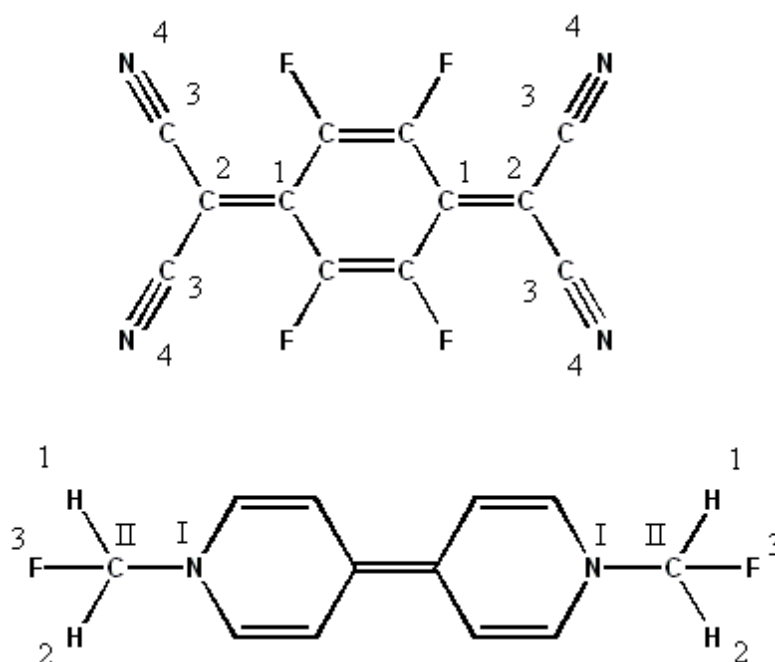


Figure 4.7: Molecular structure of F4TCNQ (top) and FMV0 (bottom), along with numbering for atoms used to define dihedral angles. Note that symmetry-identical atoms are denoted with the same numbers.

representing a loosely packed monolayer. An adsorption distance of 3.53\AA was assumed, in analogy to the FMV0 structure. As such a system is bonded to the surface mainly by van der Waals interactions, a geometry optimization using a (semi)local functional like PW91 in the framework of DFT would be futile. The change of dipole perpendicular to the surface was realized by rotation of fluorethane along its C-C bond. Note that for all cases discussed above, geometric changes of the intra-molecular bond lengths resulting from the metal-molecule charge transfer are not considered, as it has no impact on the conclusions drawn here.

As starting point of the terpyrimidine-calculations the fully optimized geometry from Ref. [236] was chosen. To calculate the effect of substituting the docking group, only the corresponding S-atom was replaced by O, Se, and Te, respectively. For the results presented in the main text, no geometry optimization was performed. Head-group modifications were only done for thiole-bonded terpyrimidines. Here, the atomic position of the head group was optimized until the remaining forces were smaller than $0.01\text{eV}/\text{\AA}$, while the remaining molecule was kept frozen. It should be noted that due to intrinsic errors of GGA-DFT (e.g., self-interaction error and lack of derivative discontinuities), the nature and energetic position of the HOMO orbital - σ or π - depends sensitively on the choice of the exchange-correlation functional. This has no impact on the conclusions drawn here, as the reasoning of the main text is based on electrostatic considerations. At most, the underestimation of the band-gap by DFT might result the need for a slightly longer oligopyrimidine to actually observe pinning.

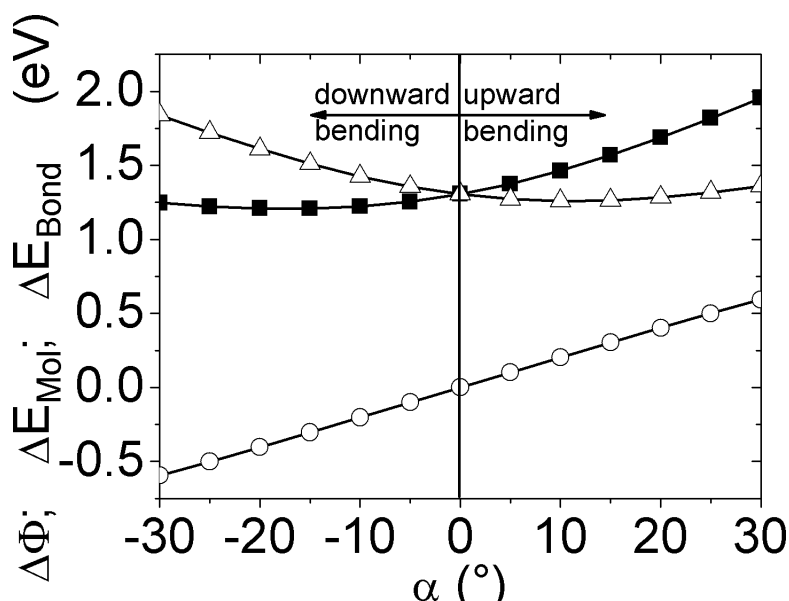


Figure 4.8: Evolution of $\Delta\Phi$ (closed boxes), ΔE_{Mol} (open circles), and ΔE_{Bond} (open triangles) as function of the bending of cyano-groups F4TCNQ adsorbed 10Å above an Ag(111) surface. In the inset, the chemical structure of F4TCNQ is shown.

Molecular gas phase properties were calculated using Gaussian03^[71]. The B3LYP functional was employed together with the 6-31+G* basis set. To obtain the ionization potentials (IP) and electron affinities (EA) discussed below, the total energy of the neutral molecules was subtracted from the total energy of the singly charged radical species.

F4TCNQ

In the data presented in the main text, F4TCNQ is located near the surface (at 3.3Å). Because the CN-groups participate in the charge transfer process^[24], the bending of the CN-groups has a significant influence on the effective charge transfer distance, which is known to strongly impact $\Delta\Phi$ ^[99]. For example, at 30° bending, the nitrogen atoms are located 0.6Å beneath / above the molecular plane. In order to test the impact of this effect and to clarify, whether the specific interaction between the -CN groups and the metal is relevant for the main conclusions of this paper, F4TCNQ has also been studied 10Å above an Ag(111) surface in a loosely packed monolayer ($5 \times 3\sqrt{3}$ unit cell). At such a large distance, a bending of 0.6Å is of only very minor relevance. Certain methodological issues notwithstanding (due to the large distance, no charge transfer would presumably take place on laboratory timescale and a single-determinant description becomes perhaps somewhat problematic), it is clearly shown that at 10Å a situation is observed that is qualitatively equivalent to that observed for a 3.3Å adsorption distance; the main difference is that the variations of $\Delta\Phi$ for downward bending are somewhat reduced.

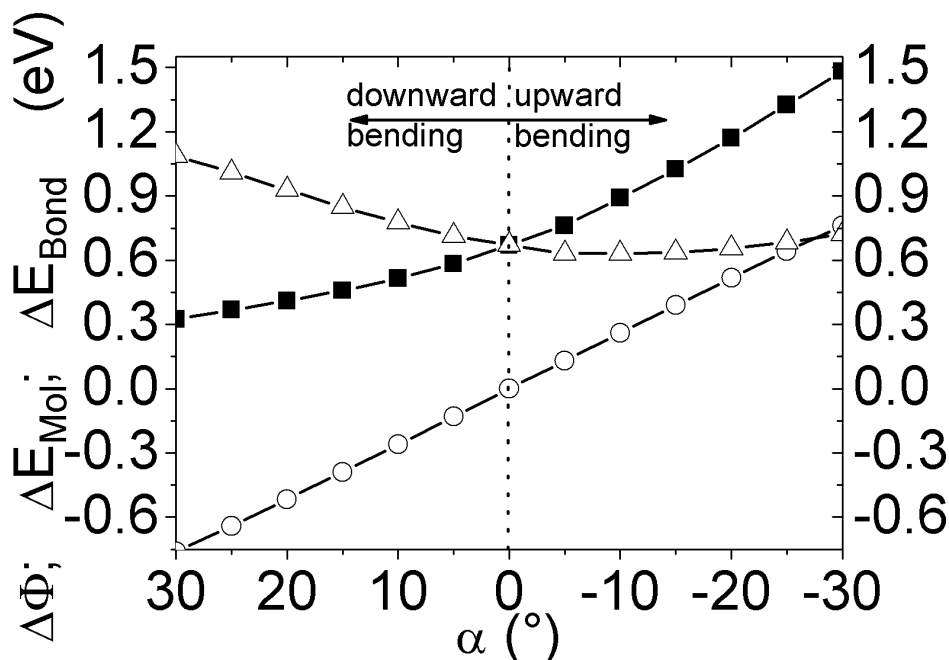


Figure 4.9: Evolution of $\Delta\Phi$ (closed boxes), ΔE_{Mol} (open circles), and ΔE_{Bond} (open triangles) as function of the bending of cyano-groups F4TCNQ adsorbed 3.3 Å above an Cu(111) surface. In the inset, the chemical structure of F4TCNQ is shown.

Also, this effect is not restricted to the interaction of F4TCNQ with the Ag-surface; as an example, the results for adsorption on Cu(111). Here also a loosely packed $5 \times 3\sqrt{3}$ unit cell has been used, along with the experimentally determined adsorption distance of 3.3 Å. Note that despite the different packing motif and density used in the main text (experimentally motivated unit cell) and here (rectangular, loosely packed $5 \times 3\sqrt{3}$ unit cell), the same trends are observed, demonstrating that the conclusions are neither an artifact stemming from molecule-molecule interaction nor depolarization effects. The results are shown in Figure 4.9.

To study the effect of bending on the molecular levels, the gas phase electron affinity (EA) of F4TCNQ in its differently bent geometries has been calculated. We find that EA changes from 4.11 eV in the planar to 4.50 eV in the 30° bent situation. Although, naturally, this effect is non-negligible, it is symmetric around the unbent (0°) situation and cannot account for the different behavior of upward and downward bending.

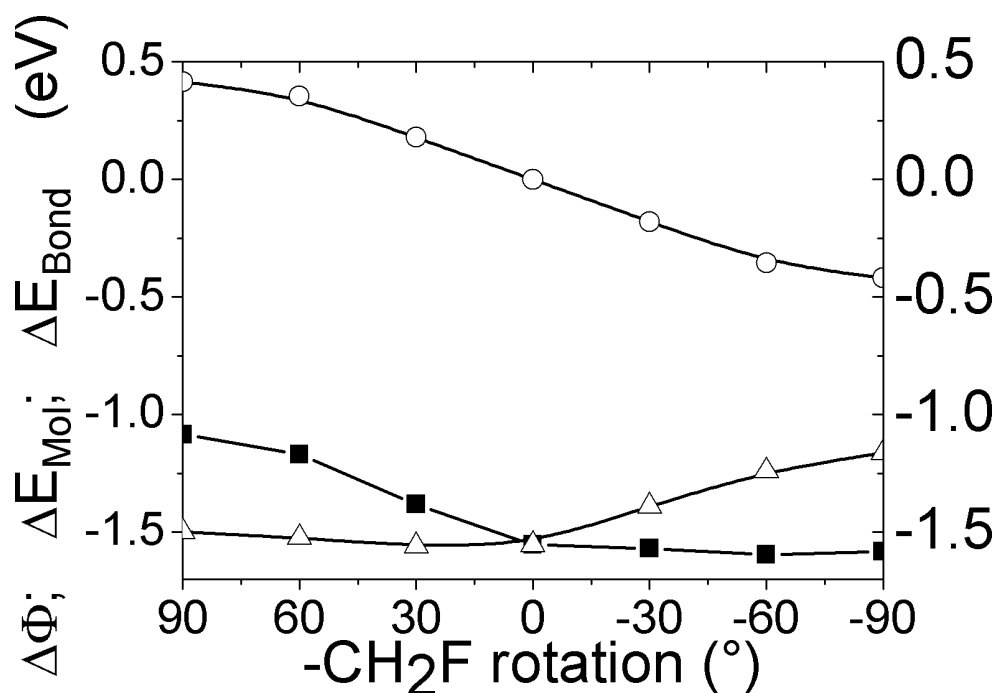


Figure 4.10: Evolution of $\Delta\Phi$ (closed boxes), ΔE_{Mol} (open circles), and ΔE_{Bond} (open triangles) as function of the rotation of the CH_2F substituent of FMV0 adsorbed 5\AA above an Au(111) surface. The connecting lines are b-spline interpolations and intended as guide to the eye

FMV0

Although unlike bending in F4TCNQ, the rotation of the fluormethyl group does not significantly affect the charge transfer distance to FMV0, it is necessary to rule out the possibility that Pauli pushback holds responsible for the observed variations. Therefore a second set of data was created with an adsorption distance of 5\AA , where the overlap of the metal and molecule wave function de facto vanishes. The obtained results are shown in Figure 4.10 and are in perfect agreement with the calculations shown in the main text.

To study the magnitude of the impact of CH_2F -rotation on the π -levels of FMV0, the IP was calculated for different rotation angles. We find that between 0° and 90° , the IP changes from 5.13eV for 0° to 5.48eV in the 90° rotated situation.

Substituted terphenyl SAMs

In the main text it is claimed that attaching terphenyl SAMs to the Au(111) surface via -O or -Te group has a significant impact on the work-function modification. Figure 4.11 shows the obtained results for the thiolate-bonded geometry (as in ref [43]). As these results have been obtained without reoptimizing the geometry to avoid interference from geometry-related effects, they cannot be taken as fully quantitative. Nevertheless, they clearly show that in the absence of pinning the nature of the docking atom has a huge impact on $\Delta\Phi$ in sharp contrast to the pinned case shown in the manuscript.

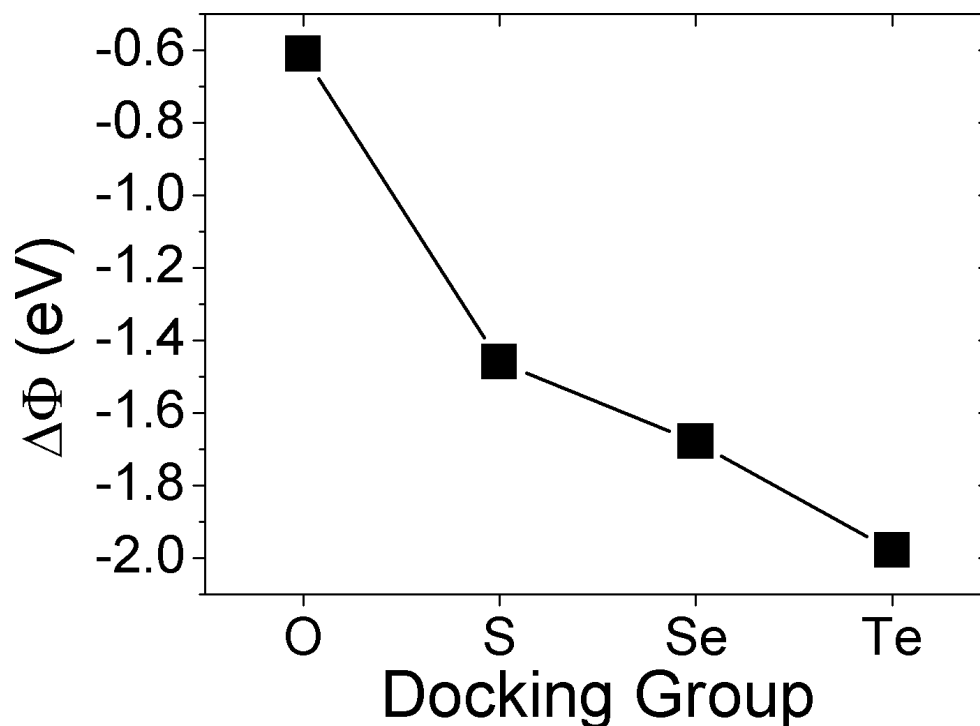


Figure 4.11: Work-function modification for 4'-substituted terphenyl at constant geometry.

4.3 Work-function modification tuning by N,N'-dialkylation of doubly reduced viologen monolayers

4.3.1 Preface

In this section, the general principles derived in the last section will be tested. To that aim, the effect of systematic modification of the molecule HV0 is studied. By introducing electron rich, bulky groups on the periphery of the organic compound, the adsorption geometry is altered, and consequently, also the work-function will be impacted. For two of the molecules shown in this section, HV0 and MV0, results have already been presented in earlier parts of this thesis. For this work, all geometries have been reoptimized using internal coordinates. These are inherently better suited to describe molecular systems, and therefore helpful when comparing such similar molecules. It should be emphasized, however, that the conclusions drawn in sections 3.1 and 3.2 are not affected by the minor changes resulting from the geometry reoptimization.

The data and interpretation shown hereafter are a reproduction of a manuscript currently in preparation for publication, which has been adopted with only minor edits. Credit for the optimization in internal coordinates goes to Ferdinand Rissner, who set up the optimizer tool gadget and researched the best input parameters to describe these kind of systems. Bonding analysis with molecular orbital density of states (MODOS) and crystal orbital overlap population (COOP) has been done by Gerold Rangger. Calculations in VASP and G03 have been performed by myself. The results were interpreted in multiple discussion between Ferdinand Rissner, Gerold Rangger, Egbert Zojer, and myself.

4.3.2 Abstract

In organic electronics, (pre)covering a metal surface with an organic layer has become an important way to tune the effective work-function and thus improve charge-carrier injection barriers. In this work, density functional theory is used to study the influence of alkyl substitution on doubly reduced viologen, a potent electron injection layer. First, the impact on the adsorption geometry is studied. Thereby, it is found that the side-groups have a two-fold effect: on one hand, the distance between metal and monolayer is increased, and on the other, the bending of the molecule upon adsorption is reversed. In a second step, the mechanism of the charge-transfer between metal and organic is investigated. It is found that in all cases, the pre-dominant process is electron donation from the HOMO to the metal, with only little backdonation into the virtual states of the molecules. Using the crystal overlap population and an extrapolation scheme, the relative contributions of covalent and ionic binding to the total binding energy are estimated. Finally, the impact of alkylation on the effective work-function of the combined systems is discussed. Surprisingly large differences are found, which are rationalized by the changes in the adsorption geometry.

4.3.3 Introduction

In the past years, interfaces between conjugated organic molecules and metal surfaces have drawn a lot of interest due to their potential in organic (opto)electronic devices^[11]. By suitable choice of the deposited molecules, the effective work function of the electrode, Φ' , and hence the charge injection barrier into subsequently deposited (electro)active material, can be optimized^[10]. A promising way to tune Φ' is the employment of strong electron donors or acceptors. Monolayers of these types of molecules undergo charge transfer reactions with the substrate^[23, 24, 123, 202, 240, 241], and it has been demonstrated experimentally that they can influence Φ' of the underlying metal by several eV. For Au, e.g., work-function modifications between -2.2eV^[123] and +0.4eV^[144] have been reported. In order to systematically develop molecular candidates for yet larger work-function modifications, it is important to study structure-to-property relationships of such interfaces. So far, most of those studies are concerned with the influence of different metals on the same adsorbate. A highlight in this context is the electron acceptor PTCDA (3,4,9,10 perylenetetracarboxylic dianhydride), which has been investigated on at least 10 different metals^[132, 179, 185, 190]. Although a quite large number of adsorbates has been studied on coinage metals, the subtle differences in packing density and motif and the differences in the metal-molecule interaction often obscure the formulation of fundamental structure-to-property relationships. To improve the understanding of organic/inorganic charge transfer interfaces, we perform density functional theory calculations on a set of structurally very similar systems. We focus on the class of doubly reduced viologens, see Figure 4.12. The aromatic nitrogen atoms at the periphery of the molecule provide defined anchors for a systematic variation of the molecule. A large number of N,N'-disubstituted derivatives are known and commercially available in their oxidized form. Doubly reduced viologens belong to the strongest electron donors in organic chemistry^[169]. Their gas phase ionization potentials are found to be below the work-function of Au(111), qualifying them as ideal candidates for charge-transfer reactions with coinage metal surfaces. Recently, DFT calculations showed that upon adsorption on Au(111), a monolayer of doubly reduced viologen (HV0, see Figure 4.12) can induce a work-function modification, $\Delta\Phi$, of more than -1.8 eV^[37]. HV0 treated Au(111) surfaces therefore exhibit the work-function of pristine Mg, making it suitable for application as anode of an electronic device. Later, a combined theoretical and experimental study showed that a derivative of this molecule, MV0, reduces Φ' of Au(111) by 2.2 eV^[123], proving that such extreme work-function modifications can actually be found in real world. The good agreement between experiment and theory also demonstrates that DFT is well suited to study these kind of systems.

In this work, we use density functional theory calculations to systematically investigate the effect of N,N'-dialkylation of doubly reduced viologen on the adsorption geometry, the bonding chemistry, the interaction energy, and the induced work-function modification on Au(111). Here, gold has been chosen because of its abundance as electrode material in organic electronics, as well as for its high work function. In particular, three organic molecules are considered: unsubstituted viologen (HV0), N,N'-dimethylviologen (MV0), and N,N'-*tert*-butyl-[4,4']Bipyridinylidene (tButV0), see Figure 4.12. In the abbreviations, the zero indicates the neutral, i.e. doubly reduced form of the molecules.

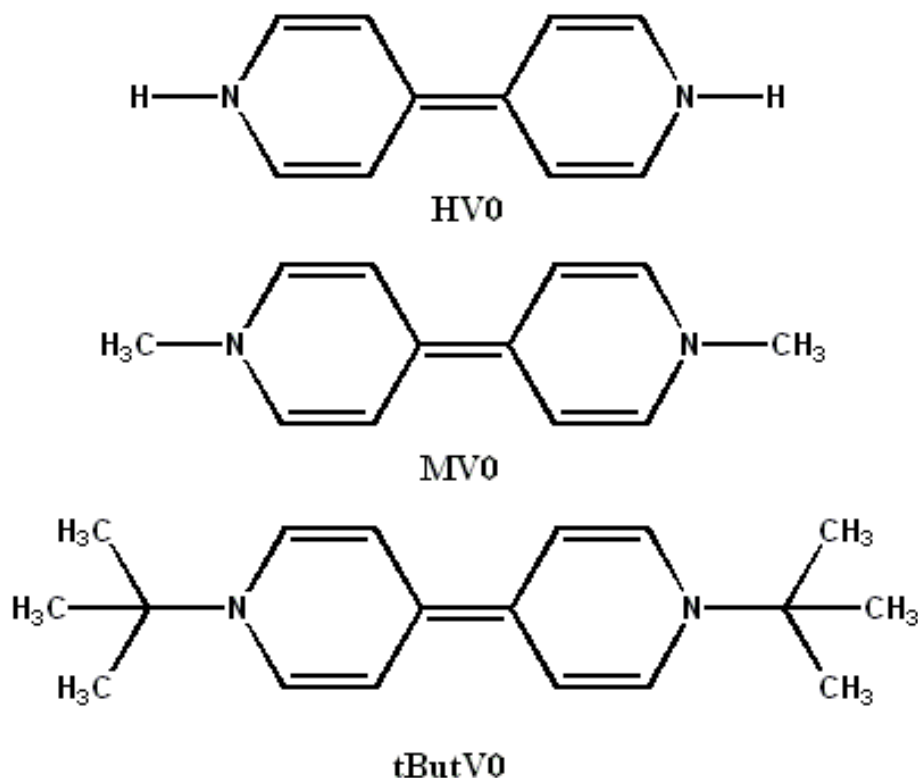


Figure 4.12: Chemical structure of the investigated molecules HV0 (top), MV0 (middle), and tButV0 (bottom).

For the sake of simplicity the molecules will be generally referred to as “viologens”.

4.3.4 Computational details and methodology

Because the employed methodology deviates somewhat from the default proceeding discussed in section 2.2, all details are re-iterated here.

All systems were calculated employing periodic boundary conditions (PBC) using the VASP^[51–53] code and the GGA-type exchange-correlation functional PW91. All systems were calculated with a single molecule in a $5 \times 3\sqrt{3}$ surface (picture shown in the supporting information) unit cell using a set of $3 \times 3 \times 1$ k-points on a Monkhorst-Pack grid^[57]. The valence-core interaction was modeled by the projector-augmented wave method^[55, 56] allowing for the very low cutoff energy of 20 Ryd for the plane-wave basis set. Using plane waves also allows reporting basis set superposition free adsorption energies. The density of states (DOS) was smeared out according to the first-order Methfessel-Paxton^[58] scheme using a broadening of 0.2 eV. For the optimization of the geometries, the external optimizer GADGET^[239] was employed. GADGET uses an efficient optimization strategy and non-redundant internal coordinates^[239]. Reciprocal power coordinates are employed to describe the distance between the monolayer and the

substrate, which is was found to be most efficient for weakly interacting subsystems^[242]. The metal was represented by a slab of 5 layers. During the geometry optimization, the top two layers were allowed to relax while the bottom three layers were kept fixed at their bulk position. In the direction perpendicular to the surface, at least 20Å of vacuum were inserted to separate the slabs, preventing mutual interaction. To avoid spurious electric fields an artificial dipole layer was inserted in the vacuum region to compensate for the non-zero net dipole moment at the interface. Optimizations were performed until each remaining force component was smaller than 0.01eV/Å.

The orbital-based analysis (MODOS and COOP, vide infra) was performed with the PBC-code SIESTA 2.0^[243] software, employing the PBE functional and the double zeta polarized (DZP) basis set using the optimized VASP-geometries as input. It was shown that double zeta basis sets are a suitable compromise between accuracy and computational demand^[244]. Despite the different methodology, the obtained densities of states differ only negligibly between VASP and SIESTA^[63].

The similarity of the three molecules allows coping with several intrinsic problems of DFT, which would otherwise prevent a reliable comparison. Perhaps the best known among these is the “band gap problem”, i.e. the fact that attribution meaning to the orbital energies, in particular those of the highest occupied molecular orbital (HOMO) and lowest unoccupied molecular orbital (LUMO), is not trivial^[111]. This issue is closely related to two infamous problems of DFT, namely the lack of derivative discontinuity^[111, 245], and the self-interaction error^[112, 246, 247]. Because the latter strongly depends on the localization of the orbitals^[248], it is important to note that the alkylation hardly affects the shape of the π -orbitals involved in the charge transfer. Hence, this error can be assumed to be roughly constant for HV0, MV0, and tButV0.

Another problem concerning the orbital energies is encountered for the adsorption of the monolayer on the metal. Due to the lack of long-range correlation in DFT the polarization response of the metal is inadequately captured^[35]. This effect depends on the distance between metal and molecule. Scanning tunneling spectroscopy measurements of pentacene, which was electronically decoupled and lifted off a Cu(111) surface by NaCl-layers, show that the HOMO-LUMO gap changes from 3.3eV to 4.1eV when going from 1 to 2 layers NaCl^[226]. Since HOMO and LUMO are equally affected the gap reduction of 0.9 eV corresponds to a 0.45eV shift of the respective orbitals, for a change in the adsorption distance of ca. 2.8Å^[249]. Here, the differences in the adsorption distance is much smaller for the molecules discussed (ca. 0.5Å, vide infra), and we therefore assume the error in the HOMO energy to be similar enough to allow a comparison between the systems. It should be emphasized here that ΔSCF calculations (i.e., direct comparison of the energies of the neutral and the charged molecules) at the B3LYP/6-31+G* level performed with Gaussian03^[71] predict the vertical ionization potential of all three viologenes to be lower than the work-function of pristine Au(111) (HV0: 5.10eV, MV0: 4.92eV, tButV0: 4.65eV). This furthermore reassures that the calculated charge transfer is not only an artifact due to the incorrect description of the DFT-HOMO energy.

A third problem in current density functionals is the inadequate treatment of van-der-Waals forces in this kind of interfaces^[110]. For organic molecules adsorbed on metal surfaces these are important contributions to the binding energy and hence the adsorption geometry^[96]. Although recently significant progress has been made in this field (among others, see e.g., ^[107, 109, 250]), the resulting functionals and/or parameters are still under heavy development and evaluation. As a result they are not commonly available in commercial DFT-software packages. One of the reasons (neutral) viologens were chosen in this work is their strong charge transfer character with the underlying metal. Compared to other systems, such as e.g. PTCDA on Ag(111) the influence of van-der-Waals forces in the total energetic picture is thus mitigated. Once again we rely on the similar size of the three investigated molecules to assume that this error cancels out in the comparison. Graphics of the molecular geometries were produced with XCrysden^[161].

The first monolayer of conjugated organic molecules adsorbed on reactive metals typically adopts a face-on geometry, i.e. with its π -system parallel to the surface^[251]. In analogy to earlier work^[37], we assume this also to be the case for the viologens. This assumption is corroborated by STM experiments on Cu(111), where HV in its doubly oxidized form was found to adsorb face-on ^[252]. In the same study, also the radical cation species of HV was shown to adsorb with the long molecular axis parallel to the surface, albeit with a somewhat tilted short molecular axis^[252]. Similar structures have been reported for diaryl-substituted viologen derivatives^[253].

4.3.5 Adsorption geometries and energies

To allow for a comparative discussion of the adsorption geometries, well-defined parameters for their description must be introduced. Intuitively, an important measure will be the adsorption distance between metal and monolayer, which we rigorously define as difference between the z-coordinate of the topmost metal layer and the average z-coordinate of the 4,4'-bipyridine backbone. Moreover, it has often been observed theoretically and experimentally that the formally planar molecules bend upon interaction with the metal^[24, 132]. Typically, this is attributed to the balance of Pauli repulsion between metal and monolayer on the one hand, and attraction due to formation of (covalent or charge-transfer driven) bonds on the other. Here, the bending is quantified by the lateral distance (along the surface normal) between the central 4,4'-bond and the nitrogen atoms. We note that during the geometry optimization no tilting of the short molecular axis was found for any system under investigation, likely because at such low coverage the intermolecular interactions are too weak to promote π -stacking of the molecules.

The effect of attaching alkyl substituents to the bipyridine backbone is twofold. On the one side, methyl and tert-butyl are electron rich substituents. Therefore, they increase the electron donor character of the molecule (vide supra), and a stronger Coulomb attraction between substrate and the molecular backbone can be expected. On the other hand, the volume of the substituents increases, and increased steric (i.e., Pauli) repul-

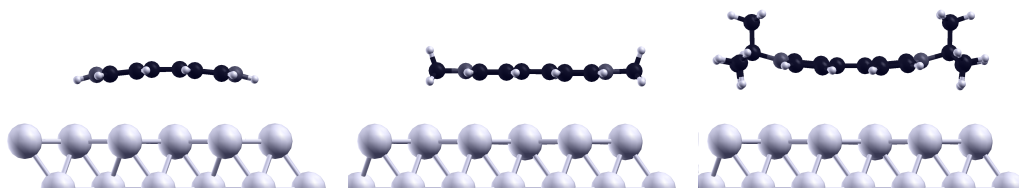


Figure 4.13: Side view of the optimized adsorption geometry of HV0 (left), MV0 (middle), and tButV0 (right).

sion between them and the underlying metal arises. Consequently, alkyl substitution has diametral different effects on the inner part of the molecule - which are drawn closer to the surface - and the peripheral parts, which are repelled. The results for the fully optimized geometries of HV0, MV0 and tButV0 are visualized in Figure 4.13.

For HV0, the central atoms are found at 3.67\AA , while the nitrogen atoms, being located at the periphery of the backbone, are at 3.41\AA above the surface. Thus an adsorption distance of 3.48\AA and a pronounced downward bending of 0.26\AA is observed. In MV0, the distance between metal and nitrogen atoms is increased to 3.57\AA . Simultaneously, the stronger charge transfer character draws the backbone closer until the central atoms are located 3.56\AA above the metal. As a net result, the substituent increases the adsorption distance only slightly to 3.56\AA . In contrast to HV0, however, MV0 remains almost perfectly planar. Extending the series to the even more bulky and electron-rich tButV0, a pronounced upward bending of the substituents is found, placing the nitrogen atoms 4.00\AA above the topmost metal layer. Obviously, the steric repulsion significantly outweighs the increased Coulomb interaction between metal and adsorbate and despite the bending being a very flexible degree of freedom (with a Gaussian03 B3LYP/6-31+G* calculation, the related out-of-plane bending frequencies in gas phase are found below 200cm^{-1}), the backbone of tButV0 cannot bend sufficiently to accommodate yet closer central carbon atoms, which are found 3.75\AA above the topmost metal layer. As net effect, the adsorption distance between metal and molecular layer increases to 3.95\AA . A summary of the adsorption distances and bends is given in Table 4.1, a graphical representation can be found in Figure 4.13.

4.3.6 Interaction energy

Changes in the adsorption geometry significantly impact the interaction energy between substrate and monolayer. In particular larger distances between reaction partners typically indicate a weaker bond^[185]. Here, in contrast we find the total interaction energy (without dispersion contributions) to increase with increasing adsorption distance, from -1.41eV for HV0 to -1.50eV for MV0 to -1.51eV for tButV0. Note that we define the interaction energy, ΔE_{int} , as the difference of the total energy of the combined system, $E_{combined}$, and the energies of the molecular monolayer in its adsorbed geometry, $E_{monolayer}^*$, and the reconstructed slab, E_{slab}^* .

$$\Delta E_{int} = E_{combined} - (E_{monolayer}^* + E_{slab}^*) \quad (4.5)$$

The asterisk in the above equation emphasizes that the coordinates of the monolayer and the slab in the geometry of the combined system is used, rather than the energy of the fully optimized geometry of the isolated components. Therefore, the obtained interaction energy only includes effects from electronic interaction and differs from the true binding energy due to neglecting the energy needed to bring the subsystems from their isolated equilibrium geometries into their adsorbed conformation, as well as the monolayer formation energy. For the sake of completeness, we report the reconstruction energies along with the binding energies in Table 4.2. Since a hypothetical packing motif was chosen, we refrain from calculating the monolayer formation energy, which, however, can contribute significantly to the total binding energy^[99]. Of course it is a priori unclear whether the increase in interaction energy is governed mainly by covalent interactions or by enhanced charge transfer.

To find out whether the covalent interaction improved by alkyl substitution, we employ Hoffmann’s COOP (Crystal orbital overlap population) formalism^[254, 255]. This methodology partitions the density of states into bonding and antibonding contributions according to

$$COOP_{x,y}(E) = \sum_{m \in X, n \in Y, i, k} c_{imk}^* c_{ilk} S_{mlk} \delta(E - \epsilon_{ik}) \quad (4.6)$$

Here, c denotes the atomic orbital coefficients. m and l represent the atomic orbital functions located on atom X and Y . S is the overlap matrix, and ϵ_{ik} are the eigenvalues of the corresponding orbitals.

Summing over all atomic orbital functions of X and Y one obtains the COOP between those two atoms, i.e. their bonding and antibonding contributions resolved on the energy scale. Integration of the COOP up to the Fermi energy yields the total overlap population (ToP), which is a measure for the bond-order and hence the covalent bond strength between two atoms^[255]. Partitioning the system so that set X contains all metal and set Y all molecular atoms, the strength of the electronic interaction between metal and molecule can be estimated^[254]. For HV0, MV0 and tButV0 an increasing ToP is found (0.105, 0.136, and 0.143, respectively). All these values are very small,

Table 4.1: Adsorption distance d , bending, gas phase HOMO orbital energy ϵ_{HOMO} , Mulliken charge Q , induced work-function modification $\Delta\Phi$, vacuum level shift induced by bond dipole ΔE_{Bond} , and vacuum level shift induced by bending ΔE_{Vac} , for a monolayer of HV0, MV0, and tButV0 adsorbed on Au(111). For definition of the quantities, see text.

	HV0	MV0	tButV0
d (Å)	3.48	3.56	3.95
bending (Å)	0.26	-0.01	-0.25
Q (-e)	0.58	0.63	0.65
$\Delta\Phi$ (eV)	1.18	1.41	-1.73
ΔE_{Bond}	-1.39	-1.45	-1.60
ΔE_{Vac}	0.19	0.03	-0.13

indicating that covalent bonding is not the main reason for the large bonding energy. (For comparison, the ToP of a typical, covalently bound self-assembled monolayer lies in the order of 0.161). Nonetheless it is interesting to note that the ToP is larger for the molecules being farther away from the surface; this is in direct contradiction to the usual behavior of a covalent bond, which becomes stronger as the bonding partners approach. Rather, this trend can be traced back to a reduction of repulsive interaction between the molecular electron cloud and the metal electrons. In order to get information about the mechanism and magnitude of charge transfer, the molecular orbital density of states (MODOS^[63, 256]) were calculated. Thereby, the electron density of the combined system is projected onto the molecular orbitals of the isolated monolayer to derive their nominal occupation. From Figure 4.14, where the results are depicted for the three title molecules, it can be seen that the vast majority of the charge transfer stems from the HOMO of the monolayer, which remains filled to $\approx 62\%$ for HV0 and $\approx 54\%$ for MV0 and tButV0. Besides the charge donation from the HOMO, a very slight back-donation is observed for LUMO+3 and LUMO+4 in all cases, corroborating the role of these orbitals for the bonding process. Summing over the occupation of all orbitals yield Mulliken type charges of 0.58, 0.63, and 0.65 for HV0, MV0, and tButV0, respectively. Although the increase of the transferred charge is in fair agreement with the increasing electron donor character of this series, the small difference between MV0 and tButV0 is at first glance somewhat surprising, but will be explained in the next section.

Although the increase of the transferred charge is in fair agreement with the increasing electron donor character of this series, the small difference between MV0 and tButV0 is at first glance somewhat surprising, but will be explained in the next section. Unfortunately, the contribution of the ionic contribution (i.e., the coulomb interaction) to the binding energy cannot be calculated directly, since the coulomb term in the Hamiltonian is burdened with the self-interaction error. We have therefore chosen to pursue an indirect approach: The viologens in their optimized geometry were taken and artificially set to adsorption distances between 5Å and 10Å and the interaction energy between the monolayer and the metal was calculated. At such large distances there is virtually no overlap between the wave-functions of molecule and metal (the ToP becomes zero), and hence the contribution from the covalent interaction in this case is zero. How-

Table 4.2: Interaction energy ΔE_{int} , given by the difference of the total energy of the combined system minus the energies of slab and monolayer in their final, i.e. adsorbed geometries. E_{slab}^* and $E_{monolayer}^*$ denote the reconstruction energy of slab and monolayer, respectively, calculated by the difference of the total energy of the isolated slab (monolayer) in its final and its fully optimized geometry. Negative signs indicate a binding interaction.

	HV0	MV0	tButV0
ΔE_{int} (eV)	-1.41	-1.50	-1.51
E_{slab}^* (eV)	0.02	0.03	0.10
$E_{monolayer}^*$	0.17	0.16	0.19

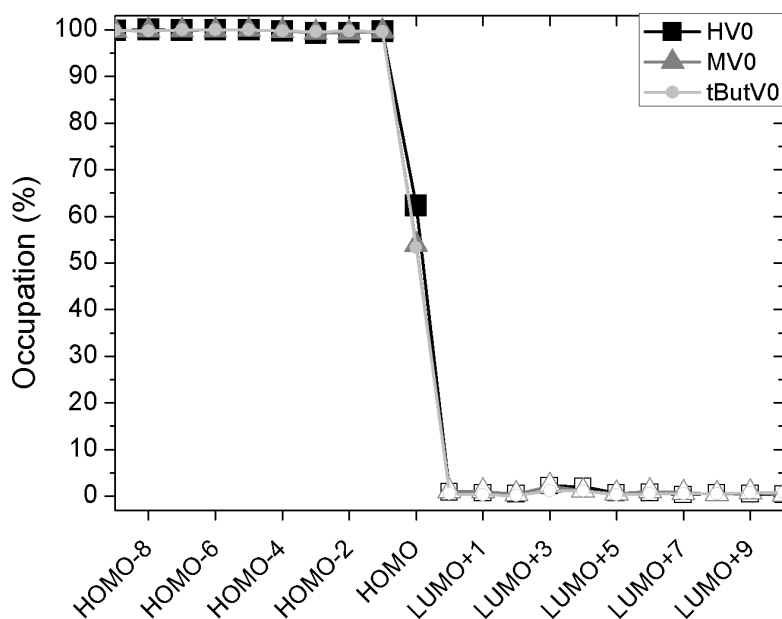


Figure 4.14: Molecular Orbital occupation derived from molecular orbital density of states (MODOS) for HV0 (black squares), MV0 (dark gray triangles), and tButV0 (light gray circles). Filled symbols correspond to orbitals occupied in the ground state, open symbols denote virtual orbitals.

ever, since DFT is an equilibrium method, charge transfer is still predicted (although it would not occur at laboratory timescale anymore). Also, in DFT the HOMO energy is not influenced by screening in the proximity of the metal^[35], and hence the energy gained by transfer of a given fraction of charge is independent of the adsorption distance.

In Figure 4.15, the interaction energies for these hypothetical systems are shown. Extrapolating the interaction energies to the actual, optimized adsorption distances we report Coulomb contributions of -1.49eV (HV0), -1.61eV (MV0), and -1.65eV (tButV0). These values are even somewhat larger than the actual interaction energies, which are the sum of coulomb, covalent, and Pauli repulsion contributions. In this context, it must be mentioned that the extrapolation is of course subject to the assumption that the changes in the charge density monitored for large distance are representative for the charge rearrangements at the correct adsorption distance. There are indications that this is indeed that case (shown in the supporting information), although of course in general it cannot be completely ruled out that the emergence of a covalent bond distorts the electrons in a completely electron distribution which renders the extrapolation meaningless. From comparison of the extrapolated values with the actually calculation interaction energies, it can be concluded that the overlap of the wave-functions (encompassing both covalent binding and Pauli repulsion) is energetically slightly unfavorable (ca. 0.1eV) in all cases, confirming the finding that the metal-monolayer bond is mainly due to Coulomb interaction rather than due to formation of a “true” covalent bond.

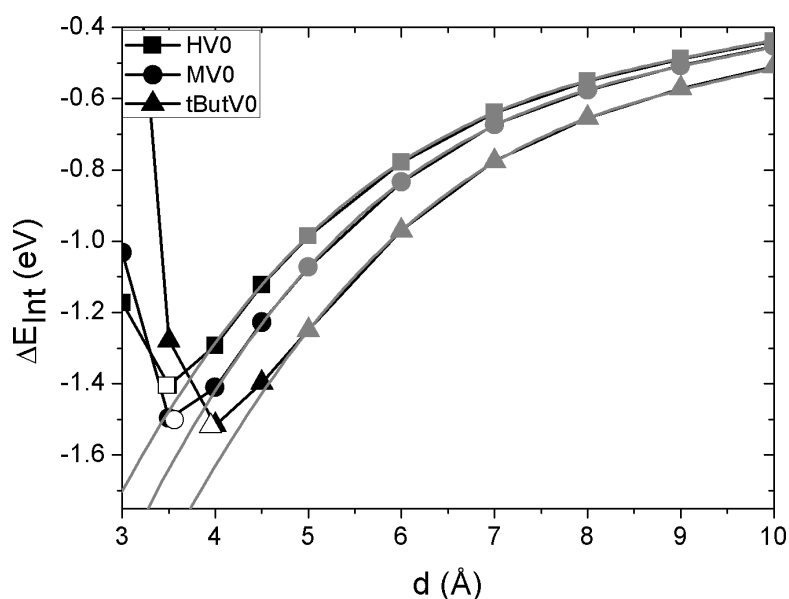


Figure 4.15: Interaction energy E_{int} between Au and a monolayer of HV0 (boxes), MV0 (circles) and tButV0 (triangles). The gray symbols show the data points which were taken for the extrapolation of the Coulomb energy (gray lines). Black symbols show the interaction energies at closer distances. Open symbols correspond to the interaction energy at the optimized adsorption height.

4.3.7 Work-function modifications

In molecular monolayers undergoing charge-transfer reactions with the underlying metal substrate, work-function pinning is observed, i.e., the apparent work-function Φ' , measured for the combined system is independent of the metal work function^[29, 44, 132, 193, 232, 233]. In the simplified case of vanishingly small interaction, Φ' is equal to the negative orbital energy, $-\epsilon$ ^[38], illustrated in Figure 4.16. Interestingly, here the DFT calculations show, however, that the orbital which is pinned to the Fermi level is not equal to ϵ in the free molecule in gas phase, but is shifted to an energy relative to the vacuum level above the surface. This effective orbital energy, which corresponds to a change of the ionization potential of the molecule, will be termed $\epsilon_{HOMO,eff}$ hereafter. For the investigated molecules, the DFT calculations for the combined systems show that the modified work function Φ' , resulting from adsorption of the monolayers, changes from 5.22 eV for pristine gold to $\Phi' = 4.04$ eV for HV0, 3.81 eV for MV0, and 3.49 eV for tButV0. These values are about 0.6-0.9 eV larger than the HOMO energies of the respective molecules (cf. Table 4.3, indicating that the strong interaction between viologens and gold significantly mitigates the work-function modification. Surprisingly, though, the difference between the calculated Φ' and $\epsilon_{HOMO,eff}$ decreases with increasing interaction strength.

This mitigating effect of the interaction can be explained by a change the energy ϵ_{HOMO} to an effective energy $\epsilon_{HOMO,eff}$ due to the interaction. There are two main effects influencing $\epsilon_{HOMO,eff}$, both of which are strongly dependent on the adsorption

geometry. The effects are (i) charging and (ii) bending. The former describes the fact that an already charged (sub)system, such as the molecular monolayer, resists further charging by virtue of Coulomb repulsion. Energetically, this is reflected as a decrease of the HOMO energy upon charge transfer with the metal, which has also been demonstrated experimentally^[39]. Since $\Phi' = -\epsilon_{HOMO,eff}$, a decrease in HOMO energy results in a larger Φ' . Naturally, the amount of charge transfer increases with increasing electron donor strength, as also shown in the previous section. However, the adsorption distance between the reaction partners also plays a decisive role, as will be rationalized in the following. In the case of Fermi-level pinning, E_F and $\epsilon_{HOMO,eff}$ align by definition, see Figure 4.16a. This is realized by the formation of a sheet of dipoles in the region between metal and monolayer, which induces a potential shift^[10]:

$$\Delta\Phi_{CT} = \frac{\mu_{CT}}{\epsilon_0 A} \quad (4.7)$$

Here, $\Delta\Phi_{CT}$ denotes the potential shift, μ the dipole moment in the unit cell, A the size of the surface unit cell, and ϵ_0 is the vacuum dielectric constant. As illustrated by Figure 4.16a, $\Delta\Phi$ is given as the difference between E_F and $\epsilon_{HOMO,eff}$. If we assumed that the HOMO energy did not change by metal/molecule interaction, this value would be constant independent of the adsorption geometry. As a consequence, the right hand side of eq. 4.7 - specifically, μ - must also remain constant upon change of geometry. If μ is imagined as point dipole, this means that the amount of charge transfer must decrease with increasing adsorption distance. By this argument it can be understood why the amount of charge donated from MV0 and tButV0 is similar despite their different electron donor character: although the difference between ϵ_{HOMO} and E_F is larger for tButV0, it is also further away from the surface, and less charge is required to induce the dipole necessary to achieve Fermi-level alignment. This trend is of course also true when the molecular levels are shifted by a charging energy. A larger adsorption distance implies a smaller charging energy, which in turn results in an energetically higher $\epsilon_{HOMO,eff}$ and thus a smaller Φ' . To demonstrate the magnitude of this effect, Figure 4.17 shows the evolution of Φ' for the adsorption of a (hypothetical planar) HV0 layer on Au(111) at different hypothetical adsorption distances. Between 3Å and 5Å, a range of more than 0.4eV is covered, showing the importance of this effect.

The adsorption induced geometry changes have a twofold impact on $\epsilon_{HOMO,eff}$. Nat-

Table 4.3: Highest occupied molecular orbital (HOMO) energy of the monolayer in its fully relaxed geometry, ϵ_{HOMO} , change in the HOMO energy due to bending, $\Delta\epsilon_{Bending}$, and change in the HOMO energy by charging, $\Delta\epsilon_{Charging}$. All values are given w.r.t. to vacuum level above the surface.

	HV0	MV0	tButV0
ϵ_{HOMO} (eV)	-3.18	-3.09	-2.87
$\Delta\epsilon_{Bending}$ (eV)	+0.22	+0.28	+0.33
$\Delta\epsilon_{Charging}$ (eV)	-1.07	-0.98	-0.96
$\Delta Total$ (eV)	-0.85	-0.70	-0.63

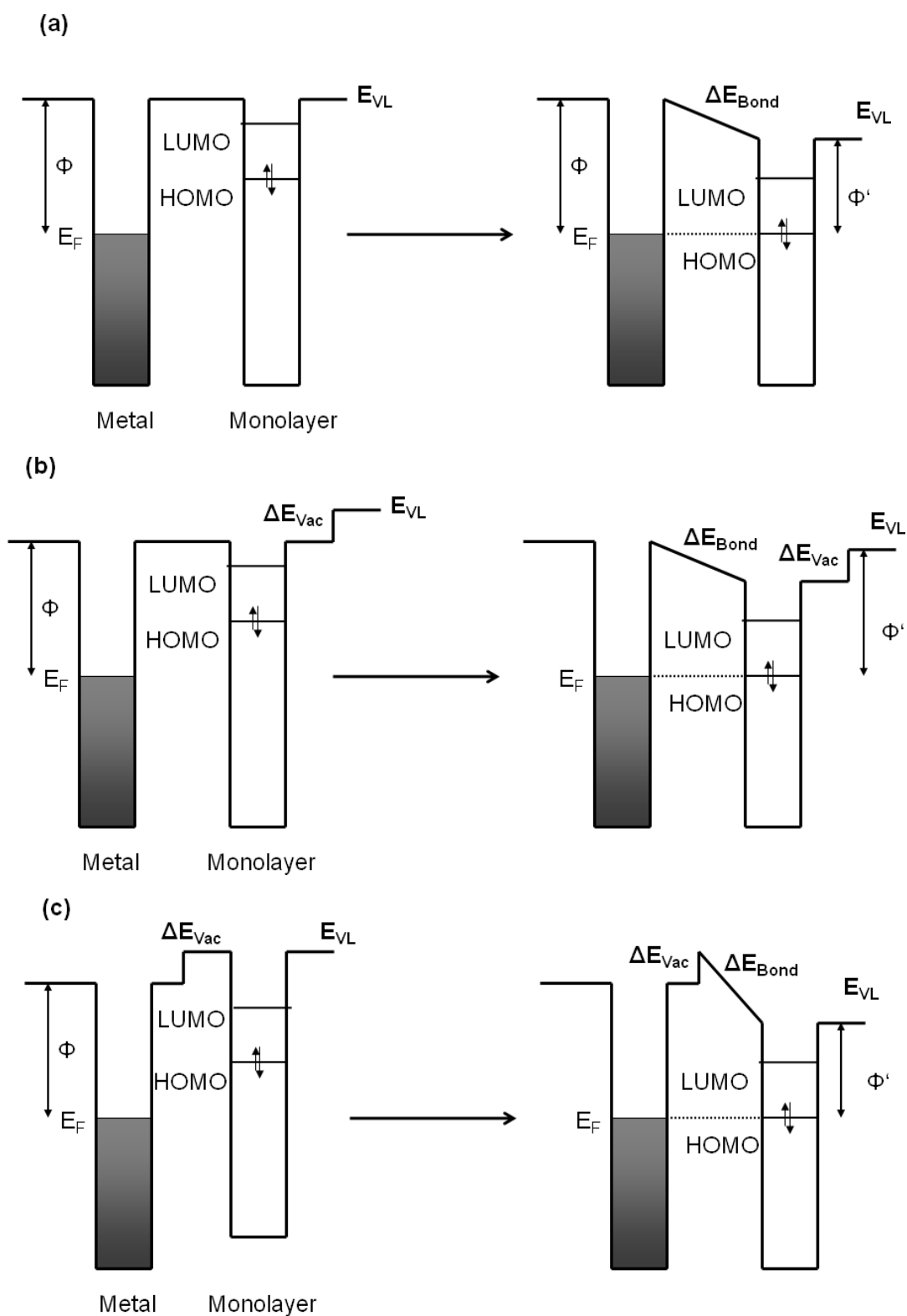


Figure 4.16: Schematic of the level alignment before (left) and after (right) achieving thermodynamic equilibrium. (a) Monolayer intrinsic dipole moment ΔE_{Vac} . (b) ΔE_{Vac} of the monolayer is located outside the metal-monolayer interface. (c) ΔE_{Vac} of the monolayer is located between metal and monolayer.

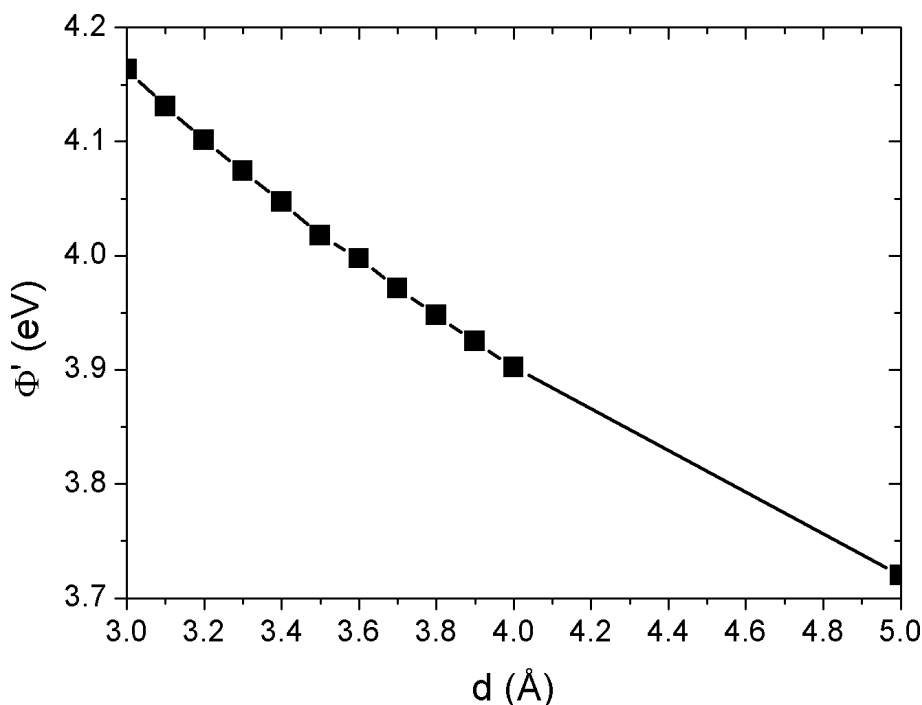


Figure 4.17: Evolution of the apparent work function, Φ' , with increasing adsorption distance d of HV0 on Au(111). Line intended as guide to the eye.

usually, the bending distorts the conjugation of the molecular π -system, decreasing the HOMO-LUMO gap. Also, the symmetry along the molecular plane is lost and a permanent molecular dipole moment is introduced perpendicular to the surface. Recently, we have shown that the spatial position of the induced dipole moment is of crucial importance for the effect on Φ' (see section 4.2). Only if the dipole is located above the molecule, $\epsilon_{HOMO,eff}$ is shifted with respect to the vacuum level above the system and a direct influence on Φ' can be observed, as shown in Figure 4.16b. In contrast, dipole moments which are located between metal and molecule are of little impact. Since the requirement that E_F and $\epsilon_{HOMO,eff}$ align is always given, a dipole moment located spatially between the corresponding charge densities in the metal (near E_F) and the molecule (at $\epsilon_{HOMO,eff}$) must be compensated for by an accordingly modified charge transfer, as shown in Figure 4.16c. Hence, Φ' is affected only indirectly via the amount of charge transfer need to achieve Fermi-level alignment, and hence via the charging energy (vide supra). A more detailed explanation and proof of these processes is given in section 4.2. In this context the question arises where, upon bending, the resulting dipole moment is located. Naively one could assume that the dipole moment is simply determined by the direction of the N-H bond. This, however, is not the whole truth. Rather, the bending induces a rehybridisation of the N-H bond, which results in electron density on the opposite side of the backbone. (More information on this is given in the supporting information). Hence, in the case of concave bending, the induced potential step is located between metal and monolayer, while it is located outside in the convex situation. A final, minor effect also that also impacts the HOMO energy

of the monolayer is that upon the geometric distortions due to the adsorption, the π -conjugation becomes perturbed, resulting in a smaller orbital gap.

To quantify the effects described in this section we have explicitly calculated the shift of the HOMO energy due to charging, $\Delta\epsilon_{Charging}$, and the orbital shift upon bending, $\Delta\epsilon_{Bending}$, for the title molecules. Note that the latter includes both the perturbation of the π -system and the shift due to dipoles outside the metal-monolayer junction, since it is unfortunately not possible to separate these two. $\Delta\epsilon_{Bending}$ has been calculated by comparing the energy of the HOMO (relative to the vacuum level above the surface) of the hypothetical, free standing monolayer in its fully optimized and its final geometries. The results, shown in Table 4.3, reveal that bending in all cases improves the donor strength of the molecules by increasing the HOMO energy by $\approx 0.2\text{eV} - 0.3\text{eV}$. As expected, the effect is most pronounced for the most strongly bent tButV0; in principle, the effect of bending alone would also be stronger for HV0 than for MV0. However, since for HV0 a dipole moment between the molecule and the vacuum level above the surface is induced, part of the HOMO shift is masked by the corresponding increase of the vacuum level. It should be noted that also for MV0, which remains virtually planar, a significant increase of the HOMO energy is observed upon reconstruction. To calculate the responsible charging energy, $\Delta\epsilon_{Charging}$, the HOMO energy of the free standing monolayer in its final geometry was compared to the HOMO energy in the adsorbed case. The results, also shown in Table 4.3, indicate that indeed the charging energy is the main reason for the mitigating interaction between metal and molecule, decreasing the HOMO energy by about 1eV. Surprisingly, however, it is found that the charging energy is smaller for MV0 and tButV0 despite the larger charge transfer from these molecules to the metal.

4.3.8 Conclusion

The influence of N,N'-disubstituting a monolayer of doubly reduced viologen adsorbed on the (111) surface of Au with methyl and *tert*-butyl moieties was studied in terms of the adsorption geometries, the bonding mechanism, the magnitude of charge transfer, and the work-function modification. It is found that the adsorption distance increases with $MV0 < HV0 < tButV0$. The bending is strongly influenced by the substituent, changing from convex (HV0), over planar (MV0) to concave (tButV0). Despite the longer bond between metal and molecule, the interaction strength increases with increasing electron donor character ($HV0 < MV0 < tButV0$). Despite the changes in the adsorption geometries and energies, the orbitals involved in the bonding process remain the same. Electron transfer is observed almost exclusively from the HOMO orbital of the monolayer to the metal. All three molecules are found to strongly reduce the work-function of the substrate. Nonetheless, it was found that the simple relation $\Phi' = -\epsilon_{HOMO}$ does not even approximately hold for these strongly interacting molecules, since charging effects and molecular distortions upon adsorption strongly influence the effective HOMO energy. Alkyl-substitution has a strong effect on both the bending and the charging energy. For the former, the work-function reducing effects is improved, while the work-function increasing effect of the latter is reduced. Together with its general electron-pushing effect, it can be concluded that alkyl substitution is a powerful

tool to improve the work-function modification induced by viologen monolayers.

4.3.9 Supporting Information

Unit Cell Used

To get a better conception about the shape of the viologen monolayers, the unit cell is shown exemplarily for MV0 in Figure 4.18

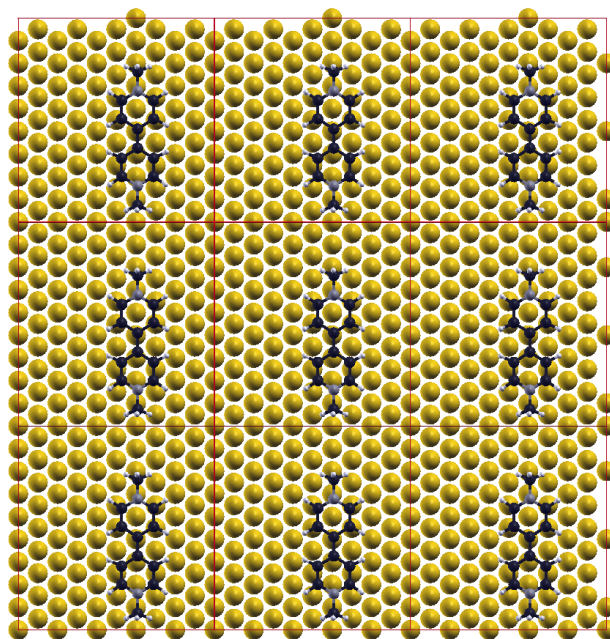


Figure 4.18: Unit cell used for the calculations, exemplarily shown for MV0. The unit cell was reproduced 3 times in x- and y-direction.

Charge-rearrangements at larger distances.

One of the prerequisites necessary to allow a meaningful extrapolation of the coulomb energy from larger to smaller distances is that the shape of the charge-rearrangement do not change significantly. To test this issue, in Figure 4.19 the plane-integrated charge rearrangements, $\Delta\rho$, of HV0 on Au(111) are shown for different adsorption distances. In analogy to the interaction energy, $\Delta\rho$ was obtained as

$$\Delta\rho = \rho_{combined} - (\rho_{monolayer}^* + \rho_{slab}^*) \quad (4.8)$$

The asterisk denotes that the subsystems were calculated at their coordinates of the combined systems, i.e., without further geometry optimization. It can be seen that in all cases, the negative charge transferred to the metal is localized ca. 1.6\AA above the top metal row. The electron donation comes mainly from the π -system of the organic compound, as evidenced by strong peaks above and below the molecular plane. Within the plane, charge-rearrangements are very weak. Between 10\AA and 3\AA , a continuous

increase of the amount of transferred charge is observed (manifesting itself by a larger charge in the electron density), as well as continuous narrowing of the peaks.

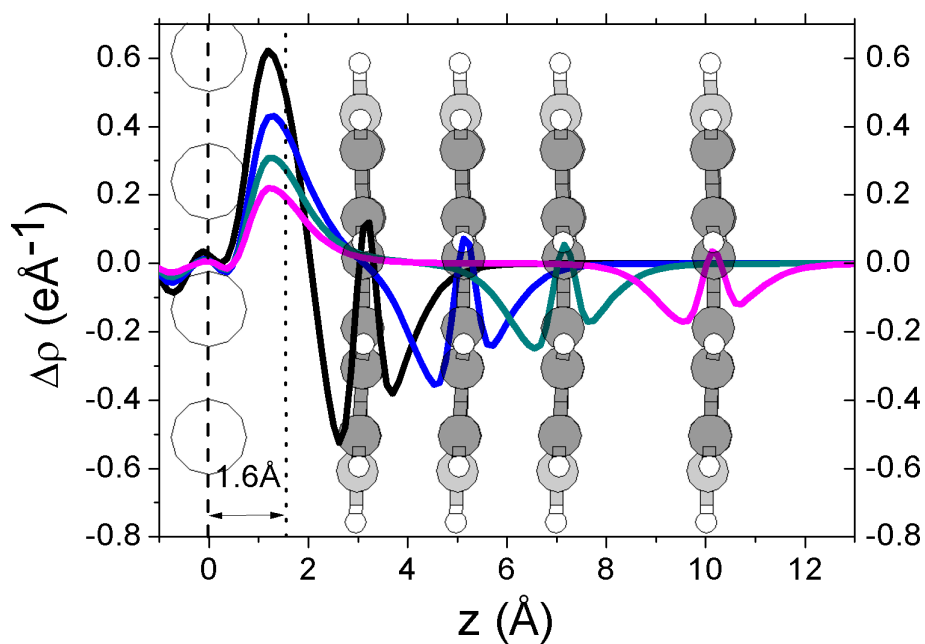


Figure 4.19: Plane-integrated electron rearrangements for HV0 on Au(111). In the background, the top metal layer and the position of the monolayer is shown.

4.4 A Semi-Classical Model for fast Estimation of the Work-Function Modification Induced by Charge Transfer Monolayers

4.4.1 Preface

During the IControl project, which was concerned with metal/organic interfaces between coinage metals and small molecular donors and acceptors, it was found that only a very limited number of potential candidates could be investigated experimentally due to the long time needed to synthesize and measure them. Unfortunately, the theoretical calculations were also unable to provide guidance, since density functional theory (DFT) calculations of molecules on surfaces require several months work, too, and hence cannot be done in a timely manner. Consequently, the idea to find (semi-)empirical relationships between molecular properties and the induced work-function modification arose. First attempts by Benjamin Bröker and Norbert Koch to directly relate ionisation potential (IP) or electron affinity (EA) to experimentally determined $\Delta\Phi$ s did not produce satisfying results. Therefore it was decided to use DFT to take a closer look at each of process involved in the work-function modification, and to create a semi-empirical model that could predict $\Delta\Phi$ s from the input of DFT gas phase calculations (which can be performed on a timescale of hours). The quality of the results would be measured on the work-function modifications that were determined experimentally within the IControl project.

A lot of people were involved in development of this semi-empirical treatment. Benjamin Bröker, Ralph-Peter Blum and Antje Vollmer performed ultraviolet photoelectron spectroscopy (UPS) measurements on more than 30 metal/organic systems and kindly provided me with the data prior to their publication. Most of the investigated molecules were synthesized at the MPI Mainz by Ralph Rieger. Norbert Koch and Egbert Zojer provided a lot of background knowledge on these kind of systems, the involved processes and level alignment in general. The work could not have been done without many fruitful discussions with Ferdinand Rissner, Gerold Rangger, and Georg Heimel. The role of Georg Heimel needs to be particularly emphasized, as he pointed out the existence of the polarization effect and the importance of the charging energy to me. It goes without saying that this turned out to be more difficult than originally thought, and the model could not be finished during the lifetime of the project. Nonetheless, it is planned to publish the results in the near future. The following parts of this section contain the manuscript in its current state.

4.4.2 Abstract

In this work, a conceptual model is presented which allows estimating the work-function modification induced by adsorption of conjugated molecules on metal surfaces much faster than periodic band-structure calculations. We report the possibility to obtain a good estimate of molecule-induced metal surface work function changes using a image-charge based model only based on the molecular ionization potentials (electron affinities) and its footprint area, which can be obtained by gas phase calculations, thus reducing

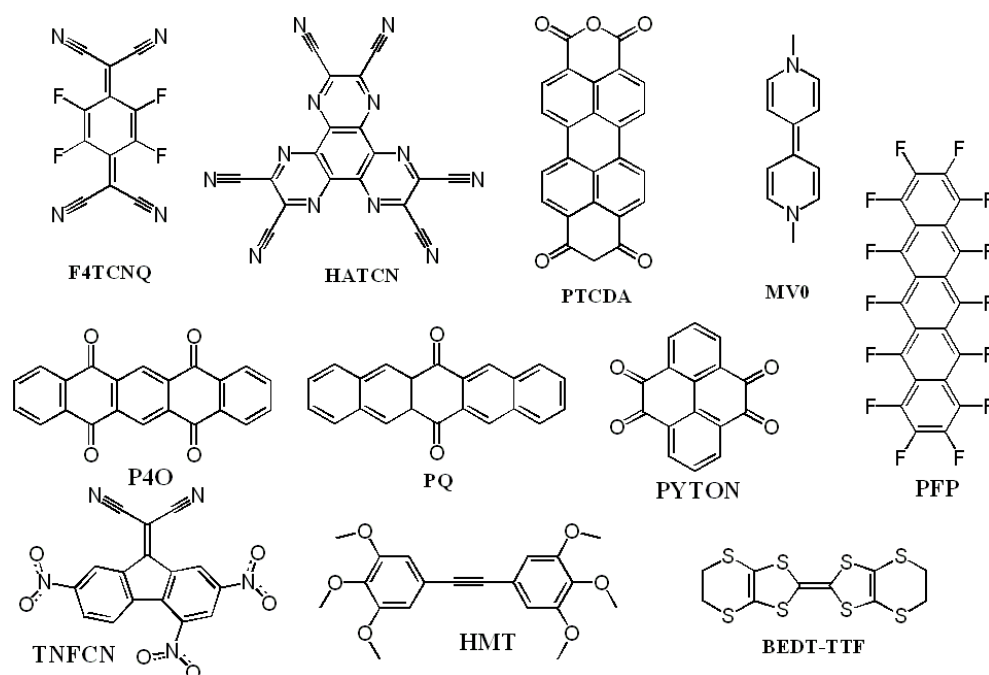


Figure 4.1: Chemical structure of the molecules used within this work. HV0: 1H,1'H-[4,4']Bipyridinylidene, BEDT-TTF: 5,6,5',6'-Tetrahydro-[2,2']bi[[1,3]dithiolo[4,5-b][1,4]dithiinyliene], F4TCNQ: 2-(4-Dicyanomethylene-2,3,5,6-tetrafluoro-cyclohexa-2,5-dienylidene)-malononitrile, HMT: 1,2-bis-(3,4,5-trimethoxyphenyl)ethene, MV0: 1,1'-Dimethyl-1H,1'H-[4,4']bipyridinylidene, PFP: Perfluoropentacene, HATCN: 1,4,5,8,9,12-Hexaaza-triphenylene-2,3,6,7,10,11-hexacarbonitrile, PTCDA: 3,4,9,10-perylene-tetracarboxylic-dianhydride, P4O: Pentacene-5,7,12,14-tetraone, PQ: pentacene-6,13-dione, TNFCN: 2-(2,4,7-Trinitro-fluoren-9-ylidene)-malononitrile, PYTON: Pyrene-4,5,9,10-tetraone

the required computational effort enormously. In order to establish the model, the dominant processes occurring at the interface between metal and adsorbate are identified and accounted for. Using band-structure DFT calculations with the proper boundary conditions for a small training set of molecules on metal surfaces, each of these processes is parameterized. To account for the strong interdependence of the processes, the set of equations is then solved by a self-consistent algorithm. Application to a fairly large test set consisting of eleven molecules of the surfaces shows excellent agreement with experiments; more than 80% of the systems are found within twice the experimental error. The reasonable error and the increased time-efficiency will allow a rough and fast testing of the effect of new molecules for their potential to optimize metal work function values for either good electron or hole injection in organic electronic devices.

4.4.3 Introduction

In modern (opto)electronic devices, the ability to control the interfacial electronic structure between the metal electrodes and the active organic layer is of critical importance. By tuning the electrode work function (Φ) and thus controlling charge injection/extraction barriers, high efficiencies in solar cells^[241, 257] or light emitting devices^[10, 258, 259] and increased currents in thin film transistors^[10, 260] can be achieved. Several methods have been proposed for this purpose. Cleaning and oxidation of Au via ozone and ultraviolet radiation yields a considerable Φ increase^[261–264]. Alternatively, doping the organic electron injection layer with alkali or earth-alkali metals can reduce its effective Φ significantly^[13–18]. A more general method is pre-treatment of the electrode with self-assembled monolayers bearing an intrinsic dipole^[19–22], which can modify Φ in either direction. A more recently proposed method is to employ a molecular (sub-)monolayer of particularly strong electron donors or acceptors^[265], which undergo a charge transfer reaction with the substrate. The such induced dipole moments have been demonstrated to allow for huge work-function modification ($\Delta\Phi$)^[23, 257] larger than -2.2 eV^[123] for donors and up to $+0.85$ eV for acceptors^[124] on high work function electrode materials such as Au, Ag, and Cu.

A large number of such charge-transfer layers has been investigated both experimentally and theoretically^[23–26, 130, 266], and still the quest for ever more potent systems continues. This is a rather slow process; for experimental studies, potential candidates need to be synthesized and subsequently tested in devices, often taking several weeks. Therefore, a pre-screening of potential molecules by means of computer simulations is advantageous. Unfortunately, theoretical treatment of molecules on surfaces on the DFT level or beyond is still very time-demanding. The situation therefore calls for a (semi)empirical treatment that allows a fast and efficient estimate of the adsorption induced work-function modification. Such a method necessarily has to build on the vast knowledge about the fundamental mechanisms at work in chemisorbed systems^[10, 12, 255] that has been developed over the past decades and which unraveled the dominant effects determining the electronic structure of such systems (*vide infra*).

The structure of this paper will be as follows: First, the currently most commonly used computational models to calculate $\Delta\Phi$ are briefly recapitulated. Then, a brief round-up of the processes governing the interface energetic as understood by ourselves will be given. The next section is concerned with the description of the empirical model and the functional forms and parameters used to describe the different types of interactions. The values of the parameters are then obtained from full band structure DFT calculations for only a few test systems, the inert hydrocarbon benzene on Cu, Ag, and Au. Then, the derived algorithm is successfully applied to a set of 31 (hitherto partly unpublished) experiments, encompassing eleven molecules with varying donor / acceptor strengths on three different metal surfaces (Au(111), Ag(111) and Cu(111); for two of the eleven molecules no experimental data on Cu(111) is available). The structure of these molecules is shown in Figure 4.1.

After the summery, a detailed description of the method

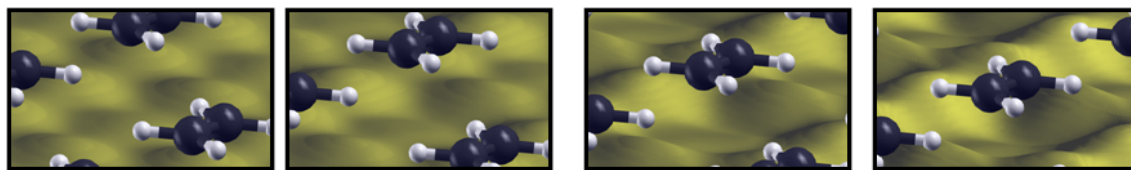


Figure 4.2: Schematic isodensity representation of the metal slab electron cloud for a hypothetical monolayer of ethene 4.0Å, 3.5Å, 3.0Å and 2.5Å above a Au(111) surface (left to right). The isodensity was obtained by subtracting the monolayer isodensity from the isodensity of the metal slab and plotting positive values only.

4.4.4 Current models

The models currently prevalent in literature are described in more detail in section ss:AlternativeModels and are omitted here for the sake of brevity.

4.4.5 Results and Discussion

I. Processes at the interface

The effects governing the level alignment between metal and conjugated donors and acceptors (forming the charge transfer (CT) monolayer) are summarized in section 2.1.2 and not repeated here for the sake of brevity.

For the reader's convenience, the processes occurring at the metal/organic interface are discussed sequentially here, i.e., as if one happened after the other. It must be kept in mind, however, that in reality all processes occur simultaneously and, thus, interfere with each other.

II. Accounting for Pushback

The first task is to find a suitable parameterization for the pushback effect. Even monolayers of atoms or molecules that do not undergo charge transfer processes, e.g. noble gas atoms^[32], alkanes^[30], or benzene^[267], strongly influence the work function of the metal substrate. In the absence of strong charge transfer, this manifests itself in reduced electron density between metal and monolayer, and increased electron density outside this region. It can be shown^[50] that the electron rearrangement always affects the metal more strongly. In figure 4.2, the electron density of the metal slab is schematically drawn for a hypothetical monolayer of ethene on Au(111) located at different distances from the surface. While at 4Å distance the electronic structure of the metal remains mostly unperturbed, the electron density becomes “dented” upon further approaching of the molecules.

Bagus et al.^[50] have deduced from basic quantum physical principles that the dipole induced by the pushback is to a good approximation given by

$$\mu \approx 2zS \quad (4.1)$$

with S being the overlap integral of the wave functions and d the distance between the reaction partners. Since the electron density of orbitals decays exponentially, so does the overlap between them, and hence S can be expressed as $m \cdot \exp(-k/d)$, k being the decay constant and m a normalizing factor. To a good approximation, the overlap increases linearly with the area of the molecule. In analogy to the Helmholtz equation, the induced change in the work function, $\Delta\Phi_{PB}$, depends inversely on the size of the unit cell, A . As the latter is itself a linear function of the molecular area for the densely packed systems modeled below (see section VII), A can be neglected for the calculation of the pushback induced shift in the electron potential. Absorbing the dielectric constant ϵ_0 and unit conversion factors of the Helmholtz equation and the overlap prefactor from the exponential form of S into m , equation 4.1 can be rewritten as

$$\Delta\Phi_{PB} = d \cdot m \cdot \exp\left(-\frac{d}{k}\right) \quad (4.2)$$

In this equation, m and k are constants for each metal, governed by the spatial extent of its electron cloud; typically, the pushback is assumed to be independent of the detailed structure of the adsorbate^[268]. Such an assumption appears reasonable, since experimental values indicate that inert molecules all give similar work function reductions^[11].

In order to obtain values for the parameters k and m , the z -dependence of $\Delta\Phi_{PB}$ was monitored calculated using band-structure DFT calculations for hypothetical monolayers of benzene on Au(111), Ag(111), and Cu(111). The coverage was chosen at 1 molecule per 45.3\AA^2 , which is in good agreement with experimental results for benzene on Au(111)^[269]. Benzene is chosen for the parameterization here, as (i) it represents a flat-lying, delocalized π -systems just like the systems we intend to describe here and (ii) it has a large enough gap so that only a minute amount of charge transfer between a benzene layer and the considered noble metals can be expected.

In Figure 4.3, the distance dependence of the push-back induced work-function modification for the three metals as calculated quantum-mechanically for the full system is shown for d between 2.5\AA and 3.9\AA (i.e., the region of distances, where push-back is particularly strong). The solid lines are fits according to eq. 4.2. The table next to figure 4.3 lists the obtained fit-parameters.

III. Metal screening

The surface polarization response to the added charge, \mathbf{P} , describes the ability of the metal electrons to screen any charge above the surface. The coulomb interaction between the charge and the such induced mirror-charge in the metal affects the ionization potential (electron affinity) of the adsorbate, reducing the gap between the levels. Experimentally, this effect has been verified by introducing NaCl spacer layers between the metal and the adsorbate^[225, 226]. For pentacene on Cu, a reduction of the gap by at least 2 eV has been observed^[226]. GW calculations confirmed for aromatic molecules on grapheme a band-gap reduction of ca. 2-3 eV^[35]. Unfortunately, \mathbf{P} is apparently not captured in the orbital energies computed by DFT^[35]. (Actually, this turns out

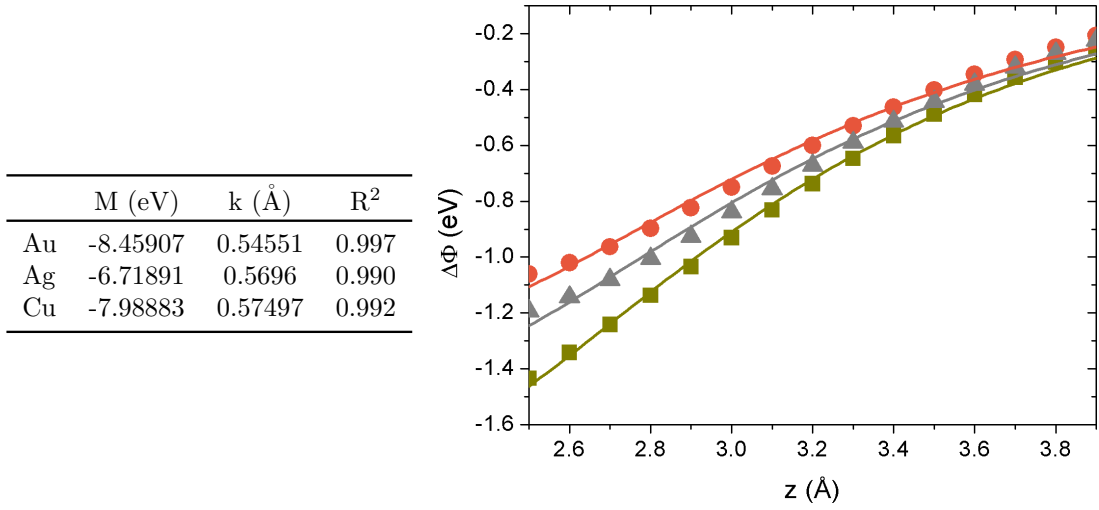


Figure 4.3: DFT calculated (symbols) and fitted (line) evolution of the work function modification induced by pushback for a tightly packed monolayer of benzene on Au (dark yellow), Ag (gray), and Cu (orange) (111) surfaces.

to be fortunate, as the band gap is underestimated in DFT anyways and hence these errors partly cancel out). However, it has been demonstrated that \mathbf{P} can be modeled well using an image charge potential^[36, 226, 249] of the type

$$P = \frac{1}{z - z_0} \quad (4.3)$$

Here, z_0 denotes the position of the metal image plane. To obtain the image plane position, we follow the method used in ref. ^[36], i.e., it is assumed that the image potential and the exchange-correlation potential intersect at one point in space and cross over smoothly, as shown in Figure 4.4 exemplarily for Au. Thus, we obtain image planes of 1.0Å for Au(111), 0.7Å for Ag(111), and 1.0Å for Cu(111), which is in good agreement with results reported in literature^[36, 270].

IV. Broadening the orbitals into molecular density of states

The magnitude of the broadening is determined by a number of properties of the full systems (i.e., the substrate and the adsorbate layer) including the amount of spatial overlap of the electron clouds as well as by the relative energies of the states and the orbital topologies. This forbids the explicit calculation of the magnitude and shape of the broadening in a screening approach in which a quantum mechanical calculation of the interacting system is to be avoided. Therefore, we chose an identical broadening for all molecular bands on all substrates. It is given by

$$DOS_{\epsilon_i} = \frac{2}{\sqrt{2\pi}\sigma} \exp\left(-\frac{E - \epsilon_i}{\sqrt{2}\sigma}\right)^2 \quad (4.4)$$

Here, $DOS(\epsilon)$ is the finite-width band derived from the orbital ϵ_i . This Gaussian type of broadening was chosen as it allows fast integration; unless otherwise noted, σ

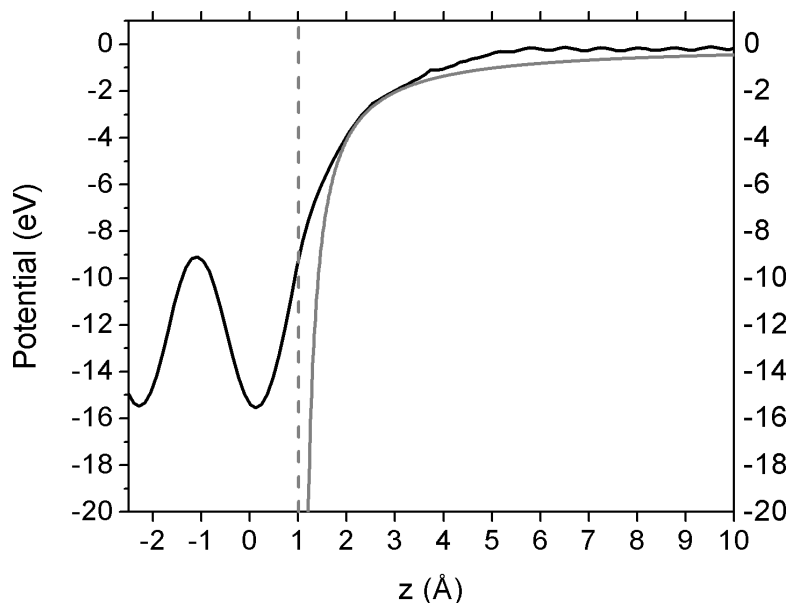


Figure 4.4: Exchange-correlation potential (solid black line), and mirror image potential (solid grey line) with an mirror plane located at $z=1.0\text{\AA}$ (dashed grey line). The top metal layer was set to $z=0\text{\AA}$.

was set to 0.1 eV equally for all orbitals. The factor of 2 ensures that total area of the peak corresponds to two electrons. Within this scheme, the total transferred charge per metal-molecule complex, ΔQ , is reasonably well described. It is given by integrating all occupied states above and all unoccupied states below the Fermi- energy, respectively: below the Fermi- energy, respectively:

$$\Delta Q = \int_{E_F}^{\infty} DOS_{\epsilon_i, occ} + \int_{-\infty}^{E_F} DOS_{\epsilon_i, virt} \quad (4.5)$$

By definition, negative charges indicate electron donation from the monolayer to the metal, while positive values of ΔQ correspond to back-donation from the metal to the molecule. We have carefully tested that neither the exact value of σ nor the broadening scheme (Gaussian or Lorentian) have significant influence on the calculated work function change.

One of the draw-backs of this simplistic approach is, however, that since all orbitals are equally broadened, only one orbital (HOMO or LUMO) will participate in charge transfer processes. Complex simultaneous charge forward and backward donation processes are not described. An example is the adsorption of the strong acceptor F4TCNQ on coinage metals^[24, 124], where the net effect of the filling of the LUMO is partly compensated by charge backward donation from nominally deep lying σ -orbitals (see appendix). Nonetheless, the $\Delta\Phi$ induced by these kind of systems is typically very well described, cf. section IX.

V. The charge-transfer dipole

For flat lying systems, a simple approximate description for the charge-transfer dipole, μ_{CT} , can be devised. Rather than accounting for the as smeared-out, delocalized shift of electron density, the charge transfer is described by localized point charges. Assuming the electron donation to / from the molecule affects the π -system equally, the charge on the molecule can be described as if it was located within the plane of the molecular π -system. For the counter-charge on the metal it must be memorized that image-charges are a not actual charges inside the metal, but a hypothetical concept to describe the electric field outside the metal, while there is no field inside the metal. Therefore, we assume that the counter charge on the metal resides on the mirror image plane, which was derived in the previous chapter. For the dipole per metal-molecule complex this yields:

$$\mu_{CT} = \Delta Q(d - z_0) \quad (4.6)$$

Note that from here on, we will use d as the distance between the monolayer and the metal substrate, and $z = (d - z_0)$ as the charge transfer distance as defined above.

VI. Charging of the monolayer

When a system becomes charged, it will, among others by virtue of coulomb repulsion, resist further charging. The charging energy \mathbf{U} can be defined as the change of the orbital energy with respect to the change in its occupation, i.e.

$$U = \frac{\delta \epsilon}{\delta n} \quad (4.7)$$

In literature, models proposed to calculate \mathbf{U} include artificially adding an small amount of charge to the adsorbate and doing a full quantum-chemical calculation^[39], or estimating \mathbf{U} from the difference of the gas phase DFT orbital energies and the IP-EA gap^[271]. Although the latter in principle provides a feasible pathway for the semi-empirical approach presented here, we chose a slightly different approach. Strictly speaking, IP and EA only yield information for occupation changes of an integer electron. In a less rigid concept, the orbital energies can also be understood as the energy gain induced by removal (addition) of an infinitesimal electron, i.e. $\Delta E = \int \epsilon dQ$. Nonetheless, the condition $IP = \int_0^1 \epsilon dQ$ must still be obeyed. If, as indicated in Figure 2.1a, HOMO = -IP in the uncharged molecule (i.e. $\epsilon(0) = -IP$), the solution to above equation is to set $\epsilon(1) = 0$. Several theoretical arguments indicate that the energy is a piecewise linear function of the occupation^[39], and therefore, for partial charge transfer, the charging energy can be interpolated

$$U = (0 - IP)\Delta Q \quad (4.8)$$

$$U = (0 - EA)\Delta Q \quad (4.9)$$

for electron donors and electron acceptors, respectively.

VII. Estimating the adsorption geometry

The last quantities to be determined are the surface area, A , occupied by each molecule and the adsorption height d .

VII.1: The size of the unit cell Owing to the two-dimensional (i.e., planar) nature of the investigated molecules, the footprint area can be estimated by calculating the molecular volume of the isolated molecule. Here, the molecular volume is defined as being encompassed in a contour of 0.001 electrons/Bohr³ density. To obtain the surface area of a molecule, one needs to (i) divide the volume by the diameter of a single carbon atom (given by the same volume calculation and assuming a spherical electron distribution, $h(\text{C})=1.98\text{\AA}$); (ii) secondly, a scaling factor needs to be introduced as the isodensity value of the volume calculation is too small to reflect densely packed layers^{II}. Because our simplistic approach overestimates the surface area per molecule by nearly 30%, we chose a value of 0.70, which yields reasonable agreement with experimental data for densely packed monolayers of PTCDA, F4TCNQ, and HATCN (HATCN: 136\AA^2 , experimental: $182\pm 15\text{\AA}^2$ ^[191], F4TCNQ 101\AA^2 , experimental $102\pm 20\text{\AA}^2$ ^[272], and PTCDA 134\AA^2 , experimental 124\AA^2 ^[132]; molecular structures see Figure 4.1). The large deviation for the HATCN molecules is due to its honey-comb-pattern, which is less tightly packed than the striped phase of F4TCNQ or the herringbone of PTCDA. Admittedly, the above approach provides only a rough estimate of the actual packing density. In this context, it, however, needs to be stressed that such complications will arise in any estimation of adsorbate-induced work-function changes unless experimental scanning tunneling (STM) or low energy electron diffraction (LEED) data are available; this is in particular also true for fully quantum-mechanical calculations of the combined metal/adsorbate systems. There, the molecular packing density is usually determined by an “educated guess”.

VII.2: The adsorption distance To provide an estimation of the adsorption distance it is necessary to compile an approximate potential well for the monolayer/metal interaction. The adsorption height will correspond to the global minimum of this potential well. There are three important factors governing the interplay between the reactants: Pauli repulsion upon overlap of two closed shell species, the van-der-Waals interaction, and the energy gained upon charge transfer.

The energy increase of a system due to Pauli repulsion stems from the same physical origin as the pushback effect. It is a purely quantum-mechanical effect which has no classical analogon. To parameterize it, the energy increase is taken from DFT calculations of the same hypothetical benzene monolayer as described in section II. The data was fitted to an exponential function. The obtained energies and fits are shown in the left part of 4.5.

Van der Waals (vdW) are not readily captured by standard DFT calculations, al-

^{II}0.001 electron/Bohr³ is the hard-coded value for the Volume keyword in Gaussian03. Because other contours can only be calculated by tinkering with the source code, it was chosen to scale the result instead.

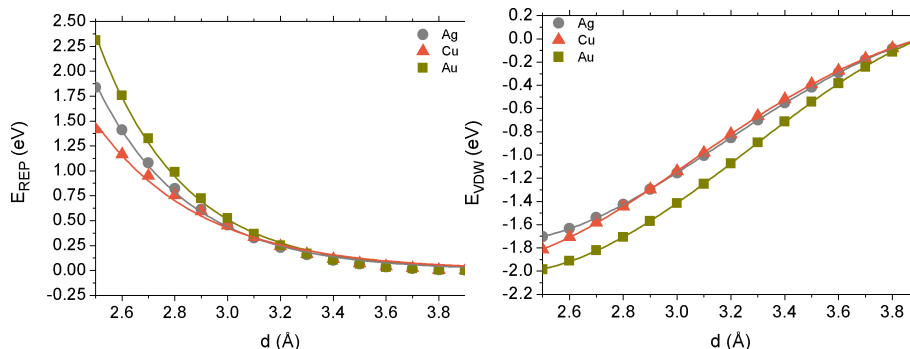


Figure 4.5: Left: Pauli repulsion of a monolayer of benzene adsorbed at different hypothetical adsorption distance on Au, Ag, And Cu. Right: Van der Waals attraction of a monolayer of benzene adsorbed at different hypothetical adsorption distance on Au, Ag, And Cu.

though significant progress has been made in this field recently [MRS-Review]. One possibility to account for this effect is to use the DFT-D^[108, 250, 273], which, put simplifying, just adds a corresponding potential to the PBE value. Recalculating the benzene monolayer from above using DFT-D, a significantly deep potential well obtained. By comparison to the calculation without Grimme’s addition, the van-der-Waals energy can be extracted. Note that this is not a simple d^{-6} term, because of the damping function included in the DFT-D approach and because benzene does not consist of one type of atoms only. Assuming that benzene is a prototypical system, the van-der-Waals energy distance dependence can be mapped onto a polynomial, as shown in 4.5b. Since both the Pauli repulsion and the van-der-Waals attraction increase with the number of atoms which is itself directly connected to the molecular area, we scale the obtained energies by a factor of $A/\text{Benzene}$, where A is the area of the molecule (see above), and Benzene the area of benzene. The original DFT-D parameterization does not extend to Au. Therefore, we used the recipe described in Ref. ^[108]. Details of these calculations, as well as the obtained C_6 and R_0 parameter for Au(111), are reported in the supporting information.

Finally, we turn to the energy gained upon charge transfer, $\Delta\Phi_{CT}$. The energetic for electron transfer is shown in Figure 4.6. The energy required to remove (or gained upon addition of) an electron to the metal is given by its Fermi energy (E_F). For the molecule, the analogous quantity is the orbital energy ϵ connected with IP or EA, respectively. In the Shottky-Moll-limit, illustrated by Figure 4.6b, the energy gained upon charge transfer is:

$$\Delta E_{CT} = (E_F - \epsilon_i)\Delta Q \quad (4.10)$$

However, in the course of charge transfer, the potential step between the metal and molecule builds up, as indicated in Figure 4.6b. This potential ramp depends on the amount of charge already transferred, and represents the energy gained by the charge

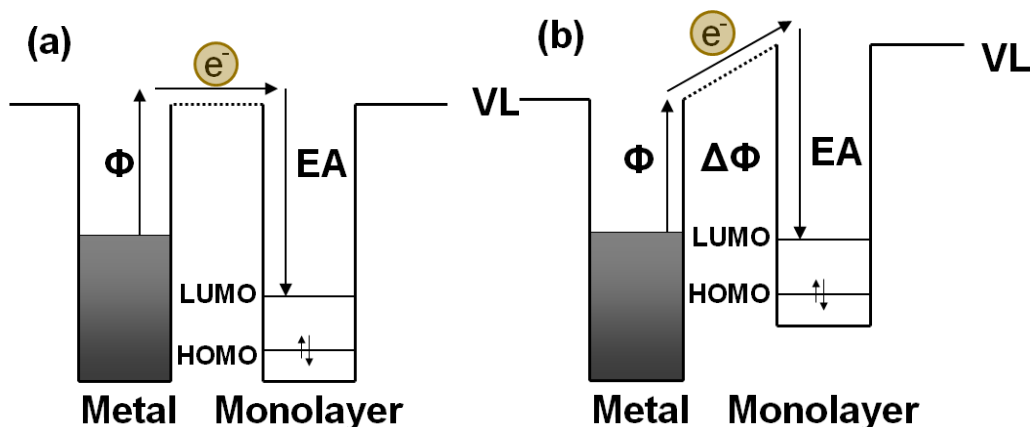


Figure 4.6: Schematic representation of the energy gained during electron transfer from the metal to the monolayer. To remove the electron from the metal, the work function Φ must be applied. The electron then transverse along the potential between metal and monolayer, which varies between 0 in the Shottky-Mott limit (a), and $\Delta\Phi$ when some charge has already been transferred (b). Finally, the electron affinity EA of the monolayer is gained.

moving through the “plate capacitor” that the 2D-periodic systems emulates. Eq. 4.10 has therefore be extended to

$$\Delta E_{CT} = (E_F - \epsilon_i)\Delta Q + \int_0^{\Delta Q} \Delta\Phi dQ \quad (4.11)$$

, where $\Delta\Phi$ is obtained from the effects described in sections II-VI. Since ΔQ increases with decreasing z , $\Delta\Phi_{CT}$ decreases monotonically with respect to the adsorption distance. As a consequence, stronger interaction between metal and molecule results in a smaller separation between the subsystems.

Using the terms acquired for the Pauli repulsion, van der Waals attraction, the charge transfer energy, a potential well can be constructed, whose global minimum is the adsorption distance. To demonstrate the construction of such a potential well, Figure 4.7 shows exemplarily the contributions of Pushback, van der Waals, and charge transfer for the system of PTCDA on Ag(111). To the best of our knowledge, the only molecule which adsorption distance has been determined on all three coinage metals is PTCDA^[132]. Applying the method described here to this prototypical case, adsorption heights of 2.90Å, 2.84Å, and 2.73Å are obtained for Au, Ag, and Cu, respectively. With an error of less 0.3Å, they compare fairly well to the experimental values of 3.27Å, 2.86Å, and 2.66Å^[181, 186, 187]. Note, however, that the depth of the energy well is not to be mistaken as adsorption or desorption energy, as besides others, the monolayer formation energy (which as no impact on the adsorption distance) is not accounted for. As an alternative to determine the adsorption distance we have also developed an approach where z as function of ΔQ is fitted to the experimental results of PTCDA (see supporting information).

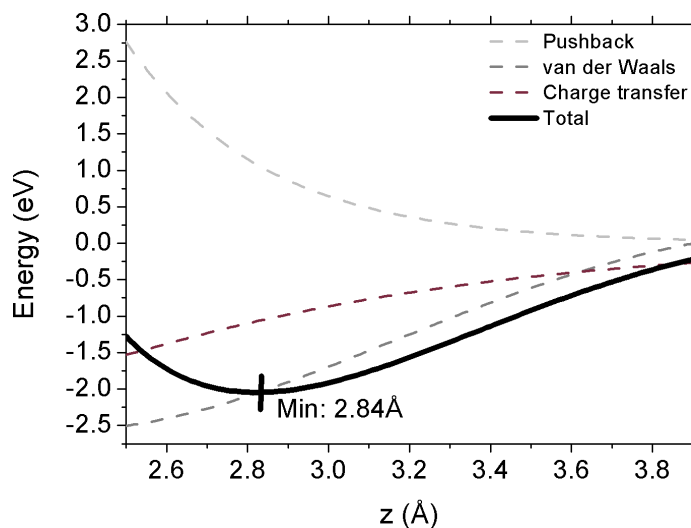


Figure 4.7: Determination of the adsorption height for PTCDA on Ag(111). The dashed lines illustrate the contribution of Pauli repulsion (light grey), van der Waals attraction (grey) and charge transfer (dark grey), which are summed up to a total potential well (think solid black line). The molecule is assumed to reside in the minimum, which in this case is found at 2.86Å.

VIII. Description of the algorithm

This section presents a short compendium of the employed algorithm, which is also depicted in the flow-chart in Figure 4.8.

The first step is to calculate the input parameters for the simulation - orbital eigenvalues ϵ_i and the molecular area A - via a gas phase DFT calculation. In parallel, adsorption height d and shift of orbital energies $\Delta\epsilon$ are set to default values ($d = d_{vdW}$, $\Delta\epsilon = 0$) for the first cycle. Also, the metal surface is specified by means of its Fermi energy E_F .

The energy eigenvalues are broadened according to eq. 4.4 and the corresponding charge transfer, ΔQ is calculated by integrating the obtained functions above and below the Fermi level of the metal for occupied orbitals and for unoccupied orbitals, respectively (eq. 4.5). Using this result, the work function change due to the induced dipole, $\Delta\Phi_{CT}$, is calculated according to equation 2.1, along with the orbital energy shift due to charging, \mathbf{U} , and the change in orbital energy due to polarization, \mathbf{P} which are given by eqn. 4.9 and 4.3, respectively. In parallel, the work function change induced by pushback, $\Delta\Phi_{PB}$, is computed via equation 4.2.

In the next step, the three just calculated quantities are combined to give a new value for $\Delta\epsilon$. If this value is not equal to the guess from the current cycle (within 0.01 eV), than a new guess is made, and the second step is repeated until convergence is achieved.

Once stable values for $\Delta\epsilon$ and thus ΔQ are found, the energy gained upon charge trans-

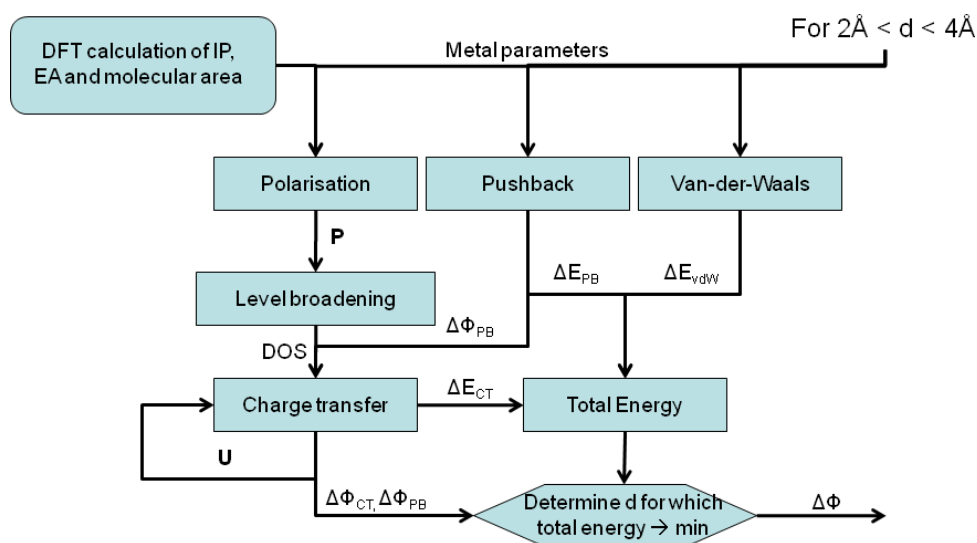


Figure 4.8: Schematic flowchart of the algorithm used to determine the work function modification.

fer is calculated using eq. 4.11. The same procedure is repeated for all metal-molecule distances between 2.0\AA and 3.5\AA . Then, the potential well for energy vs. adsorption distance is set up, and its minimum is determined. The work-function modification at the energetic minimum is then calculated using eq. 2.3 and reported as result.

It should be emphasized at this point that despite the nested iterative loops, the algorithm performs very fast. Once the input parameters are known, the complete testset described in the next section is computed in less than 5 minutes on a normal desktop PC. Considering the relatively crude parameterization of our model in sections II-VII relying on a relatively small training set (F4TCNQ on Ag(111) and viologen on Au(111)) and the conceptual shortcomings discussed above, the question arises, whether the present approach has any predictive power. To answer that question, we have applied it to a number of donor and acceptor molecules on the three coinage metal surfaces Au(111), Ag(111), and Cu(111).

IX. Predicting Experiments

The chemical structures of the 11 molecules for which the above parameterization has been tested are shown in Figure 4.1. They span a broad range from the particularly strong acceptor F4TCNQ via less potent molecules to the strong work-function reducing molecule MV0. The actual work function modification induced by a single monolayer was probed by ultraviolet photoelectron spectroscopy on three different substrates, Cu(111), Ag(111), and Au(111) apart from P4O and PQ on Cu(111) for which no experiments have been performed. Experimental work-function modifications have been published before for F4TCNQ^[24, 124] on all three metals, MV0 on Au(111)^[123], and PQ on Ag(111)^[274]. For PTCDA, the data were taken from ref. ^[185]. Note, however,

that for PTCDA on Ag(111), experimental values deviating by as much as 0.2 eV have also been reported^[182], which is due to how the experiments were conducted in detail. Because PTCDA belongs to the molecules most thoroughly investigated, we, therefore, assume the experimental error to be of the order of ± 0.2 eV. For the rest of the testset, we are not aware of any data available in literature.

Figure 4.9 compares the work function modification obtained by the UPS experiment (closed symbols) with the theoretical ones, calculated via the algorithm described above. The input parameters for the simulations were obtained using DFT calculations as described in the method

BEDT-TTF is a relatively strong donor with a gas phase ionisation potential (IP) of 6.3eV; yet in the experiments a work-function change of only -0.4 eV is observed, which is a significantly smaller reduction than what one would expect for systems in which only push-back is observed, let alone for a charge-transfer monolayer. From this discrepancy one has to conclude that this molecule upon adsorption on coinage metal surfaces most likely does not adopt the idealized structure that was assumed for our algorithm, i.e. a closed, flat lying charge-transfer monolayer without significant covalent character. Either it undergoes a more complex reaction with the surface or displays significant island growth. To further test this issue, single point DFT band-structure calculations of BEDT-TTF adsorbed on Au(111) in a low packing regime, at an adsorption heights of ca. 2.5 Å and 3.0 Å were performed. Despite the use of a grossly oversized unit cell, the $\Delta\Phi$ -values obtained (-0.90 and -0.75 eV, respectively) are significantly more negative than observed experimentally.

The other system that is particularly poorly described is TNFCN on Au. Indeed, this system appears to be a pathologically unfortunate case inasmuch as the experimental values indicate that only pushback takes place, whereas the simulation does predict weak but significant charge transfer. Apart from these three pathological systems, the semi-empirical treatment proposed in this work performs extraordinarily well. Of the remaining 28 systems, 20 systems are in full agreement with the measured value. The mean average deviation between experiment and predicted value, given as

$$MAD = \frac{\sum |\Delta\Phi^{exp} - \Delta\Phi^{sim}|}{n} \quad (4.12)$$

(with $\Delta\Phi^{exp}$ being the experimental values, $\Delta\Phi^{sim}$ being the simulation, and n being the number of systems), is found to be 0.206 eV, which is over-all an excellent agreement considering the exceedingly simple approach and can well compete with alternative, much more involved approaches.

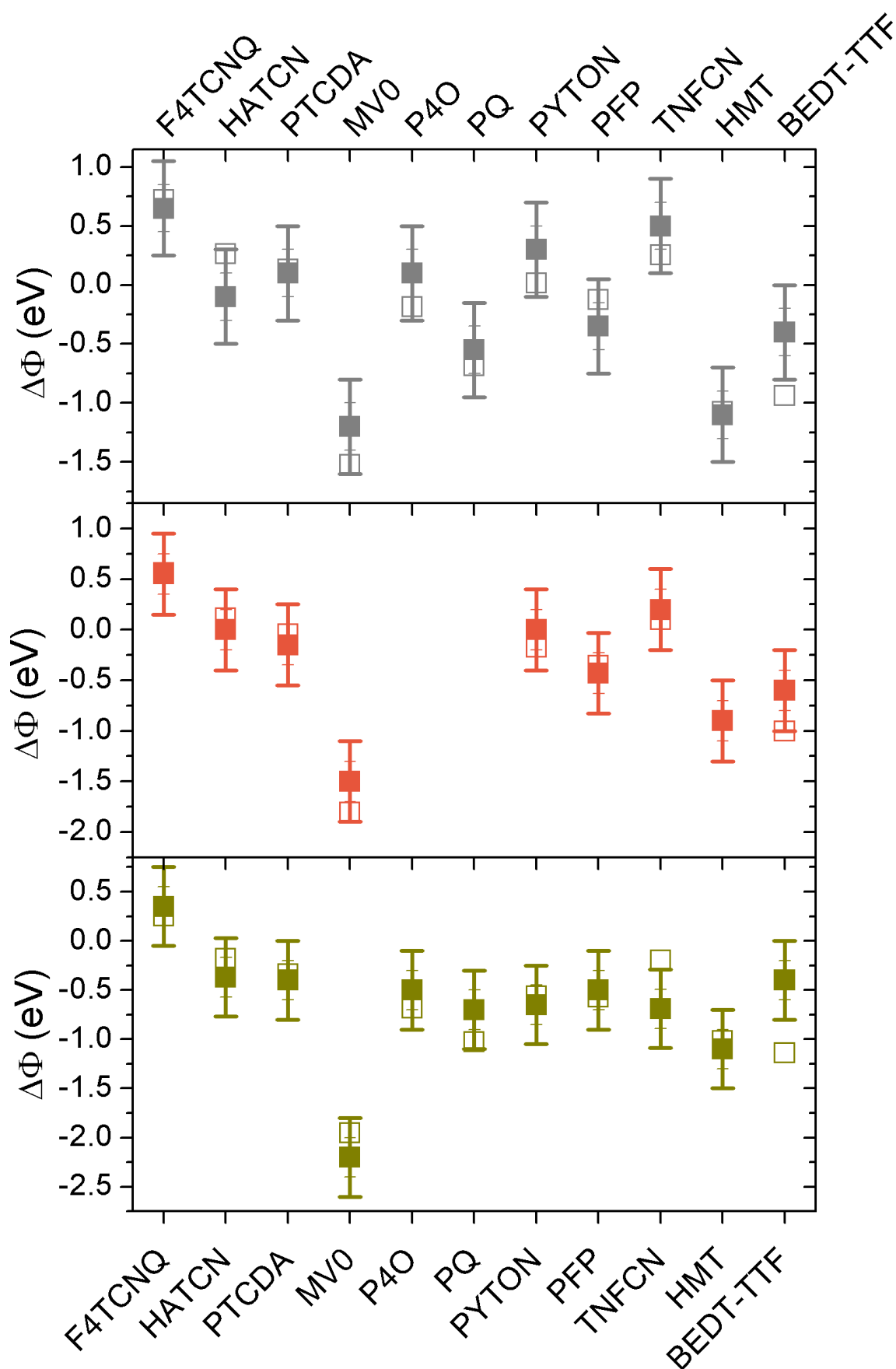


Figure 4.9: Calculated work-function modification (open symbols), and experimental work function modification (closed symbol) on Ag(111) (top, grey), Cu(111) (middle, orange) and Au(111) (dark yellow, bottom). The small error bar represents the estimated experimental error of 0.2 eV, the large error bar corresponds to twice this value

4.4.6 Conclusion

In this contribution, a model for the time-efficient prediction of work function modification induced by planar, conjugated organic molecules on top of metal surfaces is presented. The input needed are only the metal Fermi energy, as well as the frontier orbital energy and the molecular area. All molecular properties can be obtained using gas phase calculations. As such, they are available much faster than work functions explicitly calculated by band-structure DFT calculations. Nonetheless, employing the treatment proposed in this work allows for a fairly accurate prediction of the adsorption induced work-function modification. Out of 31 measured systems, 28 (>90%) were found within twice the experimental uncertainty, and 20 (i.e., almost two thirds) were in full agreement with UPS measurements.

4.4.7 Methodology

For the sake of computational consistency, all band-structure DFT calculations were performed using the periodic boundary condition code VASP^[51–53, 56], employing the PBE functional^[54, 68] and a plane-wave basis set with a cutoff value of 20 Ryd. The density of states was occupied using the Methfessel-Paxton^[58] scheme (broadening 0.2 eV). The surface was simulated by a 5 layer metal slab, the adsorbate, and a sufficiently large region of vacuum (>30Å) between the adsorbate and the next periodic replica of the metal slab in z-direction. Artificial dipoles were included in the vacuum to prevent polarization of the unit cell. Unless noted otherwise, all DFT band structure calculations were performed in a $3 \times 3\sqrt{3}$ unit cell using a set 5x5x1 k-points. More details on the computations and extensive testing of the method The isolated molecules were calculated using the Gaussian03^[71] package using the 6-31+G* basis set and the B3LYP exchange-correlation functional as implemented. To obtain ionization potentials (IP) and electron affinities (EA), the Δ SCF method has been employed, i.e. the total energies of the neutral and the respective charged species have been calculated explicitly. All moieties have been fully optimized, i.e. the obtained IPs and EAs are adiabatic values.

UPS experiments were performed at the endstation SurICat (beamline PM4) at the synchrotron light source BESSY II (Berlin, Germany) or at the FLIPPER II end-station at HASYLAB (Hamburg, Germany). Additional UPS experiments were conducted at Humboldt-Universität using HeI radiation. The secondary electron cutoff (SECO) spectra were obtained with the samples negatively biased (usually -3 V to -10 V) in order to clear the analyzer work function. All experimental setups consist of interconnected sample preparation (base pressure $< 5 \times 10^{-9}$ mbar) and analysis (base pressure 1×10^{-10} mbar) chambers, which enable sample transfer without breaking vacuum. Metal single crystals were cleaned by repeated cycles of annealing (up to 550 °C) and Ar-ion sputtering. Organic materials were sublimed from resistively heated Al_2O_3 crucibles or tantalum pinhole sources. The mass-thickness of the organic layers was monitored with a quartz crystal microbalance and all experiments were carried out at room temperature.

4.4.8 APPENDIX: Limitations of the model

Not all physical effects which affect the work function modification by an adsorbate are properly accounted for by the processes and parameters described above. In particular, geometrical distortions of the molecule due to the interaction with the metal, i.e., bending, and chemical reactions (in the sense of bond dissociations, etc.) are not considered.

The first effect, geometric distortions, is often assumed to be small^[45]. Indeed, for molecules which remain planar after adsorption, this is a good approximation. density functional theory (DFT) calculations assuming that planarity is preserved for the test molecule viologen adsorbed 4Å above a Au(111) surface show that despite the large amount of charge transferred (0.6 electrons), the bond lengths of the molecule change by less than 0.03Å. Consequently, also the change of the HOMO eigenvalue induced by the geometric distortions is small, i.e., it shifts by 0.01 eV. Similarly small bond length changes were reported for perylene-3,4,9,10-tetracarboxylic-3,4,9,10-dianhydride (PTCDA) on Au(111)^[45].

More severe changes of the energy levels are to be expected when the molecules bends upon adsorption. Such bending is, indeed, observed theoretically as well as experimentally^[24, 191]. This out-of-plane bending always disturbs the conjugation of the molecule, resulting in change of the orbital eigenvalues as well as inducing a dipole moment perpendicular to the surface, which should also impact the work function according to eq. 2.1. Fortunately, we were recently able to demonstrate that bending is almost inconsequential for the work-function modification as long as the induced dipole moments are located between metal and molecular π -system (cf. section 4.2). Naturally, such “downward” bending is the most common type of strong geometrical distortion, being a result of the balance of repulsion of the π -system and attractive forces due to bond formation of docking groups located at the periphery of the backbone. However, the odd case of upward bending cannot be ruled out, and in such situations, the predicted value will be in error by the work-function modification induced by corresponding dipole.

Chemical reactions, in contrast to the charge transfer processes, involve the breaking of existing bonds and the formation of new ones. On coinage metals, such processes occur, for example, upon adsorption of thiolate-bonded monolayers^[21]. As bond formation and breaking are quantum processes associated with severe rearrangements of electrons changing the shape and positions of orbitals – and possible the arrangement of atoms *en gross* – they cannot be captured by the present largely electrostatic model. Consequently, the present model cannot be reliably applied to situations in which the formation of strong localized metal-molecule bonds is to be expected.

A further shortcoming arises from the assumption that all orbitals broaden equally, the treatment presented here is neither able nor intended to give the correct level alignment for systems with complex charge transfer mechanisms, such as simultaneous charge transfer and back transfer. A classical example for this case is F4TCNQ on Cu(111). By projecting the electron density onto molecular orbitals, a donation of 1.8 electrons has been reported, accompanied by a back donation of ≈ 1.0 electrons^[24], i.e. 0.8 electrons

in total. Note that the respective orbitals for donation and back donation are spatially located on different distances to the surface. In contrast, we find here a net charge of just 0.3 electrons, which we ascribe partly to the different partition schemes. Note that is unfortunately not possible the same definition for both systems, because in the bent system no clear definition of d can be given.

Additionally, typically less significant effects aspects that are not considered involve dynamical image screening^[122, 275] or vibrational effects^[276], as well as the impact of finite temperature. In this context it should be mentioned that these effects also are not captured by state-of-the art DFT calculations on the interacting metal/molecule system as well, in spite of the considerably larger computational efforts.

4.4.9 Supporting Information

Generating the DFT-D parameters for Au

Note: This subsection differs somewhat from the paper manuscript, as more technical information (employed keywords, analysis tools, routes that do not work) has been added.

Generating the DFT-D Parameters for Au

The DFT-D formalism is an extension to any DFT-functional, which adds dispersion forces by addition of pairwise potentials. Being a semi-empirical method, it relies on two parameters which must be obtained for any atom present in the system. These parameters are the C6 coefficient, which governs the strength of the interaction, and the van-der-Waals radius R_0 . In the original work by Grimme^[108], values for all atoms up to Xe are given. Some of the systems of interest in this work, however, also include the heavier species Au. It was therefore decided to generate an “own” set of values. All calculations were performed using Turbomole 5.7^[277]. All energies were converged to 10^{-9} Hartree. Additionally, the electron density was set converged to 10^{-7} au. Atomic ionization potentials (IP) were obtained at the unrestricted PBE0/QZVP level as the difference of the total energy between the neutral and the positively charged species. The static polarizability, α was obtained from the neutral species at the same level of theory by performing an escf-calculation with the \$polly-keyword set. According to Grimme^[108], C_6 in $Jnm^{-6}mol^{-1}$ is then given by

$$C_6 = 0.05N \times IP \times \alpha \quad (4.13)$$

Here, N is the number of the electrons of the noble gas atom in the same period. All other values are given in atomic units. For the calculation of transition metals, a direct calculation is not recommendable. Instead, for C6 the average of the preceding group 18 (VIII) and following group 13 (III) element is to be taken^[108].

To obtain the van-der-Waals radius from ROHF/TZV calculations, the moloch script, which is delivered along with the Turbomole-suite, was employed to generate a two-dimensional electron density map with two one of the borders being the line through

the atomic core. The distance at which the electron density falls below $0.01a_0^{-3}$ is taken as R_0 ^[108]. Again, the direct calculation of R_0 for transition metals is not recommended. Instead, the average of the preceding group 2 (II) and following group 13 (III) element is used^[108]. It should be mentioned here that the alternative method of setting the `$pointval`-keyword with the option `geo=line`, which allows to print the electron density along a line directly, appears to yield different results even though in the newer version of Turbomole, this is the preferred version to output density plots. This discrepancy however, was not investigated further. Again, the direct calculation of R_0 for transition metals is not recommended. Instead, the average of the preceding group 2 (II) and following group 13 (III) element is used^[108]. For some atoms, no triple or quadruple-zeta basis set was available in the basis set file. In these cases, the correct basis set was downloaded from the EMSL basis set library (<https://bse.pnl.gov/bse/portal>). For atoms heavier than Kr, effective core potentials were used. The open shell atoms Ga, In, and Tl, require the employment of O_h symmetry of R_0 only. The define script of Turbomole thus automatically detects that the open shell is threefold degenerate and allows to split the remaining electron into all three orbitals (i.e., 1/3 occupancy). This step is crucial since in lieu of symmetry, a cylindrical electron distribution around the open shell atoms is obtained, and no R_0 can be assigned. Using symmetry for the unrestricted DFT-level as well yields significantly different values for IP and the polarizability, which are however not in agreement with the values published! It is not clear why the symmetric values have not been used by Grimme, and possibly is only an oversight. Since the rest of the DFT-D functional has been fitted to the values he shows in Ref^[108], it was decided to strictly follow this methodology. For In, the C_6 parameter obtained including symmetry is $16.51 \text{ Jnm}^6\text{mol}^{-1}$, which is markedly different from the correct $37.33 \text{ Jnm}^6\text{mol}^{-1}$. On a technical basis it should be added that obtaining converged unrestricted calculations for the open-shell atoms was not trivial. Without symmetry, it was necessary to set the occupation of In and Tl by hand to

```
$alpha shells
```

```
a 1,2 (1)
```

If symmetry was employed, the start guess for UHF did not allow for partial occupancies. As workaround, the occupation was defined for the doubly negatively charged species, which yields an occupation of (1) electron for all three degenerate t_{2g} orbitals. In the control file, the occupation was then set by hand to (1/3).

In order to test the method

Overall, the values of Grimme have been well reproduced. Small discrepancies can be attributed to the finite grid size of the electron density. The obtained R_0 -parameter for La-Hg is in good agreement with the one from Tonigold et al. (1.7\AA , [private communication]). However, the C_6 -parameter is somewhat smaller ($59.35 \text{ Jmol}^{-1}\text{nm}^6$). In order to double-check the results, C_6 and R_0 were also computed by Georg Heimel using the Gaussian03 software. Except for small discrepancies which are attributable to the differences in the basis set (Gaussian uses, e.g. a smaller core for the ecps), the values shown here were confirmed.

Table 4.1: C_6 and R_0 for selected atoms as calculated by Grimme and by ourselves.

	Published by Grimme		(Re-)calculated	
	C_6 (Jnm^6mol^{-1})	R_0 (Å)	C_6 (Jnm^6mol^{-1})	R_0
Ar	4.61	1.595	4.61	1.596
Ca	10.80	1.474		1.475
Ga	16.99	1.650	16.99	1.647
Kr	12.01	1.727	12.01	1.727
Sr	24.67	1.606		1.608
In	37.32	1.672	37.33	1.697
Xe	29.99	1.881	29.99	1.881
Ba				1.766
Tl			57.27	1.679
La-Hq			43.63	1.723

Alternative method for distance determination

Instead of employing benzene as reference system to calculate the repulsive and the attractive term, and then using the charge transfer energy to create a (pseudo)potential well in which the molecule resides, we present here an alternative method which relies on the experimentally known adsorption distances. To the best of our knowledge, the only suitable molecule for which high quality data are available on all three coinage metals is PTCDA^[132, 181, 186, 187]. Upon adsorption, this molecule experiences little geometric distortion of only some hundredth Å, and can hence be considered to be de facto planar. It is thus convenient to use this molecule for an empirical, experimental parameterization of the adsorption height. Beforehand, the boundary conditions for the corresponding potential should be discussed. It is reasonable to assume that the maximal distance corresponds to the sum of the van-der-Waals radii of metal and molecule. Indeed, this is exactly what is observed for PTCDA on Au(111), where virtually no charge transfer between adsorbate and substrate occurs^[186]. Furthermore, the distance can be expected to be smaller the larger the charge transfer is. However, linear or quadratic dependence on ΔQ is out of question, because they show (for some molecules) a self-amplifying effect, i.e., the closer a molecule comes to the surface, the larger the transferred charge becomes, which in turns forces the molecule even closer again. Many commonly used potentials, such as the Lennard-Jones(exp,6) or the Morse potential, employ an exponential dependence between energy and distance as dominant term. It thus suggests itself to use a logarithmic ansatz of the form

$$d = d_{vdW} \ln \frac{\Delta Q}{Q_0 + 1} \quad (4.14)$$

Here, d_{vdW} is the van-der-Waals distance between metal and molecule (i.e., the sum of metal and carbon van-der-Waals radius). Using equation 4.14 to fit the experimental adsorption heights of PTCDA on Au, Ag, and Cu published in Refs. ^[132, 181, 186, 187], a value of $Q_0 = 0.445e$ is obtained.

Applying the new adsorption height determination, the obtained work-function mod-

ifications agree only slightly worse with the experiment, see figure 4.10. Naturally, the results for PTCDA are in excellent agreement. Otherwise out of a total of 31 systems, 17 are found within the experimental error, and 9 more are located within 0.4eV of the measurement. The most severe errors in the simulation occur again for MV0 on Au, and also TNFCN on Au is badly described in this approximation. The other systems for which the algorithm fails are HMT on Au and Ag, PYTON on Ag, and P4O on Ag. In general, a somewhat larger distribution of the values is observed, and the mean average deviation increases to 0.234. Nonetheless, given the few data point used for the parameterization, the agreement between simulation and experiment can be considered as very good.

Impact of the method used to obtain the molecular gas phase values

To demonstrate the general applicability of the method, Figure 4.11 shows the calculated work-function modification using AM1 input parameters instead of B3LYP/6-31+G*. The agreement between simulation and experiment is still very good, 24 systems are found within twice the experimental error. Even with these parameters the same three systems as in the main text are badly described. Additionally, the simulation also apparently fails for PFP on all three metals as well as MV0 on Au; in all cases, the work-function is computed too large. In total, the mean unsigned error is found to be 0.256, which can still be considered to be good agreement between simulation and experiment.

Numerical Stability and Impact of the Actual Choice of the Chosen Parameterization

Since only a small training set has been used to obtain the model parameters, some final remarks should be made on the stability of the results with respect to the chosen parameters. To that aim, some parameters have been strongly modified and change with respect to the default parameter are shown below. The first parameter to be varied was the broadening of the peaks, shown in Figure 4.12a. In most cases, the broadening does not have significant impact on the obtained work-function modification. Only for the molecules HMT, the influence of the actual choice of σ on the simulated work function exceeds 0.1eV, which is likely related to the fact that no charge-transfer occurs at too small broadenings.

The second test parameter was the influence of the Parameter used to scale the molecular area. As shown in Figure 4.12b, the impact is much larger for this value, indicating that the packing density is indeed a very important parameter governing the interface energetic. Another importance factor to consider is the charge-transfer distance, which is given by the distance between the molecule and the mirror image plane. Figure 4.12c demonstrates the situation for larger and smaller charge-transfer distances. Naturally, the effect depends very strongly on the donor or acceptor strength of the system, and the prediction of the work-function modification for F4TCNQ changes by as much as 0.3eV upon increasing or decreasing z by $\pm 1\text{\AA}$.

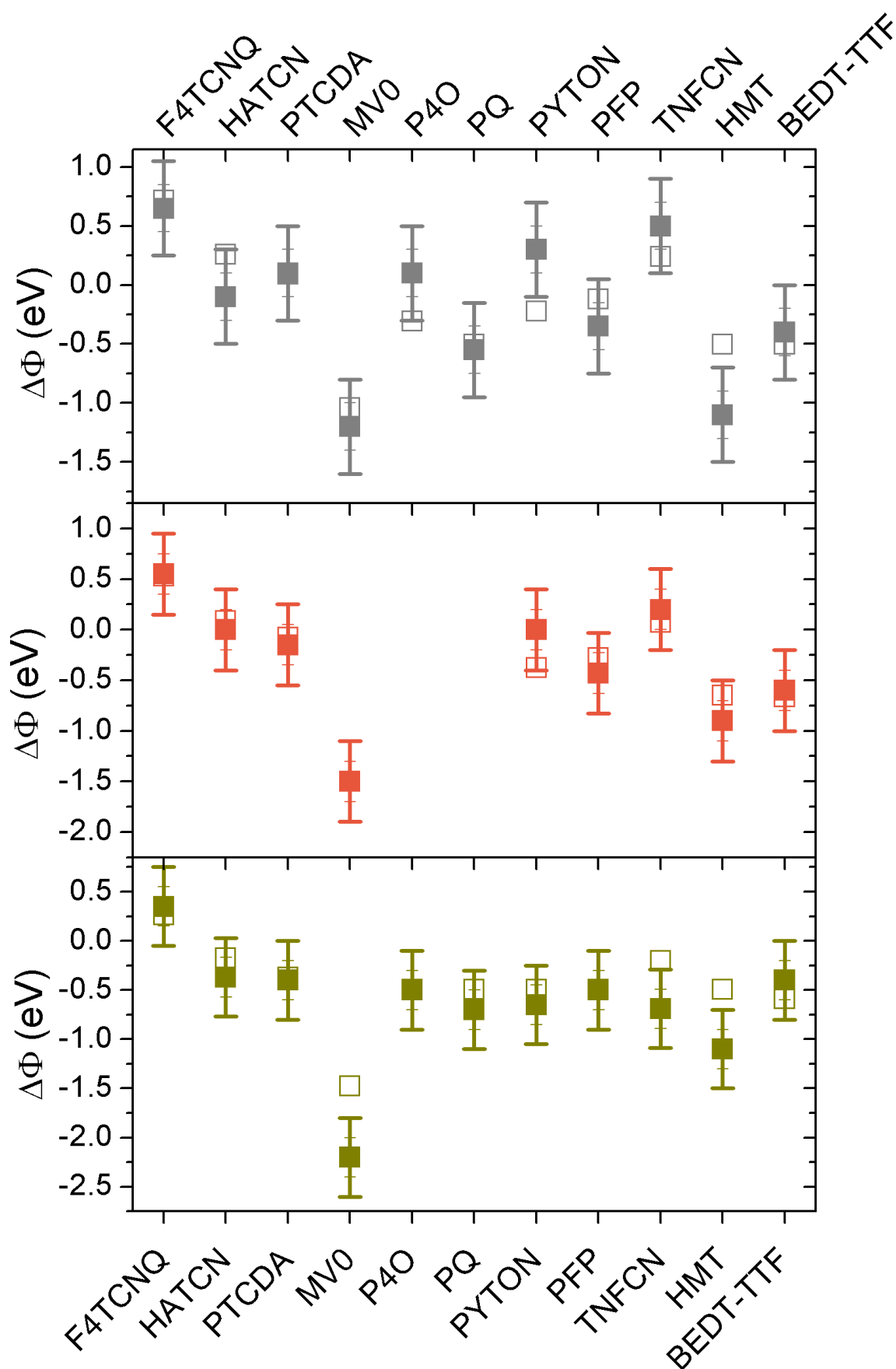
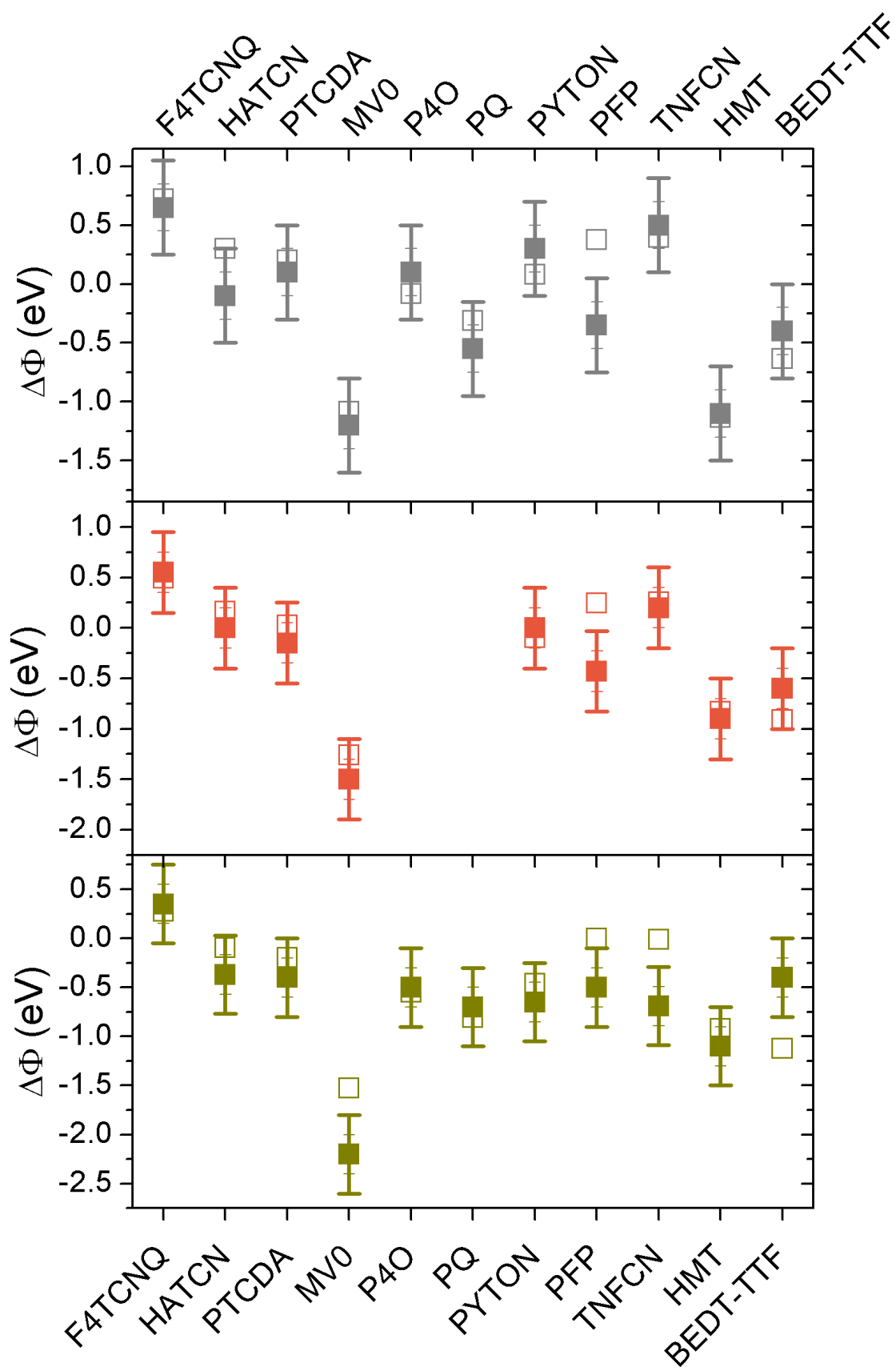


Figure 4.10: Simulated (open symbols) and experimental work-function modifications $\Delta\Phi$ on Au (dark yellow) Ag (dark gray) and Cu (orange) the electrostatic method described above



181
Figure 4.11: Simulated (open symbols) and experimental work-function modifications $\Delta\Phi$ on Au (dark yellow) Ag (dark gray) and Cu (orange) using AM1 input parameters

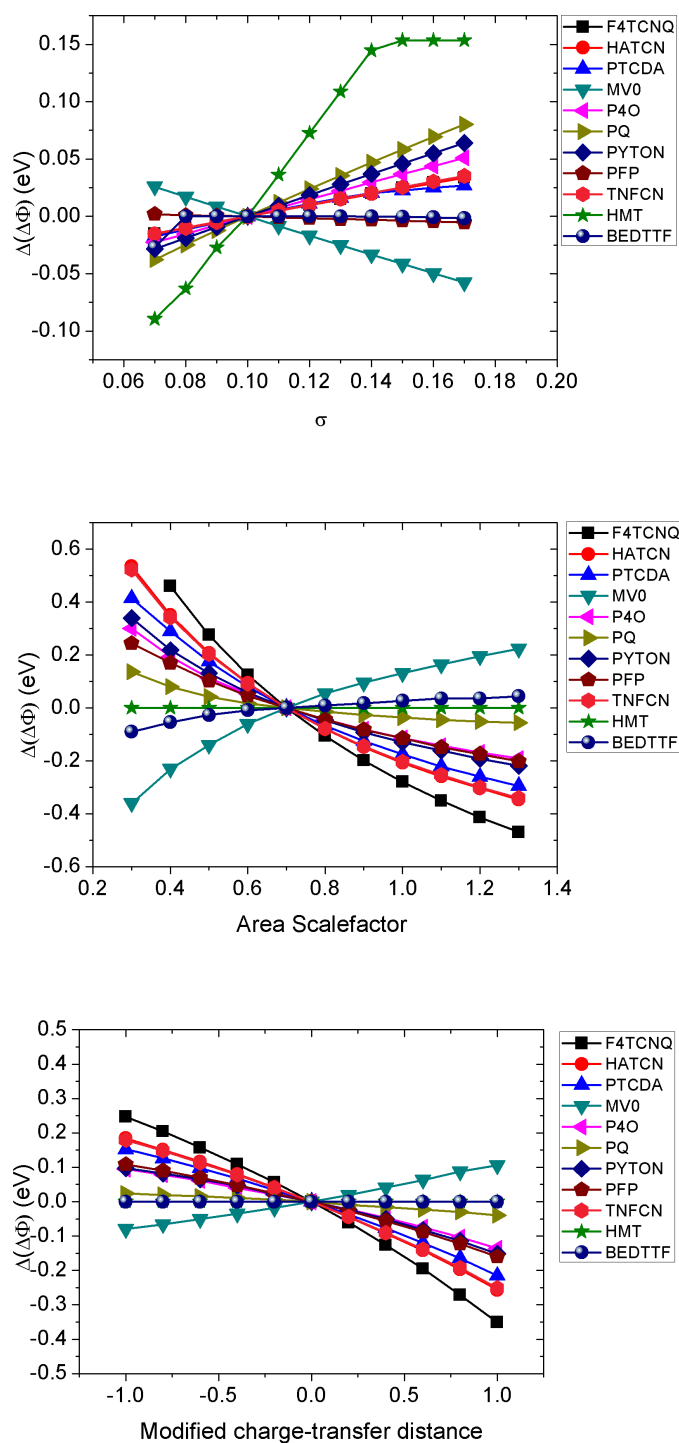


Figure 4.12: Simulated $\Delta\Phi$ as function of the orbital broadening (top), the area scaling factor (middle), and the charge transfer distance (bottom).

5 Summary and Conclusion

In this thesis, investigations on interfaces between coinage metal surfaces and strong electron donors and acceptors were performed. To get a general overview, several specific systems were investigated: At first, the ability to donate charge into high work-function materials such as gold, as well as the into the lower work-function materials silver and copper was demonstrated. In this context, the molecule 1H,1'H-[4,4']bipyridinylidene (HV0) was introduced as particular powerful electron donor. Upon deposition of a monolayer of this molecule, the effective work function of the system is strongly reduced. The result exceeds the work-function modification that can be achieved by deposition of the prototypical organic electron donor tetrathiafulvalene (TTF). The strong interaction of HV0 with the metal surfaces induces a bending in the formally almost planar molecule, which apparently counteracts the work-function reduction induced by charge transfer. Nonetheless, the net result on Au(111) is a reduction by ca. 1.4-1.8eV. Later, in a joint theoretical and experimental study, the results were verified using the HV0-derivate N,N'-dimethyl-[4,4']Bipyridinylidene (MV0). Interestingly, the bending observed for HV0 is absent in MV0. Therefore, there is no compensation of the bond-induced work-function modification by a molecular dipole. A work-function reduction on Au(111) from 5.5eV to 3.3eV was observed experimentally, equivalent to gold exhibiting the electronic properties of pristine Mg or Ca. Good agreement between density functional theory (DFT) calculations and ultraviolet photoelectron spectroscopy (UPS) results was obtained, demonstrating the applicability of the applied methodology to these kind of systems. As a third electron donor, the molecule 9,9'-ethane-1,2-diylidene-bis(N-methyl-9,10-dihydroacridine (NMA) was characterized theoretically and experimentally.

Extending the investigations to the intermediate electron acceptor 1,4,5,8,9,12-Hexaaza-triphenylene-2,3,6,7,10,11-hexacarbonitrile (HATCN) on Ag(111) revealed that metal / organic interfaces can be subject to phase transitions, in this case from the classical face-on to an edge-on, more SAM-like structure. The change of orientation was detected using multiple experimental methods, including UPS, thermal desorption spectroscopy (TDS), and reflection absorption infrared spectroscopy (RAIRS). The accompanying sharp rise in the work function of the sample was rationalized using theoretical calculations. It was also demonstrated in a joint experimental and theoretical study that on Ag, HATCN exhibits metallic character, which can be exploited to form a "soft" contact to subsequently deposited organic material without disturbing its energy levels. While for HATCN on Ag satisfying results could be obtained using standard DFT-functionals, poor performance was found for HATCN on Cu and HATCN on Au. However, the lack of agreement between theory and experiment in these cases cannot be blamed on a flawed methodology only, since also the experiments indicate that no nicely closed monolayer is formed on these materials. In other words, the system assumed by the periodic boundary conditions employed for the calculations does not represent the real-

world situation. A clear conclusion of this chapter is that reliable comparisons between DFT calculations and experiments are possible only for strongly interacting substrate / adsorbate systems. Calculating the in terms of general structure and electron affinity similar molecule coronene-1,2,5,6,9,10-hexaone (COHON) on Ag(111) reveals that despite the similar electronic properties and the identical size of the unit cell, the work-function modification induced by adsorption can be significantly different. This clearly demonstrates that details of the adsorption geometry, such as adsorption distance and bending, plays an important role for the level alignment in these kind of interfaces. An interesting similarity between COHON and HATCN, however, is that neither of them appears to be subject to depolarization, i.e., the work-function modification is almost independent of the coverage as long as no morphological changes occur. It was found that in these specific cases, this is the result of canceling the coverage-dependent effects on the work-function modification induced by bending and the work-function modification induced by charge-transfer.

From X-ray standing wave (XSW) measurements on the organometallic compound chlorogallium phthalocyanine (GaClPc) on Cu(111) it could be inferred that the strong geometry distortions generally found upon adsorption don't need to be confined to downward bending of peripheral groups. Instead, in GaClPc the Ga-Cl rod, which is located in the middle of the molecule, is pulled towards the copper surface. Computational analysis of the electronic structure showed that in this system about half of the experimentally observed work-function decrease can be attributed to the permanent dipole moment of the molecule. Of the remaining part, 50% are due to Pauli pushback from the organic macrocycle, while the other half is due to polarisation of the Ga-Cl bond. Because of the inert nature of the macrocycle, hardly any charge transfer between metal and adsorbate is observed.

Calculations on cyclophanes consisting of weak donors and acceptors covalently bound together showed that despite the enforced overlap of the wave functions, no significant charge transfer takes place. This holds true even for DFT calculations, which usually overestimates this process. A direct conclusion from the studies performed in this section is that all-organic interfaces cannot be created from relatively stable species, but strong electron donors and acceptors, like the ones studied in the earlier parts of the thesis, must be employed.

In contrast to the cyclophanes, strong charge transfer has been observed between the organic molecules HV0 and 2,3,5,6-tetrafluoro-7,7,8,8-tetracyanoquinodimethane (F4TCNQ). Adsorbing this charge-transfer complex on Au(111) or Ag(111) leads to unexpected results. DFT calculations reveal that the observed work-function modification is governed by the organic compound which is farther away from the surface. Phenomenologically, the work-function is almost the same as if the outer molecule was adsorbed at the same effective adsorption distance as in the complex, but without the sandwiched organic layer present. This effect is found for both Ag and Au as substrate, and for either orientation of the charge-transfer complex. Electronically, the computed charge-rearrangements reveal that that typically, both donor and acceptor part are involved in the formation of a (di)polar bond to the metal. An interesting exception occurs for

the Au/F4TCNQ/HV0 system, were hardly any electron rearrangements were found upon sequential deposition of HV0 on the F4TCNQ modified Au surface. Even Pauli pushback, which is generally thought to be ever-existent, is not observed for this system. It must be concluded that in strongly interacting systems, the requirement of the formation of a dipole which realizes Fermi-level alignment is a stronger condition than the displacement of electron density due to Pauli repulsion. A second conclusion that can be drawn is that, obviously, the net work function becomes pinned at the level of the outermost part of the system, i.e., the molecule closest to the vacuum level against which the effective work function is measured.

From the overall behavior of these specific systems, general structure-to-property relationships were extracted. The most obvious work-function to adsorbate-geometry relationship was found in the calculations of the three-components systems, where it became evident that increasing the adsorption distance between metal and adsorbate yields a larger work-function modification. Due to some effects not covered within DFT, it cannot be clearly stated whether this relationship will also hold for real systems; it can be concluded, however, that the source for the observed dependence on the metal/molecule separation is the charging energy, i.e. the tendency of a charged system to avoid further charging. The amount of the charging energy can be relatively large, and was shown to reduce the achievable work-function modification by up to 0.8eV; it is hence a factor which significantly mitigates the achievable net work-function of metal/organic interfaces, and it should be a goal in the development of enhanced molecules to reduce this effect as much as possible.

As next step, the impact of the molecular dipoles in Fermi-level pinning was studied in more detail. This is of particular relevance since most redox-active monolayers experience strong geometric distortions upon adsorption, typically in the form of downward bending of docking groups. In turn, a molecular dipole moment is induced, which often has the opposite sign of the dipole moment from the charge-transfer process. Here it was shown that the common interpretation that the molecular bend affects the work-function modification adversely is only partially correct. The condition of Fermi-level alignment requires that the net potential step between metal and molecule is a (to first approximation) fixed value, determined only by the energy of the pinned level and the Fermi energy. Any dipole moment introduced in the spatial region between metal and organic, e.g. by downward bending, must be compensated for by an accordingly larger charge transfer. The only impediment of the work-function modification is hence via the charging energy. In contrast, introducing a permanent dipole outside the direct metal / organic junction, e.g. by upward bending or by head-group substitution of self-assembled monolayers, does not influence the charge transfer, and such dipoles can be exploited to create extraordinarily large work-function modifications.

To find out whether the relationships just describes also hold in more realistic systems, the impact of N,N'-dialkylation on doubly reduced viologen monolayers was tested. Ever more bulky substituents were used with the aim to increase the adsorption distance, while also inverting the bending from downward to upward. As predicted, it was found that the larger work-function reductions on Au(111) can be achieved by increasing the

steric demand of the molecules.

Finally, a semi-classical model was devised to allow for a faster estimation of the work-function modification induced by adsorption of organic electron donors or acceptors. To that aim, each process occurring on the interface was re-evaluated and eventually parameterized. To avoid errors from DFT calculations, the ionization potential and electron affinity of the molecules, as obtained from the finite energy differences of the neutral and the charged species, are used. All levels are equally broadened. The screening of the metal was accounted for using a mirror image approach. From the relative position of the adsorbate levels and the metal Fermi-level, the amount of charge transfer is inferred, and the corresponding potential drop between them is calculated via the Helmholtz equation. The charging energy is accounted for by linear interpolation between the electron addition (removal) energy and the vacuum level. Pauli pushback was parameterized as a function of the adsorption distance using a monolayer of benzene as the training system. Since all these effects are interdependent, a self-consistent algorithm is used to obtain a prediction for the total work-function modification. The molecular volume, defined as fraction of the space in which the electron density is larger than a certain threshold, is exploited to estimate the molecular area and hence the unit cell size. To determine the adsorption distance, a potential well is created consisting of the energy contribution of Pauli repulsion and van-der-Waals attraction (both parameterized using the benzene monolayer on all three coinage metals), plus the energy gained upon charge transfer. It is assumed the metal / molecule separation corresponds to the position of the minimum of this potential well. The algorithm is then applied to a test set consisting of more than 30 metal/organic interfaces. Excellent agreement is obtained, with 90% of the predicted work-function modifications being within twice the experimental error.

6 Appendix: How to build flat organic donors / acceptors

6.1 Preface

The original aim of the work presented in the appendix was to present a guide how molecules could be modified chemically to tune either the position of the ionisation potential (IP), the electron affinity (EA), or the orbital gap. Of course, such a question is so basic that it was naive to believe that nobody else would have successfully tackled it if there was an easy answer. Some guidelines can indeed be found in basic chemistry textbooks. Most of them, however, are rather vague, and more general principles than rigid rules. Unfortunately, many relevant quantities, such as atomic charges or the LCAO coefficient on a particular atom, are not only no physical observables, but even cannot be rigorously defined in quantum-chemical calculations. Their values depend strongly on the choice of the employed method. As a consequence, most of the relationships found between chemical functionalization and change in IP / EA are not as rigorous as desired, and/or should be tested for their stability with respect to changes in the methodology.

This work is only indirectly relevant to metal/organic interfaces, and therefore shown in a separate appendix. Also, due to the inherent methodological problems mentioned above, some of the conclusions may be biased by the employed methodology. The following text is a wordily reproduction of a manuscript draft with only minor edits. However, in the present form it is not intended for publication in a peer-reviewed journal, and appropriate caution should be exerted when adopting the conclusions drawn herein.

The data and conclusions presented hereafter build on the knowledge generated by the bachelor thesis of Johannes Kofler, who investigated the relation of IP and EA to the various types of Hammett constants, Peter Krabb, who related the shape of the π -backbones to the polarizability, and Bernhard Kretz, who checked the consistency of various charge partition schemes. Also, the calculations and conclusions were discussed in several meetings with Karin Zojer and Egbert Zojer.

6.2 Introduction

Within organic optoelectronic devices, like organic light emitting devices (OLEDs), organic field effect transistors (OFETs), or photovoltaic cells, special attention is given to charge-injection layers connecting the metal electrodes with the (organic) active material^[278]. These layers often consist of planar, π -conjugated molecules with dedicated electron donating or accepting properties. Recently, several molecules have been

investigated both theoretically and experimentally^[130, 266], and their ability to improve above mentioned devices has been demonstrated^[279]. The material of the charge injection layer must meet several requirements: Obviously, it must lower the charge injection barrier significantly. It should also bind strongly to the metal surface, so that it will not be removed by further processing steps during the device manufacture. Air stability and solubility in standard solvents are also important features. Although the latter issues can be overcome, e.g. by working under inert gas conditions, they pose important cost factors to industry. In the case of a simple contact, the injection barrier for electrons Φ^e (holes Φ^h) is given by^[10]:

$$\Phi^e = \Phi_M - EA - \Delta \quad (6.1)$$

$$\Phi^h = IP - \Phi_M + \Delta \quad (6.2)$$

$$\Delta = \Delta_{PB} + \Delta_{DP} + \Delta_{BD} \quad (6.3)$$

In these formulas, Φ_M denotes the work function of the metal, IP the ionization potential and EA the electron affinity of the molecule. The quantity Δ designates the step in the vacuum level (VL) of the system upon adsorption (*per definitionem* positive when the vacuum level increases), which arises from the modification of the surface dipole. The latter is determined by three effects: On one hand, the electron tail of the metal, which extends beyond the nuclear bulk, is repulsed by all electrons of the adsorbate. This is often referred to as Pauli-repulsion or pushback effect (Δ_{PB}), and is always connected to a VL decrease. Since every molecule possesses at least one electron, this effect is always present, although to different amounts. It has been determined experimentally for noble gases on coinage metals Cu, Ag, and Au, where it amounts to ≈ 0.5 eV^[32], and for the inert hydrocarbon tetracontane on gold, where it reduces the VL by ≈ 0.7 eV^[30]. The second effect, Δ_{DP} , designates the intrinsic dipole moment of the molecule in the direction perpendicular to the surface. It can reach values up to several eV^[143], and can be easily tuned by the packing density, which, for sub-monolayers, influences the VL shift linearly. Only for densely packed cases, mutual depolarization of the dipoles takes place, and deviations from linearity are observed^[167]. The last effect, Δ_{BD} , arises due the additional dipole formed by charge rearrangements between metal and molecule upon adsorption, i.e. when a new bond is formed. The come about can be understood as follows. In every substance (molecule or bulk metal), all electrons share the same chemical potential μ , given as the derivate of the total energy with respect to the number of electrons.

$$\frac{\delta E}{\delta N} = \mu \quad (6.4)$$

The chemical potential μ corresponds^[280] to the negative of the total electronegativity χ as defined by Pauling and Mulliken, which, in the finite-difference-approximation, is given by the average of the ionization potential and the electron affinity. Note that for metals, IP and EA are identical, and χ corresponds to the work function.

$$-\mu = \chi \approx \frac{IP + EA}{2} \quad (6.5)$$

When two moieties come into contact, their electronegativity will tend to balance^[281], i.e., charge will flow from the higher potential to the lower one. This way, a new bond is formed. The derivate of the chemical potential with respect to number of electrons, i.e., the second derivate of the energy, has been defined as chemical hardness^[282], η . The smaller this quantity, the fewer electrons need to be transferred to equalize the potentials. Thus, it can be regarded as the resistance to change in the electron density of a given molecule. Again making use of the finite-difference-approximation, the hardness can be estimated by the difference of IP and EA^[283]

$$\eta = \frac{\delta\mu}{\delta N} = \frac{\delta^2 E}{\delta N^2} \approx \frac{IP - EA}{2} \quad (6.6)$$

The factor of $\frac{1}{2}$ in 6.6 was originally introduced arbitrarily to obtain similarity with 6.5^[284]. Clearly, this equation cannot hold for bulk metals, where IP and EA are equal and the hardness hence would be zero^[127]. It has been argued^[285] that rather two times the inverse of the density of states (DOS) at the Fermi-level, E_F should be taken as measure.

$$\eta = \frac{2}{DOS(E_F)} \quad (6.7)$$

The value of total electronegativity and chemical hardness is well appreciated in chemistry, as their inclusion into standard textbooks demonstrates. To strengthen the understanding of the use of χ and η , consider the case when a certain amount of electrons, ΔN , is transferred to or from a reaction partner. The total energy can then be expanded in a Taylor-series^[283, 286], which in the following equation is truncated after second order.

$$E = E^0 + \frac{\delta E}{\delta N} + \frac{1}{2} \frac{\delta^2 E}{\delta N^2} + \dots \quad (6.8)$$

The quantities χ and η are therefore important parameters for the assessment of charge-transfer reactions. Bearing in mind that the numbers of electrons transferred must be equal for both partners, and that χ must be equalized through that transfer, ΔN can be calculated. Between metal and adsorbed molecule, it is given by the equation^[283]

$$\Delta N = \frac{\chi_{metall} - \chi_{molecule}}{2(\eta_{metall} + \eta_{molecule})} \quad (6.9)$$

The electron transfer and hence Δ_{BD} is therefore driven by the difference of electronegativity and hindered by the combined hardness of the system. From all this said above it becomes evident that it does not suffice to concentrate on low IPs (EAs) to achieve low hole (electron) injection barriers, but that rather IP and EA must be viewed together. In the further course of this work, we will recall several structure-activity relationships which can be used to tune those quantities: (i) the shape of the molecular backbone; (ii) the effect of hetero atoms in these backbones and (iii) the impact of various substituents. Within (iii), we will show that Hammett constants or the Swain-Lupton constants can be employed to estimate the relative impact of different substituents depending on their position relative to the π -system at a glance, without needing to actually calculate all possible structures *ab initio*. Finally, we will exploit those structure-activity relationships to propose one especially potent electron electron

acceptor molecule.

6.3 Methodology

All values have been computed using the density function theory hybrid functional B3LYP with a 6-31+G* basis set as implemented in the Gaussian03^[71] program suite. A basis set including diffuse function was chosen since there is general agreement in the scientific community that for the correct calculation of the weakly bound extra electron of anions, functions which reach far out into space are *conditio sine qua non*. All convergence criteria were left at their default values. Frequencies calculations were performed to ensure that the optimized structure is a true minimum. Ionisation potential IP and electron affinity EA were obtained by performing a single point calculation of the charged radical cation / anion at the fully optimized geometry of the neutral species and taking the difference of their energies according to the equations below

$$IP = E(cation) - E(neutral) \quad (6.10)$$

$$EA = E(neutral) - E(anion) \quad (6.11)$$

I.e., in contrast to the other parts of the thesis, the correct definition of EA has been employed, to comply with the definitions of χ and η . B3LYP is known to perform well for ionization potentials and electron affinities. Riley et al.^[72] found average unsigned errors below 6 kcal/mol (0.26 eV) and below 4 kcal/mol (0.17 eV), respectively, for this method. It has been reported that EAs are in many cases computed too positive^[73, 287, 288], while IPs are often too small^[74, 287, 288]. It should be stressed that these rules of thumb do not always apply, and counter examples can be given^[289]. Since only vertical ionization potentials and electron affinities were calculated, no zero point vibration energy correction was employed. Unless stated otherwise, no symmetry constrains were allowed in order to prevent bias of the results.

6.4 Results and Discussion

6.4.1 Comparison of π -backbones

The easiest and probably most obvious way to influence ionization potential and electron affinity is by changing the spatial dimension of the corresponding π -system. With increasing size, the gap between HOMO and LUMO (which energies, via Koopmans theorem^[90], are associated with IP and EA, respectively) becomes smaller; hence, IP and EA are lowered. As a hand waving argument, it can also be thought that the more electrons are in the system, the easier it is to extract one, and the more difficult to add. Since the changes in IP and EA are almost equal, the total electronegativity χ is not affected, in contrast to the hardness η , which is significantly reduced. The latter statement is in agreement with the requirement that the hardness must go towards small values for an infinitely extended π -system like graphene, which is known to be a zero-gap semiconductor. Fig. 6.1 visualizes the principles explained above for the

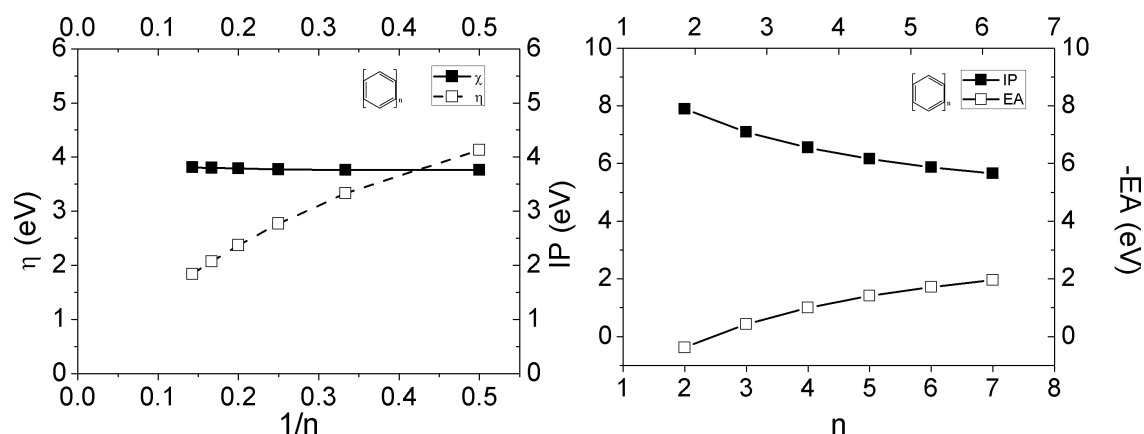
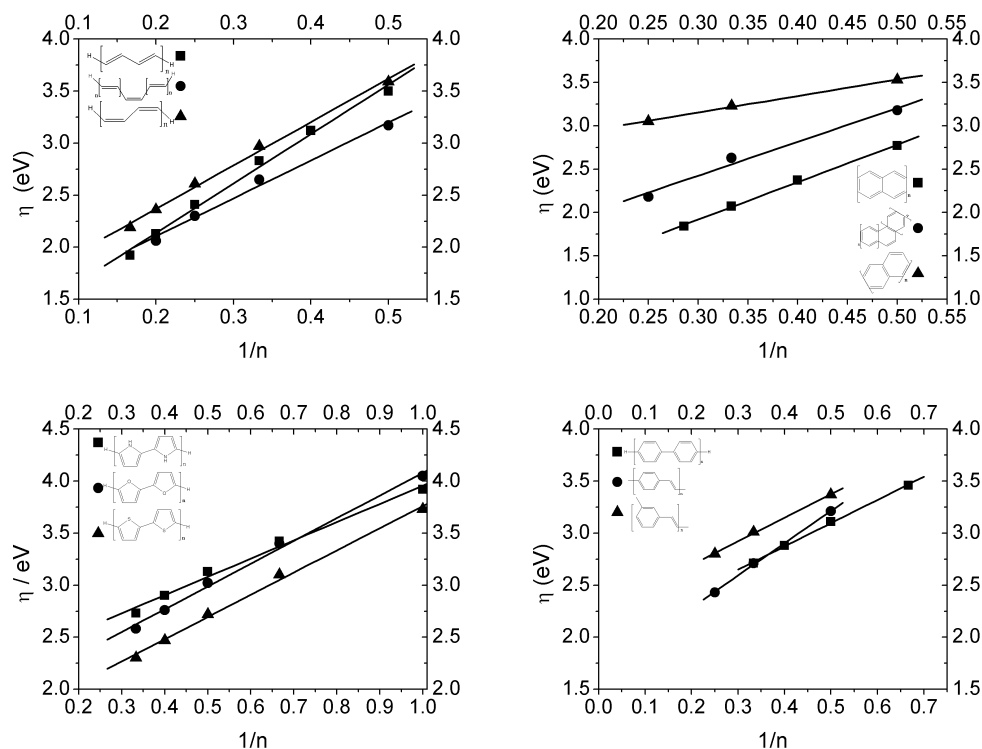


Figure 6.1: Evolution of IP and EA with increasing π -system (left). Functional dependence of total electronegativity and chemical hardness on $1/n$ (right)

special case of acenes.

It is obvious that a molecule is softer the better the conjugation. It is, however, not so clear what the topology of the molecule must look like to achieve the best conjugation possible. In order to clarify this issue, several possible homologous series of conjugated chains or aromatic rings have been tested, trying to cover the most commonly used motifs. The chemical hardness, being strongly related to the optical band gap, changes proportional to $1/n$ for small n , and eventually levels out.^[290] Here, n is the number of repeat units. In order to keep out of the “leveling out”-region, we chose to use $n=2$ to $n=4$ for condensed rings, $n=2$ to $n=6$ for oligoacetylenes and $n=1$ to $n=3$ for all other topologies investigated. Within any series, the best conjugation is achieved when the whole molecule is planar. Hence, all calculations in this section were done assuming C_s or higher symmetry. The results for η are shown in Fig. 6.2. Since χ remains constant in these series, η is a good indicator also for the evolution of IP and EA, which are not depicted here.

Within the molecules tested, the hardness varies between roughly 4eV and slightly below 2eV. The softest backbone within this test set was found to be Heptacene with $\eta=1.84$ eV. In general, acenes showed very low hardness values, followed by the various conformations of oligoacetylenes. The latter exhibit, at least within the range investigated, similar hardness within 15-20% independent of the configuration, although with the clear trend that the hardness decays faster for the all-trans motif. More complicated topologies like kinked acenes (circles and triangles in top right in Fig. 6.2) are already harder for small n and decrease their hardness slower with increasing system size. Also phenyl rings linked via single or double bonds (Fig. 6.2 bottom right) are less favorable in terms of conjugation. Finally, it should be noted that linked five-membered ring heteroaromatics (for which the absolute value of η will be discussed in a separate section) all reduce the hardness at a similar, comparably slow rate. Investigations concerning the evolution of the optical gap or the excitation energies with increasing chain length have

Figure 6.2: Hardness parameter η for various conjugated, planar systems

been done before by various authors^[290–293] for parts of this test set, as well as several other molecules, at comparable levels of theory. When extrapolating the hardness to infinite chain length assuming constant $1/n$ behavior over the whole range, we find that the relative ordering is in excellent agreement with the ordering of the band gap at infinite chain length reported in the literature cited above, as is the relative slope at small n .

Effect of hetero atoms

Inclusion of hetero atoms into the π -system provides a very efficient, easily understandable way to modify the character of a given molecule. With the exception of boron, every possible substitute has higher (atomar) electronegativity than carbon. Following the principle of electronegativity equalization, χ (for the whole system) will hence be increased in general. Both IP and EA rise, since due to the higher nuclear charge, the atomic levels are stabilized in terms of energy. As the molecular orbitals can be thought of as linear combination of the atomic orbitals, also their energy is reduced, which, via Koopmans theorem^[90], directly relates to increasing IP and EA. In the spirit of Slaters rules^[294], EA increases slightly more than IP, leading to a reduction of η . The effect of increasing nuclear charge is counteracted by the mismatch in size of carbon and hetero atom p-orbital. This leads to poorer overlap, which in turns results in a destabilization of the π -system, and hence a decrease in IP and EA. The net effect is for di-substituted

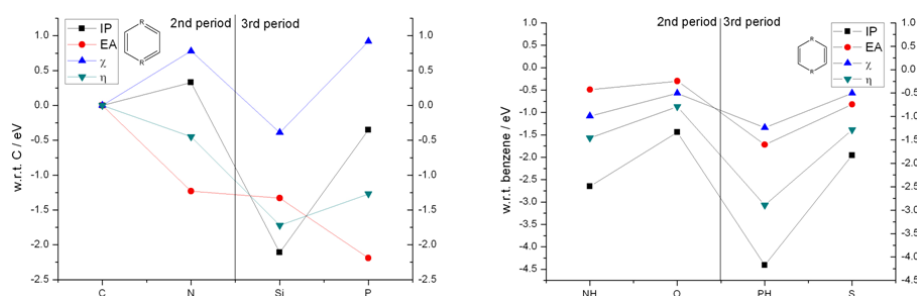


Figure 6.3: Evolution of IP/EA/ χ / η for hetero atoms for systems isoelectronic with benzene (left) and with two additional π -electrons (right)

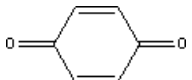

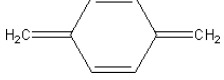

rings is depicted in Fig. 6.3.

The paragraph above is only valid for systems whose π -system are isoelectronic with the carbon counterpart. There are, however, also cases in which the π -conjugation is propagated via electron lone pairs. (See Fig. 6.3, right). In those cases, more electrons participate in the conjugated system. Hence, HOMO and LUMO come closer together, yielding reduction of IP, while EA, on the other hand, is still increased. As direct consequence of eqs. 6.5 and 6.5, χ is reduced, as is η . Fig. 6.3 demonstrates these effects for modified benzene rings. Note that simulations replacement of two atoms was performed in order to preserve closed-shell character for all systems. In literature, the effect of hetero atoms on the band gap as a function of group number and period of the hetero atom is well documented for hetero atoms in 5- and 6 membered rings^[291, 292] as well as for hetero atoms as linkage between phenyl rings^[295].

Quinoid or Benzoid

From Simple Hückel Theory, it can be shown that closed ring systems with $4n+2$ π -electrons - n being any integer number - are especially stable, while those with $4n$ electrons are not. This is called the “Hückel-rule”, and molecules obeying the former rule are called aromatic or benzoid. It can also be shown that benzoid molecules have a smaller band gap, and hence smaller chemical hardness, than non-benzoid ones. Quinons are a common class of molecules with $4n$ π -electrons. Being oxidized derivatives of benzene or related molecules, they also show strong influence on χ , thus making them well suited for the creation of acceptor molecules.

Table 6.1: Donor/Acceptor properties of selected quinoid/benzoid molecules

Molecule	IP (eV)	EA (eV)	χ (eV)	η (eV)
	9.96	1.89	5.93	4.03
	7.90	-0.90	3.50	4.40
	7.49	0.25	3.87	3.62
	8.73	-1.20	3.58	4.78

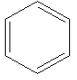
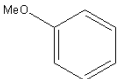
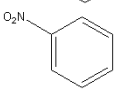
Attaching Substituents

Extending the π -system is a straight-forward way to obtain molecules with ever smaller hardness, but the total electronegativity stays, more or less, the same. To tune the latter, substituents can be used.

The influence of these functional groups can be divided into two main effects: The inductive effect (I-effect) and the mesomeric effect (M-effect). The inductive effect stems from the fact that the group has an electronegativity different from hydrogen, and will therefore add (+I) or reduce (-I) the electron density in the aromatic system. It is thought to propagate through space and through any bonds, though the exact mechanism is still a question of debate^[296, 297]. The mesomeric effect originates from the fact that the substituent can participate in the conjugation, thus also adding (+M) or lowering (-M) electron density in the backbone. Additionally, depending on the nature of the functional group, the size of the π -system is increased to some extent, which leads to a lowering of η . This is only efficient if the functional group is directly attached to the conjugation. There is another important point that can directly be deduced from this effect: -M-groups usually build stable anions, thus exhibiting high EAs. The opposite, namely low IPs due to stable cations, is true for +M substituents. Note that for either sign of M, η decreases. The M-effect is very prone to steric effects, since it is very important that the π -systems of backbone and substituent overlap as much as possible. This is best illustrated on the example of aniline ($Ph - NH_2$). The electron pushing ability of NH_2 depends almost exclusively on M (vide infra). As long as the lone pair is located in the plane of the ring, χ is reduced by 0.51 eV compared to benzene. When the calculation is repeated with the group rotated by 90° (and planarized), the overlap completely vanishes, and the effect reduced to -0.01 eV. A more detailed discussion of this effect is given below. Exemplarily, the influence of positive and negative effects are shown for the case of substituted benzene in table 6.2.

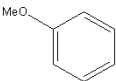
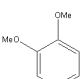
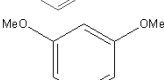
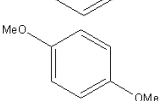
If more than one substituent is used to tune the total electronegativity, the question is where to locate it in relation to the first one. This not straightforward from first principle. Two effects - increasing the size of the π -system vs. changing its electron

Table 6.2: Substituent effect

Molecule	M/I	IP (eV)	EA (eV)	χ (eV)	η (eV)
	0/0	9.20	-1.50	3.85	5.35
	+/+	8.18	-1.12	3.53	4.65
	-/-	9.98	0.89	5.44	4.45

density - are differently pronounced on different sites. For substituents with different signs for I and M, this can go as far as changing the net effect from electron donating to electron accepting (see table 6.3). It is common chemical knowledge that the conjugation is usually most efficient in *para*-position, less pronounced for *ortho*-substitution and worst at the *meta*-position of a phenyl ring. More generally speaking, the conjugation is disturbed if you cannot find a way of alternating single/double bonds from the first to the second substituent. This can be rationalized by the resonance structures of those entities. In such cases, often the inductive effect dominates.

Table 6.3: Substituent effect

Molecule	Size	IP (eV)	EA (eV)	χ (eV)	η (eV)
	—	8.18	-1.12	3.53	4.65
	o	7.57	-1.08	3.24	4.33
	m	7.83	-1.02	3.41	4.43
	p	7.49	-1.06	3.22	4.27

Deciding for a substituent

From the chemical structure alone it is often very difficult to estimate the relative strength of substituents. Fortunately, experiments have been conducted for a huge number of functional groups. Most prominent among them are those proposed by Hammett^[298], σ , where the dissociation constant of meta- and para-substituted benzoic acids were measured and compared with the unsubstituted molecule. The ratio of both equilibria is known as “Hammett-constant” σ , and has been successfully employed in several quantum structure-activity relationships (QSPR)^[299]. Later also other reactions were employed to extend the investigation to a larger variety of substituents.

Subsequent studies by Swain and Lupton^[300] and Taft^[301] and others successfully partitioned Hammett's constant into its inductive (F) part and resonance part (R). A review and compilation of data has been given by Hansch et al.^[302].

It is clear that Hammett's constant is related to influences on the electronic system, and can conveniently be exploited to estimate the impact on molecular orbital energies^[303]. Of course, several arguments can be brought forward against that statement. First of all, Hammett's equation is purely empirical and lacks profound theoretical foundation. However, Hammett's equation has been very successful, and no one pretends that it holds perfectly; rather, the constant should be used as a guide. Furthermore, most experiments have been performed in solution and should, therefore, not be directly applicable to calculations in gas phase. This is the most problematic aspect, as the solvation energy is surely dependent on the nature, the form, and the size of the substituent. It is another serious drawback that for many groups, several different σ values exist, but there is some agreement for the most common ones^[304]. Also, it must be admitted that Hammett's constant was parametrized for reactions with a specific reaction center (the acid group), which does not exist in the calculation of IP and EA.

Despite these shortcomings, we have computed sets of 13 substituents attached to the 2-position of a series of condensed ring (naphthalene, anthracene, naphthalene and pentacene) and correlated the change of IP, EA, χ , and η (with respect to the unsubstituted moiety) with σ_p , assuming the functional dependence

$$\Delta X = \rho \sigma_p \quad (6.12)$$

With X being the property related (i.e., IP, EA, χ , and η) and ρ being a proportionality factor to be fitted.

As Fig. 6.4 shows, equation 6.12 is well fulfilled for Δ IP, Δ EA, $\Delta\chi$ and $\Delta\eta$. The correlation coefficient R is above 0.9 in all cases. As expected, the slopes of the interpolation lines, i.e., ρ , decrease predictably with the size of the backbone demonstrating that the larger the backbone, the smaller the influence of a single substituent. On the other hand, no significant correlation with η was detected. This is not surprising, as it obviously is impossible that one single parameter describes at the same time the sum and the difference of Δ IP and Δ EA. It is however interesting to notice that the values of $\Delta\eta$ do not scatter much (within roughly 0.5 eV) within the same backbone.

In a refinement of Hammett's original experiments, special measurements were performed to obtain distinct data for the delocalization of positive ($\sigma+$) and negative ($\sigma-$) charges. Using the former to estimate Δ IP and the latter to estimate Δ EA yield regression lines of higher quality ($R > 0.94$), see Fig. 6.5. It should be noted, however, that for some of the groups used for the evaluation, no values for $\sigma+$ and $\sigma-$ were available. These hence were excluded from this set. Employing those two correlations it should also be possible to estimate $\Delta\chi$ and $\Delta\eta$ with high accuracy by employing the sum of $\sigma+$ and $\sigma-$ and their difference, respectively. It is satisfying to notice that this indeed works well for $\Delta\chi$, with $R > 0.97$, although, unfortunately, the correlation with $\Delta\eta$ remains poor ($R < 0.4$). This, however, can be attributed to the fact that the change

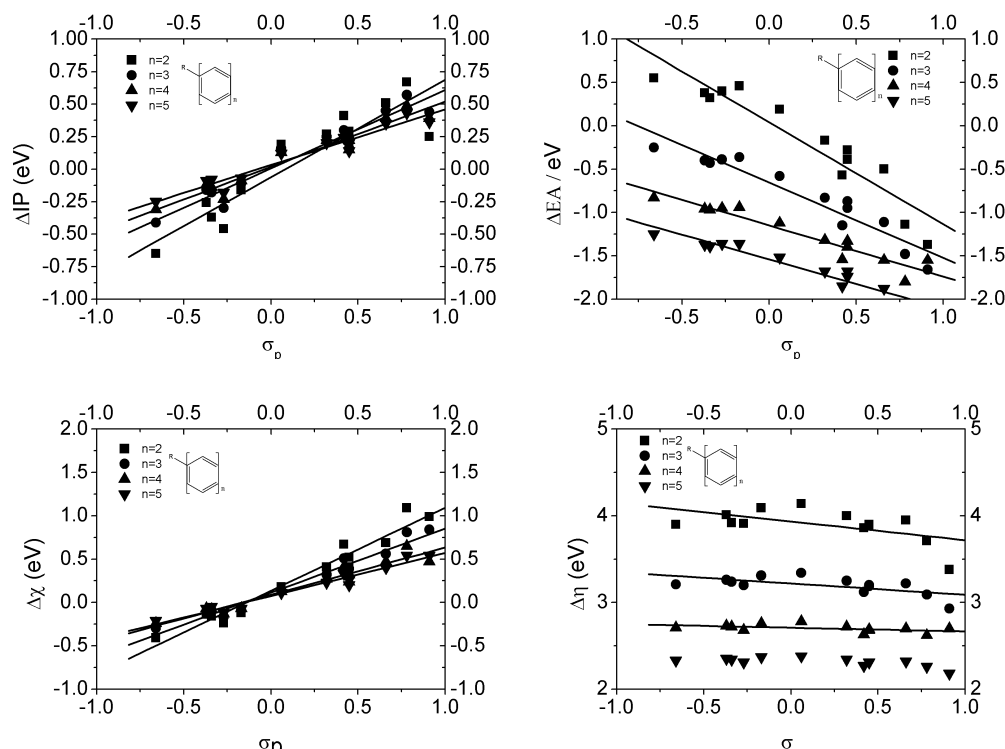


Figure 6.4: Correlations of ΔIP (top left), ΔEA (top right), $\Delta \chi$ (bottom left) and $\Delta \eta$ (bottom right) with σ_p . The substituents used and the corresponding Hammett constants are shown in Table 6.4

in hardness is roughly independent of the substituent attached.

Deviations of calculated values from the regression lines can be partly attributed to experimental errors in the determination of σ . Moreover, also the calculated values for IP and EA are not exact, due to the neglecting of solvent effects (in comparison to experiment) and due to the various approximations implicitly made in the method.

To demonstrate these effects, the molecular orbital coefficients of 1,3,5,7,9,11-Dodecahexaen has been calculated, along with the atomic charges using the atomic polar tensor (APT) approach^[66]. Unlike Mulliken, APT charges q are calculated analyzing the wave function (rather than the basis set), and do not suffer from problems connected to diffuse functions. In order to investigate resonance and inductive effect separately, substituents for which one effect clearly dominates the other have been attached to this molecule in various positions. The inductive effect has been investigated using $CHCl_2$, while for the resonance effect, the NH_2 substituent was used. Fig. 6.6 plots (the negative of) q along with IP, EA and χ of the $CHCl_2$ substituted molecule vs. the substituent position. Noteable, the trends of all three parameters agrees with the trend of q , with the exception of the 1-position. This failure probably arises due to the abrupt end of the π -system, i.e., the field cannot reach as many electrons as a more central position can do.

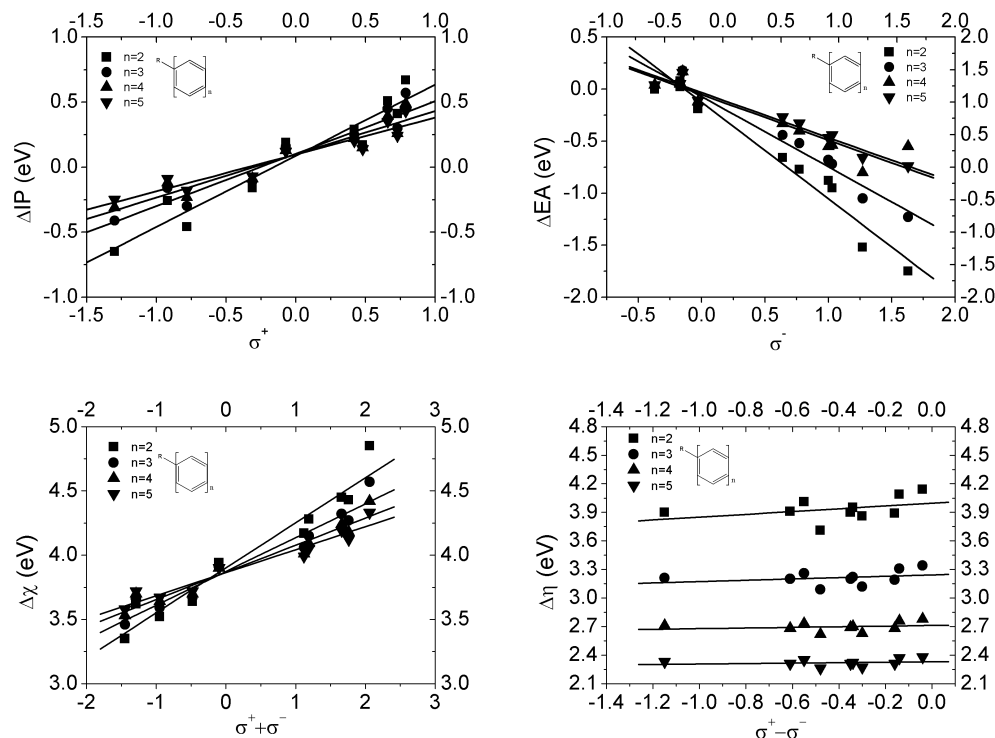


Figure 6.5: Correlation of ΔIP with σ^+ (top left), ΔEA with σ^- (top right), $\Delta\chi$ with $\sigma^+ + \sigma^-$ (bottom left) and $\Delta\eta$ with $\sigma^+ - \sigma^-$ (bottom right)

In Fig. 6.7, the evolution of the negative absolute value of the HOMO-coefficient of the pristine molecule is compared to the evolution of the ionization potential for the NH_2 -substituted moiety. Note that the qualitative agreement again is very good, but that the deviations are larger the farther outside the substituent is located. This can easily be explained by the fact that the value of the MO coefficient of the pristine molecule does not reflect the influence of an increasing π -system. As pointed out in the first section, increasing the π -system is most efficient when a rod-like molecule is obtained, i.e., when the branch is located at the end of the molecule, or when there is no branch at all, i.e. in the 1-position.

Table 6.4 lists Hammett constants as well as (modified) Swain-Lupton constants, which represent the partition into mesomeric effect R and inductive effect F, as given in reference [302] and the literature cited therein, for selected substituents. These substituents will be discussed below in more detail, with emphasis being laid on the relative quota of resonance via field effect, the relative effect of σ_p , and the effect of (hypothetical) sterically induced rotation.

The highest values for σ_p are achieved by inter-halogen compounds (like ICl_2) and substituents containing SO_2 (i.e. SO_2Cl). They are, however, known to be extremely

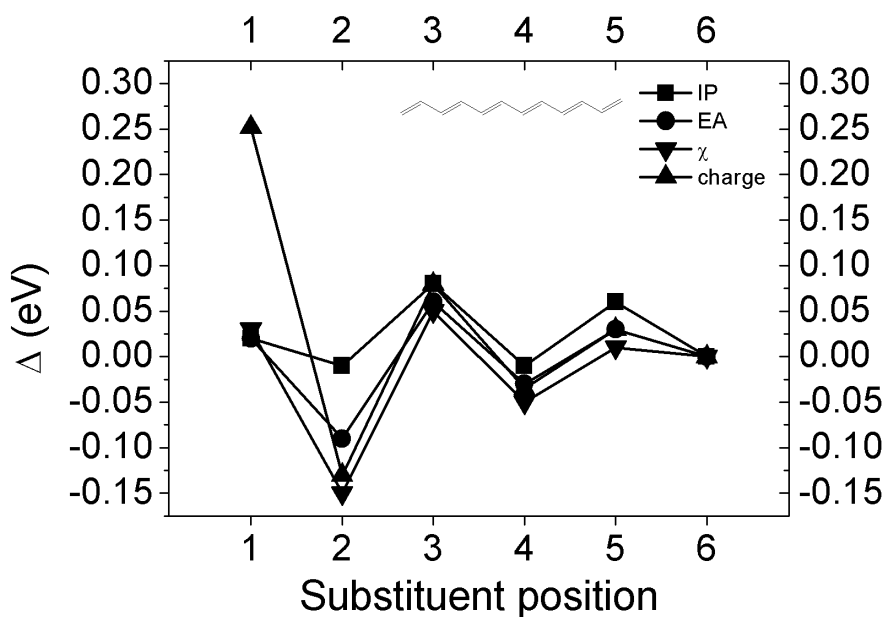


Figure 6.6: Dependence of donor/acceptor parameters on inductive effect and substitution site of $CHCl_2$ attached to 1,3,5,7,9,11-Dodecahexaen. Δ represents the difference to the value for the $CHCl_2$ substituent located at position 6.

reactive and easily undergo hydrolysis or dissociation reactions. Both types rely almost exclusively on the inductive part. Even higher values for F are only reported for charged species, which are known to be outside the validity of Hammett's equation. The nitro group (NO_2) is often viewed as substituent of “maximum electron withdrawing character”. While this is obviously an exaggeration, it indeed has a high value for σ_p . For the total value, the resonance part plays only a minor role ($R=0.13$; $F=0.65$), so rotation out of plane due to steric repulsion hardly reduces its overall strength. Upon substitution with NO_2 , the EA of benzene is increased by 2.4 eV, when the nitro group is assumed to be in plane, and 1.7 eV when the nitro group is calculated 90° rotated. In other words, only 30% of the total effect is induced by the mesomery. This robustness, together with easy synthesizability, makes the group a kind of “working horse” for the design of acceptors. A somewhat special substituent is the nitrosyl group, NO. It shows a higher σ_p than NO_2 , but in all our calculations, influenced χ less. Instead, it showed a significant lowering of the hardness, which could be a very useful property. Resonance and inductive effect are of about the same for this group. Consequently, the difference between σ_p and σ_m is large (0.29 units, about 30% of the total net effect) and significant site dependency is to be expected. Surprisingly, this substituent is hardly used in practical applications, and literature of this group mainly deals with anorganic complex compounds. Compared with NO_2 , CN exhibits a somewhat larger resonance effect. Also, due to its linear geometry, rotation of p-orbitals out of the π -plane is impossible, keeping the resonance at its maximum value independent of the surrounding. The inductive effect, on the other hand, is lower than for NO_2 , thus counteracting the

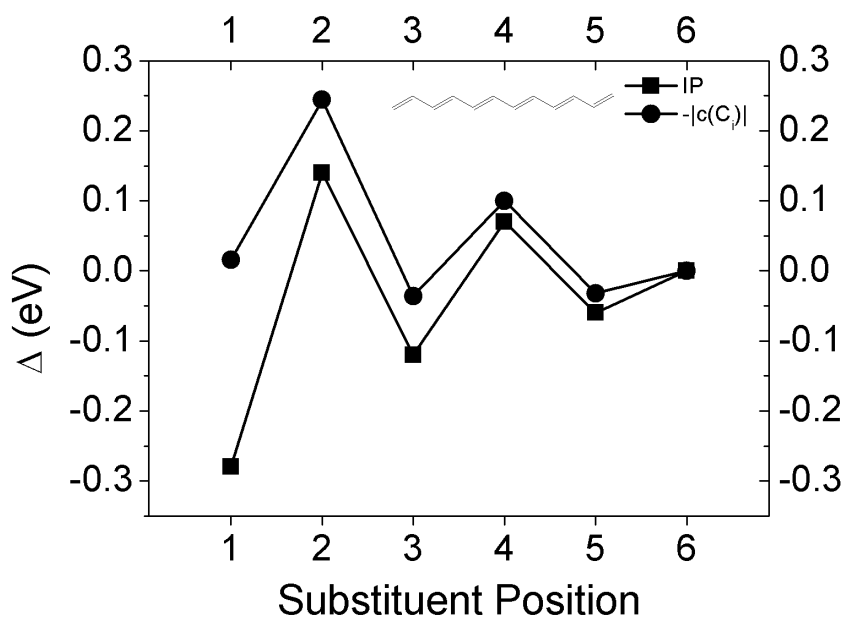


Figure 6.7: Dependence of donor/acceptor parameters on inductive effect and substitution site of NH_2 attached to 1,3,5,7,9,11-Dodecahexaen. Δ represents the difference to the value for the NH_2 substituent located at position 6.

resonance advantage. Overall, in cases where the inductive effect does not play a major role (i.e., when charges on the substitution sites are very small), both functional groups will be of similar quality, with slight preference of NO_2 . CN, however, is sterically less demanding, and therefore enjoys popularity in literature and application. Carbon acids and aldehydes, being oxidized derivatives of methyl groups, are natural electron withdrawing groups, COOH obviously stronger than CHO. For both cases, the inductive effect is almost 3 times larger than the resonance effect. Usually inferior to CN or NO_2 , these groups are valuable substituents in cases where maximum electron withdrawal is not wanted (e.g., in order to avoid too large distortions of the aromatic system). $CHCl_2$ is a rather weak electron withdrawing group which almost exclusively relies on the inductive effect. Indeed, it turns out to be an excellent test case for substitution with almost zero resonance effect. Fluorine is another substituent commonly encountered in acceptor molecules. Its delicate equilibrium between -I and +M makes it very sensitive on the nature of the backbone as well as its chemical surrounding, and its net effect is still subject to studies. Due to the large stability of C-F bonds (binding energy: 498 kJ/mol), fluorine can be used to increase electron accepting properties without introducing additional reaction centers. Note that, even in cases where both effect counteract each other completely, the size of the π -system is increased, and hence the hardness of the compound reduced. Methyl groups, like saturated hydrocarbon in general, exhibit an electron pushing effect. Since all p-orbitals are hybridized and removed from the π -system, mesomeric effects hardly take place. Rather, the net effect is almost exclusively based on the lower electronegativity of carbon compared to hydrogen. Alcohols and ethers possess a large electron pushing resonance part (negative R) counteracting

Table 6.4: Hammett and Modified Swain-Lupton Constants. Reproduced from Reference [302]

Substituent	σ_p (eV)	σ_m	R (eV)	F	$\sigma+$	$\sigma-$
<i>ICl₂</i>	1.11	1.10	0.08	1.03	—	—
<i>SO₂Cl</i>	1.11	1.20	(-0.05)	1-16	—	—
<i>NO</i>	0.91	0.62	0.42	0.49	—	1.63
<i>NO₂</i>	0.78	0.71	0.13	0.65	0.79	1.27
<i>CN</i>	0.66	0.56	0.15	0.51	0.66	1.00
<i>COOH</i>	0.45	0.37	0.11	0.34	0.42	0.77
<i>COOMe</i>	0.45	0.37	0.11	0.34	0.48	0.64
<i>CHO</i>	0.42	0.35	0.09	0.33	0.73	1.03
<i>CHCl₂</i>	0.32	0.31	0.01	0.31	—	—
<i>F</i>	0.06	0.34	-0.39	0.45	-0.07	-0.03
<i>CH₃</i>	-0.17	-0.07	-0.18	0.01	-0.31	-0.17
<i>OMe</i>	-0.27	0.12	-0.56	0.29	-0.78	-0.17
<i>NHOH</i>	-0.34	-0.04	-0.45	0.11	—	—
<i>OH</i>	-0.37	0.12	-0.70	0.33	-0.92	-0.37
<i>NH₂</i>	-0.66	-0.16	-0.74	0.08	-1.30	-0.15

an electron pulling inductive effect (positive F). The difference between both effects is very large, up to 1 unit, so that, dependent on MO coefficient and atomic charge, they might be generally employed as weak or medium electron donors. Due to the large value of R, rotation of the group induced by steric effects might alter the net effect considerably. Note that the resonance never becomes zero, as these compounds have to lone pairs, which, regardless of the rotation angle, will always at least partly overlap with the π -system. A large electron pushing resonance part (negative R) counteracting an electron pulling inductive effect (positive F). The difference between both effects is very large, up to 1 unit, so that, dependent on MO coefficient and atomic charge, they might be generally employed as weak or medium electron donors. Due to the large value of R, rotation of the group induced by steric effects might alter the net effect considerably. Note that the resonance never becomes zero, as these compounds have to lone pairs, which, regardless of the rotation angle, will always at least partly overlap with the π -system. Amines and (di)alkylamines are among the strongest electron donor groups found in literature. They draw their strength to the better part from resonance effects, which make them very sensitive to sterically induced out-of-plane rotations (cf. the example of aniline above). A more detailed review of the influence of the amine donor strength can be found elsewhere^[305].

Fig. 6.8 shows the effect on donor/acceptor parameters of selected monosubstituted benzenes as function of (hypothetically induced) rotation of the substituent. It is clearly demonstrated that the qualitative influence on IP and EA depends on the sign of R, i.e., positive R lead to decreasing IP and EA, and vice versa. The quantitative influence, however, depends not only on the magnitude of R itself, but scales σ with the overlap between substituent and backbone in the respective orbital. This is best visualized for the case of NH₂ (blue triangles). Here, IP is modified by about 1eV, while EA is almost unaffected by rotation, since the LUMO of this molecules does not contain

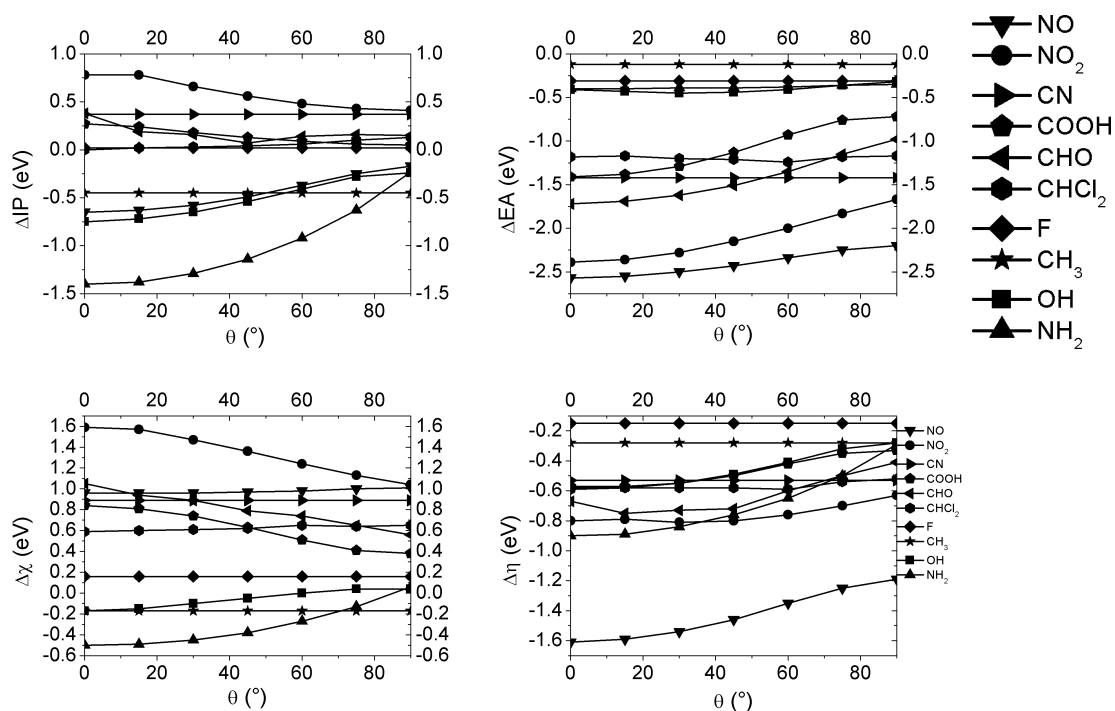


Figure 6.8: Ionisation potential, electron affinity, total electronegativity and hardness difference w.r.t. to benzene for selected substituents as function of their rotation angle (top left to bottom right).

contributions on the NH_2 group. It is also noteworthy that CHO at 0° rotation influences χ stronger than CN does, although it has both lower F and lower R. The reason for this failure can be found in the nature of the HOMO, which exhibits σ -symmetry. While all above mentioned rules apply to π -orbitals, this is not necessarily the case for σ -orbitals. Rather, they differ in a few points, which can easily be logically deduced. Since σ -orbitals do not promote conjugation, the reduction of η will be much lower. They can, on the other hand, accumulate charge much more effectively. Upon rotation, symmetry is broken. For small angles, a net nonzero overlap between substituent and π -system of the backbone exists. A “quasi- π ” orbital is formed, yielding reduced IP. As larger angles, the overlap diminishes due to the spatial separation, and IP is increased again.

6.4.2 Conclusion

Donor and acceptor molecules will show large charge transfer when the difference of absolute electronegativity χ of molecule and metal is high, and when their chemical hardness η is low. From several different backbone examples investigated, we found in general rod-like molecules, like acenes, to exhibit the lowest hardness. Heavily branched molecules, especially those which are linked in meta-position, are generally less well conjugated. Inclusion of hetero atoms into the backbone dramatically changes χ in either

direction, depending on whether the lone pair is incorporated into the π -system or not. The electronegativity increases with group number and decreases with period. Chemical hardness at the same time is always increased with respect to the pristine molecule. Transition from benzoid to quinoid structures also poses a powerful tool. Oxidizing / reducing a given molecule will obviously rise / lower its χ considerably. At the same time, the stability of an $4n+2$ electron system is abandoned, lowering η . Choosing nature and position of substituents is a more difficult task. We have shown that at least for acenes as backbone, the Hammett constant σ_p provides a good first estimate on the impact on IP, EA, or χ . The change of η was rather insensitive to the nature of the functional group. Maximization of the effect can be achieved by considering the resonance effect and the field effect separately, via Swain-Lupton constants. The net effect of F is driven by the charge difference to the substitution site: the larger the atomic charge of the substitution site, the larger the impact. Furthermore, the impact of F is the (qualitatively) the same for IP, EA, and χ . The resonance effect, R, on the other hand, is driven by the magnitude of the frontier MO-coefficients. IP is determined by the value of the HOMO, EA by that of the LUMO. By making careful use of these relation, it is possible to fine tune IP and EA more or less separately.

Bibliography

- [1] Tang, C. W. and VanSlyke, S. A. *Applied Physics Letters* **51**(12), 913 (1987).
- [2] Burroughes, J. H., Bradley, D. D. C., Brown, A. R., Marks, R. N., Mackay, K., Friend, R. H., Burns, P. L., and Holmes, A. B. *Nature* **347**(6293), 539–541 (1990).
- [3] Friend, R. H., Gymer, R. W., Holmes, A. B., Burroughes, J. H., Marks, R. N., Taliani, C., Bradley, D. D. C., Santos, D. A. D., Bredas, J. L., and Logdlun, M. *Nature* **397**(6715), 121–128 (1999).
- [4] Garnier, F., Hajlaoui, R., Yassar, A., and Srivastava, P. *Science* **265**(5179), 1684–1686 (1994).
- [5] Sirringhaus, H. *Science* **290**(5499), 2123–2126 (2000).
- [6] Horowitz, G. *Journal of Materials Research* **19**(7), 1946–1962 (2004).
- [7] Sirringhaus, H. *Advanced Materials* **17**(20), 2411–2425 (2005).
- [8] Sariciftci, N. S., Smilowitz, L., Heeger, A. J., and Wudl, F. *Science* **258**(5087), 1474–1476 (1992).
- [9] Hoppe, H. and Sariciftci, N. S. *Journal of Materials Research* **19**(7), 1924–1945 (2004).
- [10] Ishii, H., Sugiyama, K., Ito, E., and Seki, K. *Advanced Materials* **11**(8), 605–625 (1999).
- [11] Koch, N. *ChemPhysChem* **8**(10), 1438–1455 (2007).
- [12] Braun, S., Osikowicz, W., Wang, Y., and Salaneck, W. R. *Organic electronics* **8**(1), 14–20 (2007).
- [13] Nüesch, F., Forsythe, E. W., Le, Q. T., Gao, Y., and Rothberg, L. J. *Journal of Applied Physics* **87**(11), 7973 (2000).
- [14] Cao, Y., Yu, G., Parker, I. D., and Heeger, A. J. *Journal of Applied Physics* **88**, 3618 (2000).
- [15] Chan, M. Y., Lai, S. L., Fung, M. K., Tong, S. W., Lee, C. S., and Lee, S. T. *Applied Physics Letters* **82**(11), 1784 (2003).
- [16] Pfeiffer, M. *Organic Electronics* **4**(2-3), 89–103 (2003).
- [17] Wang, S., Kanai, K., Kawabe, E., Ouchi, Y., and Seki, K. *Chemical Physics Letters* **423**(1-3), 170–173 (2006).

- [18] Chan, C. K., Amy, F., Zhang, Q., Barlow, S., Marder, S., and Kahn, A. *Chemical Physics Letters* **431**(1-3), 67–71 (2006).
- [19] Prime, K. and Whitesides, G. *Science* **252**(5009), 1164–1167 (1991).
- [20] Chen, J. *Science* **286**(5444), 1550–1552 (1999).
- [21] Schreiber, F. *Progress in Surface Science* **65**(5-8), 151–257 (2000).
- [22] Heimel, G., Romaner, L., Bredas, J., and Zojer, E. *Physical Review Letters* **96**(19) (2006).
- [23] Lindell, L., de Jong, M. P., Osikowicz, W., Lazzaroni, R., Berggren, M., Salaneck, W. R., and Crispin, X. *The Journal of Chemical Physics* **122**(8), 084712 (2005).
- [24] Romaner, L., Heimel, G., Bredas, J., Gerlach, A., Schreiber, F., Johnson, R., Zegenhagen, J., Duhm, S., Koch, N., and Zojer, E. *Physical Review Letters* **99**(25) (2007).
- [25] Fernandez-Torrente, I., Monturet, S., Franke, K., Fraxedas, J., Lorente, N., and Pascual, J. *Physical Review Letters* **99**(17) (2007).
- [26] Vazquez, H., Flores, F., and Kahn, A. *Organic Electronics* **8**(2-3), 241–248 (2007).
- [27] Bröker, B., Blum, R., Beverina, L., Hofmann, O. T., Sassi, M., Ruffo, R., Pagani, G. A., Heimel, G., Vollmer, A., Frisch, J., Rabe, J. P., Zojer, E., and Koch, N. *ChemPhysChem* **10**(17), 2947–2954 (2009).
- [28] Koch, N. *Journal of Physics: Condensed Matter* **20**(18), 184008 (2008).
- [29] Braun, S., Salaneck, W. R., and Fahlman, M. *Advanced Materials* **21**(14-15), 1450–1472 (2009).
- [30] Ito, E., Oji, H., Ishii, H., Oichi, K., Ouchi, Y., and Seki, K. *Chemical Physics Letters* **287**(1-2), 137–142 (1998).
- [31] Wan, A., Hwang, J., Amy, F., and Kahn, A. *Organic Electronics* **6**(1), 47–54 (2005).
- [32] Hückstädt, C., Schmidt, S., Hüfner, S., Forster, F., Reinert, F., and Springborg, M. *Physical Review B* **73**(7) (2006).
- [33] Grobosch, M. and Knupfer, M. *Advanced Materials* **19**(5), 754–756 (2007).
- [34] Abad, E., Ortega, J., Dappe, Y. J., and Flores, F. *Applied Physics A* **95**(1), 119–124 (2008).
- [35] Neaton, J., Hybertsen, M., and Louie, S. *Physical Review Letters* **97**(21) (2006).
- [36] Li, Y., Lu, D., and Galli, G. *Journal of Chemical Theory and Computation* **5**(4), 881–886 (2009).

- [37] Hofmann, O. T., Rangger, G. M., and Zojer, E. *The Journal of Physical Chemistry C* **112**(51), 20357–20365 (2008).
- [38] Rusu, P. C., Giovannetti, G., Weijtens, C., Coehoorn, R., and Brocks, G. *The Journal of Physical Chemistry C* **113**(23), 9974–9977 (2009).
- [39] Sau, J., Neaton, J., Choi, H., Louie, S., and Cohen, M. *Physical Review Letters* **101**(2) (2008).
- [40] Johansson, N., Osada, T., Stafström, S., Salaneck, W. R., Parente, V., dos Santos, D. A., Crispin, X., and Bredas, J. L. *The Journal of Chemical Physics* **111**(5), 2157 (1999).
- [41] Tengstedt, C., Unge, M., de Jong, M., Stafström, S., Salaneck, W., and Fahlman, M. *Physical Review B* **69**(16) (2004).
- [42] Fahlman, M., Crispin, A., Crispin, X., Henze, S. K. M., Jong, M. P. D., Osikowicz, W., Tengstedt, C., and Salaneck, W. R. *Journal of Physics: Condensed Matter* **19**, 183202 (2007).
- [43] Rissner, F., Rangger, G. M., Hofmann, O. T., Track, A. M., Heimel, G., and Zojer, E. *ACS Nano* **3**(11), 3513–3520 (2009).
- [44] Braun, S. and Salaneck, W. R. *Chemical Physics Letters* **438**(4-6), 259–262 (2007).
- [45] Vazquez, H., Oszwaldowski, R., Pou, P., Ortega, J., Perez, R., Flores, F., and Kahn, A. *Europhysics Letters (EPL)* **65**(6), 802–808 (2004).
- [46] Oszwaldowski, R., Vázquez, H., Pou, P., Ortega, J., Pérez, R., and Flores, F. *Journal of Physics: Condensed Matter* **15**(38), S2665–S2678 (2003).
- [47] Vazquez, H., Flores, F., Oszwaldowski, R., Ortega, J., Perez, R., and Kahn, A. *Applied Surface Science* **234**(1-4), 107–112 (2004).
- [48] Vazquez, H., Dappe, Y. J., Ortega, J., and Flores, F. *The Journal of Chemical Physics* **126**(14), 144703 (2007).
- [49] Flores, F., Ortega, J., and Vazquez, H. *Physical Chemistry Chemical Physics* **11**(39), 8658 (2009).
- [50] Bagus, P., Staemmler, V., and Wöll, C. *Physical Review Letters* **89**(9) (2002).
- [51] Kresse, G. and Hafner, J. *Physical Review B* **47**(1), 558–561 (1993).
- [52] Kresse, G. and Hafner, J. *Physical Review B* **48**(17), 13115–13118 (1993).
- [53] Kresse, G. and Furthmüller, J. *Physical Review B* **54**(16), 11169–11186 (1996).
- [54] Perdew, J. P., Jackson, K. A., Pederson, M. R., Singh, D. J., and Fiolhais, C. *Physical Review B* **46**(11), 6671–6687 (1992).

- [55] Blöchl, P. *Physical Review B* **50**(24), 17953–17979 (1994).
- [56] Kresse, G. and Joubert, D. *Physical Review B* **59**(3), 1758–1775 (1999).
- [57] Monkhorst, H. and Pack, J. *Physical Review B* **13**(12), 5188–5192 (1976).
- [58] Methfessel, M. and Paxton, A. *Physical Review B* **40**(6), 3616–3621 (1989).
- [59] Tersoff, J. and Hamann, D. R. *Physical Review B* **31**(2), 805–813 (1985).
- [60] Heimel, G., Romaner, L., Bredas, J. L., and Zojer, E. *Surface Science* **600**(19), 4548–4562 (2006).
- [61] Soler, J. M., Artacho, E., Gale, J. D., Garcia, A., Junquera, J., Ordejon, P., and Sanchez-Portal, D. *Journal of Physics: Condensed Matter* **14**, 2745 (2002).
- [62] Nelin, C. J., Bagus, P. S., and Philpott, M. R. *The Journal of Chemical Physics* **87**(4), 2170 (1987).
- [63] Romaner, L. *PhD thesis, Graz University of Technology* (2007).
- [64] Mulliken, R. S. *The Journal of Chemical Physics* **36**(12), 3428 (1962).
- [65] Singh, U. C. and Kollman, P. A. *Journal of Computational Chemistry* **5**(2), 129–145 (1984).
- [66] Cioslowski, J. *Journal of the American Chemical Society* **111**(22), 8333–8336 (1989).
- [67] Reed, A. E., Curtiss, L. A., and Weinhold, F. *Chemical Reviews* **88**(6), 899–926 (1988).
- [68] Perdew, J. P., Burke, K., and Ernzerhof, M. *Physical Review Letters* **78**(7), 1396–1396 (1997).
- [69] Rangger, G. M. *PhD thesis, Graz University of Technology* (2010).
- [70] Gruber, M. *Diploma thesis, Graz University of Technology* (2006).
- [71] Frisch, M. J., Trucks, G. W., Schlegel, H. B., Scuseria, G. E., Robb, M. A., Cheeseman, J. R., Montgomery, Jr., J. A., Vreven, T., Kudin, K. N., Burant, J. C., Millam, J. M., Iyengar, S. S., Tomasi, J., Barone, V., Mennucci, B., Cossi, M., Scalmani, G., Rega, N., Petersson, G. A., Nakatsuji, H., Hada, M., Ehara, M., Toyota, K., Fukuda, R., Hasegawa, J., Ishida, M., Nakajima, T., Honda, Y., Kitao, O., Nakai, H., Klene, M., Li, X., Knox, J. E., Hratchian, H. P., Cross, J. B., Bakken, V., Adamo, C., Jaramillo, J., Gomperts, R., Stratmann, R. E., Yazyev, O., Austin, A. J., Cammi, R., Pomelli, C., Ochterski, J. W., Ayala, P. Y., Morokuma, K., Voth, G. A., Salvador, P., Dannenberg, J. J., Zakrzewski, V. G., Dapprich, S., Daniels, A. D., Strain, M. C., Farkas, O., Malick, D. K., Rabuck, A. D., Raghavachari, K., Foresman, J. B., Ortiz, J. V., Cui, Q., Baboul, A. G., Clifford, S., Cioslowski, J., Stefanov, B. B., Liu, G., Liashenko, A., Piskorz, P., Komaromi, I., Martin, R. L., Fox, D. J., Keith, T., Al-Laham, M. A., Peng, C. Y.,

- Nanayakkara, A., Challacombe, M., Gill, P. M. W., Johnson, B., Chen, W., Wong, M. W., Gonzalez, C., and Pople, J. A. (2004). Gaussian, Inc., Wallingford, CT.
- [72] Riley, K. E., Holt, B. T. O., and Merz, K. M. *Journal of Chemical Theory and Computation* **3**(2), 407–433 (2007).
- [73] Rienstra-Kiracofe, J. C., Tschumper, G. S., Schaefer, H. F., Nandi, S., and Ellison, G. B. *Chemical Reviews* **102**(1), 231–282 (2002).
- [74] Klein, E. and Lukes, V. *Chemical Physics* **330**(3), 515–525 (2006).
- [75] Nic, M., Jiráť, J., Kosata, B., Jenkins, A., and McNaught, A., editors. *IUPAC Compendium of Chemical Terminology*. IUPAC, Research Triangle Park, NC, 2.1.0 edition, (2009).
- [76] Kutzelnigg, W. *Einführung in die theoretische Chemie*. Wiley-VCH, Weinheim, kompaktausgabe, 1. edition, (2002).
- [77] Jensen, F. *Introduction to computational chemistry*. John Wiley & Sons, Chichester England Hoboken NJ, 2nd ed. edition, (2007).
- [78] Sholl, D. *Density functional theory : a practical introduction*. Wiley, Hoboken N.J., (2009).
- [79] Paier, J., Hirschl, R., Marsman, M., and Kresse, G. *The Journal of Chemical Physics* **122**(23), 234102 (2005).
- [80] Bloch, F. *Zeitschrift für Physik* **52**(7-8), 555–600 (1929).
- [81] Martin, R. *Electronic structure : basic theory and practical methods*. Cambridge University Press, Cambridge UK New York, (2004).
- [82] Kronik, L., Makmal, A., Tiago, M. L., Alemany, M. M. G., Jain, M., Huang, X., Saad, Y., and Chelikowsky, J. R. *physica status solidi (b)* **243**(5), 1063–1079 (2006).
- [83] Marsman, M., Paier, J., Stroppa, A., and Kresse, G. *Journal of Physics: Condensed Matter* **20**(6), 064201 (2008).
- [84] Thayer, J. S. *Journal of Chemical Education* **82**(11), 1721 (2005).
- [85] Valiron, P., Vibok, A., and Mayer, I. *Journal of Computational Chemistry* **14**(4), 401–409 (1993).
- [86] van Duijneveldt, F. B., van Duijneveldt-van de Rijdt, J. G. C. M., and van Lenthe, J. H. *Chemical Reviews* **94**(7), 1873–1885 (1994).
- [87] Hohenberg, P. *Physical Review* **136**(3B), B864–B871 (1964).
- [88] Lieb, E. *Reviews of Modern Physics* **53**(4), 603–641 (1981).
- [89] Kohn, W. and Sham, L. J. *Physical Review* **140**(4A), A1133–A1138 (1965).

- [90] Koopmans, T. *Physica* **1**(1-6), 104–113 (1934).
- [91] Janak, J. *Physical Review B* **18**(12), 7165–7168 (1978).
- [92] Gross, A. *Theoretical surface science : a microscopic perspective*. Springer, Berlin New York, (2003).
- [93] Chong, D. P., Gritsenko, O. V., and Baerends, E. J. *The Journal of Chemical Physics* **116**(5), 1760 (2002).
- [94] Risko, C., Zojer, E., Brocorens, P., Marder, S. R., and Bredas, J. L. *Chemical Physics* **313**(1-3), 151–157 (2005).
- [95] Gritsenko, O. V., Schipper, P. R. T., and Baerends, E. J. *The Journal of Chemical Physics* **107**(13), 5007 (1997).
- [96] Sony, P., Puschnig, P., Nabok, D., and Ambrosch-Draxl, C. *Physical Review Letters* **99**(17) (2007).
- [97] Track, A. M., Rissner, F., Heimel, G., Romaner, L., Kačler, D., Bashir, A., Rangger, G. M., Hofmann, O. T., Bucko, T., Witte, G., and Zojer, E. *The Journal of Physical Chemistry C* **114**(6), 2677–2684 (2010).
- [98] Tsuzuki, S. and Lüthi, H. P. *The Journal of Chemical Physics* **114**(9), 3949 (2001).
- [99] Romaner, L., Nabok, D., Puschnig, P., Zojer, E., and Ambrosch-Draxl, C. *New Journal of Physics* **11**, 053010 (2009).
- [100] Lee, C., Yang, W., and Parr, R. G. *Physical Review B* **37**(2), 785–789 (1988).
- [101] Becke, A. D. *Physical Review A* **38**(6), 3098–3100 (1988).
- [102] Becke, A. D. *The Journal of Chemical Physics* **98**(7), 5648 (1993).
- [103] Paier, J., Marsman, M., and Kresse, G. *The Journal of Chemical Physics* **127**(2), 024103 (2007).
- [104] Stroppa, A. and Kresse, G. *New Journal of Physics* **10**, 063020 (2008).
- [105] Bauschlicher, C. *Chemical Physics Letters* **246**(1-2), 40–44 (1995).
- [106] Oliphant, N. and Bartlett, R. J. *The Journal of Chemical Physics* **100**(9), 6550 (1994).
- [107] Dion, M., Rydberg, H., Schröder, E., Langreth, D., and Lundqvist, B. *Physical Review Letters* **92**(24) (2004).
- [108] Grimme, S. *Journal of Computational Chemistry* **27**(15), 1787–1799 (2006).
- [109] Tkatchenko, A. and Scheffler, M. *Physical Review Letters* **102**(7) (2009).

- [110] Tkatchenko, A., Romaner, L., Hofmann, O. T., Zojer, E., Ambrosch-Draxl, C., and Scheffler, M. *MRS BULLETIN* **35** (2010).
- [111] Kümmel, S. and Kronik, L. *Reviews of Modern Physics* **80**(1), 3–60 (2008).
- [112] Ruzsinszky, A., Perdew, J. P., Csonka, G. I., Vydrov, O. A., and Scuseria, G. E. *The Journal of Chemical Physics* **125**(19), 194112 (2006).
- [113] Ruzsinszky, A., Perdew, J. P., Csonka, G. I., Vydrov, O. A., and Scuseria, G. E. *The Journal of Chemical Physics* **126**(10), 104102 (2007).
- [114] Perdew, J., Ruzsinszky, A., Csonka, G., Vydrov, O., Scuseria, G., Staroverov, V., and Tao, J. *Physical Review A* **76**(4) (2007).
- [115] Bally, T. and Sastry, G. N. *The Journal of Physical Chemistry A* **101**(43), 7923–7925 (1997).
- [116] Tozer, D. J. *The Journal of Chemical Physics* **119**(24), 12697 (2003).
- [117] Perdew, J. P., Levy, M., and Balduz, J. L. *Physical Review Letters* **49**(23), 1691–1694 (1982).
- [118] Kümmel, S., Kronik, L., and Perdew, J. *Physical Review Letters* **93**(21) (2004).
- [119] Perdew, J. and Levy, M. *Physical Review Letters* **51**(20), 1884–1887 (1983).
- [120] Allen, M. and Tozer, D. *Molecular Physics* **100**(4), 433–439 (2002).
- [121] Chan, G. K. *The Journal of Chemical Physics* **110**(10), 4710 (1999).
- [122] Newns, D. *Physical Review* **178**(3), 1123–1135 (1969).
- [123] Bröker, B., Blum, R., Frisch, J., Vollmer, A., Hofmann, O. T., Rieger, R., Müllen, K., Rabe, J. P., Zojer, E., and Koch, N. *Applied Physics Letters* **93**(24), 243303 (2008).
- [124] Rangger, G., Hofmann, O., Romaner, L., Heimel, G., Bröker, B., Blum, R., Johnson, R., Koch, N., and Zojer, E. *Physical Review B* **79**(16) (2009).
- [125] Møller, C. and Plesset, M. S. *Physical Review* **46**(7), 618–622 (1934).
- [126] Kresse, G. personal communication, (2008).
- [127] Crispin, X., Bureau, C., Geskin, V., Lazzaroni, R., and Brédas, J. L. *European Journal of Inorganic Chemistry* **1999**(2), 349–360 (1999).
- [128] Bilic, A., Reimers, J. R., and Hush, N. S. *The Journal of Physical Chemistry B* **106**(26), 6740–6747 (2002).
- [129] Ishii, H., Sugiyama, K., Yoshimura, D., Ito, E., Ouchi, Y., and Seki, K. *IEEE Journal of Selected Topics in Quantum Electronics* **4**(1), 24–33 (1998).

- [130] Crispin, X., Bureau, C., Geskin, V. M., Lazzaroni, R., Salaneck, W. R., and Bredas, J. L. *The Journal of Chemical Physics* **111**, 3237 (1999).
- [131] Gaussian Helpdesk. private email, (2007).
- [132] Tautz, F. S. *Progress in Surface Science* **82**(9-12), 479–520 (2007).
- [133] Avilov, I., Geskin, V., and Cornil, J. *Advanced Functional Materials* **19**(4), 624–633 (2009).
- [134] Campbell, I. H., Rubin, S., Zawodzinski, T. A., Kress, J. D., Martin, R. L., Smith, D. L., Barashkov, N. N., and Ferraris, J. P. *Physical Review B* **54**(20), 14321–14324 (1996).
- [135] Campbell, I. H., Kress, J. D., Martin, R. L., Smith, D. L., Barashkov, N. N., and Ferraris, J. P. *Applied Physics Letters* **71**, 3528 (1997).
- [136] Zehner, R. W., Parsons, B. F., Hsung, R. P., and Sita, L. R. *Langmuir* **15**(4), 1121–1127 (1999).
- [137] Zuppiroli, L., Si-Ahmed, L., Kamaras, K., Nüesch, F., Bussac, M. N., Ades, D., Siove, A., Moons, E., and Grätzel, M. *The European Physical Journal B* **11**(3), 505–512 (1999).
- [138] Ganzorig, C., Kwak, K., Yagi, K., and Fujihira, M. *Applied Physics Letters* **79**(2), 272 (2001).
- [139] Hatton, R. *Thin Solid Films* **394**(1-2), 291–296 (2001).
- [140] Yan, H., Huang, Q., Cui, J., Veinot, J., Kern, M., and Marks, T. *Advanced Materials* **15**(10), 835–838 (2003).
- [141] Alloway, D. M., Hofmann, M., Smith, D. L., Gruhn, N. E., Graham, A. L., Colorado, R., Wysocki, V. H., Lee, T. R., Lee, P. A., and Armstrong, N. R. *Journal of Physical Chemistry B-Condensed Phase* **107**(42), 11690–11699 (2003).
- [142] de Boer, B., Hadipour, A., Mandoc, M. M., van Woudenberg, T., and Blom, P. W. M. *Advanced Materials* **17**(5), 621–625 (2005).
- [143] Heimel, G., Romaner, L., Zojer, E., and Bredas, J. *Nano Letters* **7**(4), 932–940 (2007).
- [144] Koch, N., Duhm, S., Rabe, J., Vollmer, A., and Johnson, R. *Physical Review Letters* **95**(23) (2005).
- [145] Koch, N., Duhm, S., Rabe, J. P., Rentenberger, S., Johnson, R. L., Klankermayer, J., and Schreiber, F. *Applied Physics Letters* **87**(10), 101905 (2005).
- [146] Duhm, S., Glowatzki, H., Cimpeanu, V., Klankermayer, J., Rabe, J. P., Johnson, R. L., and Koch, N. *The Journal of Physical Chemistry B* **110**(42), 21069–21072 (2006).

- [147] Duhm, S., Glowatzki, H., Rabe, J. P., Koch, N., and Johnson, R. L. *Applied Physics Letters* **90**(12), 122113 (2007).
- [148] Werner, A. G., Li, F., Harada, K., Pfeiffer, M., Fritz, T., and Leo, K. *Applied Physics Letters* **82**(25), 4495 (2003).
- [149] Chan, C. K., Kim, E., Breas, J., and Kahn, A. *Advanced Functional Materials* **16**(6), 831–837 (2006).
- [150] Lindell, L., Unge, M., Osikowicz, W., Stafström, S., Salaneck, W. R., Crispin, X., and de Jong, M. P. *Applied Physics Letters* **92**(16), 163302 (2008).
- [151] Lu, T., Cotton, T. M., Birke, R. L., and Lombardi, J. R. *Langmuir* **5**(2), 406–414 (1989).
- [152] Yang, H. and McCreery, R. L. *Analytical Chemistry* **71**(18), 4081–4087 (1999).
- [153] Park, Y. S., Um, S. Y., and Yoon, K. B. *Journal of the American Chemical Society* **121**(13), 3193–3200 (1999).
- [154] Ock, J., Shin, H., Kwon, Y., and Miyake, J. *Colloids and Surfaces A: Physico-chemical and Engineering Aspects* **257-258**, 351–355 (2005).
- [155] Marder, S. R., Kippelen, B., Jen, A. K., and Peyghambarian, N. *Nature* **388**(6645), 845–851 (1997).
- [156] Ferraris, J., Cowan, D. O., Walatka, V., and Perlstein, J. H. *Journal of the American Chemical Society* **95**(3), 948–949 (1973).
- [157] Coleman, L. *Solid State Communications* **12**(11), 1125–1132 (1973).
- [158] Nollau, A., Pfeiffer, M., Fritz, T., and Leo, K. *Journal of Applied Physics* **87**(9), 4340 (2000).
- [159] Takashima, W., Murasaki, T., Nagamatsu, S., Morita, T., and Kaneto, K. *Applied Physics Letters* **91**(7), 071905 (2007).
- [160] Romaner, L., Heimel, G., Gruber, M., Bredas, J., and Zojer, E. *Small* **2**(12), 1468–1475 (2006).
- [161] Kokalj, A. *Journal of Molecular Graphics and Modelling* **17**(3-4), 176–179 (1999).
- [162] Swart, M., Wijst, T., Guerra, C. F., and Bickelhaupt, F. M. *Journal of Molecular Modeling* **13**(12), 1245–1257 (2007).
- [163] Johnson, E. R. and DiLabio, G. A. *Chemical Physics Letters* **419**(4-6), 333–339 (2006).
- [164] Rohlfing, M., Temirov, R., and Tautz, F. *Physical Review B* **76**(11) (2007).
- [165] Rangger, G. M., Romaner, L., Heimel, G., and Zojer, E. *Surface and Interface Analysis* **40**(3-4), 371–378 (2008).

- [166] Blyholder, G. *The Journal of Physical Chemistry* **68**(10), 2772–2777 (1964).
- [167] Romaner, L., Heimel, G., and Zojer, E. *Physical Review B* **77**(4) (2008).
- [168] Vollmer, A., Jurchescu, O. D., Arfaoui, I., Salzmann, I., Palstra, T. T. M., Rudolf, P., Niemax, J., Pflaum, J., Rabe, J. P., and Koch, N. *The European Physical Journal E* **17**(3), 339–343 (2005).
- [169] Monk, P. *The viologens : physicochemical properties, synthesis, and applications of the salts of 4,4'-bipyridine*. Wiley, Chichester New York, (1998).
- [170] Hill, I. G., Kahn, A., Soos, Z. G., and Pascal, J. *Chemical Physics Letters* **327**(3-4), 181–188 (2000).
- [171] Lof, R., van Veenendaal, M., Koopmans, B., Jonkman, H., and Sawatzky, G. *Physical Review Letters* **68**(26), 3924–3927 (1992).
- [172] Benning, P., Poirier, D., Ohno, T., Chen, Y., Jost, M., Stepniak, F., Kroll, G., Weaver, J., Fure, J., and Smalley, R. *Physical Review B* **45**(12), 6899–6913 (1992).
- [173] Schenk, R., Gregorius, H., and Müllen, K. *Advanced Materials* **3**(10), 492–493 (1991).
- [174] Guay, J., Kasai, P., Diaz, A., Wu, R., Tour, J. M., and Dao, L. H. *Chemistry of Materials* **4**(5), 1097–1105 (1992).
- [175] Gregorius, H., Heitz, W., and Müllen, K. *Advanced Materials* **5**(4), 279–281 (1993).
- [176] Narioka, S., Ishii, H., Yoshimura, D., Sei, M., Ouchi, Y., Seki, K., Hasegawa, S., Miyazaki, T., Harima, Y., and Yamashita, K. *Applied Physics Letters* **67**(13), 1899 (1995).
- [177] Jaeckel, B., Sambur, J. B., and Parkinson, B. A. *Journal of Applied Physics* **103**(6), 063719 (2008).
- [178] McNellis, E. R., Meyer, J., and Reuter, K. *Physical Review B* **80**(20) (2009).
- [179] Hill, I. G., Rajagopal, A., Kahn, A., and Hu, Y. *Applied Physics Letters* **73**, 662 (1998).
- [180] Sellam, F. *Surface Science* **478**(1-2), 113–121 (2001).
- [181] Hauschild, A., Karki, K., Cowie, B., Rohlfing, M., Tautz, F., and Sokolowski, M. *Physical Review Letters* **94**(3) (2005).
- [182] Zou, Y., Kilian, L., Scholl, A., Schmidt, T., Fink, R., and Umbach, E. *Surface Science* **600**(6), 1240–1251 (2006).
- [183] Dori, N., Menon, M., Kilian, L., Sokolowski, M., Kronik, L., and Umbach, E. *Physical Review B* **73**(19) (2006).

- [184] Jalkanen, J. and Zerbetto, F. *The Journal of Physical Chemistry B* **110**(11), 5595–5601 (2006).
- [185] Duhm, S., Gerlach, A., Salzmann, I., Broker, B., Johnson, R., Schreiber, F., and Koch, N. *Organic Electronics* (2007).
- [186] Gerlach, A., Sellner, S., Schreiber, F., Koch, N., and Zegenhagen, J. *Physical Review B* **75**(4) (2007).
- [187] Henze, S., Bauer, O., Lee, T., Sokolowski, M., and Tautz, F. *Surface Science* **601**(6), 1566–1573 (2007).
- [188] Forker, R., Golnik, C., Pizzi, G., Dienel, T., and Fritz, T. *Organic Electronics* (2009).
- [189] Abbasi, A. and Scholz, R. *The Journal of Physical Chemistry C* **113**(46), 19897–19904 (2009).
- [190] Huang, H., Chen, S., Gao, X., Chen, W., and Wee, A. T. S. *ACS Nano* **3**(11), 3431–3436 (2009).
- [191] Glowatzki, H., Bröker, B., Blum, R., Hofmann, O. T., Vollmer, A., Rieger, R., Müllen, K., Zojer, E., Rabe, J. P., and Koch, N. *Nano Letters* **8**(11), 3825–3829 (2008).
- [192] Bröker, B., Hofmann, O., Rangger, G., Frank, P., Blum, R., Rieger, R., Venema, L., Vollmer, A., Müllen, K., Rabe, J., Winkler, A., Rudolf, P., Zojer, E., and Koch, N. *Physical Review Letters* **104**(24) (2010).
- [193] Kahn, A., Koch, N., and Gao, W. *Journal of Polymer Science Part B: Polymer Physics* **41**(21), 2529–2548 (2003).
- [194] Zhou, X., Pfeiffer, M., Blochwitz, J., Werner, A., Nollau, A., Fritz, T., and Leo, K. *Applied Physics Letters* **78**(4), 410 (2001).
- [195] Maennig, B., Gebeyehu, D., Simon, P., Kozłowski, F., Werner, A., Li, F., Grundmann, S., Sonntag, S., Koch, M., Leo, K., Pfeiffer, M., Hoppe, H., Meissner, D., Sariciftci, N., Riedel, I., Dyakonov, V., Parisi, J., and Drechsel, J. *Applied Physics A: Materials Science & Processing* **79**(1), 1–14 (2004).
- [196] DAndrade, B. W., Forrest, S. R., and Chwang, A. B. *Applied Physics Letters* **83**(19), 3858 (2003).
- [197] He, G. *Journal of Applied Physics* **95**(10), 5773 (2004).
- [198] Lim, E., Jung, B., Chikamatsu, M., Azumi, R., Yoshida, Y., Yase, K., Do, L., and Shim, H. *Journal of Materials Chemistry* **17**(14), 1416 (2007).
- [199] Ma, L., Lee, W. H., Park, Y. D., Kim, J. S., Lee, H. S., and Cho, K. *Applied Physics Letters* **92**(6), 063310 (2008).

- [200] Li, F., Jia, W., Wang, S., Zhao, Y., and Lu, Z. *Journal of Applied Physics* **103**(3), 034509 (2008).
- [201] Drechsel, J. *Synthetic Metals* **127**(1-3), 201–205 (2002).
- [202] Gao, Z. Q., Mi, B. X., Xu, G. Z., Wan, Y. Q., Gong, M. L., Cheah, K. W., and Chen, C. H. *Chemical Communications* (1), 117 (2008).
- [203] Kanakarajan, K. and Czarnik, A. W. *The Journal of Organic Chemistry* **51**(26), 5241–5243 (1986).
- [204] Rademacher, J. T., Kabajarajan, K., and Czarnik, A. W. *Synthesis (Stuttgart)* **4**, 378–380 (1994).
- [205] Szalay, P. S., Galaan-Mascaras, J. R., Clerac, R., and Dunbar, K. R. *Synthetic Metals* **122**(3), 535–542 (2001).
- [206] Szalay, P. S., Galan-Mascaras, J. R., Schottel, B. L., Bacsá, J., Perez, L. M., Ichimura, A. S., Chouai, A., and Dunbar, K. R. *Journal of Cluster Science* **15**(4), 503–530 (2004).
- [207] Beeson, J. C., Fitzgerald, L. J., Gallucci, J. C., Gerkin, R. E., Rademacher, J. T., and Czarnik, A. W. *Journal of the American Chemical Society* **116**(11), 4621–4622 (1994).
- [208] Furukawa, S., Okubo, T., Masaoka, S., Tanaka, D., Chang, H. C., and Kitagawa, S. *Angewandte Chemie International Edition* **44**(18), 2700–2704 (2005).
- [209] Laschat, S., Baro, A., Steinke, N., Giesselmann, F., Hägele, C., Scalia, G., Judele, R., Kapatsina, E., Sauer, S., Schreivogel, A., and Tosoni, M. *Angewandte Chemie International Edition* **46**(26), 4832–4887 (2007).
- [210] Liao, L. S., Slusarek, W. K., Hatwar, T. K., Ricks, M. L., and Comfort, D. L. *Advanced Materials* **20**(2), 324–329 (2008).
- [211] Chang, T., Wu, B., Chiang, M. Y., Liao, S., Ong, C. W., Hsu, H., and Lin, S. *Organic Letters* **7**(19), 4075–4078 (2005).
- [212] Methfessel, M., Fiorentini, V., and Oppo, S. *Physical Review B* **61**(8), 5229–5236 (2000).
- [213] Morikawa, Y. *Surface Science* **507-510**(1-3), 46–50 (2002).
- [214] Vackár, J., Hytha, M., and Limunek, A. *Physical Review B* **58**(19), 12712–12720 (1998).
- [215] Hoffmann, F. *Surface Science Reports* **3**(2-3), 107 (1983).
- [216] Langreth, D. *Physical Review Letters* **54**(2), 126–129 (1985).
- [217] Natan, A., Kronik, L., Haick, H., and Tung, R. T. *Advanced Materials* **19**(23), 4103–4117 (2007).

- [218] Macdonald, J. R. and Barlow, C. A. *The Journal of Chemical Physics* **39**(2), 412 (1963).
- [219] Dong, Z., Guo, X., Trifonov, A., Dorozhkin, P., Miki, K., Kimura, K., Yokoyama, S., and Mashiko, S. *Physical Review Letters* **92**(8) (2004).
- [220] Ruppel, L., Birkner, A., Witte, G., Busse, C., Lindner, T., Paasch, G., and Wöll, C. *Journal of Applied Physics* **102**(3), 033708 (2007).
- [221] Franke, K., Schulze, G., Henningsen, N., Fernández-Torrente, I., Pascual, J., Zarwell, S., Rück-Braun, K., Cobian, M., and Lorente, N. *Physical Review Letters* **100**(3) (2008).
- [222] Gerlach, A., Schreiber, F., Sellner, S., Dosch, H., Vartanyants, I., Cowie, B., Lee, T., and Zegenhagen, J. *Physical Review B* **71**(20) (2005).
- [223] Zegenhagen, J. *Surface Science Reports* **18**(7-8), 202 – 271 (1993).
- [224] Stadler, C., Hansen, S., Kröger, I., Kumpf, C., and Umbach, E. *Nature Physics* **5**(2), 153–158 (2009).
- [225] Repp, J., Meyer, G., Stojkovic, S. M., Gourdon, A., and Joachim, C. *Physical Review Letters* **94**(2), 26803 (2005).
- [226] Repp, J. and Meyer, G. *Applied Physics A* **85**(4), 399–406 (2006).
- [227] Ferri, V., Elbing, M., Pace, G., Dickey, M., Zharnikov, M., Samori, P., Mayor, M., and Rampi, M. A. *Angewandte Chemie International Edition* **47**(18), 3407–3409 (2008).
- [228] Bock, C., Pham, D. V., Kunze, U., Käfer, D., Witte, G., and Wöll, C. *Journal of Applied Physics* **100**(11), 114517 (2006).
- [229] Ge, Y., Weidner, T., Ahn, H., Whitten, J. E., and Zharnikov, M. *The Journal of Physical Chemistry C* **113**(11), 4575–4583 (2009).
- [230] Heimel, G., Rissner, F., and Zojer, E. *Advanced Materials* , 2494–2513 (2010).
- [231] Braun, S., de Jong, M. P., Osikowicz, W., and Salaneck, W. R. *Applied Physics Letters* **91**(20), 202108 (2007).
- [232] Crispin, A., Crispin, X., Fahlman, M., Berggren, M., and Salaneck, W. R. *Applied Physics Letters* **89**(21), 213503 (2006).
- [233] Osikowicz, W., de Jong, M. P., and Salaneck, W. R. *Advanced Materials* **19**(23), 4213–4217 (2007).
- [234] Koch, N., Gerlach, A., Duhm, S., Glowatzki, H., Heimel, G., Vollmer, A., Sakamoto, Y., Suzuki, T., Zegenhagen, J., Rabe, J. P., and Schreiber, F. *Journal of the American Chemical Society* **130**(23), 7300–7304 (2008).
- [235] Rusu, P. and Brocks, G. *Physical Review B* **74**(7) (2006).

- [236] Egger, D. A., Rissner, F., Rangger, G. M., Hofmann, O. T., Wittwer, L., Heimel, G., and Zojer, E. *Physical Chemistry Chemical Physics* **12**(17), 4291 (2010).
- [237] Tseng, T., Urban, C., Wang, Y., Otero, R., Tait, S. L., Alcama, M., Acija, D., Trelka, M., Gallego, J. M., Lin, N., Konuma, M., Starke, U., Nefedov, A., Langner, A., Wöll, C., Herranz, M. A., Martin, F., Martin, N., Kern, K., and Miranda, R. *Nature Chemistry* **2**(5), 374–379 (2010).
- [238] Azzam, W., Fuxen, C., Birkner, A., Rong, H., Buck, M., and Wöll, C. *Langmuir* **19**(12), 4958–4968 (2003).
- [239] Bucko, T., Hafner, J., and Ayngyan, J. G. *The Journal of Chemical Physics* **122**(12), 124508 (2005).
- [240] Frank, P., Koch, N., Koini, M., Rieger, R., Müllen, K., Resel, R., and Winkler, A. *Chemical Physics Letters* **473**(4-6), 321–325 (2009).
- [241] Li, F., Zhou, Y., Zhang, F., Liu, X., Zhan, Y., and Fahlman, M. *Chemistry of Materials* **21**(13), 2798–2802 (2009).
- [242] Baker, J. and Pulay, P. *The Journal of Chemical Physics* **105**(24), 11100 (1996).
- [243] Anglada, E., Soler, J. M., Junquera, J., and Artacho, E. *Physical Review B* **66**(20) (2002).
- [244] Garcia-Gil, S., Garcia, A., Lorente, N., and Ordejon, P. *Physical Review B* **79**(7) (2009).
- [245] Perdew, J. P., Ruzsinszky, A., Constantin, L. A., Sun, J., and Csonka, G. I. *Journal of Chemical Theory and Computation* **5**(4), 902–908 (2009).
- [246] Mori-Sanchez, P., Cohen, A. J., and Yang, W. *The Journal of Chemical Physics* **125**(20), 201102 (2006).
- [247] Mori-Sanchez, P., Cohen, A., and Yang, W. *Physical Review Letters* **100**(14) (2008).
- [248] Körzdörfer, T., Kümmel, S., Marom, N., and Kronik, L. *Physical Review B* **79**(20) (2009).
- [249] Freysoldt, C., Rinke, P., and Scheffler, M. *Physical Review Letters* **103**(5) (2009).
- [250] Grimme, S., Antony, J., Schwabe, T., and Mück-Lichtenfeld, C. *Organic & Biomolecular Chemistry* **5**(5), 741 (2007).
- [251] Schreiber, F. *physica status solidi (a)* **201**(6), 1037–1054 (2004).
- [252] Diao, Y., Han, M., Wan, L., Itaya, K., Uchida, T., Miyake, H., Yamakata, A., and Osawa, M. *Langmuir* **22**(8), 3640–3646 (2006).
- [253] Breuer, S., Pham, D. T., Huemann, S., Gentz, K., Zoerlein, C., Hunger, R., Wandelt, K., and Broekmann, P. *New Journal of Physics* **10**, 125033 (2008).

- [254] Hughbanks, T. and Hoffmann, R. *Journal of the American Chemical Society* **105**(11), 3528–3537 (1983).
- [255] Hoffmann, R. *Reviews of Modern Physics* **60**(3), 601–628 (1988).
- [256] Bagus, P. and Illas, F. *Physical Review B* **42**(17), 10852–10857 (1990).
- [257] Peumans, P. and Forrest, S. R. *Applied Physics Letters* **79**(1), 126 (2001).
- [258] Ishii, H., Hayashi, N., Ito, E., Washizu, Y., Sugi, K., Kimura, Y., Niwano, M., Ouchi, Y., and Seki, K. *physica status solidi (a)* **201**(6), 1075–1094 (2004).
- [259] Wu, K., Yu, S., and Tao, Y. *Langmuir* **25**(11), 6232–6238 (2009).
- [260] Zaumseil, J. and Sirringhaus, H. *Chemical Reviews* **107**(4), 1296–1323 (2007).
- [261] Tadayyon, S. M., Griffiths, K., Norton, P. R., Tripp, C., and Popovic, Z. *Journal of Vacuum Science & Technology A: Vacuum, Surfaces, and Films* **17**, 1773 (1999).
- [262] Beierlein, T. *Synthetic Metals* **111-112**(1-2), 295–297 (2000).
- [263] Suzue, Y., Manaka, T., and Iwamoto, M. *Japanese Journal of Applied Physics* **44**(No. 1B), 561–565 (2005).
- [264] Rentenberger, S., Vollmer, A., Zojer, E., Schennach, R., and Koch, N. *Journal of Applied Physics* **100**(5), 053701 (2006).
- [265] Koch, N., Zojer, E., Rajagopal, A., Ghjisen, J., Johnson, R. L., Leising, G., and Pireaux, J. *Advanced Functional Materials* **11**(1), 51–58 (2001).
- [266] Crispin, X., Geskin, V., Crispin, A., Cornil, J., Lazzaroni, R., Salaneck, W. R., and Bredas, J. *Journal of the American Chemical Society* **124**(27), 8131–8141 (2002).
- [267] Bagus, P. S., Hermann, K., and Woźniak, C. *The Journal of Chemical Physics* **123**(18), 184109 (2005).
- [268] Prada, S., Martinez, U., and Pacchioni, G. *Physical Review B* **78**(23) (2008).
- [269] Han, P., Mantooth, B. A., Sykes, E. C. H., Donhauser, Z. J., and Weiss, P. S. *Journal of the American Chemical Society* **126**(34), 10787–10793 (2004).
- [270] Smith, N., Chen, C., and Weinert, M. *Physical Review B* **40**(11), 7565–7573 (1989).
- [271] Lu, X., Grobis, M., Khoo, K., Louie, S., and Crommie, M. *Physical Review B* **70**(11) (2004).
- [272] Jäckel, F., Perera, U., Iancu, V., Braun, K., Koch, N., Rabe, J., and Hla, S. *Physical Review Letters* **100**(12) (2008).
- [273] Grimme, S. *Chemistry - A European Journal* **10**(14), 3423–3429 (2004).

- [274] Koch, N., Salzmann, I., Johnson, R., Pflaum, J., Friedlein, R., and Rabe, J. *Organic Electronics* **7**(6), 537–545 (2006).
- [275] Norsko, J. K. *Reports on Progress in Physics* **53**(10), 1253–1295 (1990).
- [276] Chance, R. R. *The Journal of Chemical Physics* **62**(6), 2245 (1975).
- [277] TURBOMOLE V5.7 a development of University of Karlsruhe and Forschungszentrum Karlsruhe GmbH, 1989-2007, TURBOMOLE GmbH, since 2007; available from <http://www.turbomole.com>.
- [278] Salaneck, W. *Conjugated polymer surfaces and interfaces : electronic and chemical structure of interfaces for polymer light emitting devices*. Cambridge University Press, Cambridge New York, (1996).
- [279] Seguy, I., Jolinat, P., Destruel, P., Farenc, J., Mamy, R., Bock, H., Ip, J., and Nguyen, T. P. *Journal of Applied Physics* **89**(10), 5442 (2001).
- [280] Parr, R. G., Donnelly, R. A., Levy, M., and Palke, W. E. *The Journal of Chemical Physics* **68**(8), 3801 (1978).
- [281] Sanderson, R. T. *Science* **114**(2973), 670–672 (1951).
- [282] Pearson, R. G. *Science* **151**(3707), 172–177 (1966).
- [283] Parr, R. G. and Pearson, R. G. *Journal of the American Chemical Society* **105**(26), 7512–7516 (1983).
- [284] Pearson, R. G. *Journal of Chemical Sciences* **117**(5), 369–377 (2005).
- [285] Yang, W. and Parr, R. G. *Proceedings of the National Academy of Sciences* **82**(20), 6723 (1985).
- [286] Mortier, W. J., Ghosh, S. K., and Shankar, S. *Journal of the American Chemical Society* **108**(15), 4315–4320 (1986).
- [287] Barlow, S., Zhang, Q., Kaafarani, B. R., Risko, C., Amy, F., Chan, C. K., Domercq, B., Starikova, Z. A., Antipin, M. Y., Timofeeva, T. V., Kippelen, B., Bredas, J., Kahn, A., and Marder, S. R. *Chemistry - A European Journal* **13**(12), 3537–3547 (2007).
- [288] Zhang, G. and Musgrave, C. B. *The Journal of Physical Chemistry A* **111**(8), 1554–1561 (2007).
- [289] Wu, Z. and Kawazoe, Y. *Chemical Physics Letters* **423**(1-3), 81–86 (2006).
- [290] Gierschner, J., Cornil, J., and Egelhaaf, H. *Advanced Materials* **19**(2), 173–191 (2007).
- [291] Ma, J., Li, S., and Jiang, Y. *Macromolecules* **35**(3), 1109–1115 (2002).
- [292] Salzner, U., Lagowski, J., Pickup, P., and Poirier, R. *Synthetic Metals* **96**(3), 177–189 (1998).

- [293] Luo, Y., Ruud, K., Norman, P., Jonsson, D., and Agren, H. *J. Phys. Chem. B* **102**(10), 1710–1712 (1998).
- [294] Slater, J. *Physical Review* **36**(1), 57–64 (1930).
- [295] Wang, Y., Ma, J., and Jiang, Y. *The Journal of Physical Chemistry A* **109**(32), 7197–7206 (2005).
- [296] Exner, O. *Journal of Physical Organic Chemistry* **12**(4), 265–274 (1999).
- [297] Charton, M. *Journal of Physical Organic Chemistry* **12**(4), 275–282 (1999).
- [298] Hammett, L. P. *Journal of the American Chemical Society* **59**(1), 96–103 (1937).
- [299] Soulen, R. L. *Journal of Chemical Education* **61**(8), A221 (1984).
- [300] Swain, C. G. and Lupton, E. C. *Journal of the American Chemical Society* **90**(16), 4328–4337 (1968).
- [301] Abraham, M. H., Grellier, P. L., Prior, D. V., Taft, R. W., Morris, J. J., Taylor, P. J., Laurence, C., Berthelot, M., Doherty, R. M., and et al., . *Journal of the American Chemical Society* **110**(25), 8534–8536 (1988).
- [302] Hansch, C., Leo, A., and Taft, R. W. *Chemical Reviews* **91**(2), 165–195 (1991).
- [303] Sullivan, J., Jones, A., and Tanji, K. *Journal of Chemical Information and Modeling* **40**(5), 1113–1127 (2000).
- [304] Hansch, C., Maloney, P. P., Fujita, T., and Muir, R. M. *Nature* **194**(4824), 178–180 (1962).
- [305] Kwon, O., Barlow, S., Odom, S. A., Beverina, L., Thompson, N. J., Zojer, E., Bredas, J., and Marder, S. R. *The Journal of Physical Chemistry A* **109**(41), 9346–9352 (2005).